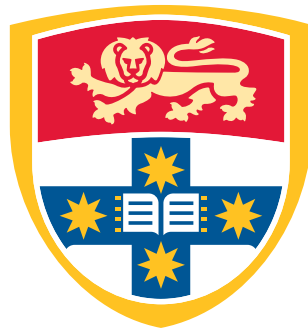


The optical physics of dielectric nanostructures: enabling improved photovoltaic designs

*A thesis submitted in fulfilment of the requirements for the degree of
Doctor of Philosophy*

by

Björn C. P. Sturmberg



*School of Physics
Faculty of Science
University of Sydney
Australia*

February 2016

Statement of originality

The work described in this thesis is mostly my own, and has not been submitted as part of any other degree. The contributions of others are explicitly acknowledged either in the following *Statement of contribution for joint author publications*.

Björn C. P. Sturmborg

Abstract

Sunlight is, by far, the world's most abundant source of energy, and may be converted directly into electricity without the emission of any greenhouse gasses using photovoltaic solar cells (SCs). While the cost of SCs has decreased tremendously in the last decade with the creation of superb economies of scale, there remains a wide scope for technological advancements to improve the cost competitiveness of SCs by reducing costs and increasing efficiencies. We investigate how nanophotonic structures may enable these developments.

A common thread of our studies is to begin by examining the basic interaction of light with a nanostructure, as embodied by the structure's modes, before designing optimised structures for a given application. The simulation tool that we have developed for our investigations is well aligned with this philosophy, and has been made freely available.

We begin by studying thin films, which are inexpensive but whose efficiency is limited by low absorption. To address this deficiency we pattern the absorbers at the nanometer and micrometer scale so that the sunlight excites resonant nanophotonic modes in which it is trapped and strongly absorbed. In particular we study nanowire and nanohole arrays with bi-periodic inclusions of high and low refractive index respectively. By understanding the optical physics of these structures we arrive at a semi-analytic routine for optimising their absorption, and we also study the effects of disorder, showing how including NWs with varying diameter into the array increases the absorption.

An alternative approach is to combine many physically separated SCs into a multi-junction SC to reach efficiencies in excess of 50%. A similar approach may also be used to achieve efficiencies of over 30% using affordable subcells, for instance made from perovskite and silicon. A crucial element in these devices is a wavelength selective filter, which may be made of dielectric gratings with regions of near 100% reflectance. We show these reflections are fundamentally due to the symmetries of these structures' Fano resonances.

Finally, we demonstrate that gratings of deeply subwavelength thickness, composed of metals or relatively weakly-absorbing semiconductors, can absorb nearly 100% of light at a target wavelength. These findings open up many practical applications because, unlike previous demonstrations that used complicated metallic metamaterials and plasmonics, weakly-absorbing semiconductors are abundantly found in nature, are compatible with optoelectronic applications, and can be patterned using standard techniques. Our theoretical findings are experimentally validated at visible wavelengths in a grating made of antimony sulphide.

Author's publications included in this thesis

1. B. C. P. Sturmberg, K. B. Dossou, L. C. Botten, A. A. Asatryan, C. G. Poulton, R. C. McPhedran and C. M. de Sterke. “Nanowire array photovoltaics: Radial disorder versus design for optimal efficiency”. *Appl. Phys. Lett.* **101**, 173902 (2012)
2. B. C. P. Sturmberg, K. B. Dossou, L. C. Botten, A. A. Asatryan, C. G. Poulton, R. C. McPhedran and C. M. de Sterke. “Absorption enhancing proximity effects in aperiodic nanowire arrays”. *Opt. Express* **21**, A964–A969 (2013)
3. B. C. P. Sturmberg, K. B. Dossou, L. C. Botten, A. A. Asatryan, C. G. Poulton, R. C. McPhedran and C. M. de Sterke. “Optimizing Photovoltaic Charge Generation of Nanowire Arrays: Simple Semi-Analytic Approach”. *ACS Photonics* **1**, 683–689 (2014)
4. B. C. P. Sturmberg, K. B. Dossou, L. C. Botten, R. C. McPhedran and C. M. de Sterke. “Fano resonances of dielectric gratings: symmetries and broadband filtering”. *Opt. Express* **23**, A1672 (2015)
5. B. C. P. Sturmberg, K. B. Dossou, F. J. Lawrence, C. G. Poulton, R. C. McPhedran, C. M. de Sterke and L. C. Botten. “EMUstack: an open source route to insightful electromagnetic computation via the Bloch mode scattering matrix method”. *Computer Physics Communications* (In Press)
6. B. C. P. Sturmberg, T. K. Chong, T. P. White, D.-Y. Choi, L. C. Botten, K. B. Dossou, C. G. Poulton, K. R. Catchpole, R. C. McPhedran and C. M. de Sterke. “Total absorption of visible light in ultra-thin weakly-absorbing semiconductor gratings”. *Optica* (Submitted)

Additional publications

1. J. L. Donnelly, B. C. P. Sturmberg, K. B. Dossou, L. C. Botten, A. A. Asatryan, C. G. Poulton, R. C. McPhedran and C. M. de Sterke. “Mode-based analysis of silicon nanohole arrays for photovoltaic applications”. *Opt. Express* **22**, A1343–A1354 (2014)
2. J. S. Brownless, B. C. P. Sturmberg, A. Argyros, B. T. Kuhlmeier and C. M. de Sterke. “Guided modes of a wire medium slab: Comparison of effective medium approaches with exact calculations”. *Phys. Rev. B* **91**, 155427 (2015)

Statement of contribution to publications

B. C. P. Sturmberg, K. B. Dossou, L. C. Botten, A. A. Asatryan, C. G. Poulton, R. C. McPhedran and C. M. de Sterke. “**Nanowire array photovoltaics: Radial disorder versus design for optimal efficiency**”. *Appl. Phys. Lett.* **101**, 173902 (2012)

BS, MdS and RM decided to investigate the effects of disorder in nanowire arrays as a progression of BS’s honours project that focussed on uniform nanowire arrays. BS carried out all simulations, modifying our simulation package, EMUstack, to handle supercells. MdS proposed comparing the absorption of designed arrays, where the radii had been carefully selected, to disordered arrays where the nanowire radii are chosen at random. LB refined the procedure by which the nanowire radii were chosen at random from a Gaussian distribution in the ensemble study. All authors contributed to discussions and interpretation of results. BS wrote the letter, which was edited and proofread by all authors.

B. C. P. Sturmberg, K. B. Dossou, L. C. Botten, A. A. Asatryan, C. G. Poulton, R. C. McPhedran and C. M. de Sterke. “**Absorption enhancing proximity effects in aperiodic nanowire arrays**”. *Opt. Express* **21**, A964–A969 (2013)

BS proposed studying the clustered nanowires as a proxy for studying arrays with disordered arrangements. BS carried out all simulations, the results of which were discussed and interpreted by all authors. BS wrote the paper, which was edited and proofread by all authors.

B. C. P. Sturmberg, K. B. Dossou, L. C. Botten, A. A. Asatryan, C. G. Poulton, R. C. McPhedran and C. M. de Sterke. “**Optimizing Photovoltaic Charge Generation of Nanowire Arrays: Simple Semi-Analytic Approach**”. *ACS Photonics* **1**, 683–689 (2014)

BS recognised that the optimal nanowire array parameters could be predicted approximately using the physical insights established by our group. MdS directed the development to be more quantitative. BS developed the general expressions that hold for many materials, with guidance from MdS, RM, LB, and CP. All authors contributed to discussions and interpretation of results. BS wrote the paper, which was edited and proofread by all authors.

Initials

B. C. P. Sturmberg, K. B. Dossou, L. C. Botten, R. C. McPhedran and C. M. de Sterke. “Fano resonances of dielectric gratings: symmetries and broadband filtering”. *Opt. Express* **23**, A1672 (2015)

The original motivation for studying dielectric gratings stemmed from work by a previous student of MdS, RM, and LB, however this research direction did not bear fruit. BS learned that the results of our study were of interest for the development of wavelength selective filters in multi-junction solar cells while visiting the Atwater group at the California Institute of Technology. BS carried out all simulations, the results of which were discussed and interpreted by all authors. MdS proposed the surface grating model and carried out the complex analysis of the resonances, which was extended and numerically implemented by BS. BS wrote the paper, which was edited and proofread by all authors.

B. C. P. Sturmberg, K. B. Dossou, F. J. Lawrence, C. G. Poulton, R. C. McPhedran, C. M. de Sterke and L. C. Botten. “EMUstack: an open source route to insightful electromagnetic computation via the Bloch mode scattering matrix method”. *Computer Physics Communications* (In Press)

The scattering matrix formulation implemented in EMUstack was developed by LB. The Finite Element Method mode solver used by EMUstack was developed and implemented by KD. A basic version of the code was implemented by BS in his honours year, with the help of KD and LB. The code has been continually updated by BS during his PhD, for instance by generalising it to handle singly periodic structures. FL restructured the program to use the f2py package to communicate between the back-end written in Fortran and the front-end written in Python. FL also provided guidance in how to structure EMUstack and its online release. BS advocated for the open source publishing of EMUstack’s source code and created the associated documentation, tutorials, and webpages. CP managed the intellectual property aspects of the release. BS wrote the paper, which was edited and proofread by all authors.

Initials

Acknowledgements

It is hard to believe that almost six years have passed since I first walked into Martijn’s office to ask if the photonics concepts I had learnt in his lectures could be applied to solar cells. I have since gotten to pursue this question in over 250 Monday morning meetings with Martijn, Ross, Lindsay, Kokou, Chris, and Ara; of which this thesis is a kind of distilled record. I want to thank you all for your unrelenting support and enthusiasm, and for being a pleasure to work with and learn from. Martijn, your attentiveness, rigour and physical intuition are to be aspired to. While it might be “a bridge too far” to claim to have been “the tail wagging the dog”, it has been a privilege to have channelled some of your interest and formidable expertise in this research direction. Tom, your guidance as my practically minded external supervisor and experimental collaborator has been much appreciated.

To the wider CUDOS community, thanks for being such a friendly social bunch. In particular I have gotten to enjoy the company of many waves of student “chumps”, including: the old guard – Bill, Milee, Chavez, Dekker, “lunchtime mosses” Sahand, and Lawrence; the middle ages – Frownless, Tuniz, Tomo, Mcoll “the wrestling physicist”, (sweet supplier) CatFish, and my comrades in simultaneously writing up Thomas, Neetesh, Matia and Young; the new kids on the block – Blair, Moritz, Fernando, Loris; and the lunchtime blow-ins – Owen, Nick, and Jeremy (for their endless discussions of all things nerdy and transcootery). Felix, thanks for righteously pushing me onto good programming paths and for your thesis template. I also thank Mark Butler for his high school physics classes; the rate at which your students go on to PhDs in physics speaks volumes.

The completion of this thesis, and all that came before it, was done with the support of my family’s unwavering and unconditional love. More recently, this has been joined by the great warmth, mitgefühl and love of Lucy. For these relationships, words are grossly inadequate.

Throughout my PhD I have had the extraordinary privilege of calling STUCCO Cooperative home. After all these years this unique space still defiantly refuses encapsulation in words, but my engagement with this unruly microcosm has no doubt had a deep impact on my life. I raise a homebrewed toast to the members of Unit 6: Owen, Mark, Loula, and Lambchop; Tui, Ruby, Maddie, Waggelstuff, and Caitlin; Hailstorm, Rosie, and Megan; Luke, Mon, Consto, Dylan, and Milly. A second beer must be shared with Freya, Margot, Imo, Louis, Tully, Sierra, Sarah K., and Jak. And a few more beverages are owed to all past stuccowits who have invested their energy into making STUCCO what it is; may the cooperative experiment continue to bloom!

To the friends with whom I have explored this absolutely incredible country: it's been rad! In particular the regular suspects have been Mic, Em, T2, Milee, Sam, T(r)ash, DWu, Austin, Chazza, Mitch, Yoda, Cat, Helzo, Pete, Pat, Goldie, the Franklin crew, and all the Ledge locals. Morro and Jez deserve a special mention for their propensity for insuring epics.

As a complement to the great outdoors, the urban jungle has been made all the more interesting by the social and cultural contributions to the inner-west's co-inhabitants: Elisa, Andi, Isaac, Chris, Alex, Bec, Rob, Audrey. And then there were the hundred plus blissful Friday morning bike rides to the salvation of the ocean, co-piloted by the ever enthusiastic Loula. Kate and Corrie, thanks for providing shelter and company during some of the crux phases of the write up process.

I most gratefully acknowledge the scholarship I received from the Australian Renewable Energy Agency, and wish them well in continuing to evade closure at the hands of all round distasteful politicians. Jochen, I still owe you for pointing me in the direction of this opportunity. I also acknowledge the National Computing Infrastructure, who provided hundreds of thousands of CPU hours.

List of Abbreviations

| | |
|------|---------------------------------------|
| 1D | one-dimensional |
| 2D | two-dimensional |
| AC | alternating current |
| AM | air mass |
| BoS | balance of system |
| CPA | coherent perfect absorption |
| DC | direct current |
| EQE | external quantum efficiency |
| FoM | figure of merit |
| GMR | guided mode resonance |
| LED | light emitting diode |
| LRSP | long range surface plasmon polariton |
| NH | nanohole |
| NIL | nanoimprint lithography |
| NW | nanowire |
| PCE | power conversion efficiency |
| PV | photovoltaic |
| S-Q | Shockley-Queisser |
| SC | solar cell |
| SRSP | short range surface plasmon polariton |
| TE | transverse electric |
| TLA | total light absorption |
| TM | transverse magnetic |
| VAT | volume averaging theory |

Contents

| | | |
|----------|---|-----------|
| 1 | Introduction | 1 |
| 2 | Photovoltaic Solar Cells | 3 |
| 2.1 | The Cost of Photovoltaic Electricity | 3 |
| 2.1.1 | Opportunities for Cost Reductions | 6 |
| 2.2 | The Efficiency of Photovoltaic Power Conversion | 6 |
| 2.2.1 | The Idealised Photovoltaic Cell | 7 |
| 2.2.2 | The Solar Spectrum | 8 |
| 2.2.3 | The Shockley-Queisser Efficiency Limit | 9 |
| 2.2.4 | Lessons from Shockley-Queisser Analysis | 10 |
| 2.2.5 | Refined Thermodynamic Efficiency Limit | 11 |
| 2.2.6 | Lessons from Refined Thermodynamic Analysis | 13 |
| 2.3 | The Photovoltaic Zoo | 14 |
| 2.4 | Opportunities for Photonics | 19 |
| 2.4.1 | Absorption Enhancement in Thin Films | 19 |
| 2.4.2 | Spectrum Splitting | 22 |
| 2.4.3 | Fabrication of Photovoltaic Nanostructures | 23 |
| 3 | EMUstack: The Workhorse | 26 |
| 3.1 | Publication: EMUstack: an open source route to insightful electromagnetic computation via the Bloch mode scattering matrix method | 28 |
| 3.2 | Wider Applications of EMUstack | 39 |
| 3.3 | Optoelectronic Modelling of Solar Cells | 39 |
| 4 | Nanowire Array Photovoltaics I: Semi-analytic Optimisation | 40 |
| 4.1 | Review of Nanowire Array Solar Cells | 41 |
| 4.1.1 | Theoretical Understanding of Nanowire Arrays | 41 |
| 4.1.2 | Experimental Demonstrations of Nanowire Array Solar Cells | 42 |
| 4.2 | Publication: Optimizing Photovoltaic Charge Generation of Nanowire Arrays: A Simple Semi-Analytic Approach | 43 |
| 4.3 | Comparison with Nanohole Array Solar Cells | 56 |
| 4.3.1 | Effective Medium Theories for Nanowire and Nanohole Array | 57 |

| | | |
|----------|---|------------|
| 5 | Nanowire Array Photovoltaics II: The Role of Disorder | 58 |
| 5.1 | Publication: Nanowire array photovoltaics: radial disorder versus design for optimal efficiency | 63 |
| 5.2 | Publication: Absorption enhancing proximity effects in aperiodic nanowire arrays . . | 68 |
| 5.3 | Comparison with Disordered Nanohole Arrays | 70 |
| 6 | Fano Resonances of Dielectric Gratings | 72 |
| 6.1 | Solar Applications of Wavelength Selective Filters | 72 |
| 6.1.1 | Silicon-based Tandems | 72 |
| 6.1.2 | Ultra-high Efficiency Spectrum-splitting Multi-junctions | 75 |
| 6.2 | Publication: Dielectric gratings as wavelength selective filter: an interplay between diffraction and interference | 77 |
| 7 | Total Light Absorption in Ultra-thin Gratings | 94 |
| 7.1 | Applications of Ultra-thin Absorbers | 94 |
| 7.2 | Publication: Total Light Absorption in Ultra-thin Weakly-absorbing Semiconductor Gratings | 96 |
| 7.3 | Publication: Total Light Absorption in Ultra-thin Weakly-absorbing Semiconductor Gratings – Supplementary Materials | 103 |
| 7.3.1 | Total Absorption in Graphene Oxide | 108 |
| 8 | Conclusion and Outlook | 109 |
| 8.1 | Optical Nanostructures for Photovoltaics | 109 |
| 8.1.1 | Nanostructured Absorbers | 110 |
| 8.1.2 | Dielectric Gratings | 111 |
| 8.2 | Outlook | 112 |

Chapter 1

Introduction

We're in a giant car heading toward a brick wall and everyone's arguing over where they're going to sit.

David Suzuki

It has been disheartening, to put it mildly, to see David Suzuki's words grow only more fitting with time. And as we continue with 'business as usual', we are emitting the greenhouse gases that will lock in an increase in global mean surface temperatures of 2°C [9]. Thankfully, while our politicians squabble, continual improvements are being made in our technical ability to harvest energy from clean, renewable sources. These improvements are increasing the efficiency of these technologies and driving down their costs, thereby reducing the investments needed for the world to transition to a carbon neutral future.

Sunlight is by far the most abundant source of energy on earth as every 2.5 hours the sun irradiates the earth with more energy than humankind used globally in 2013 [10]. Figure 1.1 compares the total known reserves of non-renewable energy with the amount of energy available from renewable sources on an annual basis; solar energy is the bright yellow sphere. The two-dimensional representation of these spheres understates the disproportion of the annual solar resource to the total known non-renewable resources; if the wind sphere is the size of a marble, coal would be the size of a bowling ball, and solar would be the size of a small house.

Photovoltaic solar cells (PV SCs) are a particularly elegant technology that generates electricity directly from sunlight. The photovoltaic effect was discovered in 1839 [11, 12] but it was not until 1961 that SCs with practically viable efficiencies of over 10% were demonstrated at Bell Labs [13, 14]. The efficiency with which SCs convert sunlight into electricity has improved dramatically since then, and the costs of PV SCs have continually declined. Efficiencies have increased due to a better understanding of the physics of SCs and the refinement of fabrication processes. The reductions in costs have primarily been driven by vast increases in the scale of production. In recent years the efficiency of conventional SCs has increased only marginally, as fundamental material constraints are approached, which has focussed the research community's attention on developing new SC designs that can dramatically reduce costs.

This thesis investigates how dielectric nanostructures may be used to improve the performance of PV SCs. We focus on understanding the optical physics of the nanostructures, which informs general design strategies. We examine how nanostructured absorbers could create cheap and moderately-high efficiency SCs, and how other nanostructures could be used to direct parts of the solar spectrum to different SCs, thereby enabling the production of high efficiency SCs with reduced costs as well as the creation of SCs with ultra-high efficiencies.

Chapter 2 motivates ongoing research into improving PV SCs, and provides a perspective on the current direction of this research. We begin with an overview of the economic factors influencing the SC market, and an analysis of the loss mechanisms that limit the efficiency

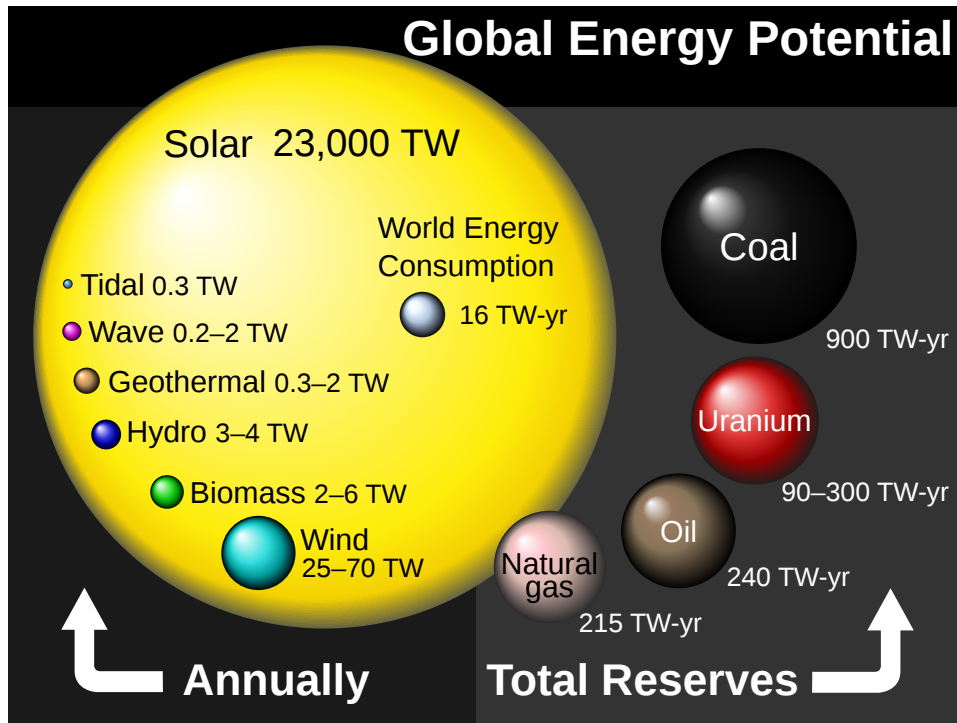


Figure 1.1: Total known global energy reserves of non-renewable (right side) and annual sources of renewable energy (left side). The quantities are represented as spheres, and as such their relative size is far more unequal than they first appear. Adopted from [15].

of the energy conversion process. These reveal a number of opportunities for nanophotonics to make significant contributions to improved SC designs.

Before delving into the results of our research, we outline the simulation method that we used throughout our work in Ch. 3. This semi-analytic method is foundational to our work because it dictates which quantities we have access to in order to investigate the interaction of light with the nanostructures. The development and implementation of the simulation program has been an ongoing part of this project.

Chapters 4 and 5 contain the results of three studies on nanowire array solar cells, as well as discussions on the similarities and differences of these structures with nanohole arrays, which have the inverse material distributions. In Ch. 6 we pursue a different aim, studying the physics of one-dimensional lamellar gratings, which may be used as solar spectrum splitting elements in multi-junction solar cells.

The final chapter of results, Ch. 7, is less focussed on solar energy applications. Here we demonstrate, theoretically and experimentally, that ultra-thin lamellar gratings can perfectly absorb light of a designed for wavelength, with zero light lost to reflection or transmission. We show that this can be achieved using a wide variety of materials, including commonly found weakly-absorbing semiconductors and metals. The applications that may benefit from these findings include photodetectors, optical modulators, and potentially ultra-thin SCs.

Chapter 8 concludes the thesis with a review of nanostructured solar cells and an assessment of our work within this field. We also assess the opportunities and challenges for nanostructures to broadly improve the performance of realistic photovoltaic solar cells.

Chapter 2

Photovoltaic Solar Cells

*I'd put my money on the sun and solar energy. What a source of power!
I hope we don't have to wait until oil and coal run out before we tackle that.*

Thomas Edison

A fundamental figure of merit (FoM) that determines the viability of a renewable energy technology is the ratio of its cost to its power conversion efficiency. This is most simply expressed as the *cost per Watt* (\$/W) of the electricity generated by installed devices. While this FoM captures the essential competitiveness of technologies, their viability is influenced by many external factors, such as the abundance of the energy resource, as well as the price of feed-in tariffs and the regulations governing the electricity market [16]. Some of these factors are included in more sophisticated FoMs such as the *levelized cost of electricity* (the ratio of costs to power generated averaged over the assets lifetime) and the *levelized avoided cost of energy*, which is more appropriate for renewable technologies as it includes savings in the distribution network [17].

The simplicity of these FoMs contrasts the multi-faceted effects that must be considered when developing non-renewable energy sources, which include: the greenhouse gas emission; the broader environmental and health impacts of the mining, transportation and combustion of the fuel (for details regarding the externalities of coal see [18, 19]); and the long term disposal of waste products, including, in the case of nuclear energy, the secure storage of potentially fissile material. While the total absence of these negative impacts from renewable energy installations ought to be highly valued in themselves, the \$/W remains the dominant driver in their adoption.

In this chapter we outline the various constituents to the cost of installed SCs, discuss the processes that fundamentally constrain the efficiencies obtainable by PV SCs, and review recent developments in existing PV technologies. The analyses reveal multiple advantages of creating SCs with thin absorbing layers, but emphasise that these opportunities can only be realised under the condition of high absorption with low parasitic losses. Dielectric nanostructures are ideally suited to realise these opportunities as they can be used to strongly manipulate the propagation of light without the intrinsic Ohmic losses of metals.

2.1 The Cost of Photovoltaic Electricity

We begin by discussing the costs embodied in an installed solar cell. The costs arise from four broad factors:

- The Materials – the cost of the raw materials and the costs associated with refining them to the purity required for the production of efficient PV SCs.

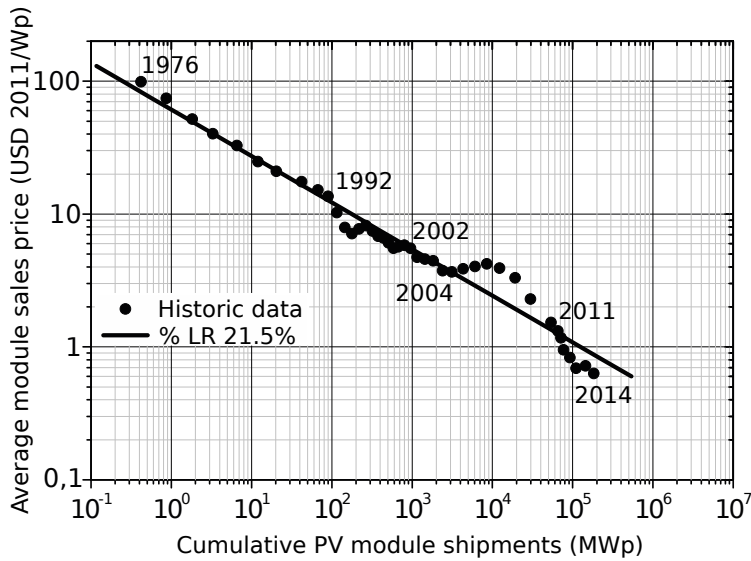


Figure 2.1: The learning curve for SC modules, showing the price as a function of cumulative shipped PV module capacity in Watt-peak (the nominal nameplate capacity of PV modules). By the time cumulative shipments have doubled, the cost has declined by on average 21.5%, which equates to the costs halving every decade [20].

- The Factory – manufacturing SCs is a complex industrial process where costs (and the potential for savings) occur at each processing step.
- The Balance of System (BoS) – these are the costs of the components that connect the PV cells to the electricity system (be that the grid or an isolated building).
- The Installation – there are large costs incurred in delivering and installing SC modules.

We elaborate on these in reverse order;

The Installation

With the recent drop in SC module prices (see Fig. 2.1), it is estimated that, in developed countries, the cost of delivering and installing SC modules now exceeds the cost of making them [21]. This trend, along with limitations in available space, is shifting the competitive advantage towards SCs with higher efficiencies, as the cost of installation is tied to the number of panels required to reach the desired power output.

Balance of System

The BoS costs associated with bringing the electricity produced by SCs to the devices that use it, are substantial. They include the wiring, switches, mounting systems, and, in many cases, inverters and transformers that convert the Direct Current (DC) produced by the photovoltaic effect into Alternating Current (AC) electricity as used by the electricity networks at both the home and grid levels.

These costs can be reduced through the use of highly efficient SC modules because these require fewer modules for the same power output, reducing the space, material and labour usages. Another approach that could dramatically reduce the BoS costs, and at the same time significantly improve the system's efficiency, is to create local DC circuits that connect the SCs directly to the electrical appliances that run on DC electricity, as well as to batteries for storage [22, 23]. For a review of the larger scale challenges of integrating large amounts of DC-producing renewables into the existing electricity infrastructure see [24].



Figure 2.2: Sand to silicon. A flow chart of the processes involved in producing extremely pure silicon wafers, where the silicates are originally found in sand.

The Factory

Since 1976 the cost of PV SCs has declined at a rate of about 21.5% with every doubling in the cumulative amount of PV modules shipped [20], approximately halving every decade. This trend, shown in Fig. 2.1 in terms of the average module sales price, has been predominantly driven by increased “(production) efficiency and scaling” [25], an effect economists call the “economies of scale”. During the same period, the absolute efficiency of PV modules has increased by only $\sim 0.2\%$ per year [25]. A moderate reduction of costs is forecast to continue into the immediate future, driven primarily by: cost reductions along the entire value chain; the introduction of specialized module products for different market applications; and improved module power/cell efficiency without significantly increasing processing costs [20]. At some stage however, the potential for savings from manufacturing efficiencies will expire, and substantial efficiency increases will be required to reduce the $\$/W$.

The Materials

The most basic cost of a SC stems from the materials consumed. This cost, in turn, is comprised of the cost of the raw material, and the costs of refining the material to the point where its electrical properties are good enough to yield efficient SCs. We illustrate these costs in Fig. 2.2, where we focus on the production of crystalline silicon wafers that are used in over 90% of commercial SCs [20]. Figure 2.2 illustrates the lengthy, involved, and energy intensive processes required to turn sand into solar-grade, 99.9999% pure, polycrystalline silicon feedstock. Solar cells are made from either multicrystalline silicon or monocrystalline wafers (as shown in Fig. 2.2). This means that, although silicon is the second most abundant mineral in the Earth’s crust by mass [26], the cost of the purified Si wafers is a substantial part of the whole cost of a SC.

The large deviation from the historic trend in Fig. 2.1 that occurred around 10^4 MWp cumulative shipments, corresponding to the years 2004-2013, was triggered by a sharp increase in the price of refined silicon that arose due to a global shortage in polycrystalline silicon, which forced manufacturers to idle about a quarter of their production capacity in 2006 [27]. The number of manufacturers producing solar-grade polycrystalline silicon has increased from 12 to over 100 [28] and technological improvements have further reduced the cost of Si wafers. The costs were decreased by factors including: the introduction of feed-in-tariffs in a number of European countries [29, 30]; the emergence of solar leasing schemes, particularly in the USA, which dramatically increased the market for SCs [31, 32]; a number of large new fabrication facilities beginning production, particularly in China [33, 34]. Figure 2.3 shows how the price of silicon SCs has declined since 2010, and the inset breaks up the costs into the raw material, the refined wafer, the fabrication of the SC, and the production of the SC module. The cost of the raw material and the refinement process account for over 30% of the SC module cost, with the rest being costs incurred in the factory.

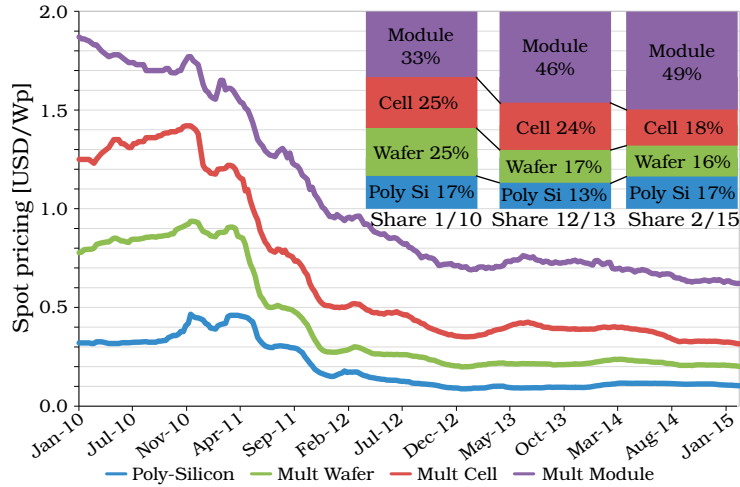


Figure 2.3: Price trends for polycrystalline silicon feedstock (poly-Si), multicrystalline silicon (mc-Si) wafers, mc-Si solar cells, and solar cell modules. Inset shows the breakdown in the cost of a SC module in 01/2010, 01/2013, and 02/2015 (which were 1.86, 0.72, and 0.62 US\$/Wp respectively). This shows that poly-Si remains the most expensive individual material, but creating the module now accounts for almost half of the total cost of manufactured SC modules. Adopted from [20], where it was assumed that wafers weighed ~ 22.7 g and that mc-Si cells had an efficiency of 17.3%.

2.1.1 Opportunities for Cost Reductions

As optics researchers there is not much we can do to influence the costs of manufacturing SCs, or the economics involved in distributing and installing SC modules, however we have seen that a substantial fraction of the cost of SCs is derived from the production of PV-grade silicon wafers. This highlights the opportunity to cut costs by developing thin film SCs that use a lower quantity of the valuable materials, and which may be made from lower quality materials because the charge carriers need to travel less far to reach the contacts. While these two attributes combine to dramatically reduce costs, we must also consider the efficiency of the SC. As the thickness of the absorbing layer is reduced, the single pass absorption also decreases. This is particularly problematic for indirect bandgap semiconductors such as silicon, where the intrinsic absorptivity is very low at wavelengths close to the bandgap. As part of this thesis we investigate nanostructures that enhance the absorption of thin films to levels far greater than their single pass absorption value (as well as being greater than the double pass value when the layers are placed above a mirror).

2.2 The Efficiency of Photovoltaic Power Conversion

In the previous section we discussed the cost of PV SCs; we now consider the other side of the $\$/W$ FoM, that is, the efficiency with which PV SCs convert sunlight into electricity. In particular, we show that decreasing the absorber volume (eg. by decreasing the layer thickness) is advantageous for fundamental, thermodynamic reasons. The analysis however stresses that these improvements can only be realised if the absorption of the layer is maintained. Techniques for producing strong absorption in thin layers are reviewed in Sect. 2.4, before being developed further in this thesis.

The power conversion efficiency (PCE) of photovoltaic SCs is limited by two types of processes: extrinsic losses that may ideally be reduced to zero through improved cell designs and optimising fabrication, such as parasitic recombination, series resistance and contact shadowing; and intrinsic losses, which on the other hand arise from energy and entropy considerations and cannot be fully eliminated. Understanding the origins of these losses allows for their contributions to be minimised, and for absolute efficiency limits to be calculated

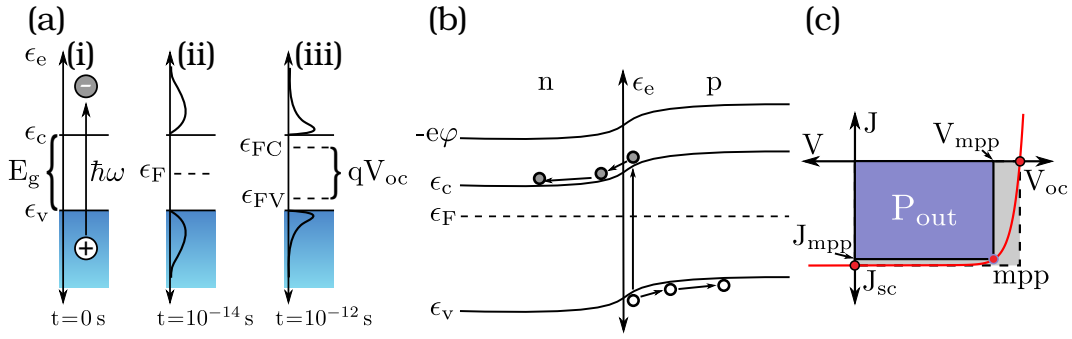


Figure 2.4: (a)(i) Energy band diagram of a semiconductor of bandgap energy E_g , showing the excitation of an electron from the valence band into the conduction band after absorption of a photon of frequency ω . (a)(ii) The initial distributions of the excited electrons and holes is identical to the energy spectrum of the illumination. (a)(iii) After 10^{-12} s the electrons and holes have thermalised, their distributions being described by quasi-Fermi levels ϵ_{FC} and ϵ_{FV} respectively. The energy difference between these levels sets the maximum V_{oc} of a solar cell. (b) The band diagram of a p-n junction showing the excitation of an electron-hole pair. The built-in potential of the junction allows the electron to pass from $p \rightarrow n$ and vice versa for the hole. (c) I-V curve of a solar cell. The maximum power that can be extracted is indicated by the purple rectangle. Diagrams (a) and (b) are based on [35].

as useful reference points.

We begin by describing the simplest idealization of a PV SC, and characterise the sun's irradiance spectrum on earth. We then review the findings of recent studies of the interrelationships of the loss processes, which reveal how the intrinsic losses may be reduced by decreasing the volume of the SC absorber.

2.2.1 The Idealised Photovoltaic Cell

The simplest model of a photovoltaic solar cell consists of a direct bandgap semiconductor with a bandgap energy, E_g . This material absorbs photons of energy $E_\nu = \hbar\omega$, when $E_\nu \geq E_g$, and is transparent (non-absorptive) to photons with $E_\nu < E_g$. Here $\omega = 2\pi c/\lambda$ is the photon's angular frequency (λ is the wavelength and c is the speed of light in vacuum), and \hbar is the reduced Planck constant. Each absorbed photon excites an electron from the valence band of the semi-conductor into its conduction band, creating a hole (a positively charged vacancy) in the valence band. In the idealised SC we assume that every incident photon with $E_\nu \geq E_g$ is absorbed, and creates one electron-hole pair.

When a SC absorbs photons, electrons are excited from the valence band into the conduction band, as indicated in Fig. 2.4(a)(i), and the charge carriers (electron-hole pairs) are excited into non-equilibrium states. These excited states are extremely short lived because energy is rapidly transferred to phonons within a matter of picoseconds (10^{-12} s) [35]. This thermalisation process leaves the electrons distributed in a Fermi distributions around the quasi-Fermi level ϵ_{FC} close to the conduction band, and the holes distributed in a Fermi distribution around ϵ_{FV} close to the valence band, as illustrated in Fig. 2.4(a)(ii). Since the charge carriers take microseconds (10^{-6} s) to diffuse to the contacts at the edge of the cell, we considered them to be fully thermalised by the time they arrive. It is therefore the energy difference between the quasi-Fermi levels that sets the maximum voltage that can be extracted from the SC, where this energy qV_{oc} (where V_{oc} is the open-circuit voltage) must be less than E_g due to entropy constrains that will be discussed in Sect. 2.2.5.

In order to convert the potential energy of the electron-hole pairs into an electrical current we must extract the electron and holes from different contacts. In general, metallic strips are used as the contacts and a p-n junction is used to separate the charge carriers. The band diagram corresponding to this situation is shown in Fig. 2.4(b), which illustrates how the difference in energy levels between the p and n type materials creates a potential energy

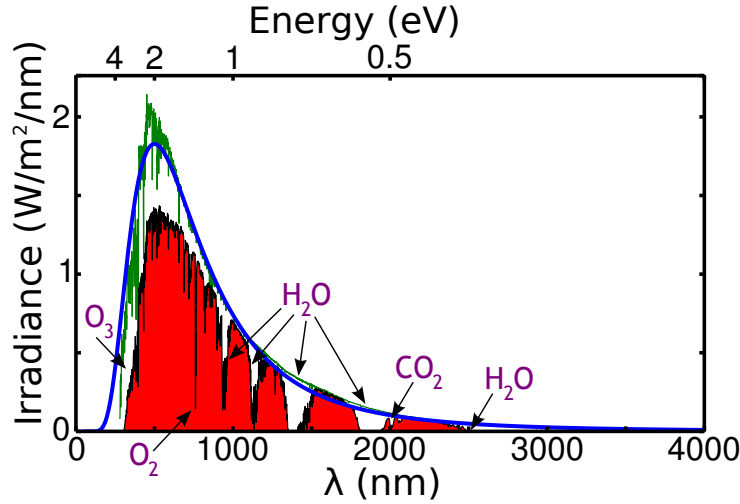


Figure 2.5: ASTM solar irradiance spectra: AMO in green, AM1.5G in black. The blackbody radiation spectrum for a body of $T_s = 5800$ K, taking up a solid angle of $\Omega_s = 6.87 \times 10^{-5}$ steradians is shown in blue. The arrows label the atmospheric molecules whose absorption cause the dips in irradiance. The useful energy at the Earth’s surface is indicated by the filled red area.

barrier that prevents electrons from diffusing from the n-type material to the p-type, and vice versa for the holes. The contact on the n-type material therefore collects the electrons and the holes are extracted at the contact with the p-type material. Work is done by the circuit that connects the positive and negative contacts. A p-n junction is only one of the many ways in which charge separation can be achieved; the fundamental principle is that some form of one-way membrane must separate the charge carriers [35].

At short-circuit, the terminals are connected by a circuit with zero impedance (ideally by a wire of zero resistance), so that the maximum number of electron-hole pairs are extracted from the SC. This produces the maximum current (the short-circuit current J_{sc}), which is less than the generation rate of electron-hole pairs because of losses to non-radiative recombinations. The opposite situation occurs at open-circuit where there is no current extracted from the SC (the connection between the terminals has infinite impedance), which maximizes the voltage (giving the open-circuit voltage V_{oc}). In this case all electron-hole pairs recombine either radiatively, where they emit a photon, or non-radiatively. Under open-circuit or short-circuit conditions there is no power extracted from the SC. The most power that can be extracted occurs when the SC is operated at a combination of voltage V_{mpp} and current J_{mpp} , known as the maximum power point.

The efficiency of PV SCs is defined as

$$\eta = \frac{V_{mpp} J_{mpp}}{P_{in}} = \frac{FF V_{oc} J_{sc}}{P_{in}}, \quad (2.1)$$

where P_{in} is the incident power and $FF < 1$ is the “fill fraction” of the SC, which is given by the ratio of the purple and grey rectangles in Fig. 2.4(c). The fill factor is influenced by the recombination rates of the SC as well as parasitic resistive losses. The majority of the analysis of Sects. 2.2.3 and 2.2.5 concerns the V_{oc} achieved by SCs, where J_{sc} is assumed to be equal to the number of above band-gap photons multiplied by the charge of an electron.

2.2.2 The Solar Spectrum

In order to optimise the PCE of a solar cell it is essential to consider the details of the optical spectrum that will illuminate it. The current, internationally agreed to, solar irradiation standard is the ASTM G-173-03, of which the AM0 and AM1.5G spectra give the values at the surface of atmosphere and after passing through Earth’s atmosphere for a distance of 1.5

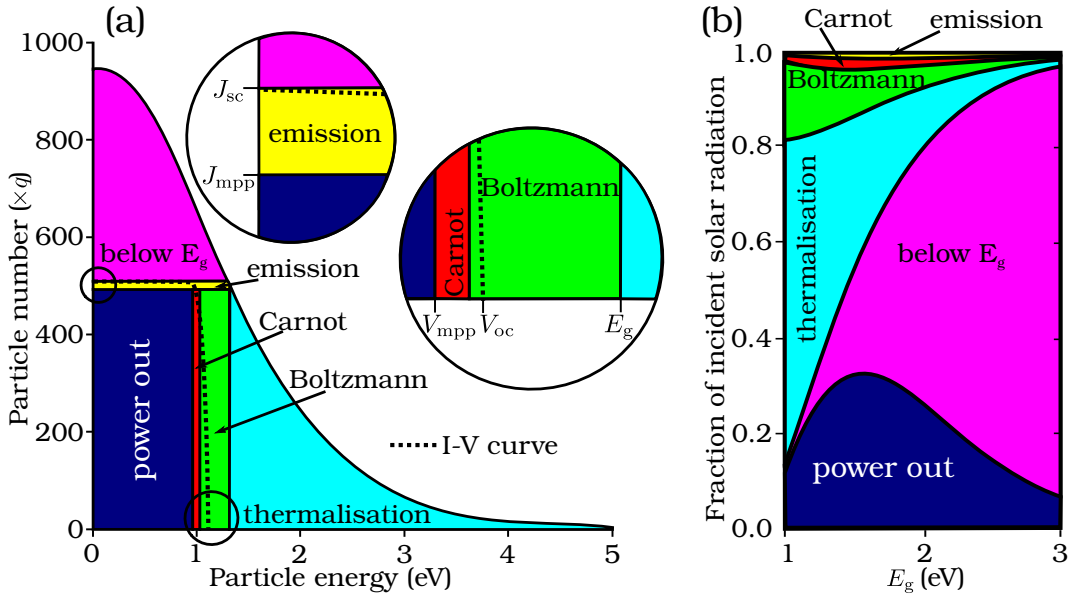


Figure 2.6: Energy losses for single junction SCs: (a) as a function of the photon energy for a SC with optimised bandgap; and (b) as function of bandgap energy of the SC, E_g , where the losses due to unabsorbed photons (pink) dominate as E_g increases. Adapted from [36].

times the atmosphere’s height (Air Mass 1.5) respectively. The AM1.5G (global) spectrum is also influenced by reflections from the Earth’s surface that contribute diffuse irradiance, in contrast the AM1.5D spectrum includes only irradiation directly incident from the sun. The spectra are shown in Fig. 2.5, along with the blackbody spectra for the sun’s temperature of $T_s = 5800$ K, which is a good match to the AM0 spectrum. The AM1.5G spectrum shows dips associated with the absorption and scattering that occurs as the light interacts with molecules and particles in the Earth’s atmosphere.

2.2.3 The Shockley-Queisser Efficiency Limit

In this section we consider the intrinsic efficiency losses of the idealised, single junction SC that we described in Sect. 2.2.1. We describe the basic physics of the processes and graphically illustrate their role in limiting the obtainable PCE, leaving their mathematical expressions for Sect. 2.2.5.

The first expression for the fundamental limits to photovoltaic energy conversion was developed by Shockley and Queisser in 1961 [37]. Their limit, known as the Shockley-Queisser (S-Q) limit, is still the basic reference point against which the demonstrated performances of PV technologies are assessed. S-Q assumed (as we did in Sect. 2.2.1), that every absorbed photon “produces a free electron-hole pair and every recombination event generates a luminescent photon” [38], that is to say that “the only recombination mechanism (considered) ... is radiative” [37], *i.e.* there are no nonradiative recombinations. While S-Q derived their limit using the principle of “detailed balance”, where the SCs photocurrent is taken as the difference between the absorbed and emitted photon fluxes, we here follow a thermodynamic argument that is consistent with the stricter limit presented in Sect. 2.2.5.

Transmission of Sub-bandgap Photons & Thermalisation of Charge Carriers

The first shortcoming of a single junction SC is that sub-bandgap photons ($E_\nu < E_g$) cannot be absorbed. This problem could be alleviated by using an extremely low bandgap semiconductor, however in this case the thermalisation losses would far exceed the additional energy absorbed. This indicates that E_g must be chosen to balance these two intrinsic losses.

Figure 2.6(a) shows the number of photons incident upon a SC from the sun as a function

of the photon energy, where the sun is assumed to be a blackbody at $T_s = 5800$ K. The differently coloured areas represent the amount of energy used by different physical processes. The areas bounded by horizontal lines (pink and yellow) correspond to photons that are lost from the SC. The areas bounded by vertical lines (light blue, green, orange) correspond to the energy lost by the charge-carriers to various physical processes before being extracted. The extracted power is indicated by the dark blue rectangle which lies within the I-V curve shown by the dashed curve (consistent with Fig. 2.4(c)).

From Fig. 2.6(a) it is clear that neither a very large, nor a very small bandgap is ideal, as the former produces an excessively large light blue region corresponding to the thermalisation of charge-carriers, and the latter produces an excessively large pink region where solar photons are wasted in transmission. This is confirmed in Fig. 2.6(b) where the extracted power is shown as a function of the material's bandgap energy, along with the breakdown of the energy losses.

Thermodynamic Losses

Thermodynamically, solar cells may be viewed as an engine generating work while heat flows from the hot reservoir of the sun (T_s) to the cold reservoir of the solar cells surroundings ($T_c = 300$ K). This process is reversible since an electron-hole pair may be injected into the SC where the charge carriers recombine to emit a photon that can travel back to the sun. The efficiency of such a process is limited by the second law of thermodynamics, with the maximum efficiency being that of the Carnot engine. The energy sacrificed in this process is indicated by the red area in Fig. 2.6.

In calculating the Carnot efficiency, the SC is assumed to be under full optical concentration, such that all emitted photons reach the sun. Our idealised SC however has no concentrator and therefore emits into the full half-space, $\Omega_c = 2\pi$, of which the sun takes up a solid angle of $\Omega_s = 6.8 \times 10^{-5}$. This inequality results in entropy generation because the directional order of the photons is decreased upon emission. The reduction in the usable energy due to this irreversible thermodynamic loss is referred to as the Boltzmann factor and is represented by the green area in Fig. 2.6.

Finally, the SC also emits thermal radiation, proportional to its temperature. Kirchhoff's law [39] dictates that the emission spectrum of a body is given by the product of its blackbody spectrum and its absorption/emissivity spectrum. Thus the emission of the SC can be calculated from its temperature using Planck's Law [40, 41] where the absorption spectrum that is assumed to be $A(\lambda) = 1$ for $\lambda < \lambda_g$ and $A(\lambda) = 0$ for $\lambda > \lambda_g$. The charge carriers lost due to this emission are indicated by the yellow region in Fig. 2.6.

Using this simple theory, whose variables T_s , T_c , Ω_s , Ω_c are known, Schockley and Queisser calculated the efficiency limit for single junction SC as a function of it E_g as shown in Fig. 2.6(a). The maximum efficiency is found to be 31% where the optimal material has a bandgap of its $E_g = 1.31$ eV [36].

2.2.4 Lessons from Shockley-Queisser Analysis

The efficiency limits in the absence of nonradiative recombinations (Fig. 2.6) have been known for over half a century, and the avenues they reveal for increasing the efficiency of SCs are well understood. These involve reducing: thermalisation losses; sub-bandgap transmission losses; and the losses due to the mismatch of the solid angle of the incident photons and the emitted photons. The first two of these can be reduced by using multiple materials with varying bandgaps, as discussed in Sect. 2.3. The third factor, the voltage drop due to the Boltzmann factor (Eq. 2.6), can be reduced by using optical components to decrease the mismatch in the emission and absorption angles. This currently only occurs in concentrator systems, where macroscopic lenses focus light onto small, high efficiency solar cells, as illustrated in Fig. 2.7(a). These systems are sensitive to the angle of the incident light and are therefore typically mounted on expensive equipment that tracks the sun. Alternatively it has recently been proposed that nanophotonic structures, such as those shown in Fig. 2.7(b) or the Bragg-like system of [42], could be used to restrict the angle

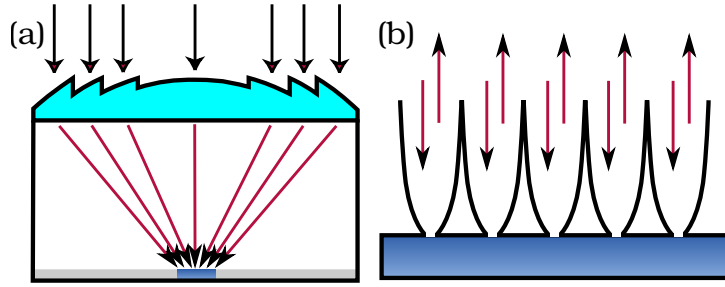


Figure 2.7: (a) A conventional concentrated SC using a bulk optics Fresnel lens. (b) A nanophotonic structure that restricts the emission angle of the SC. Adapted from [43].

of emission without concentrating the sunlight and without requiring the addition of heavy bulk optics systems (although still requiring tracking).

2.2.5 Refined Thermodynamic Efficiency Limit

The S-Q limit has recently been extended to include nonradiative recombination as well as the effects of imperfect light trapping and parasitic absorption. These developments were somewhat controversial [43–45], but were clarified by a comprehensive study by Rau *et al.* [44]. Before analysing the insights provided by the extended theory, we give the expressions for the losses included in the S-Q analysis. Note that we here define the limiting efficiency to be $\eta_{\text{limit}} = V_{\text{oc}} J_{\text{sc}} / P_{\text{in}}$ (*ie.* $FF = 1$, $\eta < \eta_{\text{limit}}$, where η is the real efficiency), which assumes that every absorbed photon contributes to J_{sc} (unity carrier collection efficiency), and disregards the decrease in current due to emission that was included in Sect. 2.2.3. Carnot losses on the other hand are included in the calculated V_{oc} , as are non-radiative losses.

Figure 2.8 shows the contribution of the loss processes to the maximum obtainable V_{oc} for a semiconductor with the bandgap $E_g = 1.38$ eV (the optimal bandgap for a single junction SC in this refined analysis). The material is assumed to have an idealised absorption of unity above the bandgap, but has a non-zero nonradiative recombination rate. The energy lost to transmission of below sub-bandgap photons is indicated by $\bar{E}_{\text{sun}}(0)/|q| - \bar{E}_{\text{sun}}(E_g)/|q|$, where q is the charge of an electron, and the average energy of photons above the band gap is derived from the photon flux of the sun $\phi_{\text{sun}}(E)$ by

$$\bar{E}_{\text{sun}}(E_g) = \frac{\int_{E_g}^{\infty} E \phi_{\text{sun}}(E) dE}{\int_{E_g}^{\infty} \phi_{\text{sun}}(E) dE}. \quad (2.2)$$

The entropic loss processes additively reduce the maximum achievable V_{oc} . They can be split into two:

$$V_{\text{oc}} = V_{\text{oc}}^{\text{rad}} + \frac{kT_c}{q} \log(Q_e^{\text{LED}}), \quad (2.3)$$

where $V_{\text{oc}}^{\text{rad}}$ is the open-circuit voltage that would be attained if the radiative processes were the only loss mechanisms (as in Sect. 2.2.3), and the second term pertains to the performance of the SC operated as a light emitting diode (LED). The Q_e^{LED} is the external LED quantum efficiency, which is the fraction of the recombination events within the SC that lead to the emission of photons into the surroundings. The recombinations events that emit photons from the SC are contributing to fulfilling the fundamental thermodynamic requirements of equilibrium, while all other recombinations are parasitic losses. In the following sections we show how the basic distinction between radiative and non-radiative recombinations demands that solar cells not only be made of high quality materials, but also that their optical properties be designed to maximise their external radiative efficiencies.

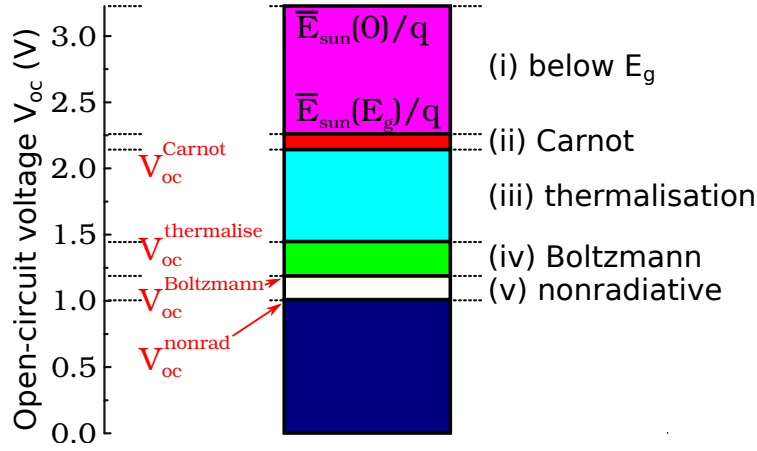


Figure 2.8: Maximum open-circuit voltage obtainable with a single junction SC made of an semiconductor with optimised $E_g = 1.38$ eV, once all thermodynamic losses are accounted for. The absorptance of the semiconductor is taken to be a step function, and $Q_e^{\text{LED}} = 10^{-3}$. Adapted from [44].

The Carnot limit for the reversible generation of work, making use of all photons with $\hbar\omega > E_g$ is

$$V_{\text{oc}}^{\text{Carnot}} = \frac{\bar{E}_{\text{sun}}(E_g)}{q} \left(1 - \frac{T_c}{T_s}\right), \quad (2.4)$$

and the losses due to thermalisation can be well approximated as

$$V_{\text{oc}}^{\text{thermalise}} \approx \frac{E_g}{q} \left\{1 - \frac{T_c}{T_s}\right\} + \frac{kT_c}{q} \ln\left\{\frac{T_s}{T_c}\right\}, \quad (2.5)$$

for bandgap energies typical for SCs. The Boltzmann factor for the mismatch in solid angle of absorption and emission is

$$V_{\text{oc}}^{\text{Boltzmann}} = \frac{kT_c}{q} \ln\left\{\frac{\Omega_c}{\Omega_s}\right\}. \quad (2.6)$$

All of these losses are included in the $V_{\text{oc}}^{\text{rad}}$ term in Eq. 2.3 and are indicated in steps (i)-(iv) in Fig. 2.8.

Nonradiative losses

We now focus on the nonradiative processes that reduce the voltage from $V_{\text{oc}}^{\text{rad}}$ to $V_{\text{oc}}^{\text{nonrad}}$, *i.e.* the step from (iv) to (v) in Fig. 2.8. The controversy referred to earlier stemmed from the oversimplification of considering the entropic loss processes to be independent. The correct expression for the energy lost due to thermalisation, the Boltzmann factor, parasitic absorption, and nonradiative recombination respectively is given in Eq. 26 of [44],

$$qV_{\text{oc}} = kT_c \ln\left[\frac{\int A(E)\phi_{\text{sun}}(E)dE}{\int A(E)\phi_{\text{bb}}(E)dE}\right] + kT_c \ln\left[\frac{\Omega_c}{\Omega_s}\right] + kT_c \ln\left[\frac{p_e}{p_e + p_a}\right] + kT_c \ln\left[\frac{(p_e + p_a)Q_i^{\text{lum}}}{(1 - Q_i^{\text{lum}}) + (p_e + p_a)Q_i^{\text{lum}}}\right], \quad (2.7)$$

where we note the interrelated dependencies of the terms.

The term Q_i^{lum} in Eq. 2.7 is the internal luminescence quantum efficiency, which is a bulk property of the photovoltaic absorber material given by the relative rate of radiative to nonradiative recombinations (R_{rad} , R_{nonrad} respectively). In contrast, the probability of

radiative emission p_e is sensitive to the volume of absorbing material and the optical performance of the SC, the latter of which can be manipulated with engineered nanostructures. It is given by

$$p_e = \frac{\epsilon_{\text{out}} \int A(E) \phi_{\text{bb}}(E) dE}{4n^2\pi S_{\text{cell}} h \int \alpha(E) \phi_{\text{bb}}(E) dE}, \quad (2.8)$$

which is inversely proportional to the volume of the absorber – S_{cell} is the surface area, h the thickness and n the refractive index of the SC – and is increased when the absorption $A(E)$ is enhanced beyond the value given by the intrinsic absorption coefficient $\alpha(E)$. Here $\phi_{\text{bb}}(E)$ is the blackbody spectrum of the SC, and the probability of radiative emission is related to the probabilities of a photon being reabsorbed (p_r) or parasitically absorbed (p_a) by $p_e + p_a + p_r = 1$.

2.2.6 Lessons from Refined Thermodynamic Analysis

The important role of radiative emission, as specified in Eqs. 2.7 and 2.8, has only been fully appreciated in the last decade, and has been accompanied by the realisation that high intensity optical fields in small volume absorbers (precisely as created in nanostructured photovoltaics) can substantially improve the performance of SCs.

The third and fourth terms in Eq. 2.7 express the decrease in V_{oc} due to parasitic absorption and nonradiative recombination. These are minimised by having $p_e \gg p_a$ and $R_{\text{rad}} \gg R_{\text{nonrad}}$, which emphasises the importance of using materials of the highest quality to minimise p_a , R_{nonrad} , as well as the importance of *optically designing* SCs to maximise their LED efficiency. The LED efficiency is important because it dictates the rate at which the recombinations within the cell contribute to fulfilling the thermodynamic requirements of thermal equilibrium with the sun, as opposed to remaining within the cell where they may recombine non-radiatively to produce nothing more than heat. The physical explanation of why smaller volume absorbers are advantageous is that the number of non-radiative recombination sites is the product of the bulk recombination density of a given material and the volume of that material.

The caveat to these directives is that the absorption of the structure must remain high. This is fundamental to achieving high efficiencies (J_{sc}) as well as being required in Eq. 2.8 to realise large p_e . Large electromagnetic field concentration inside the active medium also increases the internal luminescent efficiency Q_i^{lum} because the density of photons is increased relative to the fixed number of defect states.

The findings of the refined analysis are summarised in Fig. 2.9, which shows the dependence of J_{sc} , V_{oc} and η on the product of a layer’s intrinsic absorption coefficient and thickness (the single-pass absorptance), αh . The structure considered in these simulations has a very effective (hypothetical) light trapping scheme, which for instance increases the absorptance of the layer from a single-pass value of $\alpha h = 0.03$ to $A \approx 1$ (see [44] for details of the structure and the Monte Carlo calculations). Figures 2.9(a)-(c) show the dependences of J_{sc} , V_{oc} and η on αh when the internal luminescent efficiency of the material is varied but the parasitic absorption is taken to be zero throughout. As per the preceding discussion, the J_{sc} increases with αh , while the V_{oc} decreases, giving rise to an optimal thickness-intrinsic absorptance combination, which is relatively independent of Q_i^{lum} . In Figs. 2.9(d)-(f) Q_i^{lum} is fixed at 0.5 and the parasitic absorption is varied, which strongly affects the J_{sc} with larger values of αh required to maximise J_{sc} and η . The enhancement of V_{oc} decreases dramatically in Fig. 2.9(e) when the parasitic absorption is increased, emphasising that noticeable enhancements in V_{oc} are only obtainable in materials with high radiative, and low nonradiative recombination rates. This highlights the problem with using plasmonic metals in SCs, as these intrinsically have substantial Ohmic losses that contribute to the parasitic absorption. Dielectric nanostructures, in contrast, are well suited to taking advantage of the opportunities to increase J_{sc} , V_{oc} and η of SCs by engineering strongly confined fields with low parasitic absorption.

The prediction of improved V_{oc} values in low volume absorbers has been demonstrated in practical devices by Sandu *et al.*, who showed that a 43.8 nm thick films of GaAs (a

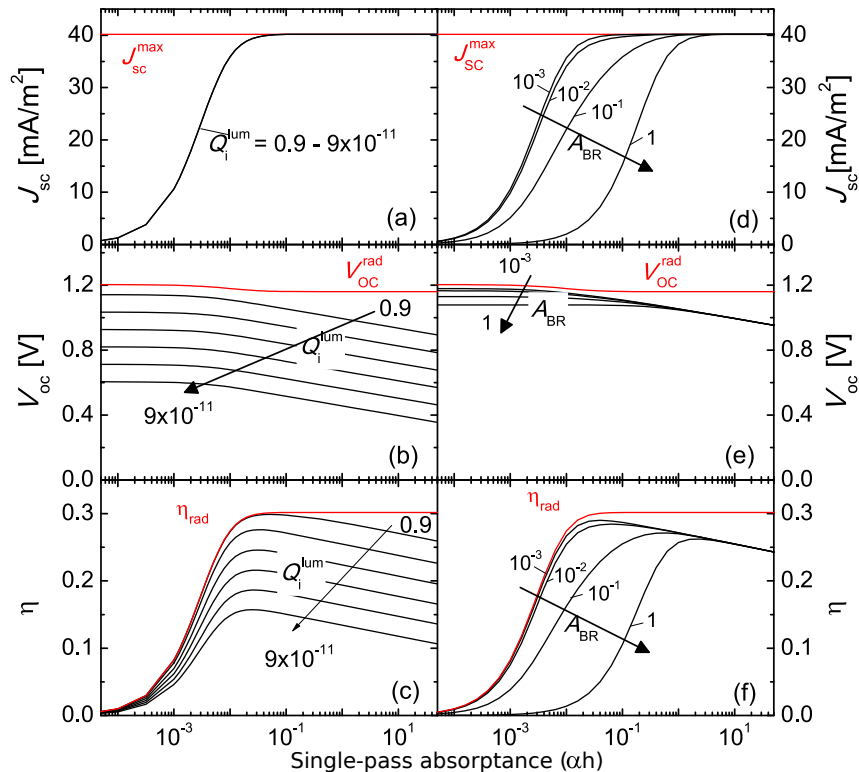


Figure 2.9: J_{sc} , V_{oc} and η of thin film absorbers as a function of the film’s single-pass absorptance αh [44]. In (a)-(c) the parasitic absorption, A_{BR} , is set to zero, while Q_i^{lum} is varied from 0.9 to 9×10^{-11} . In (d)-(f) A_{BR} is varied from 10^{-3} to 1 with $Q_i^{lum} = 0.5$. The red curves show the maximum obtainable J_{sc} , and the V_{oc} and η in the radiative limit where there are no parasitic losses.

material with high Q_i^{lum}) could have a $V_{oc} = 1.21$ V [46], which is significantly higher than the V_{oc} of 1.12 V for bulk GaAs SCs [47]. The J_{sc} in this case however was so far diminished that there was no improvement in the efficiency. A later study, also by Sandu *et al.*, showed that nanostructuring the ultra-thin GaAs film can increase the J_{sc} , while maintaining the enhancement in V_{oc} , thereby enhancing the PCE [48].

2.3 The Photovoltaic Zoo

We have so far examined the factors that contribute to the cost, and to the efficiency of photovoltaic solar cells. The wide range of solar energy applications places different emphasises on the cost, efficiency, weight, flexibility, and longevity of SCs, which allows many different technologies to produce commercially viable SC’s by combining these attributes in unique ways. Silicon is abundant, is very well understood after a wealth of research, and is processed using well established industrial techniques in large-scale, existing facilities; these factors make it difficult to displace silicon as the favoured photovoltaic material. To compete with Si SCs, technologies must promise either significantly higher energy conversion efficiencies, significantly lower processing costs, or both.

Figure 2.10 shows the record efficiencies of the various PV technologies as a function of time. Not shown in this plot is the typical cost of each technology, which varies greatly (otherwise only the most efficient technology would be viable). We briefly review the major types of PV technologies, in decreasing order of efficiency, identifying how nanophotonics can play a role in their development.

Best Research-Cell Efficiencies

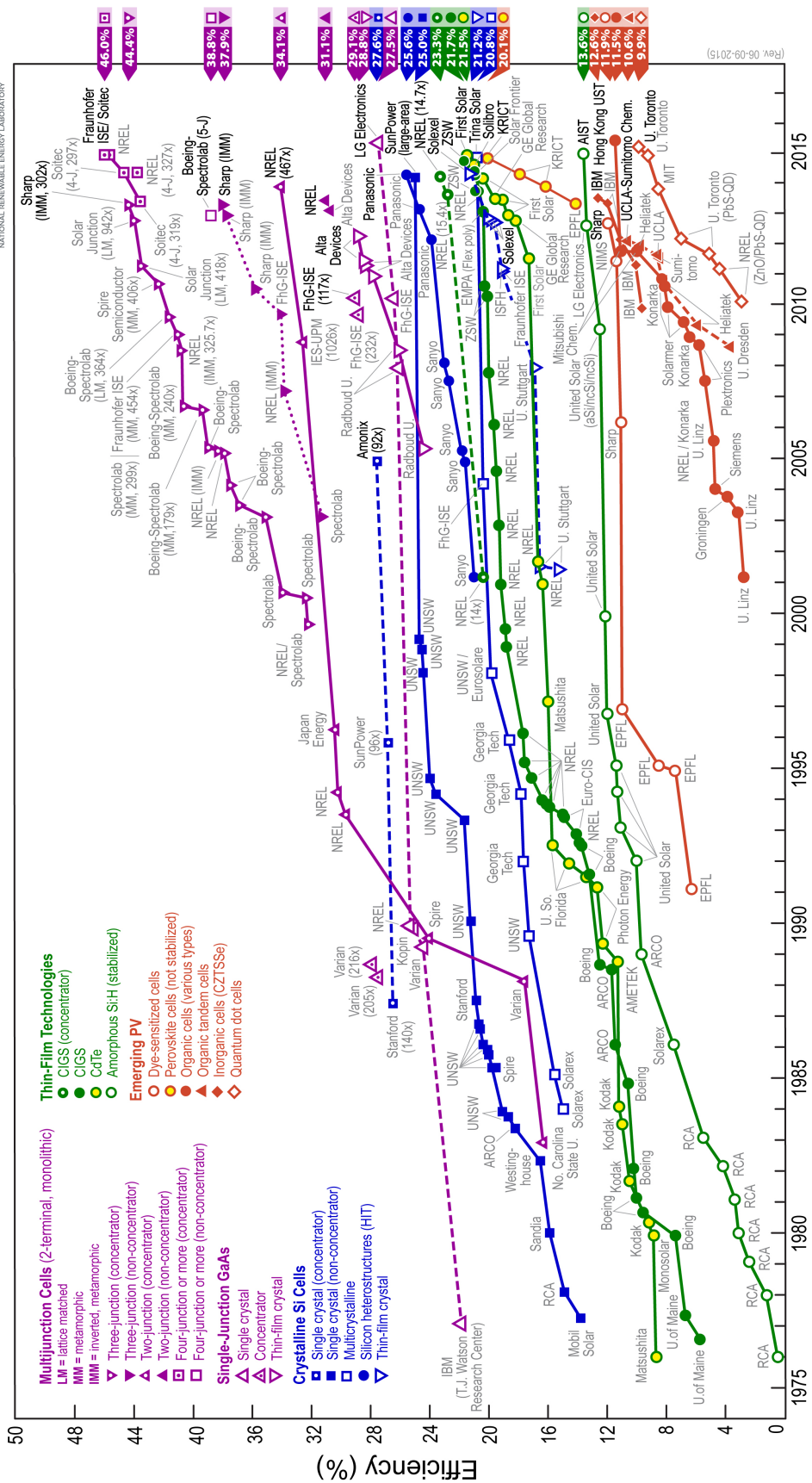


Figure 2.10: Improvement in PV efficiency of different technologies with time [49].

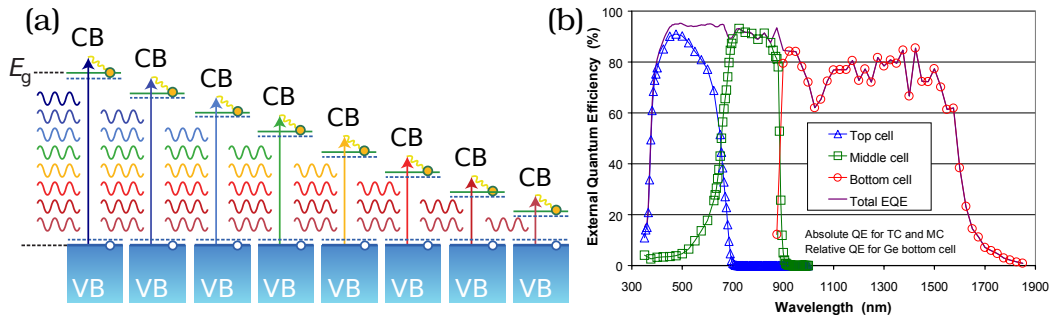


Figure 2.11: (a) Schematic of spectrum splitting (from [43]). External Quantum Efficiency measurement of triple junction SC showing EQE of each subcell (from [50]).

Multi-junctions

The largest efficiency increases beyond the single-junction S-Q limit are enabled by constructing SCs that contains multiple subcells, each with differing bandgap energies. The bandgaps of the subcells are chosen so that each efficiently converts a slice of the solar spectrum. This solution, illustrated in Fig. 2.11(a), simultaneously targets the energy lost to transmission of sub-bandgap photons, and to thermalisation of high energy photons. The multiple cells are typically integrated together into a monolithic device (Fig. 2.18(a)).

Figure 2.12(a) presents the S-Q analysis of the efficiency limit for a SC containing 2 junctions, and Fig. 2.12(b) examines the efficiencies possible if up to 6 junctions are included. The theoretical limit for 36 bandgaps, under $1000\times$ concentration, is 72% [51]. For comparison, the Carnot limit is 93% [51].

The record efficiency demonstrated for any SC is 46%, which was achieved by a cell containing 4-junctions (purple squares in uppermost part of Fig. 2.10) under $297\times$ concentration. Like most conventional multi-junction SCs, the semiconductors that make up this device are monolithically integrated (Fig. 2.18(a)). This has a number of inherent disadvantages including that the subcells are connected in series, with the current of the overall SC limited by the subcell generating the least current. This requires additional compromises to be made in the opto-electronic optimisation of the layer thicknesses.

The major practical challenges for multi-junction SCs stem from the monolithic integration of many different materials. As shown in Fig. 2.18(a), a monolithic multi-junction cell requires multiple layers for each subcell and then even more for the intermediate tunnel barrier buffer layers that electronically connect the subcells. All these layers must be of very high material quality in order to minimise parasitic losses. Their growth by epitaxial techniques under ultrahigh-vacuum is complex and expensive. Furthermore, the crystal-growth process demands that the materials be lattice-matched, which tightly restricts the materials available. So while the PCE of these SCs can be high, their cost is bound to be high also.

High Efficiency Single Junctions

After being held by researchers at UNSW for 15 years, the efficiency record for a single junction silicon SC was broken by Panasonic Corporation in December 2014 (full blue circles in Fig. 2.10). The new record of 25.6%, an improvement of 0.6%, was achieved using a heterojunction cell design featuring intrinsic (i-type) and doped a-Si:H layers on a randomly textured c-Si wafer [52]. The high efficiencies of heterojunction cells is largely due to their enhanced radiative efficiencies, which allow them to reach higher V_{oc} values (as discussed in Sect. 2.2.6). The high radiative efficiency is due to wafers of higher purity, reduced thickness and the improved passivation provided by the a-Si layers (the record cell also has a SiN layer at the front). The record breaking cell was exclusively back contacted, which removed shadowing losses and increased the J_{sc} over previous Panasonic heterojunction cells.

The record efficiency for single junction GaAs cells was also credited to improving the radiative performance of the SC [53]. The record of 28.8% is held by Alta devices (purple

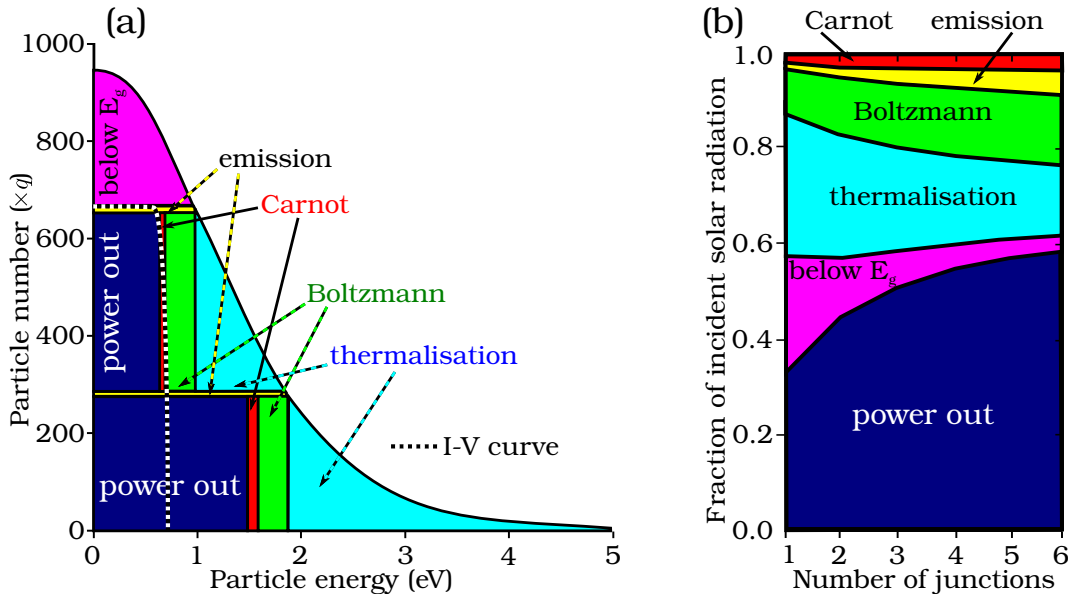


Figure 2.12: (a) Energy conversion efficiency as a function of number of band gap energies, showing how the efficiency is reduced due to different processes. (b) Efficiency breakdown of a tandem SC showing efficiency losses. Adapted from [36].

open, upright triangles in Fig. 2.10), who developed an epitaxial lift-off technique that creates very pure GaAs wafers, free of the impurities that diffuse into typical GaAs wafers during the growth process [54]. Thin silicon wafers of improved quality may also be created by epitaxial lift-off processes or wafer splicing techniques [55]. With c-Si SC approaching what is seen to be their practical limit of 26% [56] the challenges for these technology lie in transitioning these devices into commercial manufacturing and reducing their costs, for recent progress see [57].

Standard Silicon Cells

The SC market remains dominated by Si SCs (single-crystalline and multi-crystalline) that typically have module efficiencies in the range of 17-23%. The underlying technology of these cells has been stable for many years, with cost reductions and efficiency enhancements coming mostly from improvements in industrial processing, as discussed in detail in Sect. 2.1.

Thin Film Technologies

Figure. 2.10 contains many green data points that represent technologies that use thin films ($h < 1 \mu\text{m}$) as their active layers including amorphous silicon (a-Si), copper indium gallium selenide (CIGS), cadmium telluride (CdTe). These materials are cheaper than conventional semiconductors and are strongly absorptive, however their electrical properties are quite poor which limits the thickness of the active layer and their efficiencies to 13.6% (stabilized) [58], 21.7% [59] and 21.5% [60] respectively.

The “tremendous market fluctuations” [20] in the solar industry over the last five years have been particularly dramatic for these technologies, where companies were borrowing heavily to carry out research and development. The price rise in polycrystalline silicon wafers saw investments boom while the recent price drop in $\$/\text{W}$ of Si SCs has caused many of these companies to declare bankruptcy [61].

Another thin film approach is to use conventional semiconductors, such as c-Si, InP and GaAs, but with thicknesses of $h \sim 1 - 10 \mu\text{m}$ rather than the $h \sim 200 \mu\text{m}$ used in current commercial cells. This reduces costs, but also reduces the absorption unless the cell design is modified to introduce strong light trapping. Since traditional light trapping schemes are

incompatible with thin films, as they rely on macroscopic surface textures, such as inverted pyramids, that themselves are approximately $10\ \mu\text{m}$ tall, there has been substantial research into using nanophotonic structures to achieve enhanced absorption and light trapping, as discussed in Sect. 2.4.

Emerging Technologies

The lowest efficiency technologies, shown in orange in Fig. 2.10, are also by far the cheapest. They are made of materials such as dyes (PCE 11.9%) [62], or organic polymers (PCE 11.5%) [49], which are very cheap, and can be processed into SCs using roll-to-roll processes that are cheap to run and have high throughputs. In addition to their price, these SCs are generally also flexible, which together with their cost opens up new applications and markets. Flexible SCs have also been made using thin-film semiconductors such as Si and GaAs, however the market for these is slightly different because they are more expensive.

Another class of materials being developed for SCs are “earth abundant” semiconductors, such as FeS_2 , CuO , and Zn_3P_2 [63, 64]. These are inexpensive with large deposits distributed across the globe, making them far less geo-politically sensitive than Te and In. These materials are typically strongly absorbing at solar wavelengths, however their electrical properties are very poor, limiting their thicknesses to ultra-thin films ($h < 0.1\ \mu\text{m}$). Achieving decent PCEs with such materials will require substantially different cell designs that balance the competing demands of their opto-electronic properties. Addressing this challenge is one of the motivations of Ch. 7.

The technologies in this category are under pressure from the falling price of Si SCs, as well as the emergence of a new class of SC materials - perovskites. Perovskite SCs use a similar volume of active absorber material and are set to target a similar market to existing thin film technologies. The fundamental material properties of these materials are still poorly understood, with major issues surrounding their stability (the efficiency of current state of the art cells drops to essentially zero after a matter of days), their mechanical strength, and their decay with exposure to the elements. Despite this, the PCE of perovskite SCs has increased at an unprecedented rate shown in the yellow circles orange lines in Fig. 2.10, which has created great excitement in the scientific [65, 66] and broader communities [67–69]. We leave a more detailed discussion of perovskite SCs for Ch. 6.

Third Generation Photovoltaics

In addition to these existing PV technologies there are numerous exotic systems under investigation. These try to capture the energy lost to thermalisation in conventional single junction SC by exploiting multiple-exciton interactions, collecting hot-carriers [70], or by

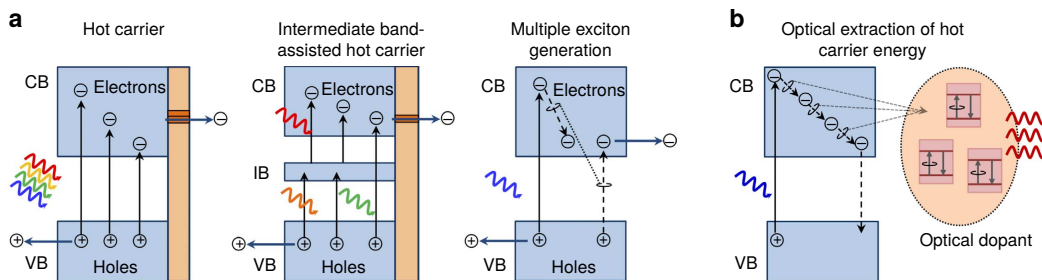


Figure 2.13: Hot-carrier solar-cell concepts. (a) Three currently considered hot-carrier solar-cell strategies: direct extraction of hot carriers through energy-selective contacts, application of an intermediate-band-assisted absorber and using multiple exciton generation, when a hot carrier induces additional excitations across the bandgap. (b) The concept of optical extraction: hot carriers transfer their excess energy to nearby Er^{3+} ions, which subsequently emit infrared photons. VB, CB and IB stand for valence, conduction, and intermediate band, respectively. [70]

using downconversion materials; or they minimise the energy lost to sub-bandgap transmission by making use of intermediate-bands [71, 72], or using additional materials to upconvert photons [73]. Figure 2.13 shows three hot-carrier SC concepts as well as a schematic for optical extraction. These concepts are still in the basis stages of development and it is unclear which, if any, will come to fruition. We do not consider them further than mentioning that some potential may exist for the engineering of photon-phonon interactions as is being explored in phononic crystals [74].

2.4 Opportunities for Photonics

There is room for improvement in the many stages that make up the costs of SCs, and there are many ways in which the efficiency, weight, flexibility, and longevity of SCs may be improved further. The research communities engaged in addressing these challenges are diverse. For photonics researchers there exist two main opportunities: increasing the absorption of thin and ultra-thin PVs (targeting cost, weight, flexibility); and creating components that enable new SC designs, such as inexpensive tandem SCs (targeting cost vs. efficiency).

We pursue these goals by designing dielectric nanostructures to control the flow of sunlight through the SC. This is similar to the work on plasmonic SCs where the propagation of light is manipulated by tailoring the plasmonic resonances of metallic nanoparticles. Plasmonic structures have received a lot of attention in the last decade [75–77], however there have been only a very limited number of demonstrations of enhanced efficiencies of realistic cells [78, 79]. This is because the use of metals invariably introduces parasitic losses in the form of Ohmic losses in the metal. The detrimental impact of these losses was highlighted in the analysis of the Sect 2.2.5. In our work we focus solely on weakly-absorbing semiconductors that offer the potential for substantial control of light with minimal parasitic absorption.

2.4.1 Absorption Enhancement in Thin Films

Anti-reflection

The simplest light management structures are anti-reflection (AR) coatings, which, as implied in the name, reduce the reflection off the front surface of a cell. The two main types of AR coatings used in conventional SCs are: graded index layers, as shown in Fig. 2.14, where the front surface is textured, for instance by creating random pyramids [80] or inverted pyramids [81], so as to smooth the transition in the refractive index from the incident medium to the absorbing layer; and dielectric interference layers that consists of a uniform layer of optical thickness $nh = \lambda_0/4$, so that the light (of wavelength λ_0) reflected off the front of the layer is out of phase with the light that has passed through the layer and has been reflected off its bottom surface.

Textured surfaces are used in conventional, thick SCs and are effective across the entire solar spectrum, however they are incompatible with thin absorbers because they themselves typically penetrate 1-10 μm into the absorber. Quarter wavelength layers on the other hand can be added to thin absorbers but are only effective for wavelengths around λ_0 (their thickness also detracts from the weight and flexibility of the thin films). The two approaches are generally combined in Si SCs, with the textured surface being coated by quarter wavelength layers of SiN/SiO₂, as is done in the “PERL” (passivated emitter with rear locally diffused) cell [82].

The primary problem with AR coatings on thin absorbers is that they do not prevent losses due to transmission through thin and/or weakly absorbing layers. Assuming a perfect AR coating as well as a perfect back reflector, the absorption of a layer of thickness h is given by $A = 1 - e^{-2\alpha h}$, where $\alpha = 4\pi n''(\lambda)/\lambda$ is the attenuation coefficient in a medium with complex refractive index $n = n' + in''$. To address the problem of incomplete absorption in SCs with modest values of αh we must develop techniques that “trap” light within the absorbing layer so that the light experiences an effective path length greater than $2h$.

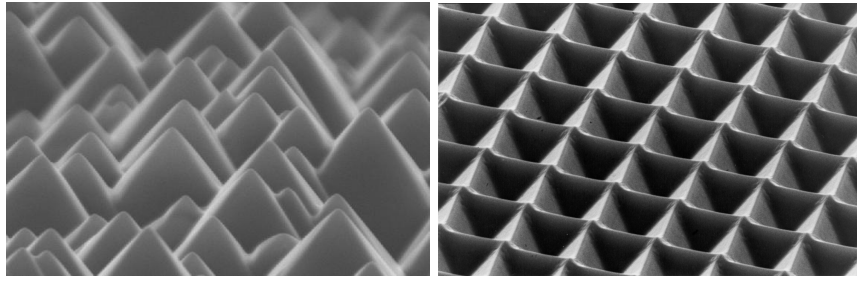


Figure 2.14: Anti-reflection layers: (a) random pyramidal surface texture (b) inverted pyramids surface texture [83].

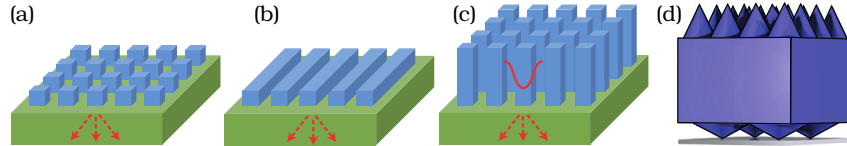


Figure 2.15: Dielectric light trapping designs: (a) a bi-periodic array of Mie scattering particles; (b) periodic array of horizontally aligned nanowires; (c) a bi-periodic array of vertically aligned nanowires; (d) front and back surface pyramids. Because one-dimensional arrays are highly polarisation sensitive and sunlight is unpolarised, it is generally preferable to use bi-periodic structures as in (a), (c), (d). In all cases light is incident from above. (a)-(c) Adapted from [90] and (d) from [91].

Light Trapping

Light trapping techniques were originally developed to address the poor performance of silicon SCs at wavelengths close to the band-edge. In this case the typical approach is to design the AR surface texture (such as inverted pyramids) to scatter light into the absorbing layer at oblique angles, which increases the likelihood that the light is totally internally reflected thereby increasing the light's path length within the layer.

In thick SCs it was found that the greatest absorption enhancement was produced by a fully randomised surface texture because this scatters light with a Lambertian distribution [84]. With an ideal Lambertian scatterer the absorption enhancement factor is $4n^2/\sin(\theta)$, where θ is the angle of the emission cone in the medium surrounding the cell. This limit is derived using geometric ray optics and is only applicable to absorbers much thicker than the wavelength. In the nanophotonic regime, where the propagation of light is governed by wave-optics and modes are confined on a deeply-subwavelength scale, the conventional limit may be exceeded. This was shown by Yu *et al.* who derived a generalised enhancement limit using statistical temporal coupled-mode theory [85, 86] and has also been shown numerically for various structures [87–89].

The optical modes are confined within the high index material because their in-plane wavevectors exceed those of the propagating modes of the surrounding media. Coupling energy into these modes requires a diffractive element that provides the additional required momentum via its reciprocal lattice vectors. The diffractive structure may be placed above, below or within the absorbing layer; or alternatively the absorbing layer itself may be periodically nanostructured. Our review of light trapping structures is arranged around this distinction.

Textured Surroundings

Figures 2.15(a)-(c) shows three types of simple light trapping nanostructures that have been used to enhance the absorption of the (green) semiconductor: (a) an array of Mie scatterers; (b) a one-dimensional array of horizontally aligned nanowires; (c) a two-dimensional array of vertically aligned nanowires. The periodic arrangement of the particles enables them to

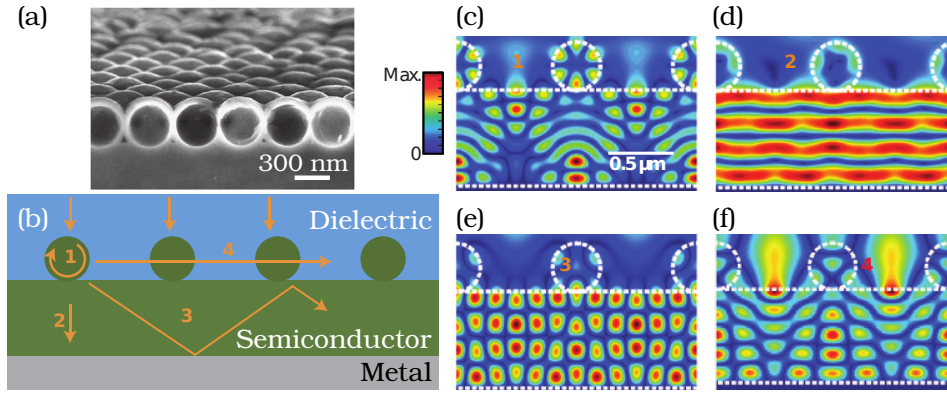


Figure 2.16: Light trapping using spherical scatterers. (a) SEM image from [92]. (b) Schematic showing different resonance pathways, the electric fields of which are shown in: (c) a mixture of a Mie resonance of the sphere and a guided mode resonance of the film; (d) a Fabry-Perot resonance of the thin film; (e) a waveguide mode resonance that is coupled to free space via the reciprocal lattice vector of the array; (f) a diffracted resonance, where the guided mode propagates laterally in the layer made up of the spheres. Adapted from [90].

couple light between the plane waves of free space and the guided modes of the substrate. The particles themselves also support resonant modes, which, on resonance, greatly increase their scattering strength beyond their geometric size.

An inherent limitation of one-dimensional gratings (b) is their polarisation sensitivity (see for example [93, 94]). The difference between (a) and the taller structures in (c) is that the tall nanowires (NWs) support waveguide modes, whereas the particles in (a) behave as Mie scatterers. As external scatterers we focus on (a), leaving the physics of vertically aligned NWs for Chaps. 4 and 5. A study of NW arrays as a window layer is contained in [95], where an efficiency of 17% was achieved in a GaAs SC.

The use of Mie resonators in SCs has been primarily developed by Polman *et al.* [96, 97]. They have shown that two-dimensional, periodic arrays of subwavelength silicon nanocylinders placed onto a SC can provide both very good anti-reflection performance [96] as well as strongly enhancing the absorption through light trapping [97]. Their central finding is that the Mie resonance can be designed to strongly preferentially scatter light into the high-index substrate where there is a high optical density of states. Figures 2.16(b)-(f) illustrate the four avenues by which the spheres, shown in Fig. 2.16(a), can enhance the absorption of the substrate layer (of the same refractive index) [90]. The processes labelled 1 and 4 in Fig. 2.16(b) are resonances of the spheres, while in 2 and 3 the spheres are intermediaries to the excitation of resonances within the film. The electric field intensity distributions corresponding to the resonances are shown in Figs. 2.16(c)-(f).

A more complicated light trapping structure is shown in Fig. 2.15(d), where the pyramids at the front interface are designed to reduce reflections, with a long narrow profile that slowly bridges the refractive index difference, and a small period so that extra propagating orders are not excited. The pyramids at the back meanwhile are short and are arranged with a larger period so as to trap the light by diffracting it sideways. Their precise dimensions were found by a numerical optimisation in [91], where they were shown to achieve an absorption very close to the Lambertian light trapping limit.

A major advantage of using light trapping structures that are separated from the absorbing layer is that the electronic properties of the absorber are unchanged. Structuring the absorber directly on the other hand increases the surface area and the associated surface recombinations, which requires specialised passivation techniques for these effects to be minimised. The advantage of nanostructured absorbers is that they can achieve greater optical confinement.

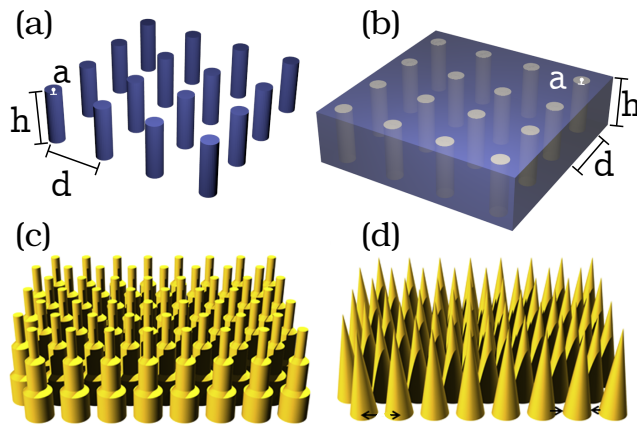


Figure 2.17: Schematics of: (a) a nanowire arrays; (b) a nanohole array; (c) a multi-diameter nanowire array (from [102]) and; (d) a nanocone array (from [102]). In all cases light is incident from above.

Structured Absorbers

An alternative route to exciting guided mode in the absorbing region is to structure the absorbing layer itself. This can be done by introducing low refractive index inclusions into the high index absorbing layer, or by creating isolated regions of high index absorber surrounded by a low index background. The canonical embodiments of these structures are nanohole (NH) and nanowire (NW) arrays respectively, which are shown in Figs. 2.17(a), and 2.17(b).

In both cases the dilution of the high refractive index of the absorber with a material with lower index reduces the reflection. Variations of these structures can be made by tapering the inclusion along the axis of the wires/holes (vertically), which reduces the reflection even further due to a more gradual transition in the effective index of the structures. A large range of different shapes has been studied, including: nanocones [98] (Fig. 2.17(d)); nanodomains [99]; nano-conical-frustums [100]; dual-diameter [101] and multi-diameter nanopillars [102] (Fig. 2.17(c)); and nano-syringes [103] (for reviews see [90, 104]).

In Chapters 4 and 5 we focus on NW arrays and, to a lesser extent, NH arrays, as the simplest and definitive examples of nanostructured absorbers. We present a detailed review of the associated literature in the introduction of Ch. 4, before examining the different optical processes that contributing to the strong light trapping.

2.4.2 Spectrum Splitting

In Sect. 2.3 we discussed how substantially higher PCEs could be achieved by combining multiple SCs with different bandgaps because these reduce the amount of energy lost to thermalisation and to sub-bandgap transmission. The major drawbacks of these cells are the high costs incurred due to specialised growth techniques, and the restriction placed on material combinations because the crystal lattice constant of all materials must be closely matched in order for them to be grown on top of one another.

An alternative approach is to construct multi-junction SCs from mechanically decoupled single junction SCs. This can be done by stacking SCs on top of each other or by using spectrum splitting optics to direct the appropriate part of the solar spectrum to the each SC, as illustrated in Fig. 2.18(b). Creating these devices is far simpler than that of monolithically integrated multi-junctions (Fig. 2.18(a)) because each SC can be fabricated independently with no constraints on the materials used in each SC. Another distinction is that the subcells of decoupled multi-junctions can be electrically connected in parallel so there is no penalty of the cells having different currents; monolithic structures in contrast are intrinsically connected in series so the current of the total device is set by the subcell

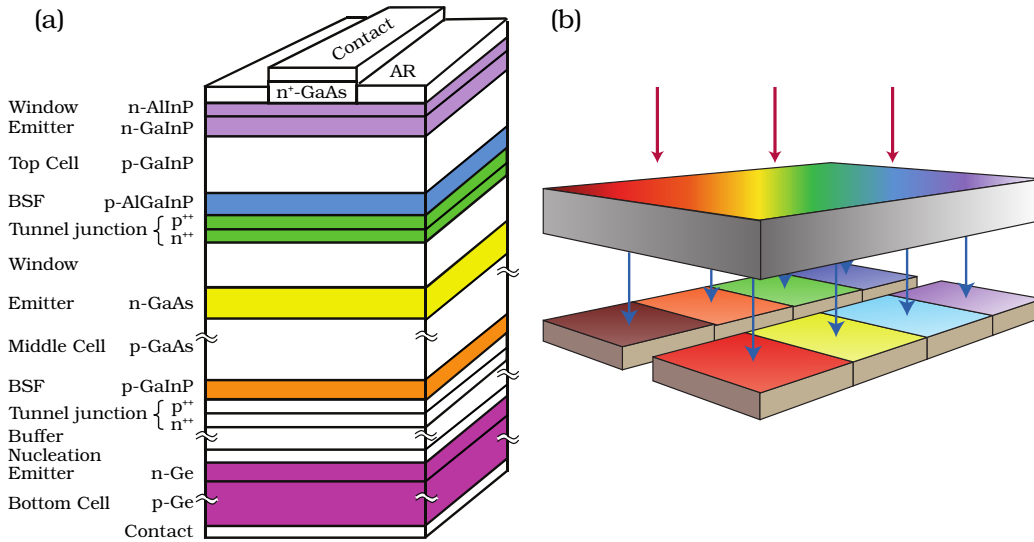


Figure 2.18: (a) Monolithically integrated multi-junction cell, adapted from [50].
 (b) Schematic of spectrum splitting, adapted from [43]

with the lowest current. A drawback of connecting subcells in parallel is that each circuit needs an inverter, however this may be alleviated by adjusting the relative areas of the cells so that their current is matched, and then connecting them in series [21].

The development of mechanically decoupled multi-junction cells has recently seen a resurgence of interest, driven by two exciting opportunities: the development of ultra-high efficiency devices with efficiencies of over 50% [43], using a greater number of subcells than can be realistically integrated monolithically, and; the creation of relatively inexpensive high efficiency ($\eta > 30\%$) tandem SCs based on cheap silicon SCs [105]. The challenge in realising these efficiency targets lies in the creation of low loss nanoscale components that split the solar spectrum into broadband slices that are directed to the appropriate subcells. In Ch. 6 we investigate the physics of dielectric gratings and how they can be used for this task.

2.4.3 Fabrication of Photovoltaic Nanostructures

The advantages of incorporating nanostructures into SCs has been proven theoretically and experimentally, but their use in commercial SCs remains hindered by the constraints on their fabrication. While experimental demonstrations can use photolithography, as is widely used for fabricating electronics and nanophotonic circuits, this technique is too expensive for mass production. There are therefore great interests in developing fabrication techniques that are low-cost, high-yield, and scalable. Potential methods include colloidal lithography, nano-imprint lithography (NIL) and roll mask lithography.

Figure 2.19(a) illustrates how roll mask lithography transfers a pattern from the outside of a quartz cylinder into the photosensitive substrate by the ultraviolet light coming from the inside of the cylinder. This technique is being commercialised by Rolith [106], who have demonstrated roll-to-roll processing over meter scaled substrates, Fig. 2.19(b). Nano-imprint lithography involves creating a reusable stamp from a master structure, which is typically created using expensive electron-beam lithography, and then reusing the stamp many times to fabricate many structures. There are three types of NIL that are distinguished by the type of stamp they use: hard-NIL, which uses a rigid high resolution stamp over small areas; soft-NIL, which uses silicone stamps over larger areas with reduced resolution; and substrate-conformal imprint lithography (SCIL), which uses a composite rubber stamp. Figure 2.19(c) shows a schematic of SCIL [107, 108], where the stamp is deposited gradually into the substrate to minimize the trapped air, and thereby achieve higher resolution than conventional soft-NIL but with the low-cost, flexibility, and robustness of rubber stamps.

SCIL has demonstrated sub-10 nm resolution over 15 cm diameter substrates [107] and has also been adapted to fabricate metallic nanostructures when combined with etching techniques [108]. Another lithographic technique is shown in Fig. 2.20 where colloidal SiO_2 nanoparticles are deposited on the substrate, distributed into a close-packed monolayer or few-layer film using a wire-wound rod, and then used as the etch mask.

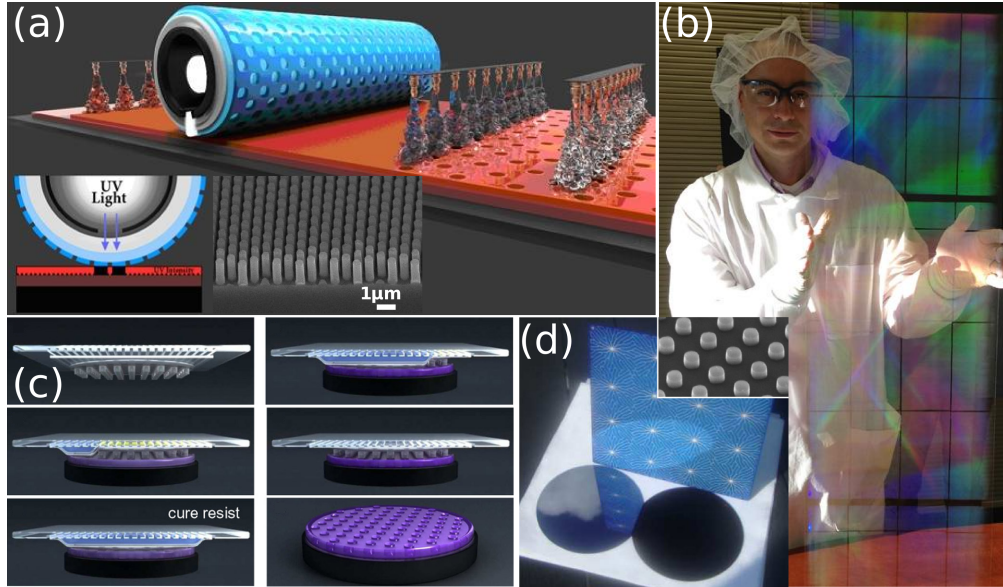


Figure 2.19: Examples of large scale nanofabrication techniques. (a) Illustration of the rolling mask lithography technique and (b) an example of this technique being used to cover a meter long glass panels with nanostructures. (c) Schematic of substrate conformal imprint lithography, where the stamp is gradually pressed into the substrate. (d) A silicon wafer (bottom left), a commercial photovoltaic wafer (back), and a silicon wafer covered with Mie scatterers (bottom right). Inset shows a SEM micrograph of the Mie scatterers (125 nm high silicon cylinders arranged with a period of 450 nm) [107].

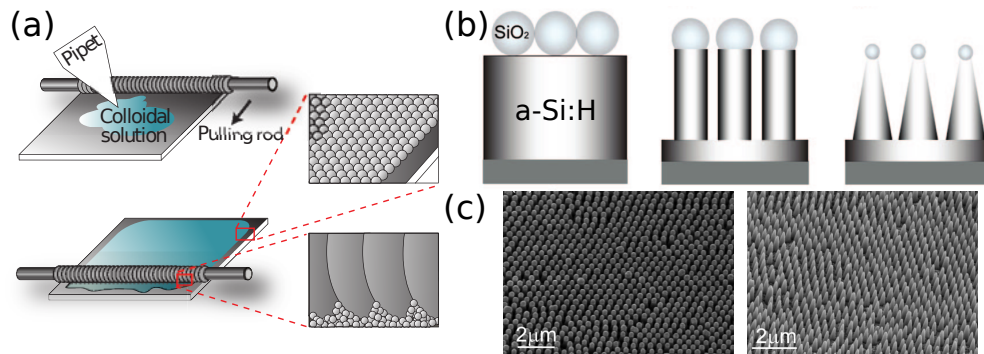


Figure 2.20: Schematic of a wire-wound rod being used to deposit close-packed monolayers or multilayers of SiO_2 nanoparticles on a substrate [109]. This pattern can then be transferred into the substrate to form nanowires or nanocones with distinct refractive-index profiles [98].

Epilogue

We presented a review of current SC technologies and the research directions being pursued to improve them, both in terms of their efficiency and their cost. Our analysis highlights a number of opportunities where nanophotonics, and in particular dielectric nanostructures can provide valuable contributions to these improvements. In this thesis we investigate the optical physics of different nanostructures, some of which enhance the absorption of thin films through light trapping, while others enable new types of multi-junction cells.

Chapter 3

EMUstack: The Workhorse

*If we had a military division with the ...
carrying capacity of these birds (Emus),
it would face any army in the world.*

Major Meredith
(the Great Emu War of 1932)

Why is the sky blue; the clouds white; and why does the sky turn red at sunrise and sunset? The answer to each question, which have fascinated humankind throughout the ages, arises from a common origin: that light behaves in interesting ways when it interacts with particles that are approximately the same size as the wavelength of the light. At a fundamental level, this thesis extends our insight into similar interactions.

At these scales, light interacts with matter as a wave and we cannot use the approximations of ray-optics. In order to carry out our investigations we require a simulation tool that solves the full Maxwell equations, and does so in a manner that produces the most physically intuitive results.

In this chapter we present the semi-analytic method that we employ throughout the remainder of the thesis. The approach and its implementation is summarised in Paper 3.1, where we highlight some of the physically meaningful quantities that we have access to. A detailed description of the mathematical formalism of the approach is given in [110].



Figure 3.1: The sky over Tennant Creek (during the writing of this chapter) and a dusty sunrise over Western Arnhem Land.

We are generally interested in the behaviour of structures under constant illumination, so we assume the fields to have harmonic, $e^{-i\omega t}$, time dependences and solve for steady state solutions of the macroscopic Maxwell equations,

$$\nabla \times \mathbf{H} = -i k \varepsilon \mathbf{E}, \quad \nabla \cdot (\varepsilon \mathbf{E}) = 0, \quad (3.1)$$

$$\nabla \times \mathbf{E} = i k \mu \mathbf{H}, \quad \nabla \cdot (\mu \mathbf{H}) = 0. \quad (3.2)$$

Here ε and μ are the relative dielectric permittivity and magnetic permeability respectively and the magnetic field \mathbf{H} has been rescaled as $Z_0 \mathbf{H} \rightarrow \mathbf{H}$, with $Z_0 = \sqrt{\mu_0/\varepsilon_0}$, the impedance of free space.

We typically focus on situations where interfaces occur in the x - y -plane, as in Fig. 1 of Paper 3.1. In these cases it is convenient to separate the fields into

$$\mathbf{E}_{\parallel} = \mathbf{E}(x, y), \quad \mathbf{E}_{\perp} = \mathbf{E}(z), \quad (3.3)$$

and likewise for \mathbf{H} . Similarly, we separate the wavevector $\mathbf{k} = n\mathbf{k}_0 = n2\pi/\lambda\hat{\mathbf{k}}$ into

$$\mathbf{k}_{\parallel} = \mathbf{k}(x, y), \quad k_{\perp} = k(z), \quad (3.4)$$

such that

$$\mathbf{k} = \sqrt{\mathbf{k}_{\parallel}^2 + k_{\perp}^2} \hat{\mathbf{k}}. \quad (3.5)$$

If n is real, there exist two classes of waves; those with real \mathbf{k} that propagate energy without loss, and those with negative imaginary \mathbf{k} that decay exponentially and do not propagate any energy through an infinitely thick medium. When the refractive index is complex, $n = n' + in'' = \sqrt{\mu\varepsilon}$, all waves have complex \mathbf{k} and propagate with some decay in amplitude.

Prelude to Paper 3.1

We now present an outline of the simulation package that we have created, and which was used throughout all of our investigations:

B. C. P. Sturmberg, K. B. Dossou, F. J. Lawrence, C. G. Poulton, R. C. McPhedran, C. M. de Sterke and L. C. Botten. “[EMUstack: an open source route to insightful electromagnetic computation via the Bloch mode scattering matrix method](#)”. *Computer Physics Communications (In Press)*



Contents lists available at ScienceDirect

Computer Physics Communications

journal homepage: www.elsevier.com/locate/cpc

EMUstack: An open source route to insightful electromagnetic computation via the Bloch mode scattering matrix method

Björn C.P. Sturmberg^{a,*}, Kokou B. Dossou^b, Felix J. Lawrence^b, Christopher G. Poulton^b,
Ross C. McPhedran^a, C. Martijn de Sterke^a, Lindsay C. Botten^{b,c}

^a CUDOS and IPOS, School of Physics, University of Sydney, Sydney, 2006, Australia

^b CUDOS, School of Mathematical and Physical Sciences, University of Technology Sydney, Sydney, 2007, Australia

^c National Computational Infrastructure, Australian National University, Canberra, Australia

ARTICLE INFO

Article history:

Received 6 June 2015

Received in revised form

13 October 2015

Accepted 26 December 2015

Available online xxxx

Keywords:

Computational electromagnetism

Finite Element Method

Scattering matrix method

Maxwell solver

ABSTRACT

We describe EMUstack, an open-source implementation of the Scattering Matrix Method (SMM) for solving field problems in layered media. The fields inside nanostructured layers are described in terms of Bloch modes that are found using the Finite Element Method (FEM). Direct access to these modes allows the physical intuition of thin film optics to be extended to complex structures. The combination of the SMM and the FEM makes EMUstack ideally suited for studying lossy, high-index contrast structures, which challenge conventional SMMs.

Program summary

Program title: EMUstack

Catalogue identifier: AEZI_v1_0

Program summary URL: http://cpc.cs.qub.ac.uk/summaries/AEZI_v1_0.html

Program obtainable from: CPC Program Library, Queen's University, Belfast, N. Ireland

Licensing provisions: GNU General Public License, version 3

No. of lines in distributed program, including test data, etc.: 154301

No. of bytes in distributed program, including test data, etc.: 5308635

Distribution format: tar.gz

Programming language: Python, Fortran.

Computer: Any computer with a Unix-like system with Python, a Fortran compiler and F2Py [1]. Also required are the following free libraries LAPACK and BLAS [2], UMFPACK [3]. Developed on 1.6 GHz Intel Core i7.

Operating system: Any Unix-like system; developed on Ubuntu 14.04 (using Linux kernel 3.16).

RAM: Problem dependent; specifically on the resolution of the FEM mesh and the number of modes included. The given example uses approximately 100 MB.

Classification: 10.

External routines: Required are the following free libraries LAPACK and BLAS [2], UMFPACK [3]. Optionally exploits additional commercial software packages: Intel MKL [4], Gmsh [5].

Nature of problem: Time-harmonic electrodynamics in layered media.

Solution method: Finite element method and the scattering matrix method.

Running time: Problem dependent (typically about 3 s per wavelength including plane wave orders ≤ 3).

* Corresponding author.

E-mail address: bjorn.sturmberg@sydney.edu.au (B.C.P. Sturmberg).

<http://dx.doi.org/10.1016/j.cpc.2015.12.022>

0010-4655/© 2016 Elsevier B.V. All rights reserved.

References:

- [1] P. Peterson, F2PY: A tool for connecting Fortran and Python programs, *International Journal of Computational Science and Engineering* 4 (4) (2009) 296.
- [2] LAPACK, <http://www.netlib.org/lapack>
- [3] T.A. Davis, Algorithm 832: UMFPACK V4.3 - An Unsymmetric-Pattern Multifrontal Method, *ACM Transactions on Mathematical Software* 30 (2) (2004) 165–195.
- [4] Intel MKL, <http://www.software.intel.com/intel-mkl>
- [5] C. Geuzaine, J.-F. Remacle, Gmsh: a three-dimensional finite element mesh generator with built-in pre- and post-processing facilities, *International Journal for Numerical Methods in Engineering* 79 (2009) 1309–1331.

© 2016 Elsevier B.V. All rights reserved.

1. Introduction

Solving Maxwell's equations in structured media is no longer the challenge it historically has been; there exist a wide range of commercial and free software that can simulate the interaction of light with a wide variety of structures. The real challenge now in computational electromagnetism lies therefore not in solving Maxwell's equations, or even doing so most efficiently; but rather it lies in doing so in a way that produces the most physically insightful results. To this end, many specialized tools have been developed that simulate a restricted subset of systems with improved detail, exploiting additional knowledge about the class of systems. If a tool is tailored to a restricted subset of systems, it can apply physical constraints to reduce the dimensionality of the problem. Examples of such methods include: photonic band solvers [1], boundary element or multipole methods [2,3], impedance methods [4], and beam propagation methods [5,6].

Here we present an approach that ploughs the middle ground; it restricts itself somewhat in problems, in exchange for improved physical insight. It allows us to calculate the propagation of light through structured layered media by solving for the eigenmodes of each layer, and calculating the scattering matrices of the interfaces that describe the coupling of light between the layers. Accelerated numerical performance is a further reward of the restriction as many calculation steps have closed-form matrix representations.

Our program, codenamed EMUstack (Electromagnetic Multi-layered stack) [7], is a type of Scattering Matrix Method (SMM) where the eigenmodes of nanostructured layers are found using the Finite Element Method (FEM). The use of the FEM endows EMUstack with a greater generality than existing SMMs, in particular when simulating structures that include fine high index inclusions. Advantages of using the FEM include being able to adaptively mesh geometries, faster convergence of the BM expansion, and avoiding the Gibbs phenomenon that occurs in Fourier based methods (these are discussed in detail in Section 3).

The program takes light of a chosen k -vector (wavelength and angle of incidence) as the input and outputs the fields and propagation constants of the modes of each layer, as well as the reflection and transmission scattering matrices of the interfaces of each layer with air and of the interfaces between adjacent layers. With these quantities we can solve driven problems, such as the transmission, reflection in each of the diffracted orders and the absorption within each layer of the structure, as well as undriven problems, such as the resonances of the structure. These results allow us to extend the physical intuition of thin film optics to complex structures as highlighted in Section 4.

Similarly to other SMMs, such as Rigorous Coupled Wave Analysis (RCWA) [8] and the Fourier Modal Method (FMM) [9–11], structures must meet two fundamental requirements to be

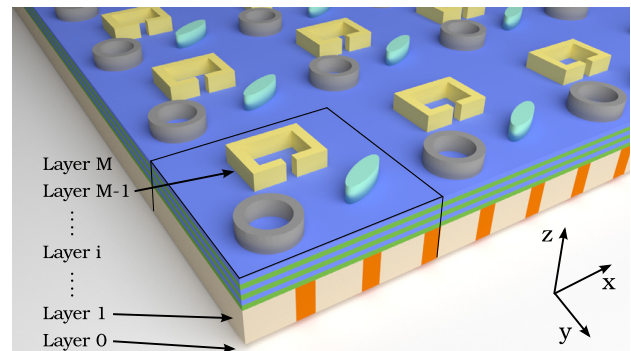


Fig. 1. Illustration of a multi-layered structure that is compatible with EMUstack. The layers 0 through M all may be regarded as sharing a common period, and each layer is invariant in the z -direction. The unit cell is marked with black lines. In this example layers 0, M are semi-infinite layers of air and all 2D nanostructures are on layer $M-1$.

compatible with EMUstack: they must be composed of a finite number of z -invariant layers, and each layer must be able to be regarded as sharing a common in-plane periodicity or be uniform (see Fig. 1). We note that the differential method [12] and the C-method [13], which are related to the SMM, can handle non-planar layers.

EMUstack is specifically designed to study materials that are lossy. In the current version materials must be linear, isotropic and non-magnetic. The top and bottom layers must be semi-infinite in the z -direction but may still be lossy and/or nanostructured, although in such cases EMUstack cannot solve the driven problems (calculating energy fluxes).

A detailed description of the mathematical formalism has been given by Dossou et al. [14], and in this article we outline the open-source implementation of this method. A detailed user manual is available online [15,16] so we here focus on the unique features of EMUstack and the physical insights it enables.

The remainder of this paper is organized as follows: in Section 2 we outline the numerical method; in Section 3 we describe our implementation and demonstrate how EMUstack is used; and in Section 4 we present examples that illustrate the type of results obtained with EMUstack.

2. Approach outline

The central idea of SMMs is to separate the scattering of light at interfaces from the propagation of light through layers. The electromagnetic field is described by a superposition of modes that acquire phase and decay/grow while propagating in the z -direction, but do not couple to one another, except at layer

boundaries. Interfaces are described by scattering matrices, \mathbf{T}_{ij} , \mathbf{R}_{ij} , which describe the transmission and reflection at the interface between layers i and j , incident from i . The propagation within layer i is represented by multiplication by a diagonal matrix \mathbf{P}_i . Calculating these matrices relies on knowing the eigenfunction solutions of Maxwell's equations in each layer, which is the most fundamental part of the calculation.

The eigenfunctions of periodic structures are Bloch modes (BMs), whose functional form matches the periodicity of the refractive index of the layers. In homogeneous media, which may be considered to have arbitrary periodicity, the BMs simplify to a Fourier series of spatial harmonics that correspond to the plane wave diffraction orders (PWs). Throughout the paper we will use the term 'modes' to refer to the general class of BMs (including the PWs), while 'orders' refers exclusively to PW diffraction orders.

While the fields and propagation constants of the PWs are known analytically, the Bloch modes of the structured layers must be found numerically. EMUstack does this using a fully-vectorial FEM routine, which solves a generalized eigensystem wherein the BMs complex vertical (z) propagation constants γ_s are the square roots of the eigenvalues, and the eigenvectors are the BMs' in-plane field distributions $\mathbf{E}_s(x, y)$ [14]. As a frequency domain method, we assume an $e^{-i\omega t}$ time dependence and the electric field is written in terms of the BMs as

$$\mathbf{E}(x, y, z) = \sum_s (c_s^+ e^{i\gamma_s z} + c_s^- e^{-i\gamma_s z}) \mathbf{E}_s(x, y), \quad (1)$$

where c_s^\pm are the amplitudes of the upward and downward propagating BM s . The corresponding form for the transverse H field is given in Eq. (10) of [14].

Eq. (1) shows how the vertical propagation of the field is separated from the in-plane components, and how each mode propagates with a simple exponential dependence independently of all others. In homogeneous layers, where the BMs are PWs, the propagation constants are $\gamma_s = \sqrt{\mathbf{k}^2 - \alpha_p^2 - \beta_q^2}$, which are related to the incident \mathbf{k} -vector $\mathbf{k}_0 = (\alpha_0, \beta_0)$ and integer multiples p, q of the reciprocal lattice vector $\mathbf{G} = 2\pi/d_i$ where d_i is the period of the structured layers in the i -direction:

$$\alpha_p = \alpha_0 + p \frac{2\pi}{d_x}, \quad (2)$$

$$\beta_q = \beta_0 + q \frac{2\pi}{d_y}. \quad (3)$$

The current version of EMUstack only handles square and rectangular unit cells.

Since we have expressed the fields in homogeneous layers and in structured layers in different bases, it is critically important that we truncate each series in a consistent manner. The FEM routine finds the requested number of eigenvalues (BM propagation constants) γ_s that lie closest to a reference value γ_{ref} . It is desirable to choose a value of γ_{ref} that is close to the propagation constants γ_s of the BMs that dominate the expansion Eq. (1). Since the modal expansions Eq. (1) must be matched at the relevant interfaces, the value $\gamma_{\text{ref}} = \sqrt{\text{Re}(n_{\text{max}})^2 k_0^2 - \alpha_0^2 - \beta_0^2}$ is a reliable choice, where n_{max} is set to the largest refractive index in the layer. We select the real part of n_{max} because complex values can split a conjugate pair of eigenvalues.

Once the eigenfunctions of each layer have been found, the problem has been reduced to quadrature and matrix manipulation. We construct the scattering matrices by taking field overlap integrals and \mathbf{P}_i is assembled from the propagation constants. The transmission matrices \mathbf{T}_{ij} are composed of the transmission coefficients of each incident mode of layer i into each mode of the lower layer j . Similarly, the reflection matrices \mathbf{R}_{ij} contain the

reflection coefficients for every permutation of incident modes and reflected modes (both in layer i). The change in phase and amplitude due to propagation through a layer m of thickness h is accounted for by the diagonal matrix $\mathbf{P}_i = \text{diag}[\exp(i\gamma_m h)]$, where γ_m is a vector containing the propagation constants of the modes of layer m .

To calculate the Fresnel scattering matrices \mathbf{T}_{ij} , \mathbf{R}_{ij} we enforce the continuity of the tangential components of the \mathbf{E} and \mathbf{H} fields across the interface. We use the Galerkin-Rayleigh-Ritz method [17], projecting the electric field PW expansion of one side onto the BM expansion for the magnetic field of the other side and vice versa. This involves taking the overlap integrals of the modes, which is done analytically for homogeneous layers and numerically for structured layers. Full expressions for these are given in Eqs. (58), (59), (71), (72) of [14]. Using this approach we have avoided the numerical instability problem, known as relative convergence [18], which can occur when the PW expansion and BM expansion are projected onto modes from only one side of the interface. The appendices of [14] present stringent test of the completeness of the modal expansions, of energy conservation and adherence to the reciprocity relations. When these criteria are satisfied we are assured of the accuracy of both near field and far field quantities.

EMUstack calculates the Fresnel scattering matrices for the interface of each layer with air. In this way each layer is represented in a standard way that is independent of its neighbours, which eases the process of combining the layers into stacks and allows the layers to be rearranged arbitrarily. When structured layers are placed in close proximity, the highly evanescent orders in the adjoining media have large amplitudes. This requires the inclusion of many PW orders in the simulation, and is particularly challenging when structured layers are placed in direct contact so that the coupling between them occurs in an infinitesimally thin air layer where all PW orders (including all evanescent orders) propagate energy. Such structures are inherently extremely challenging for SMMs. The convergence of our method for a structure where two metallic inclusions of differing shapes are stacked upon one another is studied in the Appendix.

Once the Fresnel scattering matrices have been calculated for each interface the problem is reduced to solely algebraic operations. The reflection and transmission matrices \mathcal{R}_{ij} , \mathcal{T}_{ij} that describe the scattering properties of a multi-layered structure in its entirety, and the absorption in each constituent layer are but a few of the quantities that can be obtained. We can also find the resonances of the structure by solving the homogeneous problem where there is no driving field. The versatility of the scattering matrix approach will be demonstrated in Sections 3.4 and 4.

The total scattering matrices of the stack are generated by recurrence relations. We start at the top edge of the bottom semi-infinite layer, where there is no upgoing wave (see Fig. 1). The scattering matrices \mathcal{T}_{20} , which describes the transmission of modes from layer 2 through the finitely thick layer 1 into the substrate 0, and \mathcal{R}_{20} , which details the reflection of modes back into layer 2 off the combined structure of layers 1 and 0, are given by

$$\mathcal{T}_{20} = \mathbf{T}_{10} \mathbf{P}_1 (\mathbf{I} - \mathbf{R}_{12} \mathbf{P}_1 \mathbf{R}_{10} \mathbf{P}_1)^{-1} \mathbf{T}_{21}, \quad (4)$$

$$\mathcal{R}_{20} = \mathbf{R}_{21} + \mathbf{T}_{12} \mathbf{P}_1 (\mathbf{I} - \mathbf{R}_{10} \mathbf{P}_1 \mathbf{R}_{12} \mathbf{P}_1)^{-1} \mathbf{R}_{10} \mathbf{P}_1 \mathbf{T}_{21}. \quad (5)$$

To include consecutively higher layers we replace $\mathbf{R}_{10} \rightarrow \mathcal{R}_{20}$, $\mathbf{T}_{10} \rightarrow \mathcal{T}_{20}$ and $\mathbf{P}_1 \rightarrow \mathbf{P}_2$, to obtain

$$\mathcal{T}_{30} = \mathcal{T}_{20} \mathbf{P}_2 (\mathbf{I} - \mathbf{R}_{23} \mathbf{P}_2 \mathcal{R}_{20} \mathbf{P}_2)^{-1} \mathcal{T}_{32}, \quad (6)$$

$$\mathcal{R}_{30} = \mathcal{R}_{32} + \mathcal{T}_{23} \mathbf{P}_2 (\mathbf{I} - \mathcal{R}_{20} \mathbf{P}_2 \mathcal{R}_{23} \mathbf{P}_2)^{-1} \mathcal{R}_{20} \mathbf{P}_2 \mathcal{T}_{32}. \quad (7)$$

When the top semi-infinite layer is reached we have arrived at \mathcal{R}_{M0} , \mathcal{T}_{M0} , which describe the reflection off, and transmission through, the entire layered structure.

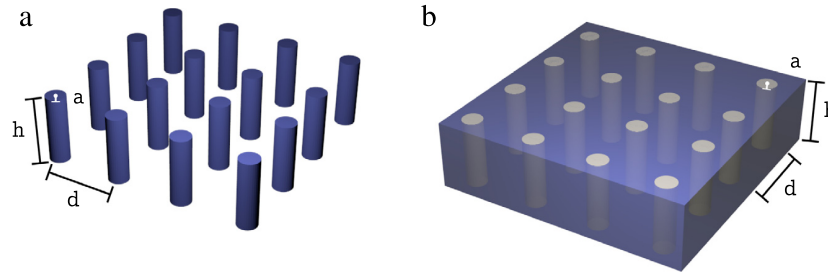


Fig. 2. Schematic of nanowire and nanohole arrays, with period d , radius a , and of thickness h . In the shown cases the arrays are suspended in air.

To calculate the propagation of energy through the structure we map an incident field, composed of a superposition of diffraction orders, onto the scattering matrices. A convenient feature of the scattering matrix approach is that the absorption within each layer can be calculated straightforwardly, which is important for the photovoltaic applications for which EMUstack was developed. Doing this with finite difference methods is computationally onerous.

Having given a brief overview of the method's framework, we next discuss the implementation and run through the steps of a basic EMUstack calculation that illustrates how EMUstack is used. For further details on the mathematical formalism we refer readers to [14].

3. EMUstack implementation

EMUstack is designed as a research tool for the scientific community. Its source code repository is freely available [15] and comes with examples and tests. Full documentation including an installation guide and a manual describing all subroutines is contained in the repository as well as being hosted on the web [16]. EMUstack combines the low-level power of Fortran with the dynamic features of the scripting language, Python. EMUstack may be easily modified by users thanks to being written in widely used languages, being thoroughly documented and being published as an online repository. The valuable contributions of users have been incorporated into the program. Following the Unix philosophy to: "Write programs that do one thing and do it well", EMUstack comes without a graphical user interface; instead we provide Python modules.

An example EMUstack simulation script is shown in Fig. 3. This simulates the sparse Nanowire (NW) array (Fig. 2(a)) studied in [19], except with a silica spacer layer and silver mirror. Using this script as a reference, we discuss the implementation and efficient use of EMUstack in Section 3.1. In Sections 3.2, 3.3, we examine the calculation steps involved in finding the Fresnel scattering matrices of each layer and the scattering matrices of the stacked structure respectively. In Section 3.4 we demonstrate how the scattering matrices may be manipulated easily to generate physical results. For more detailed descriptions of the routines that make up EMUstack we direct readers to the documentation [16]. Readers who are less interested in the implementation of EMUstack may wish to proceed straight to Section 3.5, where we summarize the physical quantities that EMUstack calculates.

3.1. Optimization and parallelization

Solving to find the BMs is by far the most computationally expensive step in EMUstack. We therefore carry out this calculation in a Fortran subroutine using f2py [20], which creates a Python wrapper around the Fortran source code, with pointers to memory blocks being passed directly to Python. This allows users to interact with EMUstack purely using Python. By default we use open source

linear algebra libraries LAPACK [21] and UMFPACK [22]; commercial libraries such as Intel MKL [23] may be used for better performance.

As a frequency domain solver, EMUstack treats each wavelength independently and spectral calculations are therefore "embarrassingly parallel", where the calculation of each wavelength may occur on separate CPUs in parallel without any communication between them. To maximize the speed enhancement of parallelization we do not introduce any parallel elements into each wavelength calculation, though users may use parallel versions of the linear algebra packages. Calculations across structural parameters are also embarrassingly parallel. Fig. 3 shows how parallelism can be easily implemented using the Python multiprocessing package. For larger computational loads, it should also be possible to use Hadoop, Apache Spark, or other tools.

In the example simulation of Fig. 3 we set the parameters of the incident light and the various layers in lines 14–32. At this point the FEM mesh of structured layers are created either by a Python function, in the case of a 1D mesh, or the open-source program Gmsh [24] for a 2D mesh. The main calculations are started within the `simulate_stack` function which is run in parallel (line 55). Once this has been completed, all the scattering matrices have been calculated, and we can choose to store all simulation objects in a compressed npz file (line 56). This allows additional calculations to be carried out at a later time, with full access to the modes (and thereby the fields) as well as the scattering matrices.

3.2. Fresnel scattering matrices of the interfaces

As outlined in Section 2, a regular EMUstack simulation can be broken down into three main steps: finding the modes of each unique layer; calculating the Fresnel scattering matrices of the interface of each layer with air, and; combining the Fresnel scattering matrices of individual layers to find the scattering matrices of the multi-layered structure. These are all carried out within the `simulate_stack` subroutine. In the example, up to 12 copies of the function `simulate_stack` are executing simultaneously in independent processes, each calculating the stack properties for a single wavelength.

The `calc_modes` function is called for each layer, and carries out the first two calculation steps: calculating the modes of a layer and then the overlap integrals of these modes with the diffraction orders of air so as to compile the Fresnel scattering matrices. While the diffraction orders of homogeneous layers are analytically prescribed as in Section 2 the BMs of structured layers are found using a fully vectorial FEM solver. EMUstack features two FEM routines: one for 1D periodic structures and one for 2D unit cells. The latter of these was adapted from Ref. [25]. In line 34 of the example we explicitly set the number of BMs to be calculated in the NW layer, overriding the default of 20 more BMs than PWs. The number of PWs is specified in line 18, where we include all PWs that lie within a circle with a radius of `max_order_PWs` centred at (α_0, β_0) . We note that the number of modes required throughout

```

1: import numpy as np
2: from multiprocessing import Pool
3: import matplotlib.pyplot
4: import matplotlib.pyplot as plt
5: import sys
6: sys.path.append("../backend/")
7: import objects
8: import materials
9: import plotting
10: from stack import *
11:
12:
13: # Light parameters
14: wl_1 = 310
15: wl_2 = 1127
16: n_wls = wl_2 - wl_1 + 1 # 1 nm steps
17: wavelengths = np.linspace(wl_1, wl_2, n_wls)
18: light_list = [objects.Light(wl, max_order_PWs=3, theta=0.0,
19:                             phi=0.0) for wl in wavelengths]
20:
21: # Structure parameters
22: period = 600 # Period must be consistent throughout simulation
23: Air = objects.ThinFilm(period, height_nm='semi_inf',
24:                        material=materials.Material(1.0 + 0.0j), loss=False)
25: Silica = objects.ThinFilm(period, height_nm=200,
26:                            material=materials.SiO2, loss=True)
27: Silver = objects.ThinFilm(period, height_nm=1000,
28:                            material=materials.Ag, loss=True)
29: NW_diameter = 120
30: NW_array = objects.NanoStruct('2D_array', period, NW_diameter,
31:                               height_nm=2000, inclusion_a=materials.Si_c,
32:                               background=materials.Air)
33: h_list = np.linspace(1000, 3000, 21)
34: num_BMs = 80
35:
36:
37: def simulate_stack(light):
38:     # Evaluate each layer individually
39:     sim_Air = Air.calc_modes(light)
40:     sim_Silica = Silica.calc_modes(light)
41:     sim_Silver = Silver.calc_modes(light)
42:     sim_NWs = NW_array.calc_modes(light, num_BMs=num_BMs)
43:     # Evaluate structure arranged bottom to top
44:     stack_list = []
45:     for h in h_list:
46:         stack = Stack((sim_Air, sim_Silver, sim_Silica, sim_NWs, sim_Air),
47:                      heights_nm=[1000, 200, h])
48:         stack.calc_scatter(pol='TE', save_scatter_list=True)
49:         stack_list.append(stack)
50:     return stack_list
51:
52: # Run simulation in parallel using num_cores CPUs
53: num_cores = 12
54: pool = Pool(num_cores)
55: stacks_list = pool.map(simulate_stack, light_list)
56: np.savez('Simo_results', stacks_list=stacks_list) # Save stack objects

```

Fig. 3. Example EMUstack simulation script. The script calculates the properties for NW arrays of many thicknesses.

a problem varies significantly with the size and index contrast of the layers. The examples in the online documentation give a guide to the number of modes needed for typical structures.

If a layer occurs in multiple places in the stack (e.g. layers 2 and 4 are the same structure), then this layer's modes and scattering matrices need only be found once, even though the layers may be of different thicknesses. This provides a substantial time saving since the majority of the calculation time is taken up by `calc_modes`, particularly in solving the eigensystem to find the BMs.

3.3. Scattering matrices of the stack

The third major simulation step is combining the Fresnel scattering matrices of individual layers into scattering matrices that describe the whole structure. In some situations this step may not be necessary, for instance the Fresnel matrices of individual

layers are all that is required to study the coupling between diffraction orders in air and the BMs of a layer.

In lines 46, 47 we define a `Stack` object wherein we list the layers of the total structure from back to front. We then use the `calc_scatter` function to calculate the scattering matrices of the stack by iteratively applying Eqs. (4)–(7) solving the problem for each layer exactly, with infinitesimally-thin air layers placed between each physical layer. To capitalize on the fast nature of the calculation steps that occur after the scattering matrices have been found, the `calc_scatter` function allows the thicknesses of layers to be redefined. Lines 45–50 show a loop that scans over NW array thicknesses, as specified in `h_list` and appends the results to the `scat_list` list. In this way the results for 21 thicknesses are calculated simultaneously with negligible additional computational cost. Multiple, different stacked structures may also be defined and simulated at this step.

```

58: # Post-processing
59: lay = 3 # looking at FP resonances of NW layer
60: Jsc_h = []
61: for s in range(len(h_list)):
62:     stacks_wl_list = []
63:     stacks_abs_list = []
64:     for i in range(len(wavelengths)):
65:         stacks_wl_list.append(stacks_list[i][s])
66:         stacks_abs_list.append(stacks_list[i][s].a_list[-1*(lay+1)])
67:
68:     plotting.t_r_a_plots(stacks_wl_list, add_height=h_list[s],
69:                         J_sc=True, active_layer_nu=lay, save_pdf=True)
70:     Jsc = plotting.J_short_circuit(np.ravel(stacks_abs_list), wavelengths)
71:     Jsc_h.append(Jsc)
72:
73: fig = plt.figure()
74: ax1 = fig.add_subplot(1, 1, 1)
75: plt.plot(h_list, Jsc_h)
76: plt.xlabel('NW array thickness (nm)')
77: plt.ylabel(r'Jsc (mA/cm$^2$)')
78: plt.savefig('Jsc_h')
79: np.savetxt('Jsc_height.txt', zip(h_list, Jsc_h), fmt='%18.11f')
80:
81: plotting.omega_plot(stacks_wl_list, wavelengths)

```

Fig. 4. Continuation of the example EMUstack simulation where the outputs of the scattering matrix calculations are processed.

We note that different thicknesses or permutations may require different numbers of modes to achieve accurate results. To further exploit this advantage `calc_scatter` keeps track of the calculated interfaces, and skips repeated occurrences, recalling them from memory.

When `calc_fluxes = True`, `calc_scatter` also calculates the energy flux through each layer and the structure as a whole. To do this we must specify the properties of the incident light. In this process, it is crucial to consider the energy in all propagating plane wave channels. In the case of propagation through the infinitesimal air layers we must also consider the energy in evanescent orders. This is done using the \mathbf{U} matrix of Eq. (C6) in the Appendix of [14]. EMUstack allows for structures to be excited with light of any polarization and composed of arbitrary combinations of the diffraction orders of the upper semi-infinite half-space. Because the FEM routines find BMs that correspond to both transverse electric (TE) and transverse magnetic (TM) polarized plane waves we must construct the PW basis to include the TE and TM diffraction orders. Subsequently all EMUstack scattering matrices are organized as follows:

| | |
|---------------------|---------------------|
| TE \rightarrow TE | TM \rightarrow TE |
| TE \rightarrow TM | TM \rightarrow TM |

where TE \rightarrow TM denotes scattering from TE modes to TM modes. EMUstack currently has the following input polarizations: TE, TM, right and left circular. Arbitrary polarizations may be constructed from superpositions of these.

3.4. Post-processing

The `simulate_stack` function returns a list of `Stack` objects that contain the scattering matrices and energy fluxes throughout the stack. The properties of individual layers can also be extracted from the `Stack` objects. In the given example, the list elements each are associated with a `Light` object of a different wavelength. These can then be post-processed to create plots or calculate dependent quantities. The `plotting` module contains over 25 plotting functions that are described in the documentation, and more may be easily added.

In lines 68–69 of Fig. 4 we plot the transmission, reflection and absorption spectra for each thickness combination considered in the loop of lines 45–50 of Fig. 3. An advantage of SMMs is that

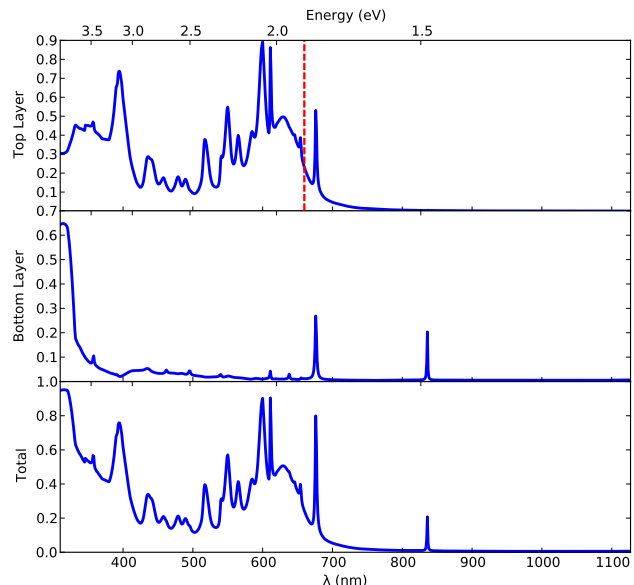


Fig. 5. Absorption in 1000 nm thick NW array (top layer), in 1000 nm thick silver mirror and in total. The absorption in the silica spacer is negligible and is not shown. The vertical line marks the $k_z = 0$ cut-off of the dominant BM.

it is straightforward to distinguish the absorption that occurs in each layer. Fig. 5 shows the resultant absorption spectra for the structure with a 1000 nm thick NW array, which is created with the `t_r_a_plots` function. The top layer is the NW array and the bottom layer is a silver mirror. The absorption in the silica spacer layer is negligible and is not shown. By decomposing the absorption in this way it is clear that the sharp absorption peaks that occur beyond 670 nm are due to absorption in the silver that occurs due to the periodic NW array coupling light to surface plasmons. There is also strong parasitic absorption in the silver film at short wavelengths. When considering the photovoltaic performance of this structure it is critical to exclude all absorption outside of the active charge generation region from the calculation of the short circuit current J_{sc} . In this case the NW array layer is the active region and we therefore specify `active_layer_nu=3` in line 69.

```

1: stack.layers[M].k_z      # Modal propagation constants in layer M.
2: stack.layers[M].sol1    # Modal field distribution in layer M.
3: stack.a_list            # Absorption in [M-1, ..., 2, total].
4: # Analogous for transmission (t_list) and reflection (r_list).
5: stack.layers[M].R12    # Reflection matrix from air onto layer M.
6: # Analogous for T12, R21, T21.
7: stack.R_net            # Reflection matrix of the entire stack.
8: # Analogous for transmission (T_net).
9: stack.vec_coef_down[M] # Amplitudes of downward propagating modes
10: # in layer M. Analogous for upward propagating (vec_coef_up).

```

Fig. 6. Summary of all the basic quantities contained in a simulated Stack object.

In lines 73–79 we plot the J_{sc} values for each NW array thickness that were collated in lines 61–71. We also store this data as a text file. In line 81 we plot the dispersion relations of each layer. Fig. 7 shows the results for the NW array layer, which are identical to Fig. 5(b) in [19] because the BM's propagation constants depend only on the in-plane geometry, which is the same. In Fig. 7, the relations are plotted in terms of frequency as a function of k_z in units of the period, d . Only points for which a BM has $|\text{Re}(k_z)| > 0$ are selected in this figure, leading to fewer points at high frequencies where Si is highly lossy. Having outlined our method, and its implementation, we now focus on some of the opportunities enabled by this approach.

3.5. Summary of calculation outputs

In Fig. 6 we list the physical quantities that EMUstack calculates. The example assumes a specific stack of layers has been simulated for a chosen wavelength. These quantities are the basis from which many other properties, such as modal resonances and short circuit currents, may be derived.

4. EMUstack features

There are two main advantages of using EMUstack: one conceptual, the other numerical. The conceptual advantage, shared with other SMMs, lies in the detailed access to the Bloch modes, which allows the formalism of thin film optics to be extended to nanostructured media. The major numerical advantage arises from combining the generality of the FEM with the semi-analytic SMM. We illustrate these advantages with examples from the fields of nanostructured photovoltaics, nanoplasmonics and metamaterials.

4.1. Combining the best of the FEM and the SMM

EMUstack is one of only a few packages that combines the FEM for calculating modes and the SMM for calculating properties of layered media. The SMM and FEM have previously been combined to study patch antennas [26]. A major advantage of this is the generality of the structures that can be efficiently and accurately studied.

The FEM can calculate the modes of unit cells with arbitrary inclusions and adaptive meshing allows small features can be accurately included with reduced speed penalty. This is a significant advantage over Fourier expansion methods where fine inclusions can only be resolved by increasing the terms in the Fourier terms throughout the whole problem. The meshing is carried out in Gmsh with users specifying meshing parameters in EMUstack. EMUstack currently includes mesh templates, which can be specified from within Python, for circular, elliptical, square, rectangular inclusions as well as for split ring resonators, dimers, coated cylinders and cylinders in strips, all in square and rectangular unit cells.

EMUstack has been designed to study lossy, as well as lossless, dielectric, metallic and metamaterial structures. Here the FEM is also advantageous because large refractive index contrasts and small inclusion sizes can be studied using adaptive meshes and without encountering the Gibbs phenomenon. This arises in RCWA/FMM due to the finite truncation of the Fourier series [27] introduces spurious modes and the effect of which cannot be decreased by increasing the number of Fourier components [11]. The ability to handle deeply subwavelength metallic inclusions (adaptively meshed) with large index contrast was critical in studying the wire metamaterials described below.

We note that the FEM representation of the BMs typically converges more rapidly within structured layers than a Fourier series would. This is because FEM calculated BMs can be discontinuous (while satisfying the continuity of tangential components) at the inclusion surfaces. In contrast, the Fourier series is made up of continuous functions that do not easily converge to the discontinuities of structured layers. The FEM calculated BMs include Fourier components that are larger than the terms included in the PW expansion. The contributions of these higher terms are discarded in the truncated PW expansion of the fields in homogeneous layers, however their inclusion in the structured layers is very important for the accurate calculation of the BMs propagation constants. Faster convergence has many flow-on effects: from a smaller eigensystem, to faster algebraic operations on smaller matrices, and an ensuing reduction in memory usage.

4.2. The natural basis

The properties of a structure are derived from the modes that it supports. Often the number of relevant modes that dominate a structure's response to illumination is quite small and the most intuitively insightful way of understanding the properties of the whole is to study the properties of its modes in detail. This clearly requires access to the modes of each layer and, for multi-layered structures, the modes of the stack. In this section we present some examples where studying the Bloch modes of a structure can reveal much about the underlying physics.

NW arrays and nanohole (NH) arrays, which are of interest to next generation solar cells, are such examples. The former consist of high index inclusions in a low index background, while the latter have the inverse composition, see Fig. 2. The modes of the physically isolated (but weakly coupled) NWs are quite distinct from the modes of the continuous high index background of NH arrays, although in both cases the properties of the whole structure are derived from a small number of modes.

In Fig. 5, the vertical line in the top plot marks the $k_z = 0$ cut-off of a particularly important BM, which is found from the dispersion diagram (Fig. 7). EMUstack provides us with a number of tools to demonstrate that the concurrent occurrence of this cut-off and the rapid rise in absorptance is not coincidental. We can inspect the in-coupling from free space into each mode as well as each mode's contribution to a resonance (as we will demonstrate in Fig. 8). Studying the energy concentration, group velocity and

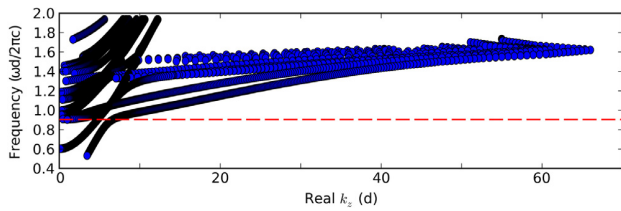


Fig. 7. Dispersion relations of the BMs of the NW array. Values are only plotted at points where a BM has $|\text{Re}(k_z)| > 0$. The propagation constants k_z are plotted in units of the period, d . The rapid changes at normalized frequencies above 1.4 are due to the strong material dispersion.

Fabry–Perot resonances of the dominant mode gives a complete picture of why its absorption is so strong between 600 nm and 660 nm [28]. Furthermore it is possible to link this BM to the TE modes of optical fibres by comparing their dispersion relations and the field profile of the BM and fibre mode. This provides a much stronger link than found in other studies [29,30], which can show only the similarity between the total field of the NWs and the modal field profiles of specific optical fibre modes.

Studies of NH arrays have gone to great lengths to link a distinct peak in transmission to a mode that is concentrated within the air hole inclusion [31]. While this task is challenging when using FDTD and experimental measurements, it is straightforward with EMUstack due to having access to the amplitudes and field profiles of the Bloch modes [32].

An advantage of the SMM approach is the ability to access the undriven physical system where there are no incident excitation fields. This is particularly useful for calculating the intrinsic resonances of structures, such as the Fabry–Perot resonances. The

Fabry–Perot resonance condition also defines the slab waveguide modes of complicated structured media. For example, this resonance condition for layer 2 is given by

$$\det(\mathbf{I} - \mathbf{R}_{21}\mathbf{P}\mathbf{R}_{23}\mathbf{P}) = 0. \quad (8)$$

While this function is common to all SMMs, the difference with EMUstack again comes from the resonances being described in the Bloch mode basis, allowing resonances to be decomposed into the dominant Bloch modes that can be studied in isolation.

Fig. 8 shows a script that calculates the Fabry–Perot condition for the NW array from the last example, where this layer is considered suspended in air. The plot composed in lines 95–100 is shown in Fig. 9, where the inset shows the BMs components of the resonance that are calculated in lines 102–116. These calculations provided important insights in linking particular Bloch modes with the absorption peaks of NW arrays [28].

Another application of studying the resonances of undriven structures is in finding the waveguide modes of wire metamaterials. To accurately find the dispersion relation of a waveguide mode we must minimize Eq. (8) using an iterative optimization routine. The use of Python allows this to be done quickly and easily by loading optimized packages. A similar root finding routine could be implemented with other SMMs, however EMUstack also calculates the Bloch modes, whose field distributions identify the modes as either TE, TM, or TEM (Fig. 10). By calculating the contribution of each of these BMs to the resonance defining the waveguide mode, we see that the waveguide mode is formed by a superposition of the evanescent TM mode and the propagating TEM mode (see [33] for more details).

```

83: # Find Fabry-Perot modes
84: FP_mats = []
85: FP_dets = []
86: I_BMs = np.matrix(np.eye(num_BMs), dtype='complex128')
87: for i in range(len(wavelengths)):
88:     Rnet_NWSi = stacks_list[i][0].rnet_list[2*lay-1]
89:     R21_NWAir = stacks_list[i][0].layers[lay].R21
90:     P = stacks_list[i][-1].layers[lay].prop_fwd(h_list[-1]/period)
91:     FP_matrix = I_BMs - R21_NWAir*P*Rnet_NWSi*P
92:     FP_mats.append(FP_matrix)
93:     FP_dets.append(np.abs(np.linalg.det(FP_matrix)))
94:
95: fig = plt.figure()
96: ax1 = fig.add_subplot(1, 1, 1)
97: plt.semilogy(wavelengths, np.real(FP_dets))
98: plt.xlabel(r'$\lambda$ (nm)')
99: plt.ylabel(r'|FP_condition|')
100: plt.savefig('FP_wls')
101:
102: selected_FP_res = FP_mats[301]
103: dim = np.shape(selected_FP_res)
104: trim_mat = selected_FP_res
105: m, v = np.linalg.eig(trim_mat)
106: min_E = np.argmin(abs(m))
107: Q = 1./min_E
108: dom_BM = np.argmax(v[:, min_E])
109: print 'Dominant BM in Fabry-Perot resonance = ', dom_BM
110: print 'Q of resonance = ', Q
111: fig = plt.figure()
112: ax1 = fig.add_subplot(1, 1, 1)
113: plt.plot(range(num_BMs), np.real(v[:, min_E]), 'ro')
114: plt.xlabel('BMs')
115: plt.ylabel('Amplitudes')
116: plt.savefig('FP_res_vector')

```

Fig. 8. Continuation of the example EMUstack simulation where the Fabry–Perot resonance spectra are calculated and plotted. The BM composition of the resonance at $\lambda = 611$ nm is also computed.

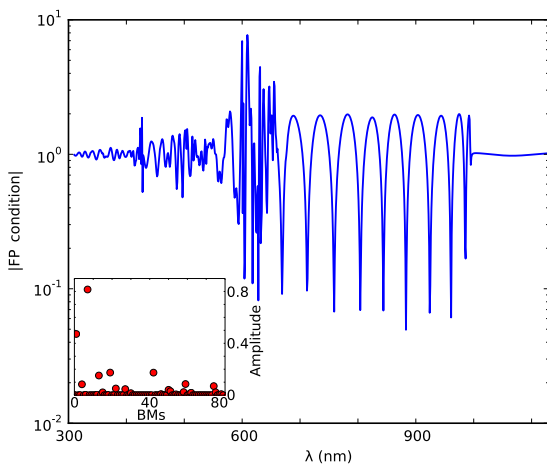


Fig. 9. Fabry-Perot resonance condition Eq. (8) for NW array suspended in air. Inset shows the amplitudes of the BMs that make up the resonance at $\lambda = 611$ nm.

4.3. General advantages of SMMs

As a frequency domain method, EMUstack can make use of measured, tabulated refractive indices. EMUstack currently comes with data for over 30 materials taken largely from Palik [34] and Johnson and Christy [35]. The Drude model is also implemented and parameters from Ref. [35] provided for gold. To illustrate the use of EMUstack with nanoplasmonic structures, and to show the discrepancies that occur in FDTD simulations, due to analytic fits to refractive indices, we study a thin gold film that is perforated by elliptical holes. It has been shown that the transmission through such a structure gives rise to circular dichroism when light is incident at off-normal angles [36]. Fig. 11 shows the difference in transmission between right-hand circularly polarized (RHCP) light and left-hand circularly polarized (LHCP) light for a 200 nm thick film with holes spaced with a period of 165 nm and with major and minor axes of 140 nm and 60 nm. The light is incident at 45° so the situation is analogous to the dashed curve in Fig. 2(c) of [36], except that the refractive indices are interpolated from the tabulated values of [35]. Though the circular dichroism peak occurs at the same wavelength, Fig. 11 shows a region of negative values where the transmission is higher for LHCP light, whereas the curve in [36] remains above zero throughout. We suspect this is a consequence of the poor agreement of the Drude model to measured values of the refractive indices of metals near the plasma frequency, which for gold occurs around $\lambda = 500$ nm.

The analytic treatment of vertical propagation inherent in the SMM makes varying layer thicknesses extremely cheap computationally. For example it takes 2571 s to simulate the 818

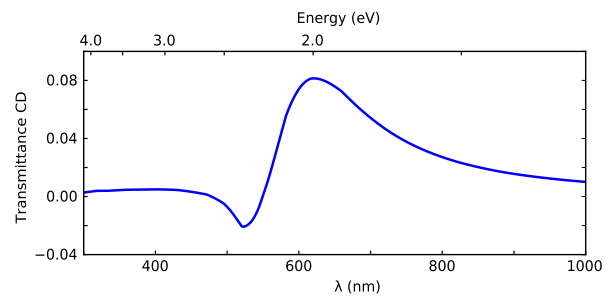


Fig. 11. Circular dichroism in transmission ($t_{\text{RHCP}} - t_{\text{LHCP}}$) through a thin gold film perforated with square holes.

wavelengths that make up the NW array spectra of Section 3 for a single thickness. Simulating a further 21 thicknesses adds a mere 153 s (6%) to the computation time, most of which is taken up in writing the additional results to disk. These times were obtained on an IBM System X 3755 M3 server with 12 AMD cores running at 2.3 GHz and exclusively using open-source libraries. Since the modes and scattering matrices of homogeneous layers are calculated analytically, EMUstack is also extremely efficient for studying sets of structures in which the structured layers are kept constant, while homogeneous layers are altered.

4.4. Amalgamating 1D and 2D scattering matrices

The EMUstack framework enables the scattering matrices calculated for singly-periodic layers using the 1D solver to be integrated with the scattering matrices of bi-periodic layers. This is done by appropriately filling the scattering matrices of the 1D layers with zeros to match the 2D arrays. This feature provides a great increase in speed for mixed structures and, to our knowledge, is unique to EMUstack.

5. Concluding remarks

We have introduced an open source software package that calculates the scattering matrices and propagation matrices of multi-layered nanostructures. The defining feature of our program is the use of the FEM to calculate the Bloch modes of nanostructured media. Compared to other Fourier series based SMMs this approach is numerically more efficient and allows for the intuition of thin film optics to be applied to a greater variety of complex structures.

EMUstack is available online with fully open source code, comprehensive documentation, automated tests and a series of instructive examples [15]. Simulations are defined and executed

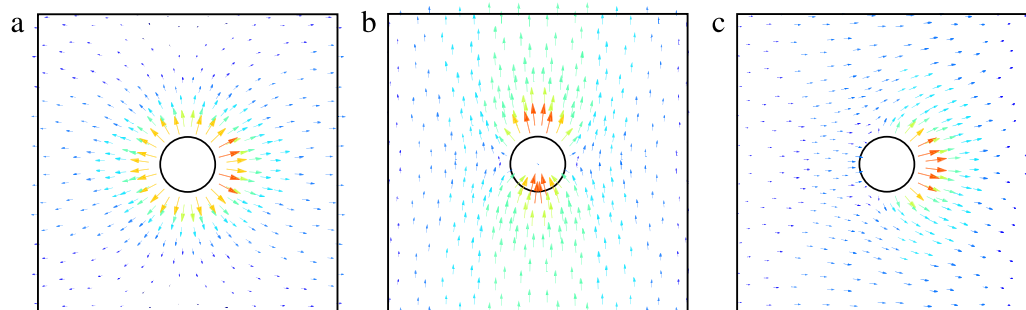


Fig. 10. Vectorial field distributions, of the fundamental (a) TEM, (b) TE and (c) TM modes of a drawn fibre wire metamaterial. The colour and length of the arrows indicate the field strength at the origin of the arrow in arbitrary units. The metallic wires are arranged in a square lattice of period 1.02 cm, have a diameter of 0.19 cm, $\mathbf{n}_{\text{wire}} = (0 + 1 \times 10^{10}i)$, are in an $n_{\text{bkg}} = 1$ background. The fields are calculated for a frequency of 2.33 GHz and $k_x = 235.6 \text{ m}^{-1}$.

using the popular scripting language Python, while an optimized Fortran routine carries out the numerically intensive steps.

EMUstack has been designed to simulate lossy high contrast nanostructures, which are difficult to simulate with Fourier SMMs. While we have used EMUstack primarily to study nanostructures for photovoltaic applications, it has been used also to study drawn fibre and split ring resonator metamaterials [33] and we have shown that it is well suited to studying plasmonic structures that include metals in Section 4.1. In Appendix we present convergence studies of dielectric and metallic structures. These examples hint at the potential for EMUstack to be applied to a wide range of structures in the future. We believe that a deeper physical understanding of these structures can be developed from the unique quantities to which EMUstack provides access.

Acknowledgements

This work was supported by the Australian Renewable Energy Agency, and the Australian Research Council Discovery Grant and Centre of Excellence Schemes CE110001018. Computation resources were provided by the National Computational Infrastructure, Australia and the NeCTAR Research Cloud, Australia. The authors acknowledge useful discussions with Dr. Marco Liscidini from the University of Pavia relating to RCWA.

Appendix. Convergence

We study the convergence of EMUstack for three situations: a dielectric NH array; a metallic film perforated with subwavelength holes; and an array of metallic nanoparticles stacked upon each other. Our studies consist of repeating simulations with increasing numbers of modes and analysing the difference in their results.

We present our results in terms of the maximum PW diffraction order included. By default EMUstack increases the number of BMs within structured media accordingly as $2 \times \text{num_pw_per_pol} + 20$, where num_pw_per_pol is the number of PWs in each polarization and the BMs cover both polarizations. The broken lines in Fig. A.12 show the quantitative results and the solid lines show the error relative to the calculation with the most PW orders.

The NH array example (Fig. 2(b)) is equivalent to the photonic crystal used to study the convergence of a recently published FMM program [11]. Fig. A.12(a) shows the normalized frequency of the transmission peak associated with a Fano resonance (labelled “Peak 1” in [11]). We see that for this simple dielectric structure the results converge very quickly, to a value in good agreement with Fig. 8(a) of [11].

The results of a more computationally difficult simulation are shown in Fig. A.12(b). In this case the structure is a thin gold film perforated by square, subwavelength holes, which exhibits Extraordinary Optical Transmission (EOT) as studied by Liu et al. [37]. Following this publication, we calculate the transmittance at the EOT peak for normal incidence and at 5° . We see that the error in transmittance is less than 0.0001 when six or more PW orders are included (226 PWs per polarization). The converged values are in good agreement with Fig. 2(b) from [37] although the transmittance is slightly greater, which we believe is due to more finely resolving the wavelengths.

The final convergence study is of two arrays of metallic nanoparticles placed one directly upon the other (Fig. A.13). This is an extremely challenging structure because the fields are tightly confined to the edges of the nanoparticles and concentrated at the corners between the nanoparticles. We choose to study a normalized wavelength of $\lambda/d = 1.03$ where there is an absorption peak, and where the simulation is even more difficult because of the proximity to the Wood anomaly, where a substantial amount of energy is in nearly cut-off orders.

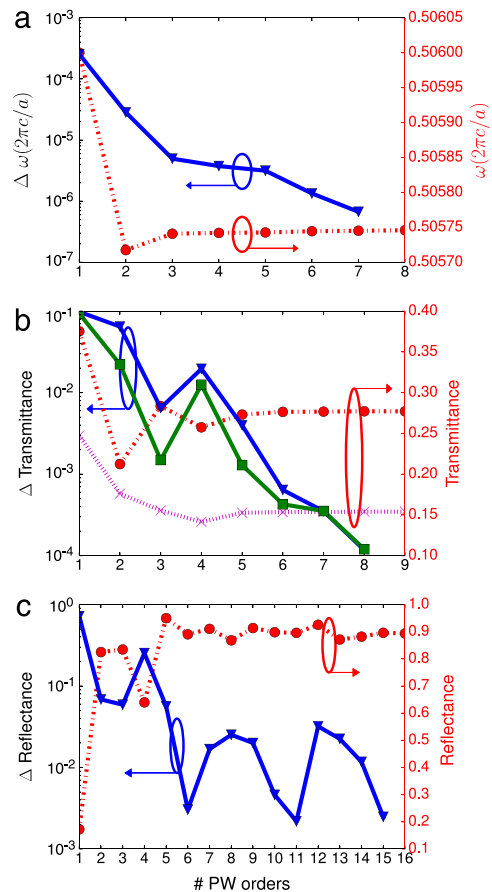


Fig. A.12. EMUstack convergence studies for (a) a dielectric NH array/photonic crystal, (b) an array of subwavelength holes in a thin gold film, (c) two arrays of metallic nanoparticles in direct contact. Results are shown as a function of the number of PW orders included. The broken lines show the numeric results, while the solid lines show the difference between the results of each point and the result with the greatest number of PW orders included. In (b) the blue and red curves are for normal incidence and the green and magenta curves are for incidence at 5° . (For interpretation of the references to colour in this figure legend, the reader is referred to the web version of this article.)

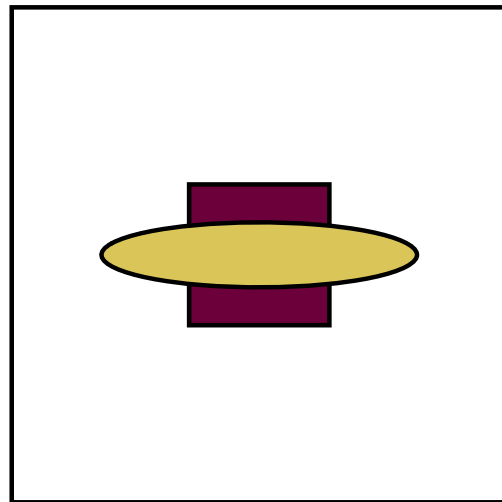


Fig. A.13. Test structure for convergence study of two arrays of metallic nanoparticles (Au data from [35]) of different shape placed on top of one another.

As discussed in Section 2, the simulation of nanostructures placed in direct contact is very challenging for SMMs because the tightly confined fields require a very large number of modes for an accurate representation. We suspect that the accuracy may be improved when the projections of the modes of each structured layer are projected directly onto each other. This has yet to be implemented in EMUstack. The convergence study shown in Fig. A.12(c) shows that fourteen or more PW orders must be used to achieve decent convergence.

References

- [1] S. Johnson, J. Joannopoulos, Block-iterative frequency-domain methods for Maxwell's equations in a planewave basis, *Opt. Express* 8 (3) (2001) 173–190. <http://dx.doi.org/10.1364/OE.8.000173>.
- [2] B.T. Kuhlmeiy, T.P. White, G. Renversez, D. Maystre, L.C. Botten, C.M. de Sterke, R.C. McPhedran, Multipole method for microstructured optical fibers. II. Implementation and results, *J. Opt. Soc. Amer. B* 19 (10) (2002) 2331. <http://dx.doi.org/10.1364/JOSAB.19.002331>.
- [3] S.B. Wang, H.H. Zheng, J.J. Xiao, Z.F. Lin, C.T. Chan, Fast Multipole Boundary Element Method for Three Dimensional Electromagnetic Scattering Problem, *ArXiv* (2012) 45 [arXiv:1211.7177](https://arxiv.org/abs/1211.7177).
- [4] F.J. Lawrence, L.C. Botten, K.B. Dossou, R.C. McPhedran, C. Martijn, de Sterke, A flexible Bloch mode method for computing complex band structures and impedances of two-dimensional photonic crystals, *J. Appl. Phys.* 111 (1) (2012) 013105. <http://dx.doi.org/10.1063/1.3674281>.
- [5] Y. Chung, N. Dagli, An assessment of finite difference beam propagation method, *IEEE J. Quantum Electron.* 26 (2) (1990) 1335–1339. <http://dx.doi.org/10.1109/3.59679>.
- [6] G.R. Hadley, Transparent boundary condition for the beam propagation method, *IEEE J. Quantum Electron.* 28 (1) (1992) 363–370. <http://dx.doi.org/10.1109/3.119536>.
- [7] EMUstack: An open-source package for Bloch mode based calculations of scattering matrices. URL physics.usyd.edu.au/emustack.
- [8] M.G. Moharam, E.B. Grann, D.A. Pommet, T.K. Gaylord, Formulation for stable and efficient implementation of the rigorous coupled-wave analysis of binary gratings, *J. Opt. Soc. Am. A* 12 (5) (1995) 1068. <http://dx.doi.org/10.1364/JOSAA.12.001068>.
- [9] D. Whittaker, I. Culshaw, Scattering-matrix treatment of patterned multilayer photonic structures, *Phys. Rev. B* 60 (4) (1999) 2610–2618. <http://dx.doi.org/10.1103/PhysRevB.60.2610>.
- [10] E. Popov, M. Nevière, *Light Propagation in Periodic Media: Diffraction Theory and Design*, Marcel Dekker, New York, 2003.
- [11] V. Liu, S. Fan, S 4: A free electromagnetic solver for layered periodic structures, *Comput. Phys. Commun.* 183 (10) (2012) 2233–2244. <http://dx.doi.org/10.1016/j.cpc.2012.04.026>.
- [12] F. Montiel, M. Nevière, Differential theory of gratings: extension to deep gratings of arbitrary profile and permittivity through the r-matrix propagation algorithm, *J. Opt. Soc. Am. A* 11 (12) (1994) 3241–3250. <http://dx.doi.org/10.1364/JOSAA.11.003241>.
- [13] J. Chandezon, M.T. Dupuis, G. Cornet, D. Maystre, Multicoated gratings: a differential formalism applicable in the entire optical region, *J. Opt. Soc. Amer.* 72 (7) (1982) 839. <http://dx.doi.org/10.1364/JOSA.72.000839>.
- [14] K.B. Dossou, L.C. Botten, A.A. Asatryan, B.C.P. Sturmberg, M.A. Byrne, C.G. Poulton, R.C. McPhedran, C.M. de Sterke, Modal formulation for diffraction by absorbing photonic crystal slabs, *J. Opt. Soc. Am. A* 29 (5) (2012) 817–831. <http://dx.doi.org/10.1364/JOSAA.29.000817>.
- [15] github. URL github.com.
- [16] readthedocs.org. URL readthedocs.org.
- [17] R.F. Harrington, *Field Computation by Moment Methods*, Vol. 10, 1993. <http://dx.doi.org/10.1109/9780470544631>.
- [18] M. Leroy, On the convergence of numerical results in modal analysis, *IEEE Trans. Antennas Propag.* 31 (4) (1983) 655–659. <http://dx.doi.org/10.1109/TAP.1983.1143095>.
- [19] B.C.P. Sturmberg, K.B. Dossou, L.C. Botten, A.A. Asatryan, C.G. Poulton, C.M. de Sterke, R.C. McPhedran, Modal analysis of enhanced absorption in silicon nanowire arrays, *Opt. Express* 19 (May) (2011) A1067–A1081. <http://dx.doi.org/10.1364/OE.19.0A1067>.
- [20] P. Peterson, F2PY: a tool for connecting Fortran and Python programs, *Int. J. Comput. Sci. Eng.* 4 (4) (2009) 296. <http://dx.doi.org/10.1504/IJCSE.2009.029165>.
- [21] LAPACK. URL netlib.org/lapack.
- [22] T.A. Davis, Algorithm 832: UMFPACK V4.3 — An unsymmetric-pattern multifrontal method, *ACM Trans. Math. Software* 30 (2) (2004) 165–195. <http://dx.doi.org/10.1145/992200.992205>.
- [23] Intel Math Kernel Library. URL software.intel.com/en-us/intel-mkl.
- [24] C. Geuzaine, J.-F. Remacle, Gmsh: a three-dimensional finite element mesh generator with built-in pre- and post-processing facilities, *Internat. J. Numer. Methods Engrg.* 79 (2009) 1309–1331. <http://dx.doi.org/10.1002/nme.2579>.
- [25] K.B. Dossou, M. Fontaine, A high order isoparametric finite element method for the computation of waveguide modes, *Comput. Methods Appl. Mech. Engrg.* 194 (6–8) (2005) 837–858. <http://dx.doi.org/10.1016/j.cma.2004.06.011>.
- [26] M.A. De Gonzalez Aza, J.A. Encinar, J. Zapata, M. Lambea, Full-wave analysis of cavity-backed and probe-fed microstrip patch arrays by a hybrid mode-matching generalized scattering matrix and finite-element method, *IEEE Trans. Antennas Propag.* 46 (2) (1998) 234–242. <http://dx.doi.org/10.1109/8.660968>.
- [27] L. Li, Use of Fourier series in the analysis of discontinuous periodic structures, *J. Opt. Soc. Am. A* 13 (9) (1996) 1870. <http://dx.doi.org/10.1364/JOSAA.13.001870>.
- [28] B.C.P. Sturmberg, K.B. Dossou, L.C. Botten, A.A. Asatryan, C.G. Poulton, R.C. McPhedran, C. Martijn de Sterke, Nanowire array photovoltaics: Radial disorder versus design for optimal efficiency, *Appl. Phys. Lett.* 101 (17) (2012) 173902. <http://dx.doi.org/10.1063/1.4761957>.
- [29] B. Wang, P.W. Leu, Tunable and selective resonant absorption in vertical nanowires, *Opt. Lett.* 37 (18) (2012) 3756–3758.
- [30] K.T. Fountaine, C.G. Kendall, H.a. Atwater, Near-unity broadband absorption designs for semiconducting nanowire arrays via localized radial mode excitation, *Opt. Express* 22 (S3) (2014) A930. <http://dx.doi.org/10.1364/OE.22.00A930>.
- [31] G. Gomard, R. Peretti, S. Callard, X. Meng, R. Artinyan, T. Deschamps, P. Roca i Cabarrocas, E. Drouard, C. Seassal, Blue light absorption enhancement based on vertically channelling modes in nano-holes arrays, *Appl. Phys. Lett.* 104 (5) (2014) 051119. <http://dx.doi.org/10.1063/1.4864267>.
- [32] J.L. Donnelly, B.C.P. Sturmberg, K.B. Dossou, L.C. Botten, A.A. Asatryan, C.G. Poulton, R.C. McPhedran, C.M. de Sterke, Mode-based analysis of silicon nanohole arrays for photovoltaic applications, *Opt. Express* 22 (S5) (2014) A1343–A1354. <http://dx.doi.org/10.1364/OE.22.0A1343>.
- [33] J.S. Brownless, B.C.P. Sturmberg, A. Argyros, B.T. Kuhlmeiy, C.M. de Sterke, Guided modes of a wire medium slab: Comparison of effective medium approaches with exact calculations, *Phys. Rev. B* 91 (15) (2015) 155427. <http://dx.doi.org/10.1103/PhysRevB.91.155427>.
- [34] E.D. Palik, *Handbook of Optical Constants of Solids*, 1998.
- [35] P.B. Johnson, R.W. Christy, Optical constants of the noble metals, *Phys. Rev. B* 6 (12) (1972) 4370–4379. <http://dx.doi.org/10.1103/PhysRevB.6.4370>.
- [36] T. Cao, M.J. Cryan, Enhancement of circular dichroism by a planar non-chiral magnetic metamaterial, *J. Opt.* 14 (8) (2012) 085101. <http://dx.doi.org/10.1088/2040-8978/14/8/085101>.
- [37] H. Liu, P. Lalanne, Microscopic theory of the extraordinary optical transmission, *Nature* 452 (7188) (2008) 728–731. <http://dx.doi.org/10.1038/nature06762>.

3.2 Wider Applications of EMUstack

The code that comprises up EMUstack was released in its entirety in December 2013 under the terms of the open-source GNU General Public License. The code repository is hosted on [GitHub](#), and although this site does not provide a full history of downloads, periodic inspection of the weekly traffic logs indicates that the package has been downloaded between one and eight times a week (with an estimated average of 1.5). As of Nov 2015 the homepage www.physics.usyd.edu.au/emustack had been viewed over 26,000 times from over 4600 unique IP addresses.

Throughout this thesis, we used EMUstack to study nanostructures for photovoltaic applications, often focussing on relatively low-loss dielectric media, we are aware of over a dozen users across Australia, Europe, the US, Iran and India who are using EMUstack to study nanophotonic [111], nanoplasmonic and metamaterial structures [8].

3.3 Optoelectronic Modelling of Solar Cells

Introducing nanostructures into SCs alters their electronic properties, as well as their optical properties. The physical laws governing the behaviour of the charge-carriers and those dictating the propagation and absorption of light are quite different, which makes combining them in a self-consistent optoelectronic model challenging.

One approach to creating an integrated model is to iteratively solve the coupled equations governing charge-carrier generation, charge-carrier transport, and thermal transport, with each calculation step being carried out in separate model [112, 113]. This has been applied to problems including the subrandom noise in textures substrates, photon recycling and the long term reliability issues arising from localised heating. A different approach is to use the FEM in three dimensions to solve for both the generation rates and the carrier diffusion rates, which has been used to study the physics of NW and NH arrays and to compare them to homogeneous absorbers [114].

The inherent drawback of full optoelectronic simulations is that they are extremely computational expensive, which hampers their use in exploring new devices. They also demands a trade-off between the level of detail that is calculated in each model, producing rather more general results compared to EMUstack or other more specialised tools. There have also been advances in analytic models of nanostructured SC, for instance Ali *et al.* derived a detailed description of radial p-n junctions [115]. It will be interesting to see what new perspectives these techniques open up, particularly as the models are developed further and available computing power increases.

Epilogue

The calculation approach presented in this chapter dictates the physical quantities we have access to, but beyond that it is also indicative of how we structure our investigates: beginning by examining the modes of each structure and the coupling between them at interfaces; before exploit this understanding to systematically design structures to manipulate the flow of light in a desired way.

In particular we have benefited greatly from knowing the propagation constant and field distribution of each BM and PW, as well as the scattering/coupling coefficients between all the modes (that determine the amplitudes of each mode when the system is driven by an incident field). The approach has allowed us to generalise the intuitive physics of thin film optics to more complicated nanostructures.

On a practical note, the use of the scattering matrix formalism makes it straightforward to calculate the absorption in individual layers, allowing the usable absorption of active regions to be clearly distinguished from parasitic absorption, for instance in metallic mirrors. Throughout this thesis we focus on the usable absorption.

Having outlined the numerical method, and its physical background, we now dive into the physics!

Chapter 4

Nanowire Array Photovoltaics I: Semi-analytic Optimisation

*When one tugs at a single thing in nature,
he finds it attached to the rest of the world.*

John Muir

In Sect. 2.4.1 we touched on the absorption enhancement potential of nanowire (NW) arrays due to their simultaneously low reflection and strong light trapping. While there are many related nanostructures, for example nanocones, we here focus on NWs as the canonical structures, from which the underlying physics of the other structures can be derived. The invariance of the inclusions through the layer also makes NWs easier to study with the scattering matrix method.

NWs present a number of opportunities from a material science perspective: they can be doped with radial p-n junctions, which orthogonalise the direction of charge carrier diffusion and light propagation, improving their tolerances to defects [116, 117]; the small cross-sectional area of the NWs reduces the strain between adjacent layers, relaxing the requirement for all the materials of multi-junction cells to be lattice matched [118–120]; and the small areas also improve alloying and epitaxy allowing NW arrays to be fabricated on flexible substrates to create flexible SCs (when encased in a flexible matrix material) [121].

These features were generally appreciated at the time we started our studies, however questions remained about the creation of high efficiency, low cost NW array SCs. Particular challenges include: optimising the NW array parameters for maximised absorption; balancing the need for optical absorption with the NW's electronic performance; minimising nonradiative recombination losses through passivation of the NWs large surface areas; and developing cheap, scalable fabrication methods. Our research addresses the first issue by improving our understanding of the optical physics, so that the arrays may be systematically designed to maximise absorption. Optics does not feature as prominently in the other issues, which are being addressed by researchers in other fields.

In this chapter we present our most recent article on NW array SCs, which provides a comprehensive overview of all the optical processes; the earlier articles that deal with the effects of disorder in NW arrays are presented in Ch. 5. We have also studied nanohole (NH) arrays, although we do not include the related publication [7] in this thesis. In Sect. 4.3 and 5.3 we discuss the similarities and differences between NH arrays and NW arrays. An outlook on the future of nanostructured SCs is presented in Ch. 8. We begin by reviewing the NW array literature, covering both theoretical and experimental developments.

4.1 Review of Nanowire Array Solar Cells

4.1.1 Theoretical Understanding of Nanowire Arrays

The use of NW arrays for solar energy harvesting was first proposed by Kayes, Atwater and Lewis [116], who focussed on the physics of radial p-n junctions. The optical absorption of NWs was first investigated numerically by Hu and Chen [122], who showed that the absorption of short wavelength light in NWs was superior to uniform thin films due to reduced reflections, and that the absorption of longer wavelengths approached that of an equally thick film as the volume fraction is increased. Lin and Povinelli [123] then demonstrated that a $2.33 \mu\text{m}$ thick array of silicon NWs could achieve a higher ultimate efficiency (defined under the assumptions of the S-Q model of Sect. 2.2.3) than an equally thick uniform film when the period was increased from previous studies to $d = 600 \text{ nm}$, with a NW diameter of $2a = 540 \text{ nm}$.

The underlying physical mechanism responsible for the enhanced absorption was not completely identified by these studies, however it was apparent that a “leaky mode resonance” [123] was being excited. The importance of a discrete set of modes was established by Kupec *et al.* who studied InAs and InP NWs and observed the “micro-concentration of the incident light by the nanowire array” [124, 125]. A popular approach to describing the modes of NW arrays is to model the individual NWs as optical fibres [126, 127], the dispersion relations of which are well known [128].

In 2010-11 we analysed the absorption processes of NW arrays in terms of the Bloch modes of the array [129]. Unlike the modes of optical fibres, Bloch modes are periodic functions that are thereby sensitive to the configuration of the lattice. Using the numerical method described in Ch. 3 we calculated the propagation constants, fields and amplitudes of the Bloch modes, from which we concluded that the absorption peaks were driven by the Fabry-Perot resonances of a small set of Bloch modes, which we labelled *key modes* (KMs). These modes are concentrated within the NWs and propagate with low group velocities. In [129] we also developed a semi-analytic theory that includes the effect of the array through the calculation of lattice sums, and accurately predicts the cut-off wavelengths of the KMs across a range of periods and volume fractions. This work provides important background for the investigations developed in this thesis, but is not itself part of this thesis.

There has been a continued tension in the literature where some authors describe the physics of NW arrays in terms of optical fibre modes, while others consider periodic modes, and yet others use the formalism of Mie resonances. In the Supporting Information of Paper 4.2, we derive the relationship between the periodic KMs of the NW arrays and the optical fibre modes of isolated NWs, showing that they are equivalent in the limit of very sparse arrays. A similar link was later made in a more qualitative fashion by Fountaine *et al.* [130] and a recent study showed the equivalence of Mie scattering resonances with optical fibre modes [131].

There have also been a large number of studies undertaken where full-field numerical tools were used to simulate the efficiencies of NW arrays across a range of geometric and material properties [123, 132–136], as well as the particularly comprehensive study presented in [137]. The range of potential structures that can be included in such studies is limited by the computational expense of simulating the full absorption spectrum, as required to calculate the efficiency. Furthermore use of full-field simulations limit the physical insight obtained by such approaches, making it difficult to predict the performance of related permutations of materials and cell designs. The predictions made about the performance of NW array SCs had therefore remained quite general and qualitative, for example that the reflection off NW arrays decreased when the volume fraction was decreased. In Paper 4.2 we building on our understanding of the optical physics of NW arrays to formulate quantitative expressions that predict the array parameters that maximise the SC’s charge generation rate.

4.1.2 Experimental Demonstrations of Nanowire Array Solar Cells

Nanowire array SCs have been made using a wide range of materials, including direct [121, 138–140] and indirect [141–144] semiconductors and excitonic materials such as dye and organic materials [145, 146]. When composed of direct bandgap materials such as InP and GaAs, the SCs typically use planar p-n junctions [138–140, 147–149], while demonstrations in silicon (with its low diffusion length) have often used radial p-n junctions [141–144]. The differences between these configurations have been experimentally compared [150], and multiple materials have also been combined into multi-junction cells [119, 151, 152].

The largest obstacle to the practical use of NW arrays remains the difficulty and cost of fabricating them over large areas. Currently used techniques include top-down approaches such as aqueous electroless etching [144] and NIL [153], as well as bottom-up growth techniques [154]. For comparative reviews see [117, 155]. These techniques are being refined to reduce their cost and improve their scalability; recent proposals include using NIL stamps [153], or self assembled beads as lithography patterns [98, 109] as in Fig. 2.20.

A promising proposition for the commercialisation of NW array SCs is that they can be fabricated on low-cost flexible substrates. If this can be done cheaply, then NW SCs could compete in the flexible SC market where other technologies, such as organics and quantum dot cells, also have efficiencies of just under 15%. Single-crystalline semiconductor NWs have been grown on aluminium foil, stainless steel and conducting glass substrates [117, 121] and have also been created by etching metallurgical grade Si [156]. For detailed reviews of NW SC fabrication see [117, 157, 158].

Since 2013 the record efficiency for NW array SCs has been held by the group of Samuelson at Lund University. In 2013 they obtained a efficiency of 13.8% [139] using a $h \sim 1.5 \mu\text{m}$ thick InP cell that had a dimension of 1 mm-by-1 mm with the NWs covering 12% of this area. Impressively “the highest open-circuit voltage of 0.906 V exceeds that of its planar counterpart, despite about 30 times higher surface-to-volume ratio of the nanowire cell” [139] showcasing both the excellent surface passivation of the NWs and the potential of enhanced V_{oc} values in low volume absorbers that was predicted theoretical in Sect. 2.2.5. In October 2015 the same group achieved an efficiency of 15.3% using GaAs nanowires whose improved passivation allowed for a V_{oc} of up to 0.923 V [148].

Prelude to Paper 4.2

We now present the paper in which we detail our semi-analytic optimisation technique that is based on a comprehensive understanding of the interrelated optical effects of NW arrays and which produces quantitative predictions that match well with numeric calculations, along with its supplementary material:

B. C. P. Sturmberg, K. B. Dossou, L. C. Botten, A. A. Asatryan, C. G. Poulton, R. C. McPhedran and C. M. de Sterke. “[Optimizing Photovoltaic Charge Generation of Nanowire Arrays: Simple Semi-Analytic Approach](#)”. *ACS Photonics* **1**, 683–689 (2014)

Optimizing Photovoltaic Charge Generation of Nanowire Arrays: A Simple Semi-Analytic Approach

Björn C. P. Sturmberg,^{*,†} Kokou B. Dossou,[‡] Lindsay C. Botten,[‡] Ara A. Asatryan,[‡] Christopher G. Poulton,[‡] Ross C. McPhedran,[†] and C. Martijn de Sterke[†]

[†]CUDOS and IPOS, School of Physics, University of Sydney, Sydney, 2006, Australia

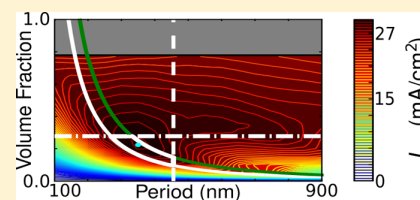
[‡]CUDOS, School of Mathematical Sciences, University of Technology Sydney, Sydney, 2007, Australia

S Supporting Information

ABSTRACT: Nanowire arrays exhibit efficient light coupling and strong light trapping, making them well suited to solar cell applications. The processes that contribute to their absorption are interrelated and highly dispersive, so the only current method of optimizing the absorption is by intensive numerical calculations. We present an efficient alternative that depends solely on the wavelength-dependent refractive indices of the constituent materials. We choose each array parameter such that the number of modes propagating away from the absorber is minimized, while the number of resonant modes within the absorber is maximized.

From this we develop a semi-analytic method that quantitatively identifies the small range of parameters where arrays achieve maximum short-circuit currents. This provides a fast route to optimizing NW array cell efficiencies by greatly reducing the geometries to study with full device models. Our approach is general and applies to a variety of materials and to a large range of array thicknesses.

KEYWORDS: photovoltaics, solar energy, nanowire arrays, light trapping, nanophotonics, diffraction gratings



A major challenge in solar energy research is to reduce the cost-per-watt of photovoltaic cells. This challenge may be met by increasing the efficiency, as in the case of multijunction cells,¹ or by reducing costs through the use of less expensive materials.^{2,3} The cost-per-watt can also be reduced by using established materials in much thinner films than standard cells.^{4,5} This last approach greatly reduces costs, but also reduces the efficiency if the cell design is not modified. The efficiency decrease is largely due to optical losses, not only from increased transmission due to incomplete absorption, but also from increased reflection at the front surface, which can no longer be coated with standard multiple micrometer-thick antireflective patterns. Structuring the thin absorbing layer into vertically aligned nanowire (NW) arrays has been shown to address both these losses simultaneously, by increasing the *light coupling* into the cell and enhancing the absorption through *light trapping*. Further advantages of NWs include compatibility with cheap flexible substrates⁶ and radial p–n junctions.^{7–9} NWs also reduce the lattice matching constraints that limit material combinations in multijunction devices.¹⁰ These structures have therefore attracted intense theoretical^{11–14} and experimental^{6,15–20} research, with efficiencies of 13.8% being reported.²¹

Optimizing the photovoltaic performance of NW arrays is challenging because their optical and electronic properties depend strongly upon the arrays' geometry. Typically, simulations are first carried out to assess the optical charge carrier generation, and then the charge carrier collection performance is calculated separately. Recently, techniques for combined optoelectronic modeling of nanostructured photo-

voltaics have been developed that recursively calculate the generation, collection, and recombination of charge carriers.²² All of these numerical approaches are limited to grid searches of small parts of parameter space, wherein they locate local optima. Finding a general optimum, or fully understanding the behavior of NW arrays using such means, is however impracticable due to the range of parameters. In particular, the high sensitivity of the charge carrier profile to experimental factors such as material quality, fabrication techniques, passivation method, and device design prohibits the carrier collection efficiency from being incorporated into a general optimization routine. These issues also limit the predictive information that can be gained from experiments. For example, the fill factors of current state of the art III–V NW array solar cell vary between 25% and 77%.²³ It is therefore valuable to fully understand the charge generation aspects of NW arrays before modeling their charge collection. A compromise between maximal charge generation and efficient charge collection can then be found to maximize the photovoltaic energy conversion efficiency.

The charge generation of NW arrays is directly related to their optical absorption,²⁴ which is less dependent on material processing. The absorption in turn however is driven by numerous competing optical effects, including the excitation of guided resonance modes and higher diffraction orders.^{11–14} Since these are resonant effects, they are highly dispersive

Received: March 24, 2014

Published: July 1, 2014

across the broad bandwidth of the solar spectrum, and it is unclear how to best balance their effects to maximize the total absorption. This is made more difficult by each wavelength contributing an amount given by the solar spectrum. These factors all combine to produce a challenging optimization problem that is currently addressed by fully numerical studies of specific sections of parameter space.^{12,13,16,18}

SEMI-ANALYTIC APPROACH

Here we present an approach that allows the optimal design parameters for maximal charge generation to be evaluated semi-analytically in negligible time for a given material and thickness. This provides an ideal starting point for numerical and experimental studies of the electrical performance of NW geometries. We do this by constructing an integrated theoretical framework that relates the reflection, transmission, and absorption of NW arrays to their geometric parameters (Figure 1): radius a , period d , thickness h , and volume fraction

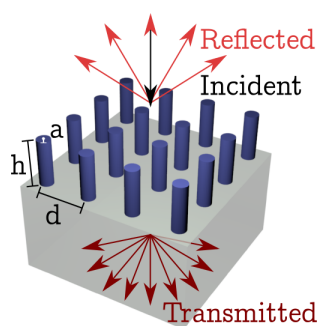


Figure 1. Geometry of vertically aligned nanowire arrays showing light incident normally and diffracted into the zeroth and higher orders in reflection and transmission. While our optimization method is independent of lattice type, numeric simulations use a square lattice as shown.

f . In our numerical calculations we consider square lattices for which $f = \pi \times a^2/d^2$; however studies have reported a weak influence of lattice type on the absorption of NW arrays,^{13,25} and our analytic model is independent of the lattice type. From these relationships we develop a simple method that quantitatively identifies the small region of optimal parameter space for charge generation.

For each choice of material system and thickness we analyze the parameter space presented in Figure 2. Here the period and volume fraction are indicated on the axes, and curves of constant radius are of the form $f \propto 1/d^2$. Arrays whose NWs intersect are excluded by the gray region, which for square arrays is $f > \pi/4$. The colored contours of Figure 2 indicate numerically calculated short-circuit currents, J_{sc} , of NW arrays where the array that produces maximal J_{sc} is marked with a blue dot. Overlaid on the numerical results, with white and green curves, are the predictions of our semi-analytic optimization. Briefly this optimization method is described as dividing parameter space into regions that have either too high a reflectance (above the horizontal dot-dashed line) or too much transmission (right of the vertical dashed line) or do not support enough resonant absorption modes (outside of the region between the white and green curves). The optimal NW design must therefore lie within the region highlighted in thick white curves. The considerations dictating these reductions make use of the coupled wave argument developed by Yu et

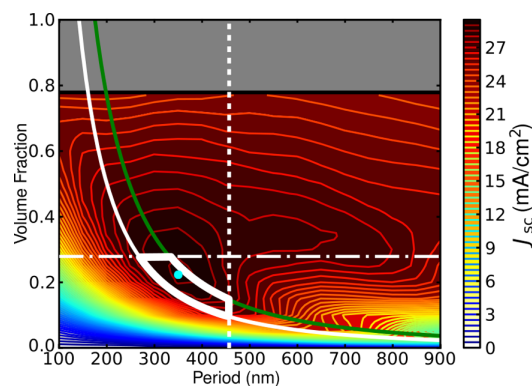


Figure 2. Numerically calculated short-circuit current of InP NW arrays across the parameter space $100 \text{ nm} < d < 900 \text{ nm}$, $0.005 < f < 0.780$. The optimal array is marked with a blue dot and has $J_{sc} = 29.2 \text{ mA/cm}^2$. Superimposed are the results of our semi-analytic optimization with the predicted optimal region emphasized with thick curves.

al.²⁶ That is, the absorption is highest when the number of outward propagating modes is minimized, while the number of resonant modes within the absorbing layer is simultaneously maximized. Here we extend this approach by considering the modal amplitudes and by integrating across the solar spectrum to calculate parameter constraints in terms of the maximum short-circuit current.

We illustrate our method using InP NWs surrounded by an air background ($n = 1$), placed upon a semi-infinite SiO_2 substrate under an air superstrate. We stress however that the method applies to a wide variety of materials including direct and indirect band gap semiconductors. Results for GaAs, silicon, and germanium are contained in the Supporting Information. We first examine the effect of radius, period, and volume fraction while fixing $h = 2.33 \mu\text{m}$ and thereafter show that the thickness determines the relative importance of reflection versus transmission losses. Our semi-analytic predictions show excellent agreement for the optimal array parameters when compared to full simulations.

Effect of NW Radius on Absorption Resonances. We begin by studying the role of the NW radius. It has been shown that NW arrays support guided resonance modes, each of which drive strong absorption peaks. These modes have been described in the literature as either leaky optical fiber modes^{14,27} or as Key (Bloch) Modes (KMs).¹¹ These descriptions are equivalent for sparse arrays, where the NW surfaces are far apart, but differ for dense arrays, where the effect of the lattice, which is included only in the Bloch mode formulation, becomes significant (see Supporting Information for derivation of equivalence in the sparse limit). Though here we consider perfectly cylindrical NWs, the lower order modes of NWs depend on the cross-sectional area so that minor perturbations in shape do not alter the dipolar nature of the fields, and for our purposes here the same equations can be applied. A fundamental property of waveguides is that the number of bound modes increases with the dimension of the cross-section. Applied to NWs this means that the number of KMs grows with increasing radius. This suggests a clear optimization goal; choose the NW radius as large as possible, so as to maximize the number of absorption resonances.

However, absorption resonances contribute to the absorption of the solar cell only if they occur at wavelengths where the

material absorbs and where there is incoming solar radiation. This is the range $\lambda_1 < \lambda < \lambda_g$, where $\lambda_1 = 310$ nm is the lower limit of the solar spectrum and λ_g is the band gap wavelength of the absorbing material, which for InP is $\lambda_g = 922.5$ nm. It is known that the symmetry of the incident light allows only HE_{1m} fiber modes to be effectively excited.^{14,28} We have found that the strongest excitations occur at frequencies slightly above the $\text{Re}(\beta_z) = 0$ cutoff of these modes, where β_z is the propagation constant of the mode. Hence, the strongest absorption occurs when

$$\frac{\varepsilon_1 J_1'(k_1 a)}{k_1 J_1(k_1 a)} - \frac{\varepsilon_2 H_1^{(1)'}(k_2 a)}{k_2 H_1^{(1)}(k_2 a)} = 0 \quad (1)$$

which can be derived from the standard transcendental equation for HE modes in the limit $\beta \rightarrow 0$. Here ε_i and $k_i = (\varepsilon_i \omega^2 / c^2 - \beta_z^2)^{1/2}$ are the permittivities and transverse wavenumbers in the NWs ($i = 1$) and background ($i = 2$), respectively, J_1 is the first-order Bessel function, and $H_1^{(1)}$ is the first-order Hankel function of the first kind. Incidentally, this expression is identical to the one obtained for the key modes, the Bloch modes that are known to dominate the absorption in NW arrays, in the limit in which the lattice period becomes arbitrarily large (i.e., as $S_0 \rightarrow 0$ in eq 10 in Sturmberg et al.¹¹). The fundamental HE_{11} fiber mode does not have a cutoff. It therefore exists for all radii at all wavelengths, but does not contribute a large absorption peak and is not counted in Figure 3a. For the derivation of eq 1 and the relationship between KMs and HE_{1m} fiber modes see the Supporting Information.

Using eq 1 we scan through possible NW radii, recording when key modes enter and leave the spectrum: $\text{Re}(\beta_z(\lambda_1)) = 0$, $\text{Re}(\beta_z(\lambda_g)) = 0$, respectively. These radii are represented in Figure 3a as black curves where an additional mode enters the

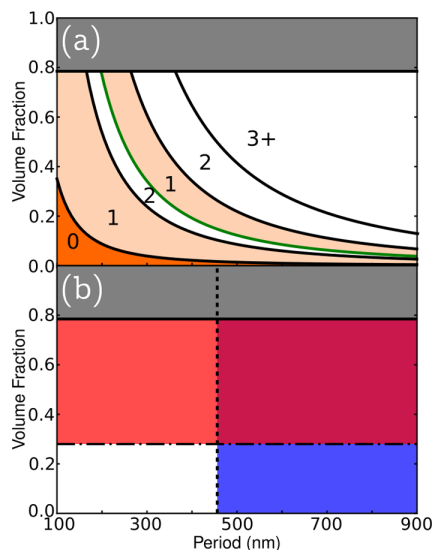


Figure 3. (a) NW array parameter space showing the NW radii at which KMs enter (black curves) and leave (red curve) the absorption spectrum. The number of KMs within the absorption spectrum is shown for each region, where darker shades of orange indicate fewer KMs. (b) Constraints placed on the optimal region of parameter space due to high transmission (blue area) and high reflection (red area). The region of high transmission and reflection is colored magenta. Optimal NW array geometries lie in the union of the white regions of (a) and (b).

spectrum and as green curves where a mode leaves the spectrum. Between the curves the number of KMs is constant, as labeled in Figure 3a. From this analysis we require the optimal arrays to be in one of the regions with at least two KMs, such as immediately to the left of the green curve or toward the top right of the figure. There is a preference for small radii because the fields of higher order modes, which are supported by larger NWs, have a greater number of nodes within the NW and therefore couple less well to the incident plane waves. For diagrammatic purposes we include only the first three KMs in Figure 3a.

Having identified the light-trapping advantages of larger NWs, we now consider two processes that impose upper limits to the optimal NW radius. These arise because the NWs are arranged in a periodic lattice; thus, increasing the radius we can either keep the volume fraction constant and adjust the period or keep the period constant and adjust the volume fraction. These correspond, respectively, to moving horizontally and vertically through Figure 2. In each case we observe that the absorption initially grows with increasing radius, but eventually decreases. It is by uncovering the origins of this behavior that we can define the vertical and horizontal restrictions shown in Figure 2.

Effect of Array Period on Transmission Channels. We investigate the role of increased period in Figure 4, where we

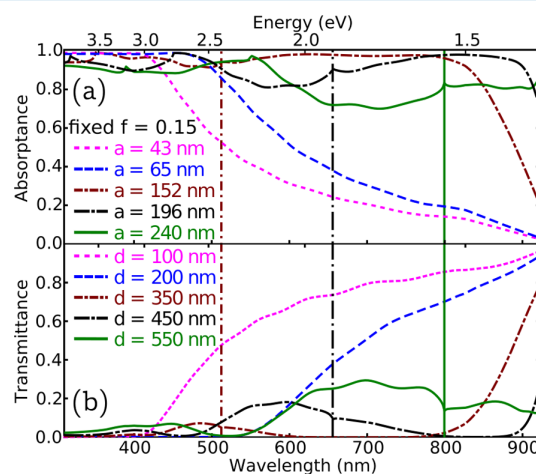


Figure 4. Absorption (a) and transmission (b) spectra as NW radius is increased with a fixed volume fraction $f = 0.15$. Vertical lines mark the shortest wavelength Wood anomalies in the substrate $\lambda_{WA} = n_{sub}d$.

show the absorption and transmission spectra of InP arrays with radii in the range 43–240 nm and fixed volume fraction $f = 0.15$, i.e., moving horizontally in Figure 2. In Figure 4a the absorption initially increases with radius, but once $a > 152$ nm ($d > 350$ nm), the absorption of long wavelengths is significantly reduced. It is clear from Figure 4b that this decrease is due to a rise in transmission, while the reflectance is relatively constant for all arrays, with $R < 7\%$ across the spectrum (see Supporting Information). The increase in transmission is caused by the periodically varying refractive index of the NW array exciting nonzero diffraction orders in the substrate, which increases the number of channels propagating energy away from the array from 1 to 5 for wavelengths below the zero-order Wood anomaly. This anomaly occurs at $\lambda = \lambda_{WA}$, which is indicated in Figure 4 by vertical lines in the line style of

the corresponding spectrum. In transmission the shortest wavelength Wood anomaly occurs at $\lambda_{\text{WA}} = n_{\text{sub}}d$, where n_{sub} is the refractive index of the substrate. For $\lambda > \lambda_{\text{WA}}$ all nonzero diffraction orders are evanescent and, as such, do not contribute to the energy flow. The excitation of higher diffraction orders therefore adds a qualifier to the optimization; incorporate large NW radii, but do so while imposing an upper limit on the period.

The strictest limit to place on the period is that no higher diffraction orders are allowed to exist within the solar spectrum, which limits the period to $d < 310 \text{ nm}/n_{\text{sub}} = 213 \text{ nm}$ for a SiO_2 substrate. This criterion however fails to consider the strong absorption of short wavelengths that do not reach the substrate, which renders the number of transmission channels irrelevant for these wavelengths. We must therefore choose a longer wavelength λ_{av} from which we can derive the maximum allowable period, $d_{\text{max}} \equiv \lambda_{\text{av}}/n_{\text{sub}}$.

Our approach is to choose λ_{av} to be an averaged wavelength, on the short wavelength side of which the nonzero transmission channels can be tolerated, while there is only a single transmission channel at longer wavelengths. To account for the highly nonuniform spectral intensity of the solar spectrum, we weight each above-band-gap wavelength by the number of solar photons incident at that wavelength, $\xi(\lambda) = I(\lambda)\lambda/hc$, where $I(\lambda)$ is the irradiance as given in the ASTM air mass 1.5 spectrum,²⁹ h is Planck's constant, and c is the speed of light in a vacuum:

$$\lambda_{\text{av}} = \frac{\int_{\lambda_1}^{\lambda_2} \xi(\lambda) \lambda \, d\lambda}{\int_{\lambda_1}^{\lambda_2} \xi(\lambda) \, d\lambda} \quad (2)$$

For InP this gives $\lambda_{\text{av}} = 665 \text{ nm}$. We take an analogous weighted average of the substrate refractive index, replacing λ in the numerator with $n(\lambda)$, which gives $n_{\text{sub}} = 1.46$. The maximum allowed period is therefore $d_{\text{max}} = 456 \text{ nm}$, which is represented in Figure 3b by the start of the blue region.

Effect of Volume Fraction on Reflectance. Having examined the effect of increasing NW radii within lattices of increasing periods (i.e., moving horizontally in Figure 2), we now move vertically through Figure 2. Figure 5 shows the

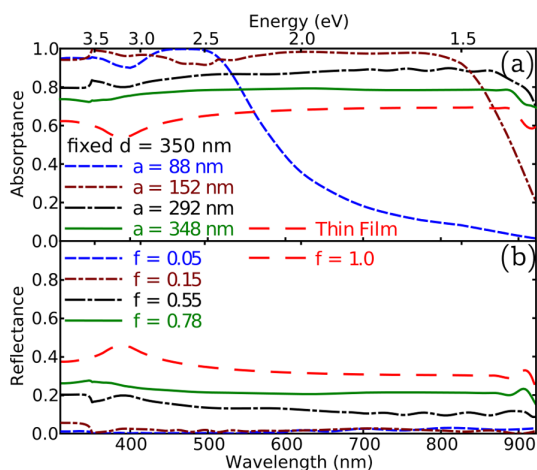


Figure 5. Absorption (a) and reflection (b) spectra as NW radius is increased with a period $d = 350 \text{ nm}$. The spectra of a homogeneous film of equal thickness are shown in red ($f = 1.0$).

absorption and reflection spectra for arrays with fixed period $d = 350 \text{ nm}$ and radii increasing from $a = 88 \text{ nm}$ to $a = 348 \text{ nm}$ ($0.05 \leq f \leq 0.78$). The spectra of a homogeneous film of equal thickness ($f = 1.0$) are also shown to emphasize the excellent antireflective light coupling performance of the NW arrays. The transmittance of these arrays, shown in the Supporting Information, is relatively constant once $f \geq 0.55$. In contrast to Figure 4a, the absorption in Figure 5a decreases uniformly across the spectrum once $a > 152 \text{ nm}$ and does so due to a uniform increase in reflectance. The Wood anomaly in reflection that occurs at $\lambda_{\text{WA}} = n_{\text{air}}d = 350 \text{ nm}$ produces only a minor enhancement in short wavelength reflection, which is unaffected by the increase in f (since d is constant). The increased reflectance is therefore due not to a larger number of reflected propagating orders but to a larger amplitude of the zeroth reflection order. This trend is not surprising: as the InP volume fraction increases, so does the average refractive index, and therefore so does the Fresnel reflection.

To incorporate the influence of Fresnel reflections on the optimization, we determine an upper bound on the volume fraction, f_{max} that does not impede the integrated absorption. This is a subtle procedure that depends on the thickness of the absorbing layer: thick layers can be expected to absorb most of the light that enters, and minimizing reflection is therefore paramount. In contrast, thin layers with limited absorption can tolerate more reflection if it leads to higher absorption. Rather than dealing with the absorption, we use the transmission as a proxy since, for example, thick layers with strong absorption have little transmission. We therefore define the largest volume fraction allowed as that for which the average reflection equals the average transmission. The reflectance $R(\lambda)$ and transmittance $T(\lambda)$ are estimated using the Fresnel equations with the NW array replaced by a thin film of equal thickness composed of an effective medium with permittivity $\epsilon_{\text{eff}}(f, \lambda)$. The critical volume fraction f_{max} is then defined as the f such that $R_{\text{av}}(\epsilon_{\text{eff}}(f)) = T_{\text{av}}(\epsilon_{\text{eff}}(f))$, where the average reflectance and transmittance are calculated as in eq 3 (see Supporting Information for derivation). For InP NW arrays with $h = 2.33 \mu\text{m}$, $f_{\text{max}} = 0.28$, which is indicated in Figure 3b by the red shading of $f > 0.28$.

$$R_{\text{av}}(f) = \frac{\int_{\lambda_1}^{\lambda_2} \xi(\lambda) R(f, \lambda) \, d\lambda}{\int_{\lambda_1}^{\lambda_2} \xi(\lambda) \, d\lambda} \quad (3)$$

It is important to note that this limit relies on the calculation of effective indices for structures that include significant loss. Existing effective index models, such as Maxwell–Garnett, poorly approximate the complex effective indices for these structures. It has recently been proposed in studies on mesoporous thin films that the real and imaginary components of the effective indices of lossy structures may be best calculated independently from different effective index formulations. As in these studies,^{30,31} we found such an approach to best replicate the observed reflectance and transmission spectra and subsequently to most reliably predict f_{max} . We calculate $\text{Re}(\epsilon_{\text{eff}})$ using the Bruggeman formulation³² and $\text{Im}(\epsilon_{\text{eff}})$ using the volume averaging theory.^{33,34}

COMPARISON TO NUMERIC SIMULATIONS

To make a final prediction of the optimal array parameters, we combine the three arguments developed above. This corresponds to placing the restrictions on period and volume

fraction of Figure 3b onto the radius goals of Figure 3a. In doing so, we remove the top right region of parameter space that supports three KMs, as well as the slightly smaller radius region that supports two KMs. The optimal region is therefore predicted to be just to the left of the green curve, where two KMs are supported without the excitation of too many transmission channels or too high a top surface reflectance. To verify this prediction, we calculate the short-circuit current J_{sc} of InP NW arrays across the parameter space of $100 \text{ nm} < d < 900 \text{ nm}$, $0.005 < f < 0.780$ with $h = 2.33 \mu\text{m}$. We sampled this parameter space with 993 simulations.

Figure 2 shows these numerical results as well as the semi-analytic predictions for f_{max} , d_{max} and the radius limits within which two KMs are supported. The agreement is excellent, with the optimal arrays located under f_{max} to the left of d_{max} and above the white solid curve ($a = 80 \text{ nm}$) that indicates the presence of the second KM resonance within the absorption range. The optimal array was found to have a period of $d = 350 \text{ nm}$ and a volume fraction of $f = 0.22$ and had a short-circuit current of $J_{sc} = 29.2 \text{ mA/cm}^2$. The optimum array is marked with a blue dot and is located to the left of the green curve ($a = 99 \text{ nm}$), where the first KM leaves the absorption range. The near-optimal arrays that are in close proximity to the green curve, but on its right side, arise because these arrays still have a large fraction of the KM resonant absorption peak within the absorption range. The contours of other regions also substantiate our approach; the horizontal contours above the f_{max} line indicate a volume fraction dominated (period-independent) decrease in absorption, while the parameter space with small f and large d exhibits near vertical contours, demonstrating the strong influence of period here.

Dependence on Array Thickness. The above analysis has been limited to arrays of fixed thickness, with the comparison in Figure 2 being for $h = 2.33 \mu\text{m}$. It is however straightforward to extend the approach to other thicknesses, requiring only f_{max} to be re-evaluated, due to the dependence of $T(\epsilon_{\text{eff}}(f))$ on the array thickness. In Figure 6 we show the semi-analytic predictions for arrays of (a) $h = 1.5 \mu\text{m}$ and (b) $h = 4 \mu\text{m}$ along with the corresponding numerical calculations for J_{sc} . The predictions continue to agree well with the numerical results, as the optimum shifts to lower f with increased h . This is well approximated by the balancing of transmission versus reflection through the effective medium, as demonstrated from the semi-analytic horizontal lines.

Comparing our calculated short-circuit currents to the best reported experimental results, we find that for $h = 1.5 \mu\text{m}$ our maximum J_{sc} of 28.2 mA/cm^2 is 4.2 mA/cm^2 greater than that reported by Wallentin et al.²¹ for InP NWs of equal thickness. While some of this difference is accounted for by the absence of carrier losses in our optical simulations, the J_{sc} we calculate for the geometry they fabricated is only 1.3 mA/cm^2 greater than their experimentally measured value. This leaves almost 3 mA/cm^2 to be gained by optical optimization. The geometry of Wallentin et al. would gain this improvement by doubling the volume fraction from 0.12 to 0.25, while keeping the radius of the NWs at the already optimal 180 nm .

We chose a thickness of $h = 4 \mu\text{m}$ in Figure 6b because this is the thickness of the record efficiency planar InP solar cell.^{35,36} This planar cell has $J = 29.5 \text{ mA/cm}^2$, while the optimal NW array ($d = 400 \text{ nm}$, $f = 0.17$) has $J_{sc} = 29.9 \text{ mA/cm}^2$. This would suggest that, at this thickness, a planar structure is superior to a NW array once carrier losses are included in fabricated NW arrays. However, the record planar cell contains an antireflective

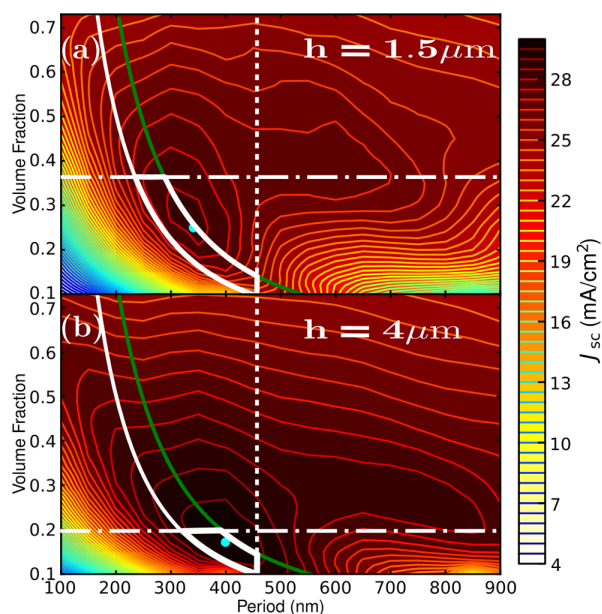


Figure 6. Numerically calculated short-circuit currents J_{sc} of InP NW arrays of height (a) $h = 1.5 \mu\text{m}$ and (b) $h = 4 \mu\text{m}$. The optimal arrays are marked with blue dots and have (a) $J_{sc} = 28.2 \text{ mA/cm}^2$ and (b) $J_{sc} = 29.9 \text{ mA/cm}^2$. Superimposed are the results of our semi-analytic optimization with the predicted optimal region emphasized with thick curves.

coating and a Zn–Au back reflector, neither of which are present in our NW simulations. Given the NW arrays' excellent antireflection properties, we do not introduce an antireflective layer; however when we include an Au back reflector, the NW arrays obtain $J_{sc} = 30.5 \text{ mA/cm}^2$ for thicknesses of $4 \mu\text{m}$. Consistent with our semi-analytic optimization the optimal arrays that included back reflectors have larger periods because there are no longer any diffraction orders excited in the substrate. The only waves that carry energy away from the NWs are in the air superstrate such that $d_{\text{max}} = \lambda_{\text{av}}/n_{\text{air}}$. These results suggest that it may be possible for NW arrays to outperform even the record planar cell that consumes 10 times the amount of InP.

We note that the results of Figure 6 were calculated simultaneously along with 49 other heights across the range 1–50 μm . This was done with negligibly increased computational expense by virtue of the generalized scattering matrix method³⁷ as implemented in the freely available EMUstack simulation package.³⁸ For all thicknesses in this range the numerically calculated optima lie within the region predicted by our optimization method.

CONCLUSION

We have constructed a simple optimization method to maximize the photovoltaic charge generation of NW arrays. Our method depends solely on the refractive indices of the constituent materials and can be evaluated essentially instantaneously, providing a refined starting point for device modeling of NW array solar cells. The physical premise of our approach is to maximize the light trapping of the structure while simultaneously enhancing the light coupling into the solar cell. To achieve optimal light trapping, we showed that the NW radius should be increased so as to support more resonant

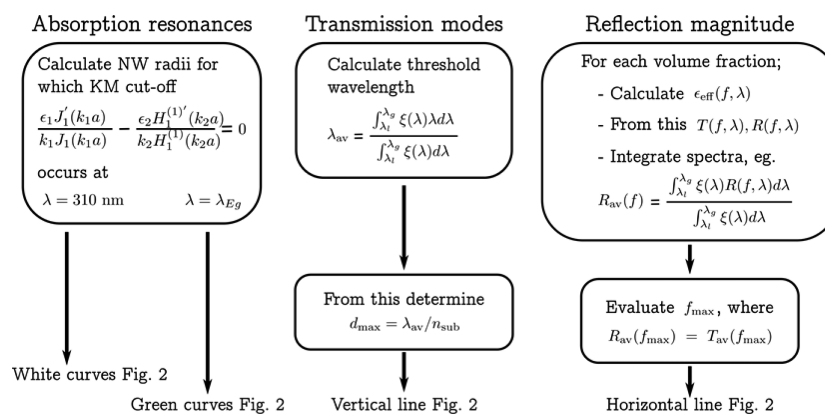


Figure 7. Flowchart outlining our semi-analytic optimization procedure. The number of resonant modes within the spectrum is found by first calculating where additional key modes enter the absorption range (plotted as white curves) and then calculating where they leave this range (green curves). Next, the upper bound on the period is determined and marked with a vertical line. The optimal region is then enclosed by the horizontal line, which limits the acceptable volume fraction of the array above which the reflection is too great.

modes and the period should remain less than d_{max} to limit the number of outwardly propagating plane waves excited. Meanwhile to enhance the light coupling into the array, the volume fraction must be restricted to $f < f_{max}$. From this simple ansatz we developed expressions that quantitatively define the region of parameter space where NW arrays have optimal J_{sc} .

Figure 7 outlines our optimization method, summarizing the equations that quantify the limits of the optimal parameter space. By following this procedure the NW array geometries that maximize charge generation can be rapidly identified, guiding further electronic modeling and experimental investigations to simultaneously optimize the charge collection efficiency.

The construction of these arguments requires a fine balance between making simplifying approximations and retaining the essential physics of the various optical effects. In the calculation of f_{max} for example, the essential physics of balancing reflection losses against transmission losses was accentuated, while all other effects, such as the modes of the NWs, were omitted through the use of an effective index treatment. Similarly, the derivation of d_{max} was based on a simple physical argument about the excitation of diffraction orders, but required the considered selection of a critical wavelength λ_{av} . Although the analysis presented here is restricted to normal incidence, it is straightforward to generalize the expressions to off-normal incidence, and we note that previous studies of NW arrays have found that the integrated absorption of NW arrays is altered little for non-normal angles of incidence up to 40° .^{11,12}

The results contained in the Supporting Information for GaAs, silicon, and germanium NW arrays show that the presented analytic optimization is robust to the very different refractive indices of these materials, including large dispersive variations in absorption coefficients. These differences produce distinct semi-analytic predictions and unique J_{sc} contour topologies. For example, silicon arrays of thickness $h = 2.33 \mu\text{m}$ have an optimal volume fraction of $f = 0.7$ due to silicon's low absorptivity and an optimal period of $d = 500 \text{ nm}$ due to its larger band gap.

■ ASSOCIATED CONTENT

Supporting Information

Supporting Information contains comparisons of our semi-analytic optimization to numerically calculated values of J_{sc} for

silicon, germanium, and GaAs NW array solar cells. It also contains the reflection and transmission spectra complementing Figures 4 and 5, the derivation of the dispersion relation of KMs and HE_{1m} fiber modes that lead to eq 1, and the derivation of f_{max} . This material is available free of charge via the Internet at <http://pubs.acs.org>.

■ AUTHOR INFORMATION

Corresponding Author

*E-mail: b.sturmberg@physics.usyd.edu.au.

Notes

The authors declare no competing financial interest.

■ ACKNOWLEDGMENTS

This work was supported by the Australian Renewable Energy Agency and the Australian Research Council Discovery Grant and Centre of Excellence Schemes. Computation resources were provided by the National Computational Infrastructure, Australia. We acknowledge useful discussions with Dr. T. White and Dr. K. Catchpole.

■ REFERENCES

- (1) King, R. R.; Boca, A.; Hong, W.; Liu, X.; Bhusari, D.; Larrabee, D.; Edmondson, K. M.; Law, D. C.; Fetzer, C. M.; Mesropian, S.; Karam, N. H. Band-gap-engineered architectures for high-efficiency multijunction concentrator solar cells. *Conf. Rec., 24th Eur. Photovoltaic Sol. Energy Conf.* **2009**, 21–25.
- (2) Todorov, T. K.; Reuter, K. B.; Mitzi, D. B. High-efficiency solar cell with earth-abundant liquid-processed absorber. *Adv. Mater.* **2010**, *22*, E156–159.
- (3) Liu, M.; Johnston, M. B.; Snaith, H. J. Efficient planar heterojunction perovskite solar cells by vapour deposition. *Nature* **2013**, *501*, 395–398.
- (4) Catchpole, K. R. Nanostructures in photovoltaics. *Philos. Trans. R. Soc. A* **2006**, *364*, 3493–3503.
- (5) Tsakalacos, L. Nanostructures for photovoltaics. *Mater. Sci. Eng. R* **2008**, *62*, 175–189.
- (6) Fan, Z.; Razavi, H.; Do, J.-w.; Moriwaki, A.; Ergen, O.; Chueh, Y.-L.; Leu, P. W.; Ho, J. C.; Takahashi, T.; Reichertz, L. A.; Neale, S.; Yu, K.; Wu, M.; Ager, J. W.; Javey, A. Three-dimensional nanopillar-array photovoltaics on low-cost and flexible substrates. *Nat. Mater.* **2009**, *8*, 648–653.
- (7) Kayes, B. M.; Filler, M. A.; Henry, M. D.; Maiolo, J. R., III; Kelzenberg, M. D.; Putnam, M. C.; Spurgeon, J. M.; Plass, K. E.;

Scherer, A.; Lewis, N. S.; Atwater, H. A. Radial p-n junction, wire array solar cells. *33rd IEEE Photovoltaic Spec. Conf.* **2008**, 1–5.

(8) Garnett, E. C.; Yang, P. Silicon nanowire radial p-n junction solar cells. *J. Am. Chem. Soc.* **2008**, *130*, 9224–9225.

(9) Mariani, G.; Scofield, A. C.; Hung, C.-H.; Huffaker, D. L. GaAs nanopillar-array solar cells employing in situ surface passivation. *Nat. Commun.* **2013**, *4*, 1497.

(10) Endo, H.; Goto, H.; Maebashi, T.; Nishijima, M.; Nakamura, N. Multi-junction solar cell and manufacturing method therefor. U.S. Patent 0327384, 2013.

(11) Sturmberg, B. C. P.; Dossou, K. B.; Botten, L. C.; Asatryan, A. A.; Poulton, C. G.; de Sterke, C. M.; McPhedran, R. C. Modal analysis of enhanced absorption in silicon nanowire arrays. *Opt. Express* **2011**, *19*, A1067–1081.

(12) Lin, C.; Povinelli, M. L. Optical absorption enhancement in silicon nanowire arrays with a large lattice constant for photovoltaic applications. *Opt. Express* **2009**, *17*, 19371–19381.

(13) Alaeian, H.; Atre, A. C.; Dionne, J. A. Optimized light absorption in Si wire array solar cells. *J. Opt.* **2012**, *14*, 024006.

(14) Wang, B.; Leu, P. W. Tunable and selective resonant absorption in vertical nanowires. *Opt. Lett.* **2012**, *37*, 3756–3758.

(15) Gunawan, O.; Wang, K.; Fallahzad, B.; Zhang, Y.; Tutuc, E.; Guha, S. High performance wire-array silicon solar cells. *Prog. Photovolt. Res. Appl.* **2010**, *19*, 307–312.

(16) Hu, L.; Chen, G. Analysis of optical absorption in silicon nanowire arrays for photovoltaic applications. *Nano Lett.* **2007**, *7*, 3249–3252.

(17) Heurlin, M.; Wickert, P.; Fält, S.; Borgström, M. T.; Deppert, K.; Samuelson, L.; Magnusson, M. H. Axial InP nanowire tandem junction grown on a silicon substrate. *Nano Lett.* **2011**, *11*, 2028–2031.

(18) Huang, N.; Lin, C.; Povinelli, M. L. Broadband absorption of semiconductor nanowire arrays for photovoltaic applications. *J. Opt.* **2012**, *14*, 024004.

(19) Madaria, A. R.; Yao, M.; Chi, C.; Huang, N.; Lin, C.; Li, R.; Povinelli, M. L.; Dapkus, P. D.; Zhou, C. Toward optimized light utilization in nanowire arrays using scalable nanosphere lithography and selected area growth. *Nano Lett.* **2012**, *12*, 2839–2845.

(20) Howell, S. L.; Padalkar, S.; Yoon, K.; Li, Q.; Koleske, D. D.; Wierer, J. J.; Wang, G. T.; Lauhon, L. J. Spatial mapping of efficiency of GaN/InGaN nanowire array solar cells using scanning photocurrent microscopy. *Nano Lett.* **2013**, *13*, 5123–5128.

(21) Wallentin, J.; Anttu, N.; Asoli, D.; Huffman, M.; Aberg, I.; Magnusson, M. H.; Siefert, G.; Fuss-Kailuweit, P.; Dimroth, F.; Witzigmann, B.; Xu, H. Q.; Samuelson, L.; Deppert, K.; Borgström, M. T. InP nanowire array solar cells achieving 13.8% efficiency by exceeding the ray optics limit. *Science* **2013**, *339*, 1057–1060.

(22) Bermel, P. Photon management modeling and beyond for photovoltaics. *Opt. Commun.* **2014**, *314*, 66–70.

(23) LaPierre, R. R.; Chia, a. C. E.; Gibson, S. J.; Haapamaki, C. M.; Boulanger, J.; Yee, R.; Kuyanov, P.; Zhang, J.; Tajik, N.; Jewell, N.; Rahman, K. M. A. Nanowire photovoltaics: review of design for high efficiency. *Phys. Status Solidi* **2013**, *16*, III–V.

(24) Kailuweit, P.; Peters, M.; Leene, J.; Mergenthaler, K.; Dimroth, F.; Bett, A. W. Numerical simulations of absorption properties of InP nanowires for solar cell applications. *Prog. Photovolt. Res. Appl.* **2011**, *20*, 945–953.

(25) Li, J.; Yu, H.; Li, Y. Solar energy harnessing in hexagonally arranged Si nanowire arrays and effects of array symmetry on optical characteristics. *Nanotechnology* **2012**, *23*, 194010.

(26) Yu, Z.; Raman, A.; Fan, S. Nanophotonic light-trapping theory for solar cells. *Appl. Phys. A: Mater. Sci. Process.* **2011**, *105*, 329–339.

(27) Anttu, N.; Xu, H. Q. Coupling of light into nanowire arrays and subsequent absorption. *J. Nanosci. Nanotechnol.* **2010**, *10*, 7183–7187.

(28) Anttu, N.; Xu, H. Q. Efficient light management in vertical nanowire arrays for photovoltaics. *Opt. Express* **2013**, *21*, 27589–27605.

(29) ASTM. *Reference Solar Spectral Irradiance: Air Mass 1.5 Spectra*. <http://rredc.nrel.gov/solar/spectra/am1.5>.

(30) Hutchinson, N. J.; Coquil, T.; Navid, A.; Pilon, L. Effective optical properties of highly ordered mesoporous thin films. *Thin Solid Films* **2010**, *518*, 2141–2146.

(31) Navid, A.; Pilon, L. Effect of polarization and morphology on the optical properties of absorbing nanoporous thin films. *Thin Solid Films* **2008**, *516*, 4159–4167.

(32) Bruggeman, D. A. G. Berechnung verschiedener physikalischer konstanten von heterogenen substanzen. *Ann. Phys.* **1935**, *416*, 636–664.

(33) del Rio, J. A.; Whitaker, S. Maxwell's equations in two-phase systems I: local electrodynamic equilibrium. *Transport Porous Med.* **2000**, *39*, 159–186.

(34) del Rio, J. A.; Whitaker, S. Maxwell's equations in two-phase systems II: two-equation model. *Transport Porous Med.* **2000**, *39*, 259–287.

(35) Keavney, C.; Haven, V.; Vernon, S. Emitter structures in MOCVD InP solar cells. *Conf. Rec., 21st IEEE Photovoltaic Spec. Conf.* **1990**, 141–144.

(36) Green, M. A.; Emery, K.; Hishikawa, Y.; Warta, W.; Dunlop, E. D. Solar cell efficiency tables (version 39). *Prog. Photovoltaic Res. Appl.* **2012**, *20*, 12–20.

(37) Dossou, K. B.; Botten, L. C.; Asatryan, A. A.; Sturmberg, B. C. P.; Byrne, M. A.; Poulton, C. G.; McPhedran, R. C.; de Sterke, C. M. Modal formulation for diffraction by absorbing photonic crystal slabs. *J. Opt. Soc. Am. A* **2012**, *29*, 817–831.

(38) EMUstack: open-source simulation package; emustack.com.

Optimizing Photovoltaic Charge Generation of Nanowire Arrays: A Simple Semi-Analytic Approach — Supporting Information

Björn C. P. Sturmberg,^{*,†} Kokou B. Dossou,[‡] Lindsay C. Botten,[‡] Ara A. Asatryan,[‡]
Christopher G. Poulton,[‡] Ross C. McPhedran,[†] and C. Martijn de Sterke[†]

University of Sydney, and University of Technology Sydney

Received August 23, 2015; E-mail: b.sturmberg@physics.usyd.edu.au

Spectra Complementing Figures 4, 5 of Main Text

Figure 1 shows the reflection spectrum corresponding to Figure 4 of main text, while Fig. 2 transmission spectra corresponding to Figure 5 of main text.

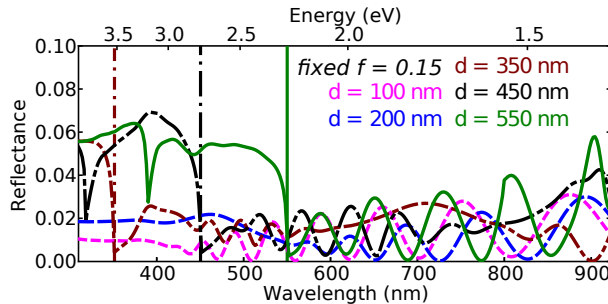


Figure 1. Reflection spectra corresponding to Figure 4 of main text, such that $a = 43, 65, 152, 196, 240$ and $f = 0.15$ throughout. Note that the vertical axis range is 0–0.1. Vertical lines mark the shortest wavelength Wood anomalies in reflection $\lambda = n_{\text{Air}}d$.

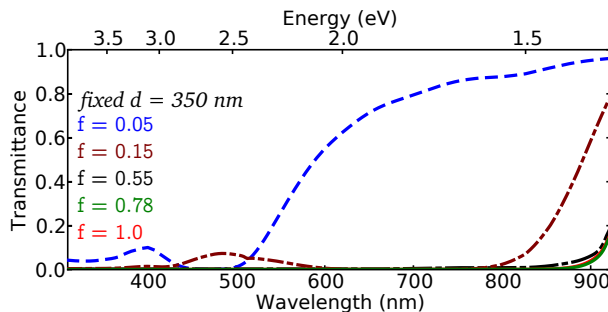


Figure 2. Transmission spectra corresponding to Figure 5 of main text, where $d = 350$ nm and increasing volume fractions correspond to $a = 88, 152, 292, 348$. The spectrum of a homogeneous film of equal thickness is shown in red ($f = 1.0$).

Results for Additional Materials

GaAs is another III-V semiconductor with good optoelectronic properties for photovoltaics. It is however expensive, which further motivates the fabrication of NW arrays to reduce the quantity of material used. Figure 3 shows the short circuit current of GaAs NW arrays along with our predictions for arrays of thickness $h = 2.33 \mu\text{m}$. The agreement between the full simulations across the parameter-space and the semi-analytic predictions is again good. The optimal array marked with a blue dot at $d = 300$ nm, $f = 0.25$ lies in the bottom right of the horizontal and vertical lines, and on the left-hand side of the left green

curve. The optimal array has a short circuit current of $J_{\text{sc}} = 25.7 \text{ mA/cm}^2$.

There is also a second peak in J_{sc} near $d = 580$, $f = 0.35$. This peak is to the right of the vertical d_{max} line, and on the left-hand side of the rightmost green curve. Arrays with these parameters support 3 resonant modes within the absorption range as opposed to the 2 of the optimum arrays around the blue dot. They however also excite higher diffraction orders across a larger part of the absorption range, which limits their J_{sc} to values less than the optimal peak. This could be altered by reducing the refractive index of the substrate to shift $d_{\text{max}} \equiv \lambda_{\text{av}}/n_{\text{sub}}$ to a larger value. In this GaAs example a substrate with $n < 1.12$ would be required to allow for optimal performance of arrays with $d = 580$ nm.

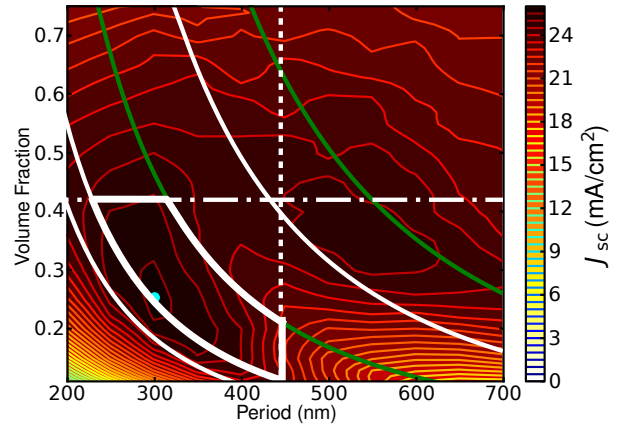


Figure 3. Numerically calculated short circuit current of J_{sc} of GaAs NW arrays with the optimal array marked with a blue dot. Superimposed are the results of our semi-analytic optimization with the predicted optimal region emphasised with thick curves.

We now show that the method is also applicable to indirect bandgap semiconductors such as silicon and germanium. The imaginary part of these materials refractive indices changes by orders of magnitude across the solar spectrum, posing a challenging test for our optimization routine. Our results however demonstrate that the method is robust to these variations.

Figure 4 shows the numerically calculated J_{sc} of silicon NW arrays of thickness $h = 2.33 \mu\text{m}$ and our semi-analytic prediction. Because of the low intrinsic absorptance of silicon, transmission losses are far more important than reflection losses. Our method therefore does not place a restriction on the volume fraction, and the optimal array is found to have $f = 0.7$. The short circuit current of this array, which has a period of $d = 500$ nm, is $J_{\text{sc}} = 17.8 \text{ mA/cm}^2$. The larger bandgap wavelength of silicon results in an increased threshold period to $d_{\text{max}} = 512$ nm. We note that when calculating the Key Mode cut-off radii for silicon, it

[†]CUDOS and IPOS, School of Physics, University of Sydney, 2006, Australia

[‡]CUDOS, School of Mathematical Sciences, University of Technology Sydney, Sydney, 2007, Australia

was found to be necessary to consider lossless silicon in order to find solutions for higher order modes at $\lambda = 310$ nm. Furthermore, because the volume fraction is substantial in this case the modes of individual NWs interact and a more accurate predictions for the cut-off radii can be found using the full expression of Eq. (10) from Sturmberg *et al.* 2011.¹ This was not done here to simplify the graphical representation of the cut-offs.

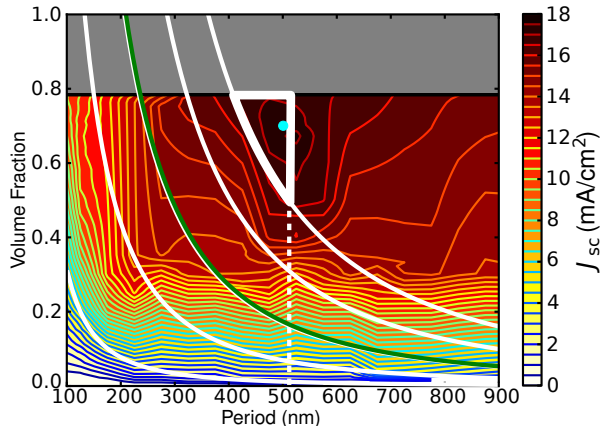


Figure 4. Numerically calculated short circuit current of J_{sc} of silicon NW arrays with the optimal array marked with a blue dot. Superimposed are the results of our semi-analytic optimization with the predicted optimal region emphasised with thick curves.

Lastly, Fig. 5 shows our results for arrays of germanium NWs of length $h = 2.33 \mu\text{m}$. The bandgap wavelength of germanium is larger than that of silicon, so that $d_{\text{max}} = 590$ nm. The average intrinsic absorptivity of germanium is not as poor as for silicon, and we predict a maximal allowed volume fraction of $f_{\text{max}} = 0.37$, which matches well with our numerical results. For germanium the optimal array has $d = 325$ nm, $f = 0.30$ and a short circuit current of $J_{sc} = 42.2$ mA/cm².

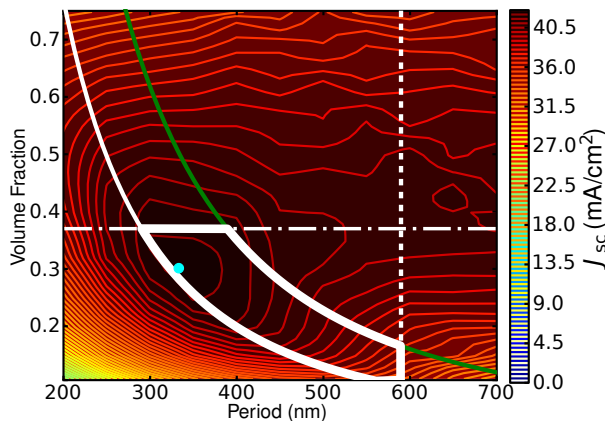


Figure 5. Numerically calculated short circuit current of J_{sc} of germanium NW arrays with the optimal array marked with a blue dot. Superimposed are the results of our semi-analytic optimization with the predicted optimal region emphasised with thick curves.

Comparison of Key Bloch Modes and Leaky Fibre Modes

There are fundamentally two ways to view the modes of NW arrays: as Bloch modes of the array, with their inherent periodicity, or as the modes of isolated high index cylinders, *i.e.* as optical fiber modes. The later is an approximation that is valid only when individual NWs are far apart such

that their interaction is negligible. To calculate properties of the former on the other hand we retain the periodicity of modes and thereby the interaction between NWs, but truncate the field expansions at the dipole term.

Below we discuss which optical fiber modes are important for the absorption of solar radiation, derive the dispersion relation of the truncated multipole series and show how the two descriptions agree exactly in the limit that the NWs are infinitely far apart.

Leaky Optical Fiber Modes

The modes of waveguides are generally composed of Transverse Electric (TE_{0m}), Transverse Magnetic (TM_{0m}), and hybrid EH_{vm} and HE_{vm} modes. In step-index optical fibers the field components tangential to the cylinder surface are in general non-zero so that the modes are of EH_{vm} and HE_{vm} type. The well known dispersion relation of HE_{vm} (and EH_{vm}) modes is,²

$$\left(\frac{\epsilon_1 J_1'(k_1 a)}{k_1 a J_1(k_1 a)} + \frac{\epsilon_2 i K_1'(ik_2 a)}{k_2 a K_1(ik_2 a)} \right) \times \left(\frac{1}{k_1 a} \frac{J_1'(k_1 a)}{J_1(k_1 a)} + \frac{1}{k_2 a} \frac{i K_1'(ik_2 a)}{K_1(ik_2 a)} \right) = \left(\frac{1}{k_1^2 a^2} - \frac{1}{k_2^2 a^2} \right)^2 \left(\frac{\beta_z}{k_0} \right)^2, \quad (1)$$

where β_z is the mode's propagation constant and ϵ_i , $k_i = \sqrt{\epsilon_i \omega^2 / c^2 - \beta_z^2}$ are the permittivities and transverse wavenumbers in the NWs ($i = 1$) and background ($i = 2$) respectively. J_1 is the first order Bessel function and K_1 is the modified Bessel function of the second kind and primes denote derivation with respect to the functions argument.

Of all possible EH_{vm} and HE_{vm} modes, only the HE_{1m} modes share the anti-symmetric in-plane field distribution of the incident plane waves, and therefore these are the only modes that contribute to the absorption of NW arrays.³

Dipole Approximation of Key Bloch Modes

When studying the absorption characteristics of NW arrays in terms of their Bloch modes we found that a small number of Bloch modes dominated the absorption, which we called Key Modes (KMs).¹ Examining the field distributions of the KMs we observed that the E_z component of the KMs is dipolar. We therefore construct a multipole model for the Bloch modes of the NW array and retain only the dipole terms, which correspond to the KMs.

To begin constructing the multipole model we write the electric and magnetic fields in a form that automatically satisfies Helmholtz's equation in cylindrical coordinates,

$$E_z^{\text{internal}}(r, \theta) = \sum_m C_m J_m(k_1 r) e^{im\theta}. \quad (2)$$

Since the KMs are dipolar in E_z we consider only the first order dipole term;

$$E_z^{\text{external}}(r, \theta) = [A^E J_1(k_2 r) + B^E H_1^{(1)}(k_2 r)] e^{i\theta}, \quad (3)$$

$$E_z^{\text{internal}}(r, \theta) = C^E J_1(k_1 r) e^{i\theta}, \quad (4)$$

$$H_z^{\text{external}}(r, \theta) = [A^H J_1(k_2 r) + B^H H_1^{(1)}(k_2 r)] e^{i\theta}, \quad (5)$$

$$H_z^{\text{internal}}(r, \theta) = C^H J_1(k_1 r) e^{i\theta}, \quad (6)$$

where $H_1^{(1)}$ is the first order Hankel function of the first kind and the k_i are defined as above.

The effect of the infinite lattice is taken into account through the Rayleigh identity,

$$A_m^{E,H} = \sum_n^\infty S_{m-n} B_n^{E,H}, \quad (7)$$

which to first (dipole) order is,

$$A_1^{E,H} = S_0 B_1^{E,H}. \quad (8)$$

This allows us to eliminate the coefficients A , C from Eqs. (3-6) after enforcing the continuity of E_z , H_z at the cylinder boundary ($r = a$),

$$C^{E,H} = \frac{1}{J_1(k_1 a)} [B^{E,H} H_1^{(1)}(k_2 a) + A^{E,H} J_1(k_2 a)], \quad (9)$$

$$= \frac{1}{J_1(k_1 a)} [B^{E,H} H_1^{(1)}(k_2 a) + S_0 B^{E,H} J_1(k_2 a)], \quad (10)$$

$$= \frac{1}{J_1(k_1 a)} [H_1^{(1)}(k_2 a) + S_0 J_1(k_2 a)] B^{E,H}. \quad (11)$$

We now write the internal and external fields in terms of the single coefficient $B^{E,H}$,

$$E_z^{ext}(r, \theta) = [H_1^{(1)}(k_2 r) + S_0 J_1(k_2 r)] B^E e^{i\theta}, \quad (12)$$

$$E_z^{int}(r, \theta) = \frac{1}{J_1(k_1 a)} [H_1^{(1)}(k_2 a) + S_0 J_1(k_2 a)] J_1(k_1 r) B^E e^{i\theta}, \quad (13)$$

$$H_z^{ext}(r, \theta) = [H_1^{(1)}(k_2 r) + S_0 J_1(k_2 r)] B^H e^{i\theta}, \quad (14)$$

$$H_z^{int}(r, \theta) = \frac{1}{J_1(k_1 a)} [H_1^{(1)}(k_2 a) + S_0 J_1(k_2 a)] J_1(k_1 r) B^H e^{i\theta}. \quad (15)$$

Assuming a field harmonic in time ($e^{-i\omega t}$), Maxwell's curl equations are,

$$\nabla \times E = i\omega\mu_0\mu_1 H, \quad (16)$$

$$\nabla \times H = -i\omega\epsilon_0\epsilon_1 E. \quad (17)$$

Which after splitting into radial and angular components and using the expression for ∇ in cylindrical coordinate read as,

$$\frac{\partial E_r}{\partial z} - \frac{\partial E_z}{\partial r} = i\omega\mu_0\mu_1 H_\theta, \quad (18)$$

$$\frac{\partial H_r}{\partial z} - \frac{\partial H_z}{\partial r} = -i\omega\epsilon_0\epsilon_1 E_\theta, \quad (19)$$

$$\frac{1}{r} \frac{\partial E_z}{\partial \theta} - \frac{\partial E_\theta}{\partial z} = i\omega\mu_0\mu_1 H_r, \quad (20)$$

$$\frac{1}{r} \frac{\partial H_z}{\partial \theta} - \frac{\partial H_\theta}{\partial z} = -i\omega\epsilon_0\epsilon_1 E_r. \quad (21)$$

Now, propagation along the z -direction is given by the wavevector $k_z = \beta_z$, so we write Eqs. (18) - (21) in the form $\frac{\partial E_r}{\partial z} = i\beta_z E_r$ etc. We thereby find two relations between the z , θ components of the fields (*i.e.* eliminating r components) by substitution of Eqs. (18), (20) and (19), (21),

$$E_\theta = \frac{i}{k^2} \left[\frac{\beta_z}{r} \frac{\partial E_z}{\partial \theta} - \omega\mu_0\mu_1 \frac{\partial H_z}{\partial r} \right], \quad (22)$$

$$H_\theta = \frac{i}{k^2} \left[\frac{\beta_z}{r} \frac{\partial H_z}{\partial \theta} - \omega\epsilon_0\epsilon_1 \frac{\partial E_z}{\partial r} \right]. \quad (23)$$

We now match the internal and external fields, Eqs. (22, 23), at the cylinder boundary using the expressions (12-15),

$$\begin{aligned} & \frac{1}{k_1^2} \left[\frac{i\beta_z}{a} [H_1^{(1)}(k_2 a) + S_0 J_1(k_2 a)] B^E \right. \\ & \quad \left. - \omega\mu_0\mu_1 k_1 \frac{J_1'(k_1 a)}{J_1(k_1 a)} [H_1^{(1)}(k_2 a) + S_0 J_1(k_2 a)] B^H \right] \\ & = \frac{1}{k_2^2} \left[\frac{i\beta_z}{a} [H_1^{(1)}(k_2 a) + S_0 J_1(k_2 a)] B^E \right. \\ & \quad \left. - \omega\mu_0\mu_2 k_2 [H_1^{(1)'}(k_2 a) + S_0 J_1'(k_2 a)] B^H \right], \quad (24) \end{aligned}$$

and

$$\begin{aligned} & \frac{1}{k_1^2} \left[\frac{i\beta_z}{a} [H_1^{(1)}(k_2 a) + S_0 J_1(k_2 a)] B^H \right. \\ & \quad \left. + \omega\epsilon_0\epsilon_1 k_1 \frac{J_1'(k_1 a)}{J_1(k_1 a)} [H_1^{(1)}(k_2 a) + S_0 J_1(k_2 a)] B^E \right] \\ & = \frac{1}{k_2^2} \left[\frac{i\beta_z}{a} [H_1^{(1)}(k_2 a) + S_0 J_1(k_2 a)] B^E \right. \\ & \quad \left. + \omega\epsilon_0\epsilon_2 k_2 [H_1^{(1)'}(k_2 a) + S_0 J_1'(k_2 a)] B^E \right], \quad (25) \end{aligned}$$

where exponential and $J_1(k_1 a)$ terms have been cancelled. Further division by the terms in square brackets leads to the expressions,

$$\begin{aligned} & \frac{1}{k_1^2} \left[\frac{i\beta_z}{a} B^E - \omega\mu_0\mu_1 k_1 \frac{J_1'(k_1 a)}{J_1(k_1 a)} B^H \right] \\ & = \frac{1}{k_2^2} \left[\frac{i\beta_z}{a} B^E - \omega\mu_0\mu_2 k_2 \frac{H_1^{(1)'}(k_2 a) + S_0 J_1'(k_2 a)}{H_1^{(1)}(k_2 a) + S_0 J_1(k_2 a)} B^H \right], \quad (26) \end{aligned}$$

$$\begin{aligned} & \frac{1}{k_1^2} \left[\frac{i\beta_z}{a} B^H + \omega\epsilon_0\epsilon_1 k_1 \frac{J_1'(k_1 a)}{J_1(k_1 a)} B^E \right] \\ & = \frac{1}{k_2^2} \left[\frac{i\beta_z}{a} B^H + \omega\epsilon_0\epsilon_2 k_2 \frac{H_1^{(1)'}(k_2 a) + S_0 J_1'(k_2 a)}{H_1^{(1)}(k_2 a) + S_0 J_1(k_2 a)} B^E \right]. \quad (27) \end{aligned}$$

To calculate the full dispersion relation we rearrange Eqs. (26, 27) into the matrix equation,

$$\left[\omega \left[\frac{\epsilon_0 \epsilon_1 J_1'(k_1 a)}{k_1 J_1(k_1 a)} - \frac{\epsilon_0 \epsilon_2 (H_1^{(1)'}(k_2 a) + S_0 J_1'(k_2 a))}{k_2 (H_1^{(1)}(k_2 a) + S_0 J_1(k_1 a))} \right] \right. \\ \left. \frac{i\beta_z}{a} \left[\frac{1}{k_1^2} - \frac{1}{k_2^2} \right] \right] \omega \left[\frac{-\mu_0 \mu_1 J_1'(k_1 a)}{k_1 J_1(k_1 a)} + \frac{\mu_0 \mu_2 (H_1^{(1)'}(k_2 a) + S_0 J_1'(k_2 a))}{k_2 (H_1^{(1)}(k_2 a) + S_0 J_1(k_1 a))} \right] \begin{bmatrix} B^E \\ B^H \end{bmatrix} = \begin{bmatrix} 0 \\ 0 \end{bmatrix}. \quad (28)$$

Solutions of which are found from the zeros of the determinant,

$$\left[\frac{\epsilon_0 \epsilon_1 J_1'(k_1 a)}{k_1 J_1(k_1 a)} - \frac{\epsilon_0 \epsilon_2 (H_1^{(1)'}(k_2 a) + S_0 J_1'(k_2 a))}{k_2 (H_1^{(1)}(k_2 a) + S_0 J_1(k_2 a))} \right] \times \\ \left[\frac{-\mu_0 \mu_1 J_1'(k_1 a)}{k_1 J_1(k_1 a)} + \frac{\mu_0 \mu_2 (H_1^{(1)'}(k_2 a) + S_0 J_1'(k_2 a))}{k_2 (H_1^{(1)}(k_2 a) + S_0 J_1(k_2 a))} \right] \\ + \frac{\beta_z^2}{\omega^2 a^2} \left[\frac{1}{k_1^2} - \frac{1}{k_2^2} \right]^2 = 0. \quad (29)$$

Agreement of Models in the Dilute Array Limit

In the limit where the NWs are very far apart, such that their fields do not overlap we set $S_0 = 0$ in the dispersion relation for the KMs (Eq. 29).

$$\left[\frac{\epsilon_0 \epsilon_1 J_1'(k_1 a)}{k_1 J_1(k_1 a)} - \frac{\epsilon_0 \epsilon_2 H_1^{(1)'}(k_2 a)}{k_2 H_1^{(1)}(k_2 a)} \right] \times \\ \left[\frac{-\mu_0 \mu_1 J_1'(k_1 a)}{k_1 J_1(k_1 a)} + \frac{\mu_0 \mu_2 H_1^{(1)'}(k_2 a)}{k_2 H_1^{(1)}(k_2 a)} \right] \\ + \frac{\beta_z^2}{\omega^2 a^2} \left[\frac{1}{k_1^2} - \frac{1}{k_2^2} \right]^2 = 0. \quad (30)$$

Moving the last term to the RHS, multiplying both sides by $c^2 = 1/\epsilon_0 \mu_0$, and setting $\mu_1 = 1$ we have

$$\left[\frac{\epsilon_1 J_1'(k_1 a)}{k_1 J_1(k_1 a)} - \frac{\epsilon_2 H_1^{(1)'}(k_2 a)}{k_2 H_1^{(1)}(k_2 a)} \right] \left[\frac{\mu_1 J_1'(k_1 a)}{k_1 J_1(k_1 a)} - \frac{\mu_2 H_1^{(1)'}(k_2 a)}{k_2 H_1^{(1)}(k_2 a)} \right] \\ = \frac{c^2 \beta_z^2}{\omega^2 a^2} \left[\frac{1}{k_1^2} - \frac{1}{k_2^2} \right]^2. \quad (31)$$

To compare this to the dispersion relation for HE_{1m} (EH_{1m}) fiber modes we rewrite Eq. 1 multiplying both sides by a^2 and with $k_0 = \omega/c$,

$$\left(\frac{\epsilon_1 J_1'(k_1 a)}{k_1 J_1(k_1 a)} + \frac{\epsilon_2 K_1'(ik_2 a)}{k_2 K_1(ik_2 a)} \right) \left(\frac{1 J_1'(k_1 a)}{k_1 J_1(k_1 a)} + \frac{1 K_1'(ik_2 a)}{k_2 K_1(ik_2 a)} \right) \\ = \left(\frac{c^2 \beta_z^2}{\omega^2 a^2} \right) \left(\frac{1}{k_1^2} - \frac{1}{k_2^2} \right)^2. \quad (32)$$

We see that we need to convert the modified Bessel functions of the second kind K into Hankel functions of the first kind. Using relation 9.6.4 from Abramowitz and Stegun,⁴

$$K_v(z) = \frac{\pi}{2} i e^{\frac{i v \pi}{2}} H_v^{(1)}(z e^{\frac{i \pi}{2}}), \text{ for } -\pi < \arg(z) \leq \frac{\pi}{2}. \quad (33)$$

For $v = 1$,

$$K_1(z) = -\frac{\pi}{2} H_1^{(1)}(iz), \quad (34)$$

$$K_1(ik_2 a) = -\frac{\pi}{2} H_1^{(1)}(-k_2 a) \quad (35)$$

To convert the K' term we use the recurrence relations of 9.6.26,⁴

$$K'_v(z) = -\frac{\pi}{2} i e^{\frac{i v \pi}{2}} (v+1) H_{v+1}^{(1)}(iz) + \frac{v \pi}{2} i e^{\frac{i v \pi}{2}} H_v^{(1)}(iz), \quad (36)$$

which for $v = 1$ is

$$K'_1(z) = \frac{\pi}{2} i H_2^{(1)}(iz) - \frac{1}{z} \frac{\pi}{2} H_1^{(1)}(iz), \quad (37)$$

$$= \frac{\pi}{2} i H_2^{(1)}(iz) - \frac{i}{iz} \frac{\pi}{2} H_1^{(1)}(iz), \quad (38)$$

$$= -\frac{\pi}{2} i \left(-H_2^{(1)}(iz) + \frac{1}{iz} H_1^{(1)}(iz) \right). \quad (39)$$

Using the substitution $y = iz$ (s.t. $dz = -idy$) this can be written as

$$\frac{K'_1(-iy)}{-i} = -\frac{\pi}{2} i \left(-H_2^{(1)}(y) + \frac{1}{y} H_1^{(1)}(y) \right), \quad (40)$$

and comparing this with 9.1.27,⁴

$$H_v^{(1)'}(z) = -H_{(v+1)}^{(1)}(z) + \frac{v}{z} H_v^{(1)}(z), \quad (41)$$

we see that, for $v = 1$,

$$\frac{K'_1(-iy)}{-i} = -\frac{\pi}{2} i \left(H_1^{(1)'}(y) \right). \quad (42)$$

Substituting in $ik_2 a = -iy$, s.t. $y = -k_2 a$ we find that

$$K'_1(ik_2 a) = -\frac{\pi}{2} \left(H_1^{(1)' }(-k_2 a) \right) \quad (43)$$

Substituting Eq. 35 and Eq. 43 into Eq. 32 gives

$$\left(\frac{\epsilon_1 J_1'(k_1 a)}{k_1 J_1(k_1 a)} + \frac{\epsilon_2 H_1^{(1)' }(-k_2 a)}{k_2 H_1^{(1)}(-k_2 a)} \right) \times \\ \left(\frac{1 J_1'(k_1 a)}{k_1 J_1(k_1 a)} + \frac{1 H_1^{(1)' }(-k_2 a)}{k_2 H_1^{(1)}(-k_2 a)} \right) \\ = \left(\frac{c^2 \beta_z^2}{\omega^2 a^2} \right) \left(\frac{1}{k_1^2} - \frac{1}{k_2^2} \right)^2. \quad (44)$$

To write the $H_1^{(1)}$ terms as a function of $k_2 a$ we note that the real part of the Henkel function of the first kind is symmetric while the imaginary part of this function is anti-symmetric, *i. e.*

$$H_1^{(1)}(-z) = \text{Re}(H_1^{(1)}(z)) - i \text{Im}(H_1^{(1)}(z)). \quad (45)$$

The first derivative of a symmetric function is anti-symmetric and vice versa, therefore

$$H_1^{(1)' }(-z) = -\text{Re}(H_1^{(1)' } (z)) + i \text{Im}(H_1^{(1)' } (z)). \quad (46)$$

Taking the fraction containing the Henkel functions we have

$$\text{Re} \left(\frac{H_1^{(1)' }(-z)}{H_1^{(1)}(-z)} \right) = \frac{-\text{Re}(H_1^{(1)' } (z))}{\text{Re}(H_1^{(1)}(z))}, \quad (47)$$

$$\text{Im} \left(\frac{H_1^{(1)' }(-z)}{H_1^{(1)}(-z)} \right) = \frac{\text{Im}(H_1^{(1)' } (z))}{-\text{Im}(H_1^{(1)}(z))}, \quad (48)$$

$$\frac{H_1^{(1)' }(-z)}{H_1^{(1)}(-z)} = -\frac{H_1^{(1)' } (z)}{H_1^{(1)}(z)}. \quad (49)$$

Our final expression for the dispersion relation for the

HE_{1m} (EH_{1m}) modes is therefore

$$\begin{aligned} & \left(\frac{\epsilon_1}{k_1} \frac{J_1'(k_1 a)}{J_1(k_1 a)} - \frac{\epsilon_2}{k_2} \frac{H_1^{(1)'}(k_2 a)}{H_1^{(1)}(k_2 a)} \right) \times \\ & \left(\frac{1}{k_1} \frac{J_1'(k_1 a)}{J_1(k_1 a)} - \frac{1}{k_2} \frac{H_1^{(1)'}(k_2 a)}{H_1^{(1)}(k_2 a)} \right) \\ & = \left(\frac{c^2 \beta_z^2}{\omega^2 a^2} \right) \left(\frac{1}{k_1^2} - \frac{1}{k_2^2} \right)^2. \end{aligned} \quad (50)$$

This agrees exactly with the dipole expression when $S_0 = 0$ and $\mu_1 = \mu_2 = 1$, *i. e.* Eq. 31.

Derivation of Key Mode Cut-off

To find the cut-off of the KMs we take the limit $\beta_z \rightarrow 0$ in Eqs. (26, 27). Doing so we find 2 uncoupled equations,

$$\left[\frac{\mu_0 \mu_1}{k_1} \frac{J_1'(k_1 a)}{J_1(k_1 a)} - \frac{\mu_0 \mu_2}{k_2} \frac{H_1^{(1)'}(k_2 a) + S_0 J_1'(k_2 a)}{H_1^{(1)}(k_2 a) + S_0 J_1(k_2 a)} \right] B^H = 0, \quad (51)$$

$$\left[\frac{\epsilon_0 \epsilon_1}{k_1} \frac{J_1'(k_1 a)}{J_1(k_1 a)} - \frac{\epsilon_0 \epsilon_2}{k_2} \frac{H_1^{(1)'}(k_2 a) + S_0 J_1'(k_2 a)}{H_1^{(1)}(k_2 a) + S_0 J_1(k_2 a)} \right] B^E = 0, \quad (52)$$

for a TE and a TM mode respectively. When $S_0 = 0$ and $\mu_1 = \mu_2 = 1$ these are equivalent to the first and second terms on the LHS of Eq. 50 (the HE_{1m} (EH_{1m}) dispersion relation). The TE modes have dipolar magnetic fields and the TM modes have dipolar electric fields. Since the strongly excited modes of NW arrays have dipolar electric fields and $B^H > B^E$, we consider only the cut-offs of the TM modes,

$$\frac{\epsilon_1}{k_1} \frac{J_1'(k_1 a)}{J_1(k_1 a)} - \frac{\epsilon_2}{k_2} \frac{H_1^{(1)'}(k_2 a) + S_0 J_1'(k_2 a)}{H_1^{(1)}(k_2 a) + S_0 J_1(k_2 a)} = 0. \quad (53)$$

This is consistent with the fields being HE_{1m} modes rather than EH_{1m} modes, which they must to satisfy the symmetry requirements for coupling to the incident plane waves.

When $S_0 = 0$ this gives Eq. 1 of the main text,

$$\frac{\epsilon_1 J_1'(k_1 a)}{k_1 J_1(k_1 a)} - \frac{\epsilon_2 H_1^{(1)'}(k_2 a)}{k_2 H_1^{(1)}(k_2 a)} = 0. \quad (54)$$

Derivation of f_{\max}

As discussed in the main text, we derive f_{\max} by limiting the magnitude of the reflection. This is done using an effective index treatment that removes a and d from the calculation, combined with a Fresnel calculation of the reflection and transmission of the thin film with the effective properties. The method is illustrated in Fig. 6.

We calculate the real part of the effective refractive index from the Bruggeman formulation⁵ for the effective permittivity $\epsilon_{\text{eff_BR}}$. Defining the permittivity of the complex background/inclusion as $\epsilon_{\text{bkg/inc}}$ this is,

$$(1-f) \frac{\epsilon_{\text{bkg}}^2 - \epsilon_{\text{eff_BR}}^2}{\epsilon_{\text{bkg}}^2 + 2\epsilon_{\text{eff_BR}}^2} + f \frac{\epsilon_{\text{inc}}^2 - \epsilon_{\text{eff_BR}}^2}{\epsilon_{\text{inc}}^2 + 2\epsilon_{\text{eff_BR}}^2} = 0, \quad (55)$$

such that

$$n'_{\text{BR}} = \text{Re}(\sqrt{\epsilon_{\text{eff_BR}}}). \quad (56)$$

The absorptivity of the effective medium is however severely underestimated using the Bruggeman formulation, and so we calculate the imaginary part of the effective index using the Volume Averaging Theory.^{6,7} Keeping the nomenclature for f and writing the real and imaginary part of the refractive

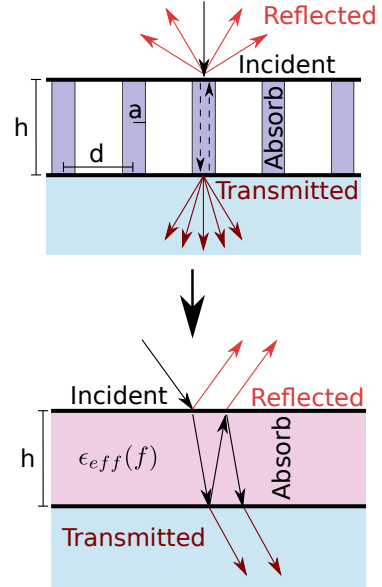


Figure 6. Representation of the effective index treatment showing the first 2 terms of the infinite Fabry-Perot reflection and transmission series.

index of the inclusion/background material as $n'_{\text{inc/bkg}}$ and $n''_{\text{inc/bkg}}$ respectively this is,

$$A = f(n_{\text{inc}}'^2 - n_{\text{inc}}''^2) + (1-f)(n_{\text{bkg}}'^2 - n_{\text{bkg}}''^2), \quad (57)$$

$$B = 2fn'_{\text{inc}}n''_{\text{inc}} + 2(1-f)n'_{\text{bkg}}n''_{\text{bkg}}, \quad (58)$$

$$n_{\text{VAT}} = \sqrt{\frac{A + \sqrt{A^2 + B^2}}{2}} + i\sqrt{\frac{-A + \sqrt{A^2 + B^2}}{2}}. \quad (59)$$

Taking the imaginary part of the effective index, $n''_{\text{VAT}} = \text{Im}(n_{\text{VAT}})$, we write the complex effective refractive index as

$$n_{\text{eff}} = n'_{\text{BR}} + in''_{\text{VAT}}. \quad (60)$$

Using this effective index we calculate the Fresnel coefficients of the top and bottom interfaces for each value of $0 < f < \pi/4$,

$$r_{ij} = \frac{n_i - n_j}{n_i + n_j}, \quad (61)$$

$$t_{ij} = \frac{2n_i}{n_i + n_j}, \quad (62)$$

where i, j label the incident and outgoing media respectively for each interface.

The transmittance and reflectance are then obtained using the Fresnel equations, with the propagation constant within the absorbing layer $\beta_z = \frac{2\pi n_{\text{eff}}}{\lambda}$,

$$r(\lambda) = \frac{r_{12} + r_{23}e^{2i\beta_z h}}{1 + r_{12}r_{23}e^{2i\beta_z h}}, \quad (63)$$

$$t(\lambda) = \frac{t_{12}t_{23}e^{i\beta_z h}}{1 + r_{12}r_{23}e^{2i\beta_z h}}. \quad (64)$$

In the presence of the substrate with refractive index n_3 and superstrate with n_1 the reflection and transmission spectra are therefore

$$R(\lambda) = r(\lambda)r(\lambda)^\dagger, \quad (65)$$

$$T(\lambda) = \frac{\text{Re}(n_3)}{\text{Re}(n_1)} t(\lambda)t(\lambda)^\dagger. \quad (66)$$

We integrate the spectra after weighting them by the solar

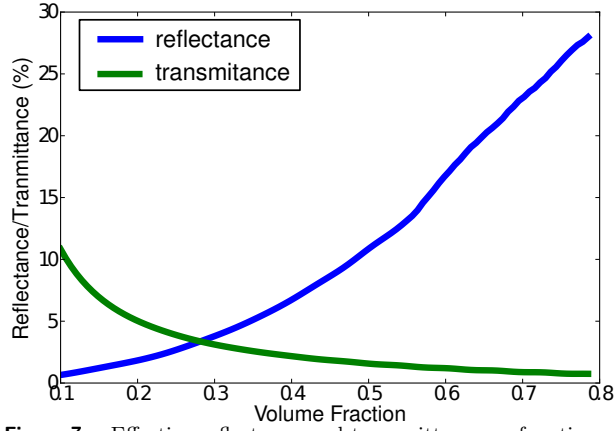


Figure 7. Effective reflectance and transmittance as function of volume fraction for $h = 2.33 \mu\text{m}$.

flux to arrive at a single averaged value for each f . For instance the average transmission is,

$$T_{\text{av}}(f) = \frac{\int_{\lambda_l}^{\lambda_g} \xi(\lambda) T(\lambda) d\lambda}{\int_{\lambda_l}^{\lambda_u} \xi(\lambda) d\lambda}, \quad (67)$$

where, as in the main text $\xi(\lambda) = I(\lambda)\lambda$. Finally we evaluate where $R_{\text{av}}(f) = T_{\text{av}}(f)$, which defines the volume fraction f_{max} .

As an example, Fig. 7 shows the reflectance and transmittance calculated with the presented effective index model, as a function of InP volume fraction for an array of thickness $h = 2.33 \mu\text{m}$.

References

- (1) Sturmberg, B. C. P.; Dossou, K. B.; Botten, L. C.; Asatryan, A. A.; Poulton, C. G.; de Sterke, C. M.; McPhedran, R. C. *Optics Express* **2011**, *19*, A1067–81.
- (2) Snyder, A. W.; Love, J. D. *Optical Waveguide Theory*; Chapman and Hall, 1983; Vol. 2.
- (3) Wang, B.; Leu, P. W. *Optics letters* **2012**, *37*, 3756–8.
- (4) Abramowitz, M.; Stegun, I. A. *Handbook of Mathematical Functions*; 1972.
- (5) Bruggeman, D. A. G. *Annalen der Physik* **1935**, *416*, 636–664.
- (6) del Rio, J. A.; Whitaker, S. *Transport in Porous Media* **2000**, *39*, 159–186.
- (7) del Rio, J. A.; Whitaker, S. *Transport in Porous Media* **2000**, *39*, 259–287.

4.3 Comparison with Nanohole Array Solar Cells

The complements of nanowire arrays are nanohole arrays, where the connected background medium has the higher refractive index than the inclusions [159, 160]. In this section we summarize the similarities and the striking differences that were revealed by our study of NH arrays [7].

The major difference between NW arrays and NH arrays is the type of optical modes that the structures support. The Bloch modes of nanostructured media are predominantly determined by the high index part of the structure; in the case of NWs these are the isolated inclusions, while for NH arrays this is the connected matrix. Though the majority of the modes are concentrated within the background (as in Fig. 4.1(b)), there are also BMs that are concentrated within the low index inclusions (see Fig. 4.1(c)). These were earlier identified in [161, 162] using full-wave simulations and experiments, which made their identification far more challenging than it was using EMUstack. These “channelling modes” have both positive and negative effects: drastically reducing the reflection, at the expense of increasing transmission.

The NH arrays also support guided mode resonances, which are superpositions of BMs, that propagate laterally in the plane of the high index layer. These resonances are excited when their transverse propagation constants match that of the incident light with the addition of the in-plane momentum provided by the array’s reciprocal lattice vector [7]. The light that is coupled into these modes experiences greatly enhanced absorption because it propagates a long distance transversely while trapped within the slab. Figure 4.2 shows the dispersion diagram of a 2.33 μm thick silicon slab on a silica substrate, where the waveguide modes exist above the silicon and under the silica light lines. The lower horizontal line in Fig. 4.2 marks the bandgap wavelength of silicon, while the dashed horizontal line indicates the wavelength at which the silicon layer becomes too lossy to support waveguide modes, which we approximate as where $\alpha h = 0.5$. The vertical line marks where the dashed horizontal line intersects the silica light line, thereby indicating the period that maximises the number of waveguide modes (and resonant absorption peaks) excited by normally incident light in the silicon layer.

Our optimisation of NH arrays begins as in Paper 4.2, by defining an upper bound on the volume fraction of absorber to limit specular reflection, except that we use Maxwell-Garnett theory [163] to calculate the effective index, and restrict the maximum period to limit the number of diffracted orders excited in the surrounding media. A lower bound on the period is derived from Fig. 4.2. What we lack is a bound on the maximum diameter of the inclusions (*i.e.* a lower bound on the volume fraction). We have not been successful in deriving such a quantity because we observe that the net effect of the channelling modes is positive or a negative influence depending on the other parameters of the array, in particular the thickness. Despite this limitation, our analysis defines a refined range of structures that are well suited to SC applications, in good agreement with numerical results. For a more detailed analysis of NH arrays see [7].

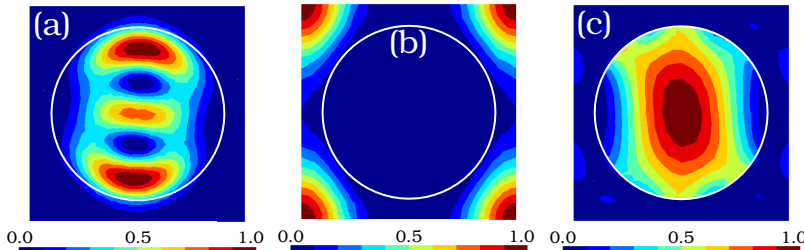


Figure 4.1: Plots of $\|E\|^2$ at $\lambda = 669$ nm for (a) a SiNW array and (b), (c) SiNH arrays with period 500 nm and inclusion diameter of 400 nm. The mode in (a) is a KM; (b) shows a BM that is concentrated in the high index background; and (c) is a channelling mode with energy concentrated in the low index inclusion.

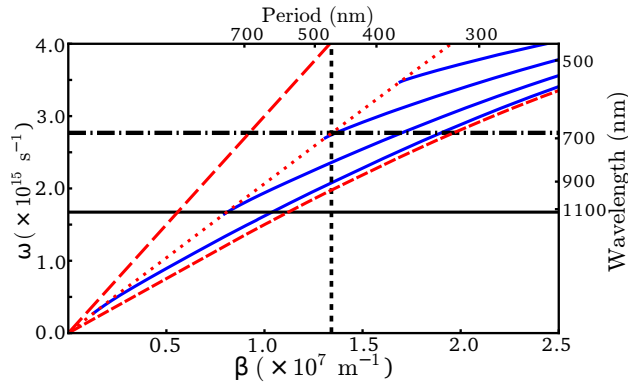


Figure 4.2: Dispersion diagram of 2.33 μm thick silicon slab on a silica substrate. Shown are the air, silica and silicon light lines (with decreasing slope), as well as the curves for the guided slab modes. The lower horizontal line lies at the bandgap wavelength of silicon, while the dashed horizontal line marks the wavelength at which the silicon layer becomes too lossy to support waveguide modes. The horizontal line marks the edge of the solar irradiance peak and the vertical line marks where the horizontal line intersects the silica light line, which indicates the period that excites the greatest number of waveguide modes in the silicon NH array.

4.3.1 Effective Medium Theories for Nanowire and Nanohole Array

In Paper 4.2 we approximated the complex refractive index of lossy NW arrays using different effective index formulations for the real and imaginary parts of the refractive index: the Bruggeman formulation [164] for n' , and volume average theory (VAT) [165, 166] for n'' . This was done because it produced the most accurate approximations to both n' and n'' , and thereby improved the accuracy of our semi-analytic predictions of optimal absorption; the Bruggeman equations overestimate n''/n' , while VAT underestimates n''/n' .

While previous studies of *lossy* nanoporous films have also to mixing two different theories [167, 168], there is a fundamental problem in these approaches: the resultant $n = n' + in''$ does not adhere to the Kramers-Kronig relations and therefore breaks causality [169]. Hopefully these ad hoc procedures can be replaced in the future by valid and accurate effective medium theory for structures containing isolated lossy dielectrics. For the NH case where the lossy dielectric forms a connected background, we found that the Maxwell-Garnett theory [163] produced accurate approximations for both n' and n'' .

Epilogue

We presented our analysis of the interrelated optical effects that occur in NW arrays, from which we constructed a semi-analytic method of optimising the broadband absorption of the arrays. We also compared the physics of NW arrays and NH arrays.

Throughout these studies we assumed that the NWs were identical, and were arranged in a regular square lattice, characterised by a single optimal value for a and d respectively. The relationship between the location of the absorption resonances and the diameter of the NWs hints at the possibility that the integrated absorption could be increased further by including NWs of multiple diameters. The dependence of the reflectance on the effective index of the array (*i.e.* the volume fraction f) meanwhile indicates that variations in NW diameter would not alter the reflectance, as long as f remained fixed. In the next chapter we explore the potential to improve the efficiencies of NW arrays by including multiple diameters in the array, as well as by introducing disorder into the position of the NWs.

Chapter 5

Nanowire Array Photovoltaics II: The Role of Disorder

*The stars of the city night
aren't as numerous,
as they are in the country side,
where they humble us.
There your sight is cast,
further into the vast.*

kooii

The propagation and absorption of waves in disordered media is a rich field of physics that includes the study of light in dielectric structures [170], electrons in semiconductors [171], and cold atoms in laser speckles [172, 173]. Two prominent optical effects are the localisation of light [174, 175], and the emergence of random lasing [176, 177]. For photovoltaic applications the interest in disorder arises from the potential to improve the broadband/wide-angle response of resonant light trapping structures [178]. The most studied disorder nanostructures are NW arrays [2, 179–181] and NH arrays [182–187], with studies generally considering the effect of randomising the arrangement of the inclusions. The physics of these arrays is best investigated numerically because meaningful results pertain to statistical quantities derived from an ensemble of different random realisations. Obtaining these experimentally would be extremely time consuming.

Investigating the optical physics of disorder using simulations is also challenging. By definition, it is impossible to reduce a fully randomised structure to a unit cell (with a small computational domain). This means that the random structure must be approximated by a periodic quasi-random unit cell, the size of which is limited by the computational resources available. Even with modern supercomputers this is limited to an area smaller than tens of periods, far smaller than the macroscopic size of a solar cell. It is also difficult to derive physical insights from absorption values alone.

Our studies focussed on NW arrays, where the limited number of previous studies had shown examples of disordered arrays outperforming their ordered counterparts [179–181]. These studies however had not identified the mechanisms driving this enhancement, and it was unclear how general the findings were; how do the disordered arrays compare to optimised ordered arrays, and how do fully randomised structures compare to arrays where the disorder is managed within some constraints, such as selecting the NW diameters from a Gaussian distribution (as was done by Bozzola *et al.* [188] with 1D structures)?

In Paper 5.1 and Paper 5.2 we addressed the first question, asking respectively: (i) does including NWs with varying diameters improve the absorption, and if so why; (ii) and does arranging the NWs in disordered arrays enhance the absorption, and if so why? To examine these questions in detail we simplified the structures, stripping back disordered systems to the essential features that differentiate them from ordered arrays.

To address question (ii), recent studies have probed the transition between periodic arrays, arrays with correlated disorder, and fully random arrays [184, 186]. These studies have shown that the spectral and angular responses of disordered photonic structures can be tuned through structural correlations to achieve strongly enhanced absorption, however a definition of the ideal type of disorder remains illusive. We partially addressed this issue in Paper 5.1, where we showed that non-uniform arrays that are systematically designed working from physical insights could achieve superior integrated absorption than randomised structures. A comprehensive comparison between the performance of fully optimised ordered structures and fully optimised disordered structures remains an open challenge for the community. Such a study is difficult because the outcomes may be influenced substantially by the bounds placed on the optimisation, and the specific details of the structures (for example the thickness of the absorber).

Note that throughout the papers in this chapter we use the “ultimate efficiency”, as derived in Sect. 2.2.3, as the FoM to assess the performance of the NWs. This only considers thermalisation losses and is directly proportional to the J_{sc} used in Paper 4.2.

Prelude to Papers 5.1 and 5.2

We now present the two papers in which we examine the effects of disorder in NW array SCs:

B. C. P. Sturmberg, K. B. Dossou, L. C. Botten, A. A. Asatryan, C. G. Poulton, R. C. McPhedran and C. M. de Sterke. “Nanowire array photovoltaics: Radial disorder versus design for optimal efficiency”. *Appl. Phys. Lett.* **101**, 173902 (2012)

B. C. P. Sturmberg, K. B. Dossou, L. C. Botten, A. A. Asatryan, C. G. Poulton, R. C. McPhedran and C. M. de Sterke. “Absorption enhancing proximity effects in aperiodic nanowire arrays”. *Opt. Express* **21**, A964–A969 (2013)

Nanowire array photovoltaics: Radial disorder versus design for optimal efficiency

Björn C. P. Sturmberg,^{1,a)} Kokou B. Dossou,² Lindsay C. Botten,² Ara A. Asatryan,² Christopher G. Poulton,² Ross C. McPhedran,¹ and C. Martijn de Sterke¹

¹CUDOS and IPOS, School of Physics, University of Sydney, Sydney 2006, Australia

²CUDOS, School of Mathematical Sciences, University of Technology Sydney, Sydney 2007, Australia

(Received 30 August 2012; accepted 8 October 2012; published online 22 October 2012)

Solar cell designs based on disordered nanostructures tend to have higher efficiencies than structures with uniform absorbers, though the reason is poorly understood. To resolve this, we use a semi-analytic approach to determine the physical mechanism leading to enhanced efficiency in arrays containing nanowires with a variety of radii. We use our findings to systematically design arrays that outperform randomly composed structures. An ultimate efficiency of 23.75% is achieved with an array containing 30% silicon, an increase of almost 10% over a homogeneous film of equal thickness. © 2012 American Institute of Physics. [<http://dx.doi.org/10.1063/1.4761957>]

Strongly absorbing nanostructures are of increasing importance in photovoltaics, as solar cell thicknesses are reduced to minimise costs.^{1–3} Popular approaches to achieve light trapping in these cells include the use of plasmonic nanoparticles and diffraction gratings, as well as nanostructuring the absorbing layer.^{4–6} These subwavelength nanostructures allow for the macroscopic light trapping limit to be exceeded,^{7,8} and unlike random texturing are compatible with the scale of thin-films. Here, we focus on silicon nanowire (NW) arrays as a general form of two-dimensional nanostructured active layer.^{9–12} These structures allow for the decoupling of the charge carrier and absorption lengths and provide a strong enhancement of absorptance compared to homogeneous films of equal thickness.^{13–15}

For NW arrays to achieve optimal photovoltaic efficiency, it is of crucial importance to carefully design their geometric parameters. To this end parameter searches across radius and period have been carried out,^{16,17} concluding that arrays of period greater than 500 nm with approximately 60% fill fractions maximise efficiency. Further studies introduced disorder in NW position, radius, and length, finding that variations in any and all parameters enhance absorption.^{18–20} These studies were however unable to elucidate the physical mechanism, which is responsible for the increased absorption, or the role played by disorder, as they were solely based on purely numerical simulations. Here, we resolve this issue by clarifying the mechanism for enhanced absorption for the particular case of radius disorder. Using a mode-based numerical method in combination with a simple analytic approximation,^{21,22} we study arrays containing increasing numbers of sublattices of different radius NWs. This approach shows that the NWs' absorption resonances can be widely and predictably tuned by varying their radii. Since the absorption resonance depends on NW radius, random arrays with a variety of NW radii have a broader absorption spectrum than arrays with identical NWs, leading to higher photovoltaic efficiency. However, yet higher efficiency is achieved in arrays in which

the NW radii are carefully chosen so as to match the solar irradiance spectrum.

We begin with arrays containing two square sublattices (inset Fig. 1). Our aim is to compare the efficiency when all NWs have the same radius, to the case in which the NW radii $a_{1,2}$ on the two sublattices differ while keeping the fill fraction $f \equiv \pi(a_1^2 + a_2^2)/(2d^2)$ constant at $f = 30\%$. We found this fill fraction to be approximately optimal because it allows for the incorporation of a greater degree of disorder than the 60% found to be optimal for uniform arrays. Our results are compiled in Fig. 1, which shows the ultimate efficiency²³ η for NW radii varying between $50 \leq a_1, a_2 \leq 300$ nm. The distance between adjacent NWs d is varied between $115 \leq d \leq 492$ nm, so as to keep f constant. The silicon NW arrays have a thickness (NW height) of 2330 nm and are placed on a SiO₂ substrate. In this figure, arrays of equal period lie on circular arcs. Though we see substantial variation of η with lattice spacing d , the key observation for the present purpose is that for any given lattice spacing, the introduction of radial variation, i.e., moving off the diagonal $a_2 = a_1$, enhances the efficiency. This indicates that the

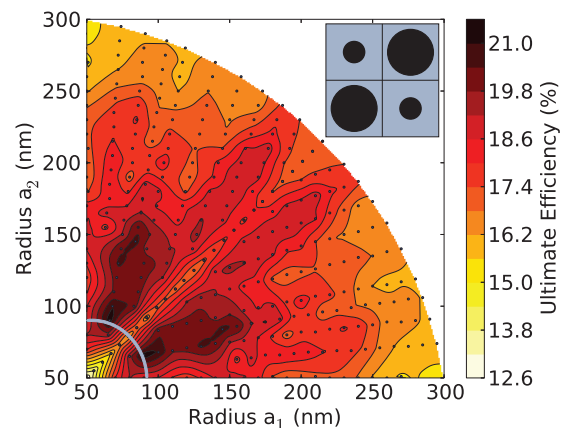


FIG. 1. Ultimate efficiency for 30% silicon NW arrays containing 2 sublattices with differing radius (inset shows a typical unit cell). Dots indicate simulation results and the arc marks arrays with $d = 181$ nm.

^{a)}b.sturmberg@physics.usyd.edu.au.

effect of introducing radial disorder is universal and does not depend on the lattice spacing. We, therefore, henceforth present results for $d=300$ nm only, though we obtained similar results for $d=150$ nm and 600 nm. In the case of $d=181$ nm, which is marked in Fig. 1, η increases from 16.2% ($a_1 = a_2 = 79$ nm) to 21.4% ($a_1 = 90$ nm, $a_2 = 66$ nm).

To analyse this enhancement, we plot the absorption spectra of complex arrays with $d=300$ nm composed of two sublattices: $a_1 = 60$ nm and $a_2 = 70, 105,$ and 125 nm in Figs. 2(a)–2(c), respectively (black curves). Also, plotted are the absorption spectra of each sublattice separately, i.e., where NWs of one radius have been removed such that $a_1 = 60, 70, 105,$ and 125 nm and $a_2 = 0$ nm (coloured broken curves). We observe that the superposition of the individual sublattice's spectra is a good approximation to the complex array's spectrum. This is also the case for the dispersion diagrams (not shown), where the modes of the array containing both radii are the combination of each sublattice's modes in only slightly altered form. Examining the modal field plots at the absorption peaks confirms that at these wavelengths the fields of the complex array are predominantly concentrated within the NWs of the respective sublattice.

Before examining the superposition phenomenon in detail, we summarise the results of our modal analysis of regular periodic NW arrays.²¹ Our central finding was that NW array absorption spectra are determined predominantly by a small set of *key modes* (KMs). These are ideally suited

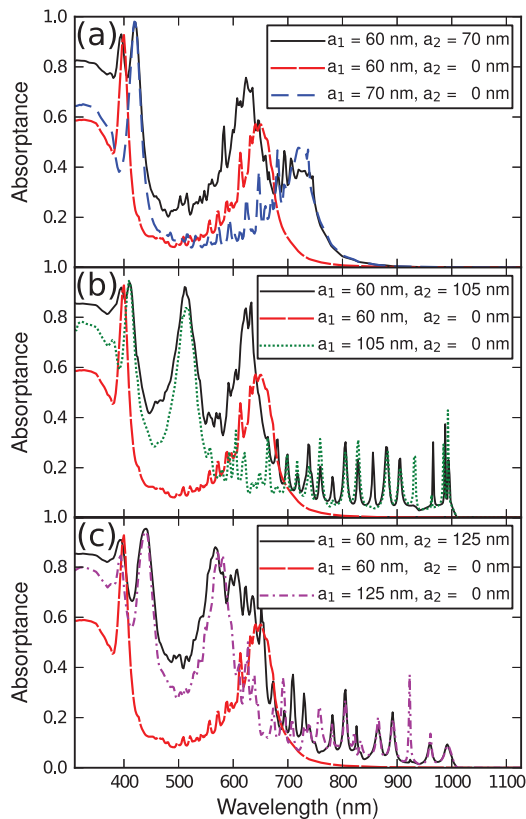


FIG. 2. Absorption spectra of complex arrays containing two radii, where $d=300$ nm, $a_1 = 60$ nm and $a_2 = 70, 105, 125$ nm in (a), (b) and (c) respectively. Broken curves show the spectra of individual sublattices.

to strong absorption due to their confinement of light within the absorbing media, low group velocity, and efficient coupling to the incident fields. They also exhibit Fabry-Pérot resonances. The strong dispersion of NW arrays however means that the KMs are highly absorbing over only a limited wavelength range of tens of nanometers (see Fig. 2). The long-wavelength edge of the absorption peak is given by the KM's cut-off wavelength, where its complex valued propagation constant becomes predominantly (due to weak material loss) real and positive. Using a dipole approximation for the KMs, we found a simple expression for their cut-off wavelength.²¹

Here, we extend the dipole model to describe more complex arrays containing multiple sublattices. This analysis indicates that the cut-offs of the modes of a particular sublattice depend only weakly on the presence of other sublattices. In turn, this implies that the absorption of each of the sublattices is essentially independent of the presence of the other sublattices, consistent with Fig. 2. Such weak sensitivity of modes near cut-off to variations in the surroundings has previously been found in studies of microstructured optical fibres.^{24,25}

Building on this understanding of arrays with two sublattices, we now optimize the absorption of a NW array composed of four sublattices. To do this, we use the dipole model to calculate the KM cut-off wavelengths of a range of NW radii for a set NW spacing. The result (for $d=300$ nm) is shown in Fig. 3, where discontinuities occur when no real solutions exist for the cut-off wavelength. Such a plot is produced in under 10 s, making the dipole model an extremely efficient design tool.

We maximise the ultimate efficiency η by selecting KM cut-offs at roughly 70 nm spacing, corresponding to the characteristic width of an absorption peak, across the 450–750 nm peak in solar irradiance (inset Fig. 3). As a proof-of-concept design, we select $a = 60, 70, 105,$ and 125 nm, such that $f=30\%$. These radii are marked by crosses in Fig. 3. The absorption spectrum of the designed array (D4) is shown in Fig. 4 (black curve) along with the spectra when all but one of the sublattices is removed (coloured broken curves). We see that the design process leads to high absorbance across the target wavelength range and that the absorbance is well approximated by the superposition of the 4 sublattice

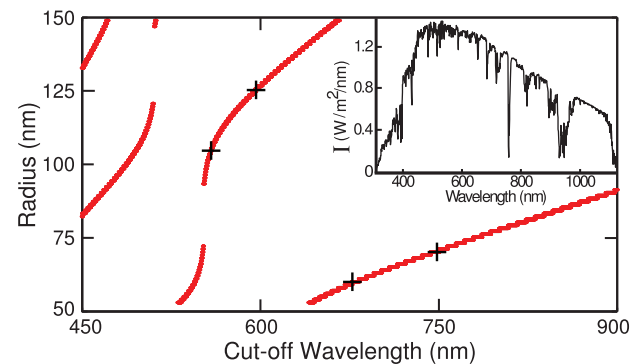


FIG. 3. Key mode cut-off wavelengths for $d=300$ nm as a function of NW radius as calculated by the dipole model. Radii selected are marked by crosses and the inset shows the AM 1.5 solar irradiance spectrum.

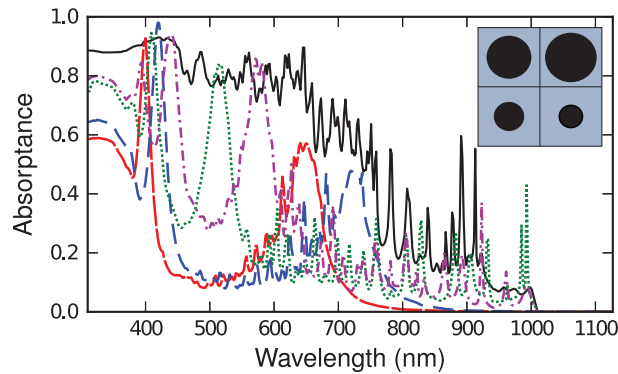


FIG. 4. Absorption spectra of the proof-of-concept designed array D4 (black solid curve) with spectra for each individual sublattice (coloured broken curves).

spectra. Consistent with our earlier argument, permutation of the positions of the 4 NWs does not alter the absorption spectra discernibly. The ultimate efficiency achieved with D4 is $\eta = 22.7\%$, which is a significant increase over a regular array with uniform NWs at equal spacing and fill fraction, for which $\eta = 17.6\%$.

To elucidate the effects of disorder, we simulate arrays with large supercells in which the radii are chosen randomly. Specifically, we simulate an ensemble of 100 arrays with supercells that contain 16 NWs. The spacing between adjacent NWs is again $d = 300$ nm, and the radii are selected from an uniform distribution ranging between 50–150 nm (comparable results were obtained for other distributions). To make a fair comparison, we select arrays for which $29.999\% \leq f \leq 30.001\%$. Figure 5 shows that the efficiency η of the ensemble members (blue bars) varies between 21.4% and 23.6%, with an average of $\eta = 22.6\%$ (dashed line). This is a very significant increase over the comparable regular array ($\eta = 17.6\%$), but is slightly less than the designed array D4 for which $\eta = 22.7\%$ (dotted-dashed line). However, the ensemble members with the highest efficiencies easily outperform the D4 array. These results indicate that high absorption efficiency requires NWs of different radii, each of which absorbs strongly over a relatively narrow wavelength range. This suggests that even

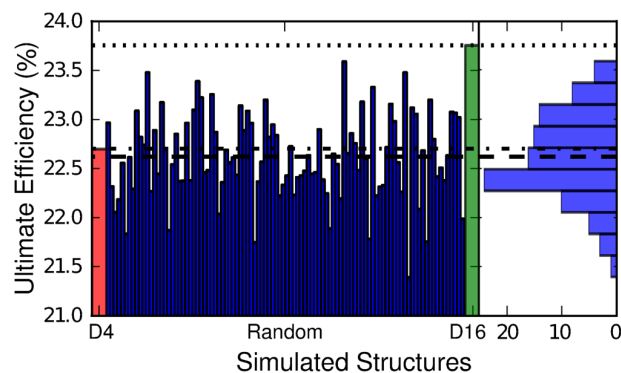


FIG. 5. Ultimate efficiency comparison of 100 disordered arrays (blue), their average (dashed line), the D4 designed array (red bar, dot-dashed line), and the designed D16 array (green bar, dotted line). Occurrence histogram of the random structures is shown on right.

higher efficiencies can be achieved in carefully designed arrays with sufficient freedom to match the solar emission spectrum more completely.

To this end, we design an array containing 16 different radii (D16). As for the 4 radius case, the dipole model is used to select radii for their KM cut-off wavelengths. Taking the D4 design as a starting point, we achieved an efficiency of 23.75% with radii of 60, 64, 66, 70, 72, 76, 78, 89, 91, 93, 95, 100, 116, 120, 125, and 129 nm. This efficiency is more than 2.6 standard deviations above the random arrays' mean, as shown in the histogram on the right of Fig. 5. Assuming Gaussian statistics, the likelihood of achieving an equal or higher efficiency with a random array is, therefore, estimated at less than 0.4%. Indeed in Fig. 5, we see that the D16 array outperforms even the best random structure by about 0.15%.

In summary, we have shown how the inclusion of different radii in NW arrays produces an absorption spectrum that is the superposition of each of the sublattice's spectra. This dramatically enhances the ultimate efficiency of such structures relative to arrays with NWs of uniform radius. When the NW radii are selected at random, the average enhancement over uniform arrays is 5%. Furthermore, when the radii are chosen in an informed manner, the efficiency can be increased further. In total, the efficiency of a NW array with $f = 30\%$ can thereby exceed that of a homogeneous film by almost 10%, rising from $\eta_{\text{HF}} = 13.8\%$ to $\eta_{\text{D16}} = 23.75\%$.

We thank Dr. Kylie Catchpole and Dr. Thomas White for helpful discussions. This work was supported by the Australian Solar Institute, and the Australian Research Council Discovery Grant and Centre of Excellence Schemes. Computation resources were provided by the National Computational Infrastructure, Australia.

¹N. S. Lewis, *Science* **315**, 798–801 (2007).

²L. Tsakalacos, *Mater. Sci. Eng. R* **62**, 175–189 (2008).

³A. J. Nozik, *Nano Lett.* **10**, 2735–2741 (2010).

⁴R. A. Pala, J. S. White, E. Barnard, J. Liu, and M. L. Brongersma, *Adv. Mater.* **21**, 3504–3509 (2009).

⁵H. A. Atwater and A. Polman, *Nature Mater.* **9**, 205–213 (2010).

⁶L. Zeng, P. Bermel, Y. Yi, B. A. Alamariu, K. A. Broderick, J. Liu, C. Hong, X. Duan, J. Joannopoulos, and L. C. Kimerling, *Appl. Phys. Lett.* **93**, 111111 (2008).

⁷Z. Yu, A. Raman, and S. Fan, *Opt. Express* **18**, A366–A380 (2010).

⁸E. D. Kosten, E. L. Warren, and H. A. Atwater, *Opt. Express* **19**, 3316–3331 (2011).

⁹L. Hu and G. Chen, *Nano Lett.* **7**, 3249–3252 (2007).

¹⁰E. C. Garnett and P. Yang, *Nano Lett.* **10**, 1082–1087 (2010).

¹¹M. D. Kelzenberg, S. W. Boettcher, J. A. Petykiewicz, D. B. Turner-Evans, M. C. Putnam, E. L. Warren, J. M. Spurgeon, R. M. Briggs, N. S. Lewis, and H. A. Atwater, *Nature Mater.* **9**, 239–244 (2010).

¹²O. Gunawan, K. Wang, B. Fallahazad, Y. Zhang, E. Tutuc, and S. Guha, *Prog. Photovolt. Res. Appl.* **19**, 307–312 (2010).

¹³B. M. Kayes, H. A. Atwater, and N. S. Lewis, *J. Appl. Phys.* **97**, 114302 (2005).

¹⁴E. C. Garnett and P. Yang, *J. Am. Chem. Soc.* **130**, 9224–9225 (2008).

¹⁵K. R. Catchpole, S. Mookapati, and F. J. Beck, *J. Appl. Phys.* **109**, 084519 (2011).

¹⁶C. Lin and M. L. Povinelli, *Opt. Express* **17**, 19371–19381 (2009).

¹⁷J. Li, H. Yu, M. Wong, X. Li, and G. Zhang, *Appl. Phys. Lett.* **95**, 243113 (2009).

¹⁸H. Bao and X. Ruan, *Opt. Lett.* **35**, 3378–3380 (2010).

¹⁹Q. G. Du, C. H. Kam, H. V. Demir, H. Y. Yu, and X. W. Sun, *Opt. Lett.* **36**, 1884–1886 (2011).

²⁰C. Lin and M. L. Povinelli, *Opt. Express* **19**, A1148–A1154 (2011).

- ²¹B. C. P. Sturmborg, K. B. Dossou, L. C. Botten, A. A. Asatryan, C. G. Poulton, C. M. de Sterke, and R. C. McPhedran, *Opt. Express* **19**, A1067–A1081 (2011).
- ²²K. B. Dossou, L. C. Botten, A. A. Asatryan, B. C. P. Sturmborg, M. A. Byrne, C. G. Poulton, R. C. McPhedran, and C. M. de Sterke, *J. Opt. Soc. Am. A* **29**, 817–831 (2012).
- ²³W. Shockley and H. J. Queisser, *J. Appl. Phys.* **32**, 510–519 (1961).
- ²⁴T. P. White, R. C. McPhedran, C. M. de Sterke, N. M. Litchinitser, and B. J. Eggleton, *Opt. Lett.* **27**, 1977–1979 (2002).
- ²⁵N. M. Litchinitser, S. Dunn, B. J. Eggleton, B. Usner, T. P. White, R. C. McPhedran, and C. M. de Sterke, *Optical Fiber Communications Conference, 2003. OFC 2003* (2003), pp. 493–494.

Absorption enhancing proximity effects in aperiodic nanowire arrays

Björn C. P. Sturmberg,^{1*} Kokou B. Dossou,² Lindsay C. Botten,² Ara A. Asatryan,² Christopher G. Poulton,² Ross C. McPhedran,¹ and C. Martijn de Sterke¹

¹ CUDOS and IPOS, School of Physics, University of Sydney, 2006, Australia

² CUDOS, School of Mathematical Sciences, UTS, Sydney, 2007, Australia

*b.sturmberg@physics.usyd.edu.au

Abstract: Aperiodic Nanowire (NW) arrays have higher absorption than equivalent periodic arrays, making them of interest for photovoltaic applications. An inevitable property of aperiodic arrays is the clustering of some NWs into closer proximity than in the equivalent periodic array. We focus on the modes of such clusters and show that the reduced symmetry associated with cluster formation allows external coupling into modes which are dark in periodic arrays, thus increasing absorption. To exploit such modes fully, arrays must include tightly clustered NWs that are unlikely to arise from fabrication variations but must be created intentionally.

© 2013 Optical Society of America

OCIS codes: (350.6050) Solar energy; (310.6628) Subwavelength structures, nanostructures; (040.5350) Photovoltaic; (050.0050) Diffraction and gratings; (350.4238) Nanophotonics and photonic crystals.

References and links

1. K. R. Catchpole, "Nanostructures in photovoltaics," *Phil. Trans. R. Soc. A* **364**, 3493–503 (2006).
2. L. Tsakalakos, "Nanostructures for photovoltaics," *Mater. Sci. Eng. R* **62**, 175–189 (2008).
3. O. L. Muskens, J. G. Rivas, R. E. Algra, E. P. A. M. Bakkers, and A. Lagendijk, "Design of Light Scattering in Nanowire Materials for Photovoltaic Applications," *Nano Lett.* **8**, 2–6 (2008).
4. S.-F. Leung, M. Yu, Q. Lin, K. Kwon, K.-L. Ching, L. Gu, K. Yu, and Z. Fan, "Efficient photon capturing with ordered three-dimensional nanowell arrays," *Nano Lett.* **12**, 3682–3689 (2012).
5. H. A. Atwater and A. Polman, "Plasmonics for improved photovoltaic devices," *Nat. Mater.* **9**, 205–213 (2010).
6. C. Lin and M. L. Povinelli, "Optical absorption enhancement in silicon nanowire arrays with a large lattice constant for photovoltaic applications," *Opt. Express* **17**, 19371–19381 (2009).
7. B. C. P. Sturmberg, K. B. Dossou, L. C. Botten, A. A. Asatryan, C. G. Poulton, C. M. de Sterke, and R. C. McPhedran, "Modal analysis of enhanced absorption in silicon nanowire arrays," *Opt. Express* **19**, A1067–A1081 (2011).
8. K. Seo, Y. J. Yu, P. Duane, W. Zhu, H. Park, M. Wober, and K. B. Crozier, "Si Microwire Solar Cells: Improved Efficiency with a Conformal SiO₂ Layer," *Nano* **7**, 5539–5545 (2013).
9. D. B. Turner-Evans, C. T. Chen, H. Emmer, W. E. McMahon, and H. A. Atwater, "Optoelectronic analysis of multijunction wire array solar cells," *J. Appl. Phys.* **114**, 014501 (2013).
10. J. Wallentin, N. Anttu, D. Asoli, M. Huffman, I. Aberg, M. H. Magnusson, G. Siefert, P. Fuss-Kailuweit, F. Dimroth, B. Witzigmann, H. Q. Xu, L. Samuelson, K. Deppert, and M. T. Borgström, "InP Nanowire Array Solar Cells Achieving 13.8% Efficiency by Exceeding the Ray Optics Limit," *Science* **339**, 1057–1060 (2013).
11. E. C. Garnett, M. L. Brongersma, Y. Cui, and M. D. McGehee, "Nanowire Solar Cells," *Annu. Rev. Mater. Res.* **41**, 269–295 (2011).
12. M.-P. Lu, M.-Y. Lu, and L.-J. Chen, "p-Type ZnO nanowires: From synthesis to nanoenergy," *Nano Energy* **1**, 247–258 (2012).
13. O. Gunawan, K. Wang, B. Fallahazad, Y. Zhang, E. Tutuc, and S. Guha, "High performance wire-array silicon solar cells," *Prog. Photovolt. Res. Appl.* **19**, 307–312 (2010).

14. H. Bao and X. Ruan, "Optical absorption enhancement in disordered vertical silicon nanowire arrays for photovoltaic applications," *Opt. Lett.* **35**, 3378–3380 (2010).
 15. Q. G. Du, C. H. Kam, H. V. Demir, H. Y. Yu, and X. W. Sun, "Broadband absorption enhancement in randomly positioned silicon nanowire arrays for solar cell applications," *Opt. Lett.* **36**, 1884–1886 (2011).
 16. C. Lin and M. L. Povinelli, "Optimal design of aperiodic, vertical silicon nanowire structures for photovoltaics," *Opt. Express* **19**, A1148–A1154 (2011).
 17. K. B. Dossou, L. C. Botten, A. A. Asatryan, B. C. P. Sturmberg, M. A. Byrne, C. G. Poulton, R. C. McPhedran, and C. M. de Sterke, "Modal formulation for diffraction by absorbing photonic crystal slabs," *J. Opt. Soc. Am. A* **29**, 817–831 (2012).
 18. W. Shockley and H. J. Queisser, "Detailed balance Limit of Efficiency of p-n Junction Solar Cells," *J. Appl. Phys.* **32**, 510–519 (1961).
 19. B. C. P. Sturmberg, K. B. Dossou, L. C. Botten, A. A. Asatryan, C. G. Poulton, R. C. McPhedran, and C. Martijn de Sterke, "Nanowire array photovoltaics: Radial disorder versus design for optimal efficiency," *Appl. Phys. Lett.* **101**, 173902 (2012).
-

1. Introduction

Well-designed nanostructures are known to strongly enhance the absorption of photovoltaic devices [1–5], thereby allowing for the reduction of the active layer thickness to only a few micrometers. This significantly reduces costs, as less material is used and the material quality requirements are eased by shorter charge extraction distances. Nanowire (NW) arrays are a prominent class of nanostructures that build on these advantages by incorporating radial p-n junctions, which further reduce the charge carrier diffusion length requirements. Periodic NW arrays have been studied theoretically [6, 7] and numerous cost-effective fabrication methods are under development [8–13].

It is known that the absorption of NW arrays is increased when they are arranged in aperiodic lattices, which may occur through random fabrication variations or may be designed on purpose [14–16]. Studying such aperiodic arrays is difficult due to the large parameter space and because of the broadband nature of the photovoltaic conversion process. The origin of the absorption enhancement of aperiodic arrays has therefore remained unclear.

Here we avoid the difficulties of large parameter spaces by focussing on a common underlying property of aperiodic arrays: the localised clustering of NWs with reduced gaps between adjacent NWs. This approach provides physical insights that apply to all aperiodic arrays; disordered or designed. The importance of clustered NWs was highlighted by Lin and Povinelli [16], who showed strong field concentrations within NW clusters at peak absorption wavelengths.

2. Absorption Enhancement

We begin our study with clusters of 4 NWs of radius a , as shown in the inset of Fig. 1. The NWs are initially periodically spaced in a square lattice with period $d/2$, in a unit cell of width d , before being gradually shifted towards the cell's centre. As soon as the NWs are moved, the periodicity of the structure becomes d . We measure the *clustering level* l , as a fraction of the maximum distance the NWs can be moved before touching at $t = (d/4 - a)$. The *gap* between the NW surfaces is therefore $g = (1 - l) \times (d/2 - 2a)$ (see Fig. 1 inset). Throughout the clustering process the volume fraction of the array is constant, $f = \pi a^2 / (d/2)^2$. Our simulations are carried out using a combination of the Finite Element Method (FEM) and the scattering matrix method as described earlier [17]. This calculation in the Bloch mode basis is numerically efficient and provides convenient access to physical quantities that are inaccessible in other methods, thereby allowing for greater insights. Throughout this work the absorption spectra are calculated for normally incidence radiation from the short wavelength edge of the solar spectrum at 310 nm to the band-edge of silicon at 1127 nm.

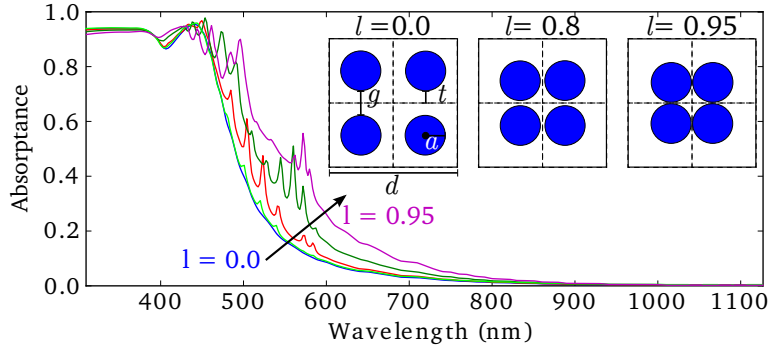


Fig. 1. Absorption spectra of NW arrays with $a = 31$ nm, $f = 30\%$, with increasing clustering $l = 0.0, 0.2, 0.5, 0.8, 0.95$. Inset shows cluster geometry where a is the NW radius, d is the unit cell dimension, g is the gap size between NW surfaces, and t is the distance a NW can be moved before touching its neighbour.

In Fig. 1 we show the absorption spectra for NW arrays with radius $a = 31$ nm in a unit cell of $d = 200$ nm ($f = 30\%$ silicon) as they are clustered with increasing l from 0.0 to 0.95. Note that the absorption increases with increasing clustering level of the arrays, particularly across the $\lambda = 500 - 600$ nm range. The parameters of Fig. 1 are chosen to best illustrate the effect of clustering with clear spectra, rather than to achieve high photovoltaic efficiencies. Nonetheless, the increase in total absorption is significant. At $\lambda = 550$ nm the absorbance increases from 0.16 in the unclustered array to 0.46 at $l = 0.95$. The numerous sharp absorption peaks in this range indicate that resonant modes are excited in the clusters that are not present in the equivalent unclustered array (blue curve).

We quantify the efficiency enhancement produced through the ultimate efficiency, η [18], which weights the absorption spectrum by the solar spectrum and by the maximum fraction of energy which can be harvested. In Fig. 2 we show the ultimate efficiency enhancement $\delta\eta = \eta_{\text{clustered}} - \eta_{\text{unclustered}}$ for two intersecting slices through the clustered array parameter-space of a, f, l . Figure 2(a) shows $\delta\eta$ for arrays with fixed radius arranged with a range of f , while in Fig. 3(b) the radii are varied and $f = 50\%$ throughout. This volume fraction produces near-optimal efficiencies when large radii are used, as in Fig. 2(b), and is consistent with multiple studies [6, 16, 19]. When $a = 239$ and $l = 0.95$ in Fig. 2(b) the efficiency is $\eta = 22.54\%$.

In Figs. 2(a),(b) the efficiency monotonically increases with decreasing gap size, moving right to left, but substantial enhancements only occur once the NWs are tightly clustered, typically to a gap distance of less than 20% of the NW radius. Calculations with different volume fractions and radii, not shown here, show that these observations are true in general; accordingly all NW arrays benefit from increased efficiency with increased clustering, while substantial enhancements are only achieved for small gaps. The enhancement in the ultimate efficiency η can be almost 5% for the parameters in Fig. 2, a relative improvement of 85%.

3. Excitation of cluster modes

To understand the increased absorption we study the modal properties of periodic and clustered arrays. Though both support a multitude of Bloch modes, we need only consider those modes that couple to incident plane waves. We refer to such modes as bright modes, in contrast to dark modes, which cannot couple to external radiation at normal incidence. In our scattering matrix method the coupling coefficient between two modes (plane waves or Bloch modes) is derived from the overlap integral of the modes fields across the unit cell (see Eqs. (64, 65) of [17]). From

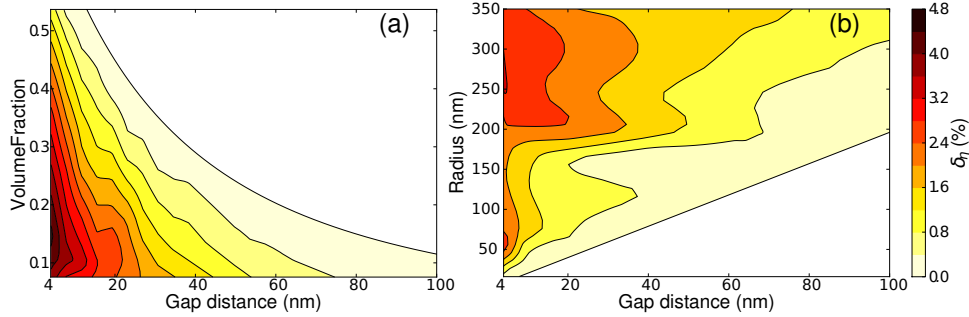


Fig. 2. Ultimate efficiency increase $\delta\eta$ versus the gap between NW surfaces. (a) Arrays of different volume fractions with fixed NW radius $a = 31$ nm. (b) Arrays with different NW radii but fixed volume fraction, $f = 50\%$.

this we calculate the element of the transmission matrix for these modes as in Eq. (69) in [17], giving the coupling coefficient. Calculating the coupling at the peak absorption wavelength of 550 nm, we find that unclustered arrays support a single bright mode, while clustered arrays have a second such mode.

To explain the existence of the second bright mode we show Bloch mode electric field vectors in Fig. 3(a)–(d). Here both colour and length indicate the field strength at the arrows' origin. For the unclustered array we show the fundamental bright mode in Fig. 3(a) and a dark mode in Fig. 3(b). The bright mode has all strong field components directed from left to right, while the dark mode has field components of equal strength oriented in opposite directions. The overlap integral with a plane wave therefore vanishes for the dark mode of Fig. 3(b). In contrast it is non-zero for the bright mode of Fig. 3(a) for horizontally polarised incoming light. Vertically polarized plane waves couple to a vertically oriented mode degenerate with that in Fig. 3(a).

Once the NWs are clustered, the symmetry of the dark mode of Fig. 3(b) is lowered as the fields between the cylinders strengthen, and those on the outside of the cluster weaken. As shown in Figs. 3(c) and (d), this results in an electric field that is predominantly oriented from left to right, allowing for coupling to an incoming field. The asymmetry strengthens with increasing clustering, leading to stronger coupling. This is shown in Fig. 4 where the coupling coefficient of the incident plane wave to the fundamental mode at $\lambda = 550$ nm decreases with decreasing gap (blue) as the coupling into the second bright mode increases (green).

To be highly absorbing a Bloch mode must not only couple to the incident field but also concentrate its energy within the absorbing material [7]. In Figs. 3(e)–(h) we show the energy concentration $\text{Re}(\epsilon)|E|^2$ of modes at $\lambda = 550$ nm. At this wavelength, the bright mode of the unclustered array in Fig. 3(e) has little energy within the silicon, resulting in the low absorption of this structure (see Fig. 1). In contrast, the bright mode of the clustered arrays has significant energy in the silicon, as shown in Fig. 3(f) and (g) for $l = 0.5$ and 0.8 , respectively. When combined with strong coupling this produces the enhanced absorption of Fig. 1. Consistent with this, the red curve in Fig. 4 shows that the clusters' ultimate efficiency improves as the coupling into the second bright mode increases. Though the coupling is shown for a single wavelength, this is a broadband effect which occurs for all wavelengths below the bright mode's cut-off at $\lambda = 600$ nm. The absorption of this mode, which is associated with all absorption peaks in Fig. 1, is enhanced by its low group velocity and strong Fabry-Pérot resonances between the top and bottom interfaces. Both of these effects are characteristics of the *Key Modes* (KMs) of periodic NW arrays [7]. We therefore refer to the bright mode of the cluster as a *Clustered Key Mode* (CKM). In Fig. 3(h) we show how the energy concentration of the CKM is similar to the

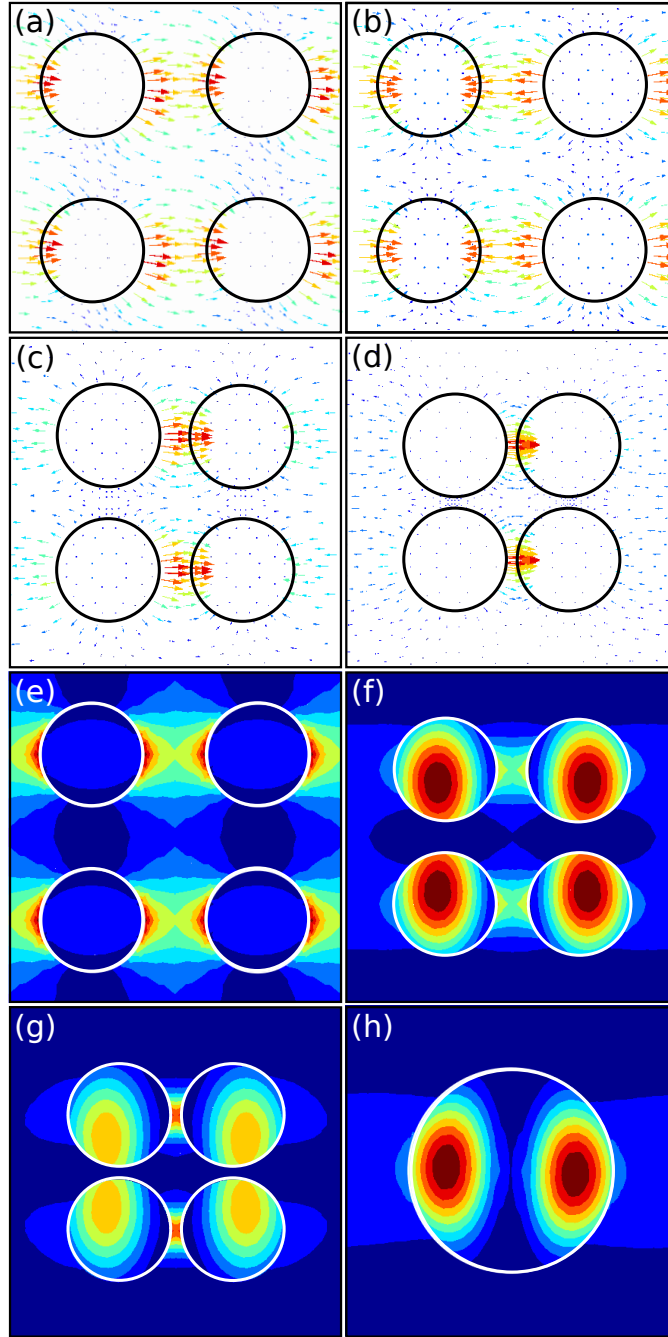


Fig. 3. (a)–(d) Electric field vector of Bloch modes where colour and length indicate the field strength at the arrows' origin. (a) Fundamental mode of the unclustered array; (b) CKM of unclustered array; (c) CKM with $l = 0.5$; (d) CKM with $l = 0.8$. (e)–(h) Bloch mode energy $\text{Re}(\epsilon)|E|^2$ where red and blue indicates high and low energy density, respectively. (e) Fundamental mode of the unclustered array; (f) CKM with $l = 0.5$; (g) CKM with $l = 0.8$; (h) KM of an array with twice the radius, *i.e.*, $a = 62$ nm. For all figures $\lambda = 550$ nm, $d = 200$ nm and in (a)–(g) $a = 31$ nm.

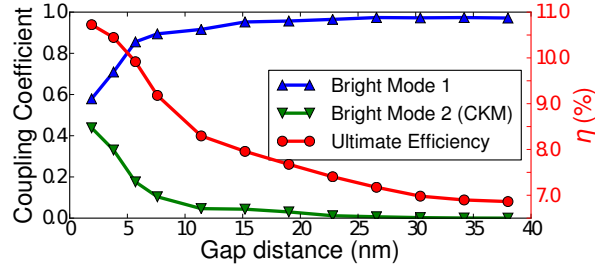


Fig. 4. Coupling coefficient (left axis) of the incident plane wave to the fundamental mode (blue upward triangles) and the second bright mode (green downward triangles) versus gap between NW surfaces. The ultimate efficiency η of the clusters is also shown (red circles and right axis).

KM of a periodic array with doubled radius NWs ($a = 62$ nm).

4. Discussion and conclusion

We have concentrated on one consequence of aperiodicity, namely that, compared to periodic arrays of the same density, it inevitably leads to the clustering of NWs. The associated symmetry lowering leads to the coupling of plane waves into a previous inaccessible mode, thereby significantly increasing the array's absorption. When the clustering is quite pronounced these Clustered Key Modes are similar to the strongly absorbing Key Modes that exist in periodic arrays of large radius NWs. Though we concentrated on the clustering of 4 NWs, we also studied clusters of 2, 3, and 5 NWs and came to similar conclusions. This suggests that our results are general and not specific to the geometry studied here.

The absorption enhancement mechanism identified here differs from that in structures consisting of NWs of different radii. There, the diversity of the radii produces a wide spectrum of modal absorption resonances across the solar spectrum, hence increasing the absorption efficiency [19]. Here, in contrast, the lowering of the translational symmetry through the clustered NW arrangement produces bright modes which are inaccessible in unclustered arrays.

Our results in Fig. 2, and others not shown here, show that, compared to the unclustered periodic case with period $d/2$, clustering always increases absorption. The degree to which it does so depends not only on the cluster parameters but also on the array's global properties such as the value of d . It is therefore difficult to draw specific quantitative conclusions. However, we have observed that the clustering only significantly enhances the absorption when the NW are brought close, typically such that the gap between their surfaces is approximately 20% of the NW radius. This is consistent with Fig. 4(b) of Lin and Povinelli [16]. As a consequence of this, the random variations in NW positioning that arise naturally during fabrication of periodic arrays are unlikely to be sufficient to exploit the efficiency enhancement potential of aperiodic arrays. Rather, the potential of aperiodic arrays may only be harnessed by purpose fabrication of aperiodic arrays with closely clustered NWs.

Acknowledgments

We acknowledge helpful discussions with Dr Kylie Catchpole and Dr Thomas White. This work was supported by the Australian Renewable Energy Agency, and by the Australian Research Council (ARC) Center of Excellence for Ultrahigh bandwidth Devices for Optical Systems (Project CE110001018) and by an ARC Discovery Grant. Computation resources were provided by the National Computational Infrastructure, Australia.

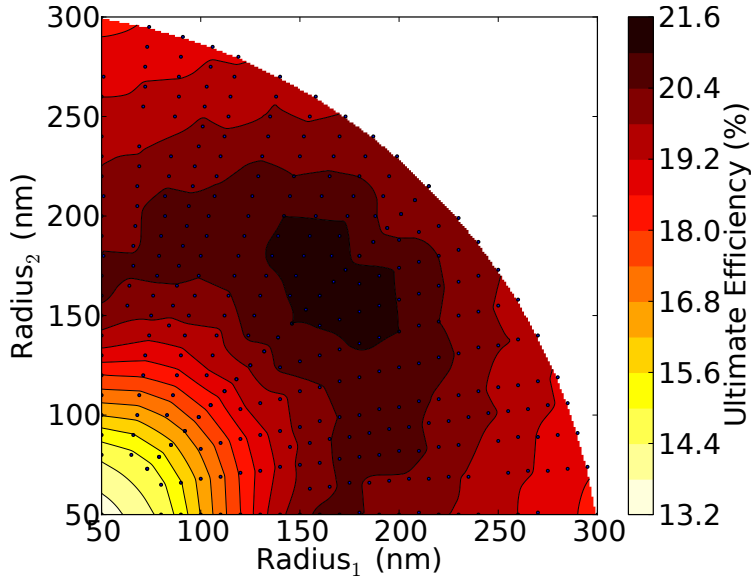


Figure 5.1: Ultimate efficiency for a $h = 2.33 \mu\text{m}$ thick silicon NH array containing two sublattices with differing radius, where in all arrays the air inclusions make up $f_{\text{inc}} = 30\%$ of the structure. The arrays are equivalent to Fig. 1 in Paper 5.1, but with the air background replaced by silicon and vice versa for the inclusions.

5.3 Comparison with Disordered Nanohole Arrays

We now present some unpublished results from our study of disorder in NH arrays, in particular the effect of multiple diameter inclusions. Figure 5.1 is the direct counterpart to Fig. 1 in Paper 5.1 for NH arrays; the diameters of the inclusions is varied in such a way that the arrays have an inclusion volume fraction of $f_{\text{inc}} = 0.3$ air in a silicon background. The contrast between the figures is striking: for NW arrays the optima occur off the diagonal (where the array includes NWs with differing diameters), while for NH arrays the optimum lies on the diagonal (where all inclusions are identical).

Arrays with common period lie on circular arcs in Fig. 5.1, which are closely followed by the contour lines of equal efficiency η , particularly when the period is small (the bottom left of the figure). This indicates that the period of the NH arrays is their most important parameter, which is because the period dictates the reciprocal lattice vector of the arrays, \mathbf{G} , which in turn determines what guided mode propagation constants can be excited by the incident plane wave. The peak in Fig. 5.1 occurs when the period of the NH arrays is such that the incident light is phase matched to the guided mode. There is exactly one peak in Fig. 5.1 because all the arrays have the same thickness and approximately the same n_{eff} (since f is constant) and therefore support the same guided modes resonances. The maximum efficiency occurs on the diagonal in Fig. 5.1 because the addition of different diameter inclusions increases the spectral range over which the arrays support channelling modes, which increase transmission losses. In the NW case the number of inclusion-bound modes was also increased when multiple diameters were included, but in that case these modes contributed strongly to the absorption.

We note that a very similar study to Paper 5.2 for NH arrays was recently published by Wu *et al.* [189]. We believe that the absorption enhancement observed in their study is due to the increased period of the arrays when the inclusions are brought into close proximity, which, as shown in Fig. 5.1 is the key driver of improved absorption.

Epilogue

The papers presented in this chapter complete our investigations into the optical properties of NW and NH arrays. We demonstrated how physical insights revealed the optimal radius, period and volume fraction of NW arrays for maximising their integrated solar absorption, and how a similar approach restricted the range of optimal NH geometries. We also showed how including multiple radii into the array increased the bandwidth of enhanced absorption because the resonant wavelength of the NW is directly linked to its radius. Lastly we saw how bunching NWs together, as necessarily occurs in aperiodic arrays, can improve the absorption of NW arrays in the cases where the NWs are sub-optimally thin.

Chapter 6

Fano Resonances of Dielectric Gratings

*Turn your face to the sun
and the shadows fall behind you.*

Maori Proverb

To this point, we have focussed on investigating nanostructures that can enhance the absorption of thin films across the solar spectrum, in particular studying nanowire and nanohole arrays. In the remainder of the thesis we shift our attention to nanophotonic structures that have a broad range of applications, of which solar cells are but one.

This chapter is motivated by the spectrum-splitting multi-junction cells, discussed in Sect. 2.4.2, where nanophotonic structures direct discrete slices of the solar spectrum to different (single junction) SCs. The challenge is to have these filters separate the wavelengths with high contrast (with little light being directed to the non-targeted subcells), and for the filters to introduce as little parasitic absorption as possible. Although we focus here on the solar applications of wavelength selective filters, these structures have a wide variety of applications, as outlined in Paper 6.2. Our analysis concerns the symmetries of Fano resonances in thin, periodic dielectric media, which are fundamental to many optical structures. (We do not here enter into describing the taxonomy of grating anomalies and resonances, for which there is an excellent recent review by Maystre [190]).

6.1 Solar Applications of Wavelength Selective Filters

Before presenting our study of the Fano resonances of dielectric diffraction gratings, and describing how these can be tuned to create wavelength selective filters, we review the recent developments that are driving interest in mechanically decoupled multi-junction cells. In particular, we review two types of SCs: silicon-based tandems; and ultra-high efficiency spectrum-splitting multi-junctions.

6.1.1 Silicon-based Tandems

As discussed in Sect. 2, silicon SCs dominate the PV market with very well established industrial processes and supply chains, which makes it difficult for emerging technologies to compete. There has recently emerged an alternative strategy: to literally “build upon” cheap and moderate-efficiency Si SCs by adding a higher bandgap SC, thereby forming a low-cost high-efficiency ($\eta > 30\%$) tandem solar cell [105, 191–197]. That silicon is well suited to the creation of tandem SCs has been well known for over 30 years; Vos *et al.* calculated the theoretical efficiency limit of Si-based tandem SCs to be 42% [198], close to the 45%

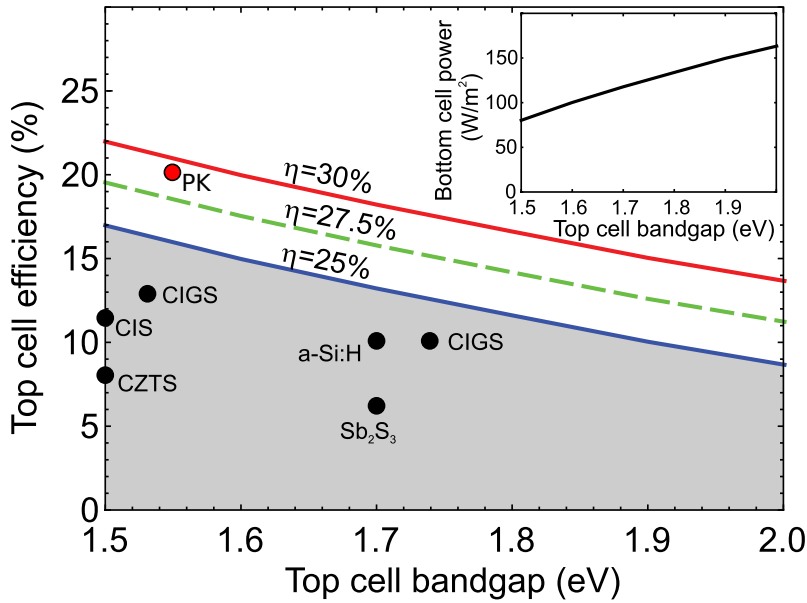


Figure 6.1: Contour plot of the efficiency of a tandem SC with an $\eta = 24.4\%$ Si SC bottom cell, as a function of the bandgap energy and efficiency of the other cell [105]. The black dots indicate the maximum achieved efficiencies of SCs made of various materials, where we have added the most recent record efficiency for a perovskite SC in red.

limit when arbitrary bandgaps are included. Such high efficiencies have however not been achievable with existing SC technologies.

In 2014 White *et al.* developed a sophisticated model of Si-based tandems that included the optical absorption, electronic bandgap, carrier transport properties and luminescence efficiency of the high-bandgap material [105]. They considered the four-terminal configuration where the current is extracted from each SC independently, and based the properties of the Si SC on a $\eta = 24.4\%$ PERL cell [199]. Figure 6.1 shows the efficiency they calculated for Si-based tandem SCs as a function of the bandgap energy and efficiency of the non-silicon cell [105]. The blue, dashed green, and red curves indicate the bandgap and efficiency combinations required for the tandem SC to have an efficiency of 25%, 27.5% and 30% respectively. The black dots mark the current record efficiencies of potential material classes, all of which fail to produce tandems with $\eta > 25\%$, *i.e.*, they are less efficient than current Si cells.

This situation changed drastically recently, with the rapid emergence of mixed organic-inorganic halide perovskite (PK) SCs. The current confirmed efficiency record for a PK SC is 20.1%, which was achieved by the group of Seok [200]. This result, when added to Fig. 6.1 (red dot) indicates that PK-Si tandem SCs could theoretically achieve efficiencies close to 30%. Furthermore, PK SCs are still undergoing rapid advancements, suggesting that their efficiency will likely continue to improve in coming years, taking the efficiency of the PK-Si tandem SCs with them. In the following sections we focus on perovskites SCs and their applicability to Si-based tandems.

Perovskite Solar Cells

Some of the appealing properties of perovskites have been known for over 20 years, namely: strong absorption, a direct-bandgap of 1.55 eV ($\lambda = 800$ nm), and carrier diffusion lengths of 100 – 1000 nm. It has however only been in last five years that “the extraordinary potential of hybrid perovskites in photovoltaic applications” has been realised [201], after efficiencies of 3.8% [202] and 6.5% [203] were reported in 2009 and 2011 respectively, by researchers working with liquid-electrolyte-based dye-sensitized SCs.

Since then, the focus has shifted to solid-state PK SCs, where the rise in efficiency has

been “meteoric” [201], proceeding at an “unprecedentedly rapid” rate [66]; in November 2014 (only 7 months after achieving $\eta = 18\%$), “perovskites joined the selected cohort of materials demonstrating a certified $\eta > 20\%$ ” [204]. The observation that the highest performing devices have been achieved, using a broad range of different fabrication approaches and device concepts, suggests that their performance is still far from fully optimized [66].

The two most fundamental challenges for PK SCs are: the use of toxic elements, in particular, lead, which raises issues during device fabrication, deployment and disposal; and cell stability, since current cells generally undergo rapid degradation on exposure to moisture and ultraviolet radiation [204]. Solving these problems is the focus of intense research, which aims to find modified compounds that do not contain lead [205] and which are more stable [206]. The concerns about the hysteresis that occurs between forward-bias and backward-bias measurements of the IV curves of perovskite SCs seems to have been resolved, being explained by ion migration [207]. For recent reviews of this rapidly evolving field see [66, 201, 204, 208, 209].

Perovskite on Silicon Tandems

Perovskites are very well suited to the creation of high-efficiency Si-based tandems: their bandgap energy is in the appropriate range as shown in Fig. 6.1; they are more absorbing than III-V semiconductors with equivalent bandgaps, and have no sub-bandgap parasitic absorption [191]; and their external radiative efficiency (the fraction of recombinations whose photons are emitted from the SC) is well matched to Si: 0.02 - 0.1 and ~ 0.06 respectively [210]. Their low non-radiative recombination rates, compared to other thin-film poly-crystalline semiconductors, give rise to experimental V_{oc} values close to their effective bandgap potential, which provides a substantial efficiency advantage. Furthermore, PK SCs can be fabricated using low-temperature approaches, which enhance the prospects of PK as components of economical tandem SCs.

Perovskite on silicon tandem SCs are being developed using monolithically integrated (two-terminal) and mechanically decoupled (four-terminal) configurations. The decoupled configurations (either four-terminal stacked cells or physically separated spectrum splitting configuration) avoid many of the optical and electronic challenges involved in integrating cells [204].

Theoretical studies have shown that monolithic devices benefit from the inclusion of an intermediate reflector located between the subcells, thereby increasing the current from the top cell [192, 193]. When including idealised light trapping and a wavelength-dependent reflector Löper *et al.* calculated idealised efficiencies of 35.67% for a two-terminal monolithically integrated PK-Si SC, and 37.17% for a four-terminal mechanically stacked cell [193].

A major challenge for vertically stacked multi-junctions is the creation of semi-transparent conducting contacts for the back of the top cell, which the McGhee group is addressing with the use of networks of silver nanowire electrodes [194]. Experimentally, the group of McGhee have reported efficiencies of 13.7% for two-terminal PK-Si SCs [211] (as well as $\eta = 18.7\%$ for a mechanically stacked four-terminal tandem SC made of a PK and CIGS [194]).

In contrast, Uzu *et al.* have achieved efficiencies of 28% with the spectrum-splitting configuration, using a PK SC and a Si heterojunction SC, with efficiencies of $\eta = 15.3\%$ and $\eta = 25.2\%$ respectively [195]. Although many different kinds of spectrum splitting techniques have been developed [212], the standard device today is a Bragg stack [195, 213]. These are expensive because they are fabricated by sputter deposition to achieve nanometer precision on the thickness of the layers. The dielectric gratings studied in this chapter are potentially a cheaper spectrum splitting device.

The concerted effort to develop Si-based tandems has only been under way for a few years, but already has revealed some promising directions, particularly the development of PK-Si tandems which potentially could be produced economically with efficiencies of over 30%. Continued research is required to realise this potential, with immediate aims being focussed on improving the efficiency and stability of PK SCs and on developing either transparent back contacts or low-loss spectrum splitting geometries.

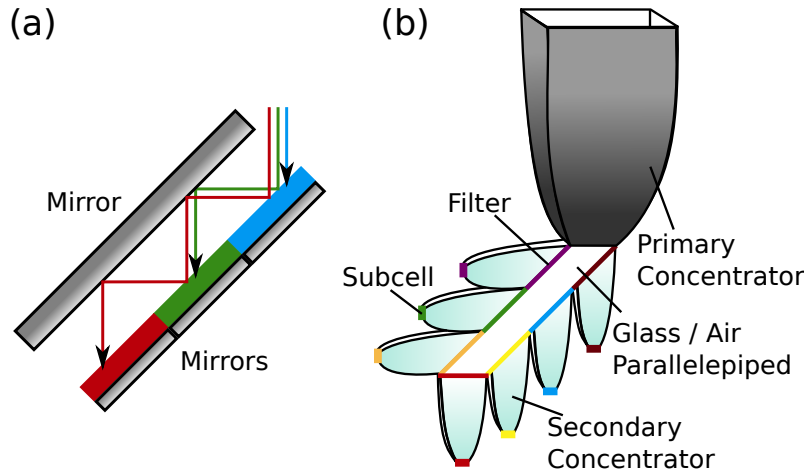


Figure 6.2: Polyhedral specular reflector designs for creating spectrum-splitting multi-junction solar cells with $\eta > 50\%$. (a) The spectrum is split through the absorption of high energy photons in consecutive SCs, which have progressively lower bandgap energies. (b) Uses short-pass filters to isolate the wavelengths that reach each subcell and incorporates a moderate amount of optical concentration. Adopted from [215, 216] respectively.

6.1.2 Ultra-high Efficiency Spectrum-splitting Multi-junctions

The second opportunity enabled by the spectrum-splitting approach is the creation of multi-junction SCs with ultra-high efficiencies of $\eta > 50\%$ [43], *i.e.* greater than the current world record by 4% or more. Reaching such efficiencies with conventional monolithic multi-junction devices is extremely difficult since it requires the integration of four or more subcells, where layers must be lattice matched, and the current from the entire device is limited by the lowest current from the subcells. Mechanically decoupled multi-junctions remove these constraints and enable the incorporation of many more subcells without constraints on the material properties or current matching. Foundational work on these SCs is presented in [214].

The major advances towards the realisation of 50% efficient SCs using the spectrum splitting approach have been made by the Atwater group [43, 215–217]. This group has investigated the use of holograms to direct the appropriate solar wavelength to the optimal subcell (as in Fig. 2.18) [43, 217], and more recently they have proposed “polyhedral specular reflector” designs where light is filtered progressively as shown in Fig. 6.2. In Fig. 6.2(a) the filtering occurs through the absorption of high energy photons in consecutive SCs, which have progressively lower bandgap energies [215, 218]. The design of Fig. 6.2(b) uses a similar geometry, but uses shortpass filters to isolate the wavelengths that reach each subcell [216]. In order to increase the efficiency to over 50% their latest design (Fig. 6.2(b)) includes concentration of roughly 25-suns. The Atwater group has also investigated using InAlAs, InGaAsP, and InGaAs SCs, which are lattice matched and which together have a theoretical efficiency of $\eta = 51\%$ under 100-suns concentration [219]. With the efficiency record for SCs currently at 46%, the creation of a SC with $\eta > 50\%$ remains a major challenge for the solar research community.

Prelude to Paper 6.2

We now present our study of *high-contrast* dielectric diffraction gratings that are known to feature broadband regions of near unity reflectance, where we show that these features arise because of the symmetries of the grating’s Fano resonances:

B. C. P. Sturmberg, K. B. Dossou, L. C. Botten, R. C. McPhedran and C. M. de Sterke. “Fano resonances of dielectric gratings: symmetries and broadband filtering”. *Opt. Express* **23**, A1672 (2015)

Associated with Paper 6.2 are a series of animations that show the evolution of the complex transmission coefficient t through the complex plane as a function of wavelength, which are available online: [Visualization 1](#), [Visualization 2](#). In Fig. 6.3 we present a few frames from [Visualization 1](#) which corresponds to Fig. 4 in Paper 6.2.

Fano resonances of dielectric gratings: symmetries and broadband filtering

Björn C. P. Sturmberg,^{1,*} Kokou B. Dossou,² Lindsay C. Botten,^{2,3}
Ross C. McPhedran,¹ and C. Martijn de Sterke¹

¹ CUDOS and IPOS, School of Physics, University of Sydney, Sydney, 2006, Australia

² CUDOS, School of Mathematical and Physical Sciences, University of Technology Sydney, Sydney, 2007, Australia

³ National Computational Infrastructure, Australian National University, Canberra, Australia

*b.sturmberg@sydney.edu.au

Abstract: The guided mode resonances (GMRs) of diffraction gratings surrounded by low index materials can be designed to produce broadband regions of near perfect reflection and near perfect transmission. These have many applications, including in optical isolators, in hybrid lasers cavities and in photovoltaics. The excitation of rapid GMRs occurs in a background of slowly varying Fabry-Perot oscillation, which produces Fano resonances. We demonstrate the critical role of the polarity of adjacent Fano resonances in the formation of the broadband features. We design gratings for photovoltaic applications that operate at wavelengths where material absorption must be considered and where light is incident at non-normal angles.

© 2015 Optical Society of America

OCIS codes: (050.0050) Diffraction and gratings; (310.6628) Subwavelength structures, nanostructures; (350.4238) Nanophotonics and photonic crystals; (040.5350) Photovoltaic; (350.6050) Solar energy.

References and links

1. D. Maystre, "Diffraction gratings: An amazing phenomenon," *Comptes Rendus Phys.* **14**, 381–392 (2013).
2. C. Chang-Hasnain and W. Yang, "High-contrast gratings for integrated optoelectronics," *Adv. Opt. Photonics* **4**, 379–440 (2012).
3. S. S. Wang and R. Magnusson, "Theory and applications of guided-mode resonance filters," *Appl. Opt.* **32**, 2606–2613 (1993).
4. S. Tibuleac and R. Magnusson, "Narrow-linewidth bandpass filters with diffractive thin-film layers," *Opt. Lett.* **26**, 584–6 (2001).
5. C. F. R. Mateus, M. C. Y. Huang, Y. Deng, A. R. Neureuther, and C. J. Chang-Hasnain, "Ultrabroadband mirror using low-index cladded subwavelength grating," *IEEE Photonics Technol. Lett.* **16**, 518–520 (2004).
6. P. Lalanne, J. P. Hugonin, and P. Chavel, "Optical properties of deep lamellar gratings: A coupled bloch-mode insight," *J. Light. Technol.* **24**, 2442–2449 (2006).
7. Y. Kanamori, K. Hane, H. Sai, and H. Yugami, "100 nm period silicon antireflection structures fabricated using a porous alumina membrane mask," *Appl. Phys. Lett.* **78**, 142–143 (2001).
8. T. Glaser, S. Schröter, H. Bartelt, H.-J. Fuchs, and E.-B. Kley, "Diffractive optical isolator made of high-efficiency dielectric gratings only," *Appl. Opt.* **41**, 3558–3566 (2002).
9. A. Taghizadeh, J. Mørk, and I.-S. Chung, "Ultracompact resonator with high quality-factor based on a hybrid grating structure," *Opt. Express* **23**, 17282–17287 (2015).
10. Z. Wang, B. Zhang, and H. Deng, "Dispersion engineering for vertical microcavities using subwavelength gratings," *Phys. Rev. Lett.* **114**, 73601 (2015).
11. S. S. Wang, R. Magnusson, J. S. Bagby, and M. G. Moharam, "Guided-mode resonances in planar dielectric-layer diffraction gratings," *J. Opt. Soc. Am. A* **7**, 1470 (1990).

12. A. W. Snyder and J. D. Love, *Optical Waveguide Theory* (Chapman and Hall, 1983).
13. R. Magnusson, "Wideband reflectors with zero-contrast gratings," *Opt. Lett.* **39**, 4337–40 (2014).
14. S. Collin, "Nanostructure arrays in free-space: optical properties and applications," *Reports Prog. Phys.* **77**, 126402 (2014).
15. S. Fan, W. Suh, and J. D. Joannopoulos, "Temporal coupled-mode theory for the Fano resonance in optical resonators," *J. Opt. Soc. Am. A.* **20**, 569–572 (2003).
16. A. Polman and H. A. Atwater, "Photonic design principles for ultrahigh-efficiency photovoltaics," *Nat. Mater.* **11**, 174–177 (2012).
17. L. C. Hirst, and N. J. Ekins-Daukes, "Fundamental losses in solar cells," *Prog. Photovoltaics Res. Appl.* **19**(3), 286–293 (2010).
18. P. Löper, B. Niesen, S.-J. Moon, D. Nicolas, J. Holovsky, Z. Remes, M. Ledinsky, F.-j. Haug, J.-H. Yum, S. D. Wolf, and C. Ballif, "Organic-inorganic halide perovskites: Perspectives for silicon-based tandem solar cells," *IEEE J. Photovoltaics* **4**, 1545–1551 (2014).
19. C. D. Bailie, M. G. Christoforo, J. P. Mailoa, A. R. Bowring, E. L. Unger, W. H. Nguyen, J. Burschka, N. Pellet, J. Z. Lee, M. Grätzel, R. Noufi, T. Buonassisi, A. Salleo, and M. D. McGehee, "Semi-transparent perovskite solar cells for tandems with silicon and CIGS," *Energy Environ. Sci.* **8**, 956–963 (2015).
20. T. P. White, N. N. Lal, and K. R. Catchpole, "Tandem solar cells based on high-efficiency c-Si bottom cells: Top cell requirements for > 30% efficiency," *IEEE J. Photovoltaics* **4**, 208–214 (2014).
21. H. J. Snaith, "Perovskites: The emergence of a new era for low-cost, high-efficiency solar cells," *J. Phys. Chem. Lett.* **4**, 3623–3630 (2013).
22. M. Liu, M. B. Johnston, and H. J. Snaith, "Efficient planar heterojunction perovskite solar cells by vapour deposition," *Nature* **501**, 395–398 (2013).
23. B. C. P. Sturmberg, K. B. Dossou, F. J. Lawrence, C. G. Poulton, R. C. McPhedran, C. M. de Sterke, L. C. Botten, "EMUstack: an open source route to insightful electromagnetic computation via the Bloch mode scattering matrix method," *Comp. Phys. Comm.*, *submitted*.
24. "EMUstack: An open-source package for Bloch mode based calculations of scattering matrices," physics.usyd.edu.au/emustack.
25. K. B. Dossou, L. C. Botten, A. A. Asatryan, B. C. P. Sturmberg, M. A. Byrne, C. G. Poulton, R. C. McPhedran, and C. M. de Sterke, "Modal formulation for diffraction by absorbing photonic crystal slabs," *J. Opt. Soc. Am. A* **29**, 817–831 (2012).
26. K. R. Catchpole and M. A. Green, "A conceptual model of light coupling by pillar diffraction gratings," *J. Appl. Phys.* **101**, 063105 (2007).
27. M. Born and E. Wolf, *Principles of Optics* (Cambridge University Press, 2005).
28. E. T. Whittaker and G. N. Watson, *A Course of Modern Analysis* (Cambridge University Press, 1996).
29. L. C. Botten, R. C. McPhedran, and J. M. Lamarre, "Inductive grids in the resonant region: Theory and experiment," *Int. J. Infrared Millimeter Waves* **6**, 949 (1985).
30. B. S. Richards, "Single-material TiO₂ double-layer antireflection coatings," *Sol. Energy Mater. Sol. Cells* **79**, 369–390 (2003).
31. I.-S. Chung, "Study on differences between high contrast grating reflectors for TM and TE polarizations and their impact on VCSEL designs," *Opt. Express* **23**, 16730 (2015).

1. Introduction

Diffraction gratings are fundamental structures in optics, however their study has historically been focused on surface gratings [1], where the grooves of the grating do not extend all the way through the layer or the grating is placed on top of another high index material. Here we study *high-contrast gratings* (HCGs) [2], where the grating is surrounded by lower refractive index materials, such as air, and the inclusions penetrate the whole layer (see Fig. 1).

The resonances of HCGs lead to rapid transitions in transmission/reflection from near-zero to near-unity, which can be used to make narrow and ultra-wide bandwidth filters [3–6]. HCGs have been applied as anti-reflection coatings [7], as optical isolators [8], and as cavities in hybrid lasers [2, 9]. It has also been shown that dispersion engineering the angular response of HCGs opens further possibility, including enhancing the Purcell effect, creating polariton-based lasers and quantum circuits, and exotic quantum phases in polaritons [10].

The resonances of gratings have been explained using three different conceptual frameworks: the excitation of leaky guided mode resonances (GMRs) [11], which are the waveguide modes of the homogenised slab that couple to the incident propagating waves [12]; the Fabry-Perot

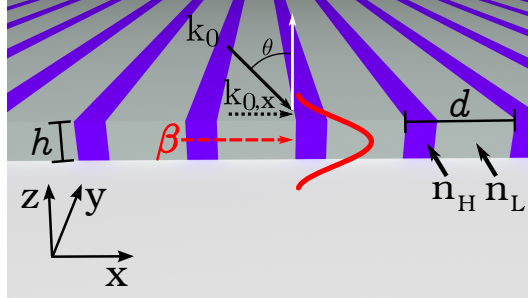


Fig. 1. Schematic of a grating of period d and thickness h , consisting of high and low index rulings: n_H , n_L . Also shown are the incident wave vector k_0 at an angle of θ , its x -component and the propagation constant β of a slab waveguide mode. The field of the slab waveguide mode is illustrated in red.

(F-P) resonances of the grating's eigenmodes, which are quasi-periodic in the $\pm x$ -direction and propagate in the $\pm z$ -direction, and may be considered as either Bloch modes (BMs) [6] or approximated as the waveguide modes of the high index rulings [2]; and by studying the zeros and poles of the transmission and reflection functions [1]. The GMR analysis is consistent with the results of Magnusson showing that broadband near-unity reflections can be achieved using gratings placed upon anti-reflection layers that totally remove the bottom high contrast interfaces that are central to the vertical F-P resonance formulation [13]. Our analysis includes aspects of all three approaches, which clarifies the relationship between these currently disparate literatures [2, 13, 14].

Previous theoretical studies have focussed on predicting the locations of the resonances. An important issue that has remained unresolved is the relationship between isolated resonances and the occurrence of broadband regions of near perfect transmission or reflection. In this paper we answer this question by understanding the specular anomalies as Fano resonances [15], where the sharp resonant excitation of a leaky GRM (or equivalently a set of BMs) occurs in the presence of a slowly varying F-P resonance of the homogenized layer. We make the important step of showing that consecutive Fano resonances have opposite polarity, which allows them to form broadband regions of uniformly high reflection when the resonances broaden.

In the Sect. 5 we consider HCGs as wavelength selective filters operating at visible wavelengths, such as those being considered for photovoltaic applications [16], as well as those mentioned above [2, 7–9]. In the solar application their role is to direct different wavelength bands of the solar spectrum to solar cells that have different bandgap energies, and therefore convert their allocated wavelengths more efficiently than if the whole spectrum were incident upon any one cell [17]. This type of design has attracted much interest recently [18, 19] as it could lead to relatively cheap tandem cells with efficiencies greater than 30% [20], as well as ultra-efficient modules with efficiencies exceeding 50% [16]. The reduced cost of the tandem structures is achieved by using cheap silicon cells as the low bandgap subcell and a low-cost emergent material, such as a Perovskite [21, 22], in the other subcell.

These solar energy applications differ from those studied to date in two ways, they require: the grating to have minimal absorption; and to operate at angles of incidence far off-normal, often at $\theta = 45^\circ$ where the reflected light exits at $\theta = 90^\circ$ to the incident and transmitted light. In the wavelength range of primary interest for photovoltaic applications, $310 \text{ nm} < \lambda < 1 \mu\text{m}$, high refractive index materials are all, to some degree, lossy. In previous studies the materials were assumed to be lossless, which is valid at the wavelengths targeted, $1 \mu\text{m} < \lambda < 3 \mu\text{m}$.

Our study was carried out using the freely available EMUstack package [23–25]. This is

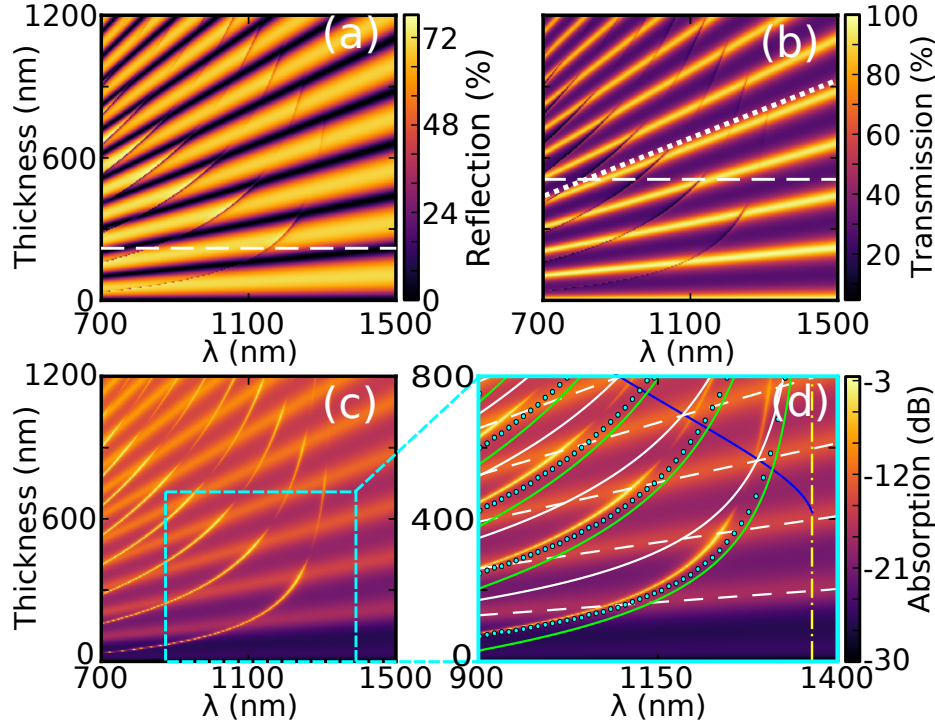


Fig. 2. (a) Reflection, (b) transmission, and (c) absorption spectra as a function of grating thickness. In (d) we magnify a section of (c) and overlay the results of the model described in the text: the dashed and solid white curves are the F-P resonances of the 0 and ± 1 orders respectively; the green curves are like the solid white curves but uses n_{eff} ; the cyan dots approximate the waveguide modes; the blue curve marks the trough in resonance amplitude; and the yellow dot-dashed line is the cut-off of the ± 1 orders in n_H .

ideally suited to such a study because it provides access to the Bloch modes of the grating, and allows variations in thickness to be calculated with negligible computational cost.

The paper is organized as follows: Sect. 2 reviews the physics that governs where the resonances occur; in Sect. 3 we examine their spectral characteristics, focussing on the factors influencing their Fano line-shape; and in Sects. 4 and 5 we design HCGs as wavelength selective reflectors for applications where the effects of material absorption and angle of incidence are critical.

2. The modes of dielectric gratings

As our initial example we study a weak diffraction grating, where only 5% of the layer is the low index material ($f_L = 0.05$, $f_H = 0.95$). The grating period is chosen to be $d = 400$ nm so that, at the wavelengths considered, only the specular order propagates in the surrounding air. The materials are chosen to be dispersionless, with complex refractive indices $n_H = 3.5 + 0.005i$, which is similar to silicon, and $n_L = 1.0$. We include loss not only because it is important for practical applications, but also because the resonances of light are clearly visible as peaks in the absorption spectra. Throughout this paper we consider light that has Transverse Electric (TE) polarization (E-field along x -axis), and we begin by considering the case of normal incidence.

Figure 2 shows the reflection, transmission and absorption spectra of the example grating

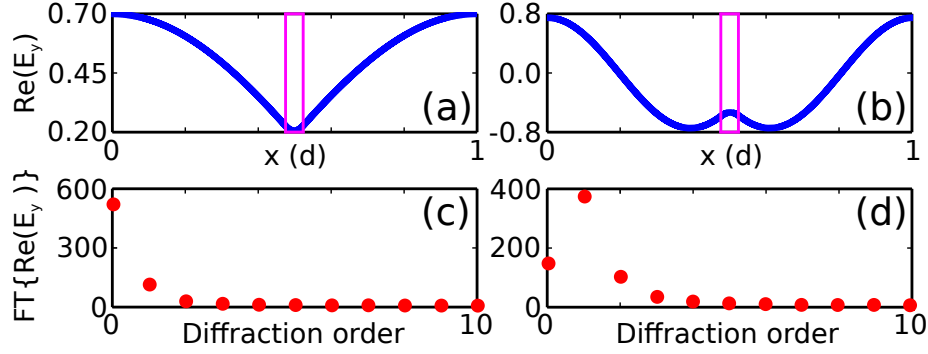


Fig. 3. $E_y(x)$ field distributions of (a) BM-A and (b) BM-B of the example grating for $\lambda d = 9/8$. The edges of the inclusions are indicated in pink and the x -axis is normalised to the period. (c) and (d) show the Fourier decompositions of the fields of (a) and (b) respectively.

as a function of the grating thickness h . The reflection and transmission spectra are dominated by Fabry-Perot fringes that run diagonally through Figs. 2(a) and 2(b) respectively. The F-P resonances are also visible in the absorption spectra of Figs. 2(c) and 2(d), where absorption peaks occur on-resonance. There is also a second class of curves, where anomalies cause the spectra to vary rapidly. A striking feature of these curves, which are most obvious as peaks in the absorption spectra, is that their amplitudes vary strongly along the curves. These are the resonances that form the broadband reflection regions in stronger gratings, with their properties and underlying physics being examined in detail.

We initially choose to study a weak grating because it simplifies the analysis, allowing us to approximate the BMs of the grating by plane wave diffraction orders (PWs). This is demonstrated in Fig. 3, where we show the E_y field distributions of the two dominant lowest order BMs modes, which we label BM-A, BM-B, and their Fourier decompositions into PWs. Figure 3(c) shows that BM-A is closely related to the specular diffraction order, while Fig. 3(d) shows that BM-B is associated with the ± 1 orders. Approximating the BMs by PWs allows us to proceed analytically, approximating the propagation constants of the BMs by the propagation constants of their respective PW diffraction orders, within a homogenized grating layer.

Figure 2(d) shows a magnified section of Fig. 2(c), where we overlay a number of analytic and semi-analytically calculated curves that capture all of the observed features. We now explain how these were derived.

The dashed white lines show where the specular PW order, $m = 0$, satisfies the F-P resonance condition, $2k_{z,m}h = 2\pi p$, with $1 < p < 6$. The vertical propagation constant within the homogenized grating is

$$k_{z,0} = k_{\text{eff}} \cos(\theta_g) = n_{\text{eff}} \frac{2\pi}{\lambda} \cos(\theta_g), \quad (1)$$

where θ_g is the angle of propagation within the grating, and the effective refractive index of the grating is calculated using the linear mixing formula of the permittivity for TE polarization, $n_{\text{eff}} = \sqrt{f_H \epsilon_H + (1 - f_H) \epsilon_L}$. Though we do not present results for TM polarization, the applicable effective index for this case is $n_{\text{eff}} = 1 / \sqrt{f_H / \epsilon_H + (1 - f_H) / \epsilon_L}$.

The cyan dots correspond to the waveguide (WG) modes of the homogenized slab. They are calculated by solving the dispersion relations for the WG modes [12] for the transverse k -vector

values of the grating,

$$\beta_{\text{WG}} = k_{x,m} = k_{\text{eff}} \sin(\theta_g) + mG = k_{\text{eff}} \sin(\theta_g) + \frac{2\pi m}{d}, \quad (2)$$

where G is the reciprocal lattice vector. In the wavelength range shown, all dots correspond to coupling via the $m = \pm 1$ reciprocal lattice vector, which are degenerate at normal incidence. Each curve corresponds to a different order waveguide mode. The curves are a good fit to the observed resonances, with discrepancies only arising due to the approximation of an effective index, which is corroborated by observation that the fits improve as $f_L \rightarrow 0$.

The solid white and green curves approximate the waveguide modes as F-P resonances of the ± 1 PW orders, whose vertical propagation constants are

$$k_{z,\pm 1} = \sqrt{k_{\text{eff}}^2 - k_{x,\pm 1}^2}. \quad (3)$$

The quantitative accuracy of the green curves is improved by the inclusion of the phase shift acquired by the higher diffraction orders when they reflect off the top and bottom interfaces of the grating at oblique angles. This effect is similar to the Goos-Hänchen shift [12], and analogously we incorporate it into our model by introducing an effective thickness

$$h_{\text{eff},m} = h + \frac{2i}{\gamma_m}, \quad (4)$$

where

$$\gamma_m = \sqrt{k_{\text{air}}^2 - (k_{\text{air}} \sin(\theta) + mG)^2}, \quad (5)$$

where $m = \pm 1$ for the ± 1 PWs, is purely imaginary.

The yellow vertical line marks the cut-off wavelength of the ± 1 PW orders, above which these orders (and the corresponding BMs) are evanescent.

The blue curve indicates where the amplitude of the anomalies is at a minimum. This variation in the resonance amplitudes is due to the beating between the grating modes as they propagate with different k_z , acquiring different phases. At the bottom of the grating, the electric field outside of the grating must match the superposition of the grating. If, at the bottom interface, the superposition of the grating modes has a waveform that matches that of a propagating PW order, then light is efficiently transmitted [26]. If, on the other hand, the superposition has little overlap with the waveform of any propagating order, then there is little transmittance and the strength of the resonance is enhanced. Since the superposition of the grating modes is equal to the incident PW at the top interface, we know that maximum transmission occurs when the phase difference of the grating modes is a multiple of 2π [26], *i.e.*,

$$\Delta k_z = \frac{2\pi l}{h}, \quad (6)$$

where l is an integer. These points are marked by the blue curve of Fig. 2(d), where we approximate the k_z of each BM by their respective PW order.

The analytic calculations presented in Fig. 2 demonstrate how the complicated spectral response of HCGs can be understood in simple terms, and illustrate the relationships between the slab waveguide modes, the F-P resonances of the BMs of the grating, and the F-P resonances

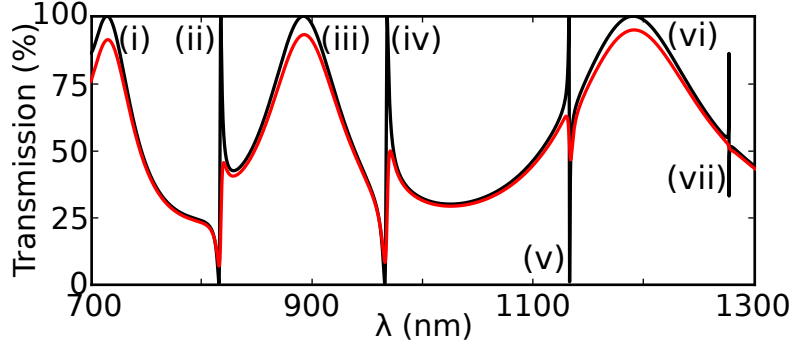


Fig. 4. Transmission spectrum for the weak grating with $h = 520$ nm. The red curve includes loss (and is marked by the horizontal white dashed in line in Fig. 2(b)), while the black curve is calculated for the same grating but ignoring loss. Individual resonances are labelled.

of non-specular diffraction orders within the homogenized layer. The PW approximation to the BMs breaks down as f_L is increased, while the formalism that considers the grating as an array of waveguides becomes more accurate as the high index inclusions become increasingly separated [14].

We have so far focused on predicting the location of the resonances of grating. In the next section we examine the line shape of the resonances, which governs the creation of broadband regions of near total reflection or transmission. The analysis builds on our observations that the BMs can be accurately approximated by PW orders and that the waveguide modes can be approximated by F-P resonances of higher diffraction order PWs.

3. Analysis of Fano resonances

In Fig. 4 we show the transmission spectra of our initial grating when loss is (red), and is not (black), included. The thickness of the gratings is $h = 520$ nm, as indicated by the horizontal white dashed line in Fig. 2(b). We see that the superposition of phases from the F-P resonances and the waveguide modes produces resonances with a characteristic Fano line shape. The inclusion of loss dampens the resonances, with the absorption being highly localized to the resonant wavelengths.

We note that the polarity of the Fano resonance's line shape changes sign for consecutive resonances; *i.e.*, for the resonance labelled (iv) $\lambda(t = 0) < \lambda(t = 1)$, whereas the resonance labelled (v) has the opposite symmetry with $\lambda(t = 0) > \lambda(t = 1)$. Furthermore, we see that consecutive Fano resonances that occur on opposite sides of a F-P resonance (iii), such as those labelled (ii) and (iv), have the same polarity.

To clarify this effect, it is instructive to study spectra where the contribution of the F-P resonance to the complex transmission coefficient t is held constant. We do this by adjusting the thickness of the grating as a function of the wavelength,

$$h = \frac{p}{2n_{\text{eff}}}\lambda. \quad (7)$$

Figure 5(a) shows the transmission along the diagonal white dotted line of Fig. 2(b), where $p = 4.1$. We chose this value of p because the resultant line lies between the resonance and anti-resonance conditions of the F-P oscillation intersects many GMRs. Keeping the F-P component of the transmission fixed highlights the opposite symmetry of the consecutive GMRs.

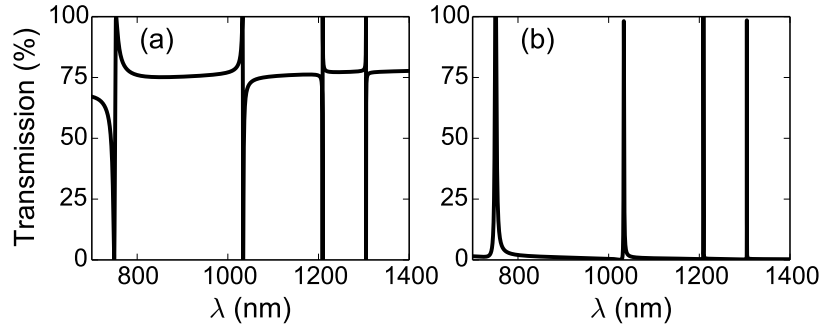


Fig. 5. (a) Transmission spectrum where the thickness of the grating is adjusted as a function of λ such that Eq. 7 is satisfied, indicated by the diagonal dotted line in Fig. 2(b). (b) Transmission along the same diagonal line, where the t corresponding to the F-P resonance has been subtracted, leaving the transmission due to the GMRs.

The opposite symmetry of consecutive Fano resonance is critical for the formation of the broadband reflection and transmission regions, as it enables the resonance spectra of two Fano resonances to merge without passing through a zero. Furthermore, since there are no resonances in these regions, the absorption is low.

In Sect. 2 we showed how the GMRs are related to F-P resonances of higher order plane waves in an homogenized medium. This allows us to make an analogy between the GMRs and a classic Fabry-Perot cavity. Figure 5(b) is for the same parameters as Fig. 5(a), where we now show the transmission that is due solely to the GMR. This is found by calculating t for the equivalent homogenized film and subtracting this from the t of the grating. We see that, precisely as in the case of a high finesse F-P cavity, the transmission is zero, except for on resonance where it goes briefly to unity. The finesse of the resonance is set by the coupling coefficient of the ± 1 PW orders of the grating to the specular PW outside, directly analogously to the reflectivity of the mirrors of a F-P cavity.

In the following subsections we analytically analyse the F-P resonances, showing how the alternating polarity of consecutive orders is related to the poles of the transmission function, and then extend this analysis to the GMRs through numerical calculations. It is the superposition of these two effects that explains the features observed in Figs. 4, and 5.

3.1. Functional analysis of Fabry-Perot resonances

The complex transmission (t) and reflection (r) coefficients associated with light incident upon a homogeneous film are well known analytical functions [27] that can be derived using the transfer matrix method. For instance,

$$r = \frac{[v - v^{-1}] \sin(kh)}{-2i \cos(kh) + [v + v^{-1}] \sin(kh)}, \quad (8)$$

at normal incidence, where $v = \frac{n_{TF}}{n_{out}}$ is the ratio of the refractive indices of the layer (n_{TF}) and the index of the surrounding media (n_{out}). The zeros of r occur at real frequencies, when $k_{z,m}h = \pi p$, which reproduces the F-P result. r and t have common poles, which in contrast lie in the lower half of the complex frequency plane, as required by causality.

For a homogeneous film we find that the poles occur at

$$\omega_p = \omega_{r,p} + i\omega_{i,p} = \frac{c}{n_{TF}} \left[\frac{p\pi}{h} - i \frac{\ln(\rho^{-1})}{h} \right], \quad (9)$$

where $\rho = (n_{out}n_{out} - n_{TF})/(n_{out} + n_{TF})$ is the Fresnel reflection coefficient for light within the layer incident upon the interface with the surrounds. The position of a pole directly relates to the Q-factor of the resonance,

$$Q_p = \frac{\omega_{r,p}}{2\omega_{i,p}}. \quad (10)$$

For real frequencies close to $\omega_{r,p}$ the response is dominated by pole p , and is of the form

$$t(\omega_r) \approx \frac{\text{Res}_{\omega_p} t(\omega)}{\omega_r - \omega_p}, \quad (11)$$

where $\text{Res}_{\omega_p} t(\omega)$ is the residue of pole p [28]. The general result is that $t(\omega_r)$ traces out a circle in the complex plane as ω_r passes through $\omega_{r,p}$. As a function of increasing ω_r the circle is followed in an anti-clockwise manner. The circle passes through the origin, and is centred at

$$[\text{Re}(t), \text{Im}(t)] = \frac{i}{2\omega_{i,p}} |\text{Res}_{\omega_p} t(\omega)| [\sin(\varphi), -\cos(\varphi)], \quad (12)$$

where $\varphi = \arg[\text{Res}_{\omega_p} t(\omega)]$. For a homogeneous film we find that

$$\text{Res}_{\omega_p} t(\omega) = i(-1)^p \frac{2n_{out}n_{TF}}{(n_{out} - n_{TF})^2}. \quad (13)$$

This shows that $t(\omega_r)$ traces out circles that are centred on the real axis, with consecutive F-P resonances (p) lying on opposite sides of the imaginary axis. The blue curves in Fig. 6 illustrate schematically how $t(\omega_r)$ evolves in a frequency range that covers two consecutive F-P resonances, where the Q-factor of the resonance is sufficiently small that the effect of the two poles merge, forming a peanut shape. The arrows indicate how the curves are traced out for increasing wavelengths.

3.2. Functional analysis of guided mode resonances

In order to study the poles of the GMRs we construct a model structure that contains the same essential physics of the HCGs: where light is coupled to the leaky waveguide modes by a grating, but in which the GMRs are described exactly by PWs. The model structure consists of infinitesimally thin gratings placed at the top and bottom of a uniform thin film, which we refer to as the *surface grating structure*. The refractive indices of the grating must be very large to ensure that the grating scatters significant energy into higher diffraction orders. For simplicity we take all materials to be lossless in this model. We use a grating of thickness $h_g = 1$ nm and composed of equal parts $n_H = 20$, $n_L = 1$ and with $d = 400$ nm. The uniform film is chosen to be $h_{TF} = 600$ nm thick with $n_{TF} = 2$, such that the ± 1 PW orders propagate within the uniform film for $\lambda < 800$ nm.

The major advantage of the surface grating model is that the analytic expressions for the PWs within the uniform layer can be generalized to complex frequencies, allowing us to locate the poles of t , r and the associated residues. Here t and r are the elements of the scattering matrices corresponding to the single propagating order (*i.e.* the specular order). To do this we calculate the scattering matrices that describe the surface grating for a fixed real frequency (3.77 PHz) and then use these values for all other frequencies. The transmission spectrum of this surface grating structure, presented in Fig. 7(a) as a function of real frequencies, exhibits precisely the same types of features as the gratings in Fig. 4.

Figure 7(b) shows a contour plot of the transmission for complex frequencies, where two classes of poles can be seen. One class has small $\omega_{i,p}$ and large Q-factors (from Eq. 10), and

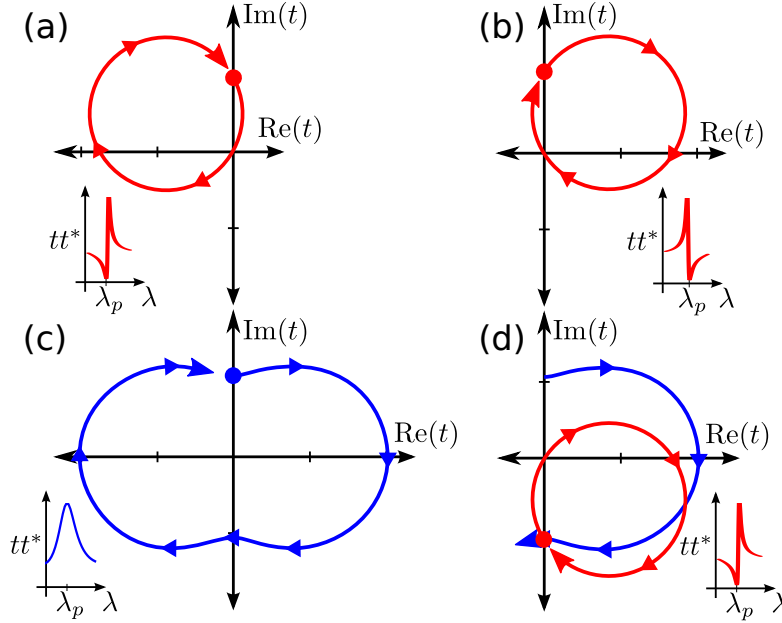


Fig. 6. Schematic of the trajectories of $t(\omega_r)$ through the complex-plane, where blue curves represent the change in t due to the F-P resonance and red curves due to GMRs. The insets illustrate the line-shapes of the transmission associated with each trajectory (in (d) following just the red curve). (a), (b) Illustrate how GMRs whose residues lie on opposite sides of the real axis produce lines-shapes of opposite symmetry, despite the loops having the same starting point. (c) Shows the trajectory of two consecutive F-P resonances, whose low Q-factors makes them merge without going through the origin. (d) Features the same GMR as in (b), but occurring on the other side of a F-P resonance, which is seen to produce the opposite symmetry Fano resonance.

correspond to the GMRs. The other class correspond to F-P resonances and lie further away from the real axis with smaller Q-factors. The respectively high-Q and low-Q nature of these resonances is visible in the spectra of Fig. 7(a).

The residue of each pole is calculated using numerical contour integration. The results for the F-P resonances agree well with the analytic expressions; the residues are purely imaginary, and have opposite sign for consecutive resonances (*i.e.* their phase of the residues differs by π). This produce $t(\omega_r)$ trajectories centred around points on the real axis with consecutive resonances lying on opposite sides of the imaginary axis. For the GMRs we find that the phase of the residues also differs for consecutive resonances, such that $t(\omega_r)$ follows circles in the complex plane that lie on opposite sides of the imaginary axis. Physically, this difference is related to odd or even order resonances having an odd or even number of half wavelengths within the grating layer, which dictates the phase of the transmitted light.

We illustrate the trajectories of $t(\omega_r)$ in the vicinity of a GMR by the red curves of Fig. 6. The trajectories of the GMRs shown in Figs. 6(a) and 6(b) begin from the same point, but the residues of the resonances lie on opposite sides of the real axis. Following the trajectories we see that in Fig. 6(a) the transmission goes through zero before going through its maximum value, while the opposite is true for Fig. 6(b). This is shown schematically in the inset. The effect of combining the GMRs with the F-P resonance is shown in Fig. 6(d), which features the

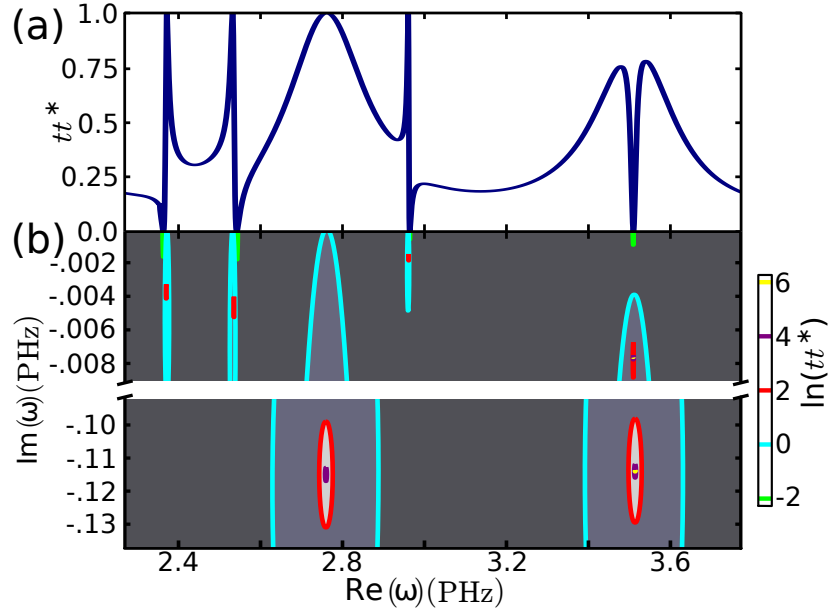


Fig. 7. Transmittance of the surface grating structure. In (a) the transmission is a function of real angular frequencies, while in (b) the transmission is calculated across a range of complex frequencies.

same GMR as in Fig. 6(b), however the GMR now occurs on the other side of a F-P resonance, which produces a Fano line-shape of opposite symmetry.

In our weak gratings, the GMRs occur over frequency bandwidth of approximately 0.03 PHz and each F-P resonances spans approximately 0.8 PHz, which is consistent with the difference in $\omega_{r,p}$ for the two classes of poles. The large difference in the frequency ranges of the resonances means that the combined effect of the blue and red curves is as follows: $t(\omega_r)$ follows the blue curve until ω_r approaches $\omega_{r,q}$ for a WG resonance q ; now $t(\omega_r)$ completes a loop around a red curve, which is completed in such a small frequency interval that the phase of the F-P resonance has changed very little (causing little movement along the blue curve) and the red curve almost closes on itself; once the frequency range of the GMR is passed, $t(\omega_r)$ resumes following the blue curve. The supplementary materials contain animations that shows the numerically calculated progression of $t(\omega_r)$ corresponding to Fig. 4 (Visualization 1), and Fig. 5 (Visualization 2). Similar trajectories of have been measured experimentally at infrared frequencies by Botten et. al [29].

3.3. Stronger diffraction gratings

Our analysis has been focused on weak gratings, where the modes of a grating are well approximated by plane wave orders. Our general findings however hold for all gratings, because the existence and parity of the poles is topologically preserved. As the diffraction strength of the grating is increased, by increasing the refractive index contrast and/or increasing f_L , light is coupled more efficiently into, and out of, the waveguide modes. This reduces the Q-factor of the GMR and broadens the spectral response of the Fano resonances.

The broadening is shown in Fig. 8(a) where $f_L = 0.05$ (corresponding to the marked line in Fig. 2(a)), and in Fig. 8(b) where $f_L = 0.35$, which is marked in Fig. 8(d). We note that

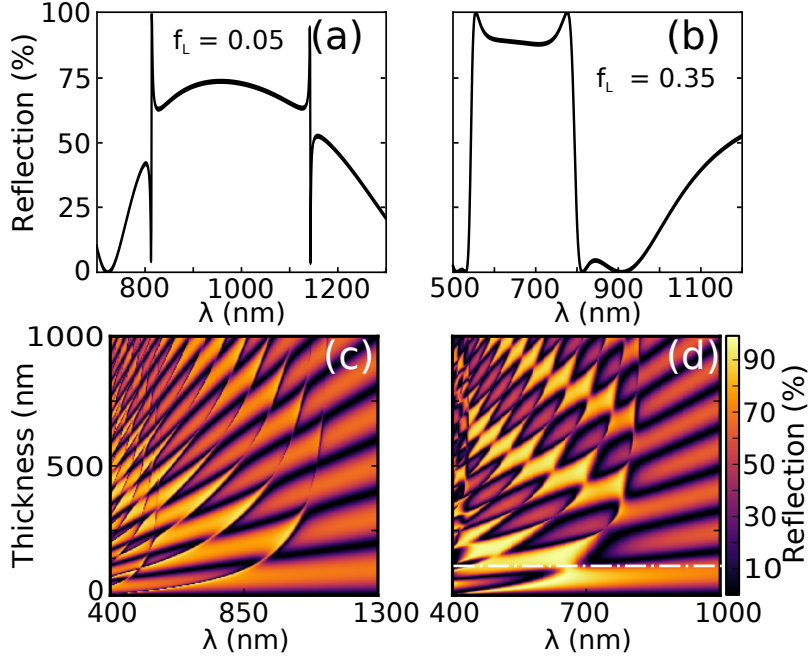


Fig. 8. (a) Reflection spectrum corresponding to the dot-dashed line in Fig. 2(a) ($f_L = 0.05$, $h = 210$ nm). (b) Reflection spectrum of a grating with $f_L = 0.35$ and $h = 150$ nm (indicated by dot-dashed line in (d)). (c) Reflection spectra with $f_L = 0.2$ as a function of grating thickness. (d) Reflection spectra with $f_L = 0.35$ as a function of grating thickness. Additional resonances occur at short wavelengths in (c), where the waveguide modes are excited by the ± 2 PW orders.

adjacent Fano resonances continue to have opposite polarity, so that when they broaden to the extent that they overlap, they form broad regions of uniformly high reflectivity.

Having understood both the location *and* the polarity of the Fano resonances, we can now fully explain the striking “checkerboard” pattern observed in Figs. 8(c) and 8(d) where $f_L = 0.2$ and $f_L = 0.35$ respectively: high reflectivity occurs between consecutive Fano resonances whose line-shapes have opposite symmetry; the transmission is high on the other side of these Fano resonances; and the areas are bounded by the specular F-P resonances, because these invert the polarity of the Fano resonances. Regions of high transmissivity are formed by the same process, between Fano resonances with the opposite symmetry. This fully explains the physics that causes the broadband regions of near total reflectivity or transmission that are the stand-out features of HCGs.

4. Dependence on incident angle

So far we have considered only normally incident light. For spectrum splitting applications, however, light is typically incident at $\theta = 45^\circ$, such that the transmitted and reflected light are at $\theta = 90^\circ$ to each other. At normal incidence the $\pm m$ PW orders are degenerate ($k_{x,-1}^2 = k_{x,1}^2$ in Eq. 2, when $\theta = 0$). The major effect of moving to non-normal angles of incidence is that this degeneracy is lifted, with one PW having a larger, and the other a smaller, k_z . This doubles the number of wavelengths at which the grating couples to waveguide modes, doubling the number of Fano resonances. The $m = +1$ set occurs at shorter wavelengths than at normal incidence,

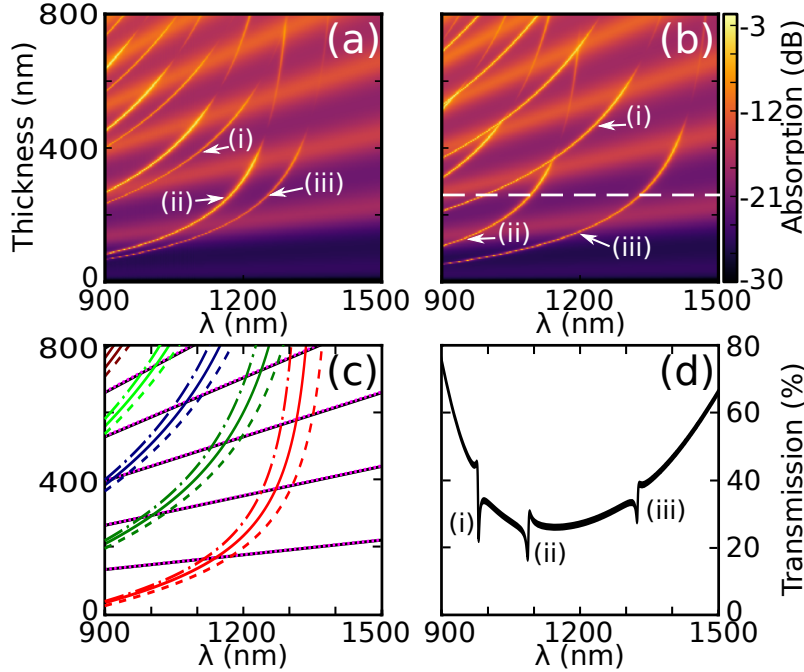


Fig. 9. Absorption for our canonical grating ($f_L = 0.05$) at angles of incidence of (a) $\theta = 5^\circ$, (b) $\theta = 20^\circ$. (c) The F-P resonances of the $m = +1$ (dotted) and the $m = -1$ (dashed) PW order at $\theta = 5^\circ$. The solid lines are for normal incidence and different colours are different WG orders. (d) The transmission spectrum corresponding to the marked slice through (b).

and the $m = -1$ set at longer wavelengths.

In Figs. 9(a) and 9(b) we show the absorption spectra of the grating from Fig. 2 illuminated at $\theta = 5^\circ$ and $\theta = 20^\circ$, where we use the absorption peaks as proxies for the location of the Fano resonances. In Fig. 9(c) we show the analytic curves equivalent to the red curve of Fig. 2(d) at $\theta = 5^\circ$, which exhibits the splitting of the degeneracy, although their quantitative agreement to Fig. 9(a) is not as good as in Fig. 2. The -1 PW order are shown in dashed lines, the $+1$ PW order in dot-dashed lines, and the ± 1 PWs at normal incidence are shown for comparison as solid lines. The different colours represent different order WG modes.

Figure 9(d) shows the transmission spectrum of the grating at $\theta = 20^\circ$ with $h = 250$ nm (marked in Fig. 9(b)). We see that the GMRs that correspond to coupling into the same order waveguide mode (labelled (ii), (iii)) have the same polarity, as they must, given that they are degenerate at normal incidence. Consecutive WG order resonances still have opposite polarity, as can be seen by comparing (i) and (iii). Because (ii) and (iii) have the same symmetry, the transmission dip that extended uniformly from (i) to (iii) at normal incidence now has an anomaly in it. As θ increases, (ii) shifts to shorter wavelengths, passing through (i), so that the broadband region is restored. In the next section $\theta = 45^\circ$, such that the resonances associated with the -1 PW orders occur at $\lambda < 450$ nm and are not observed in the range of interest.

5. Application as a wavelength selective reflector

Building on the results of the previous sections, we now design wavelength selective reflectors operating at the visible and near infrared wavelengths of importance in photovoltaic applica-

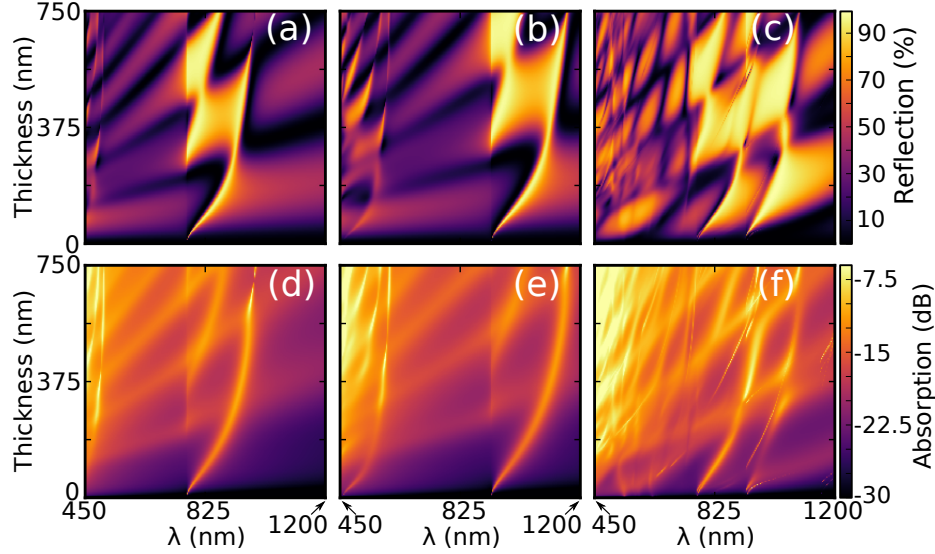


Fig. 10. (a)-(c) Reflection spectra and (d)-(f) absorption spectra of gratings as a function of their thickness. In (a), (d) $d = 450$ nm, while in (b), (e) $d = 540$ nm. The spectra of the stacked structure; grating with $d = 450$ nm, $1 \mu\text{m}$ thick air spacer, grating with $d = 540$ nm, is shown in (c), (f), where the y-axis gives the thickness of each grating, which are equal. In all cases $f_{\text{TiO}_2} = 0.25$ and the angle of incidence is 45° .

tions, with light incident at $\theta = 45^\circ$. We investigate gratings composed of annealed, amorphous TiO_2 , with air inclusions. For simplicity we follow previous studies [2, 6] and consider HCGs suspended in air, with similar results be obtainable in the presence of low index substrates. We focus on TiO_2 as it is a standard material for nanofabrication that has relatively low absorptivity. The complex refractive index data for TiO_2 is taken from [30], with values varying from $n_{\text{TiO}_2} = 2.13 + 0.0084i$ at $\lambda = 450$ nm to $n_{\text{TiO}_2} = 2.02 + 0.0017i$ at $\lambda = 1200$ nm (the long wavelength limit of the data). Figure 10 shows the reflection and absorption spectra of gratings composed of TiO_2 ($f_{\text{TiO}_2} = 0.45$) for $450 \text{ nm} < \lambda < 1200 \text{ nm}$, which covers the peak of the solar spectrum.

In Figs. 10(a) and 10(b) we see how reducing the refractive index and f_H from our previous examples has significantly reduced the Q-factors of the Fano resonances, broadening the wavelength range of high reflectance, and slightly decreasing the amplitude of the reflection peak. The resonances associated with the fundamental WG mode and the first higher order WG mode overlap; and since, in the absence of an intermittent F-P resonance, their symmetries are opposite they form broadband reflection regions.

The bandwidths of the reflection regions in Figs. 10(a) and 10(b) are smaller than in previous studies [5], which is due to the lower refractive index. The only difference between the gratings in Figs. 10(a) and 10(b) is the period, which is $d = 450$ nm in Fig. 10(a) and $d = 540$ nm in Fig. 10(b). We see that this tunes the location of the Fano resonances, and of the cut-off wavelength, below which the Fano resonances associated with the ± 1 orders disappear. This later cut-off is where the ± 1 orders become propagating in air, and are therefore no longer highly reflected at the grating-air interface.

Figures 10(d) and 10(e) show the absorption spectra corresponding to Figs. 10(a) and 10(b). The substantial absorption at $\lambda < 500$ nm, particularly for thick gratings, is due to the imaginary part of n_{TiO_2} increasing dramatically at shorter wavelengths. We limit the scale bar to

$\alpha < 25\%$ to bring out the absorption at longer wavelengths. Associated with each Fano resonance is an absorption peak, which occurs due to the light spending a prolonged time in a waveguide mode. These peaks are of relatively low amplitude and remain highly localized to the centre of the Fano resonance, even when the resonances broaden to form the broadband feature.

The reflection bandwidth may be increased to meet practical requirements by combining multiple gratings. This can be achieved while maintaining relatively low absorption in the region of interest. Figure 10(c) shows the results for a stack where the grating of Fig. 10(a) are placed above the grating of Fig. 10(b), separated by an air layer of thickness $1 \mu\text{m}$. The spectra are quite insensitive to the separation distance as long as $h_{\text{spacer}} > 2d$ such that the gratings do not couple evanescently. The resultant reflection band spans approximately 300 nm ($\Delta\lambda/\lambda \approx 0.3$), similar to previous studies [5]. The absorption peak at approximately $\lambda = 950 \text{ nm}$ is strengthened in Fig. 10(e) because it corresponds to both the $d = 450 \text{ nm}$ and $d = 540 \text{ nm}$ HCGs being on resonance, coupling to the fundamental and first higher order WG modes respectively.

The Fano line-shape ensures that the reflection is close to zero on the other side of the reflection bands. At longer wavelengths, beyond the cut-off of the ± 1 order (here around $\lambda = 1200 \text{ nm}$), the grating acts as a homogenised film with slowly varying F-P resonances. These preliminary results show that dielectric gratings are well suited to being used as spectrum splitting elements with low loss and high wavelength selectivity. Because the HCG reflectors are only a single thin layer (in this case $h < 750 \text{ nm}$), their parasitic absorption may be less than in a multi-layered Bragg stack composed of the same material.

6. Conclusion and discussion

We studied the Fano resonances that occur in high-contrast gratings when guided mode resonances are excited in the presence of slowly varying Fabry-Perot resonances. The broadband regions of near 100% reflection and near 100% transmission were shown to arise because consecutive GMRs have opposite polarity. The checker-board patterns, that are signatures of HCGs, were shown to be caused by the polarity of the Fano resonance flipping when a F-P resonance is passed. We also examined the effect of material absorption and non-normal angles of incidence, finding that good wavelength selectivity can be achieved with little parasitic absorption, even when using lossy materials.

Our results are for TE polarized light. Many applications, such as solar spectrum splitting, however use unpolarized light. One-dimensional structures are intrinsically highly polarization sensitive, and a recent study of HCGs showed that gratings optimized for TM polarized light were substantially thicker than gratings designed for TE polarized light [31]. This strengthens the case for investigating bi-periodic structures for applications involving unpolarized light. The insights developed in this paper are, however, quite general, and should apply also to bi-periodic structures, which support guided modes for both TE and TM polarized light.

Acknowledgments

We thank S. Darbe and H. Atwater from the Californian Institute of Technology, and T. White and K. Catchpole from the Australian National University for fruitful discussions. This work was supported by the Australian Renewable Energy Agency, and the Australian Research Council Discovery Grant and Centre of Excellence Schemes CE110001018. Computation resources were provided by the National Computational Infrastructure, Australia and the NeCTAR Research Cloud, Australia.

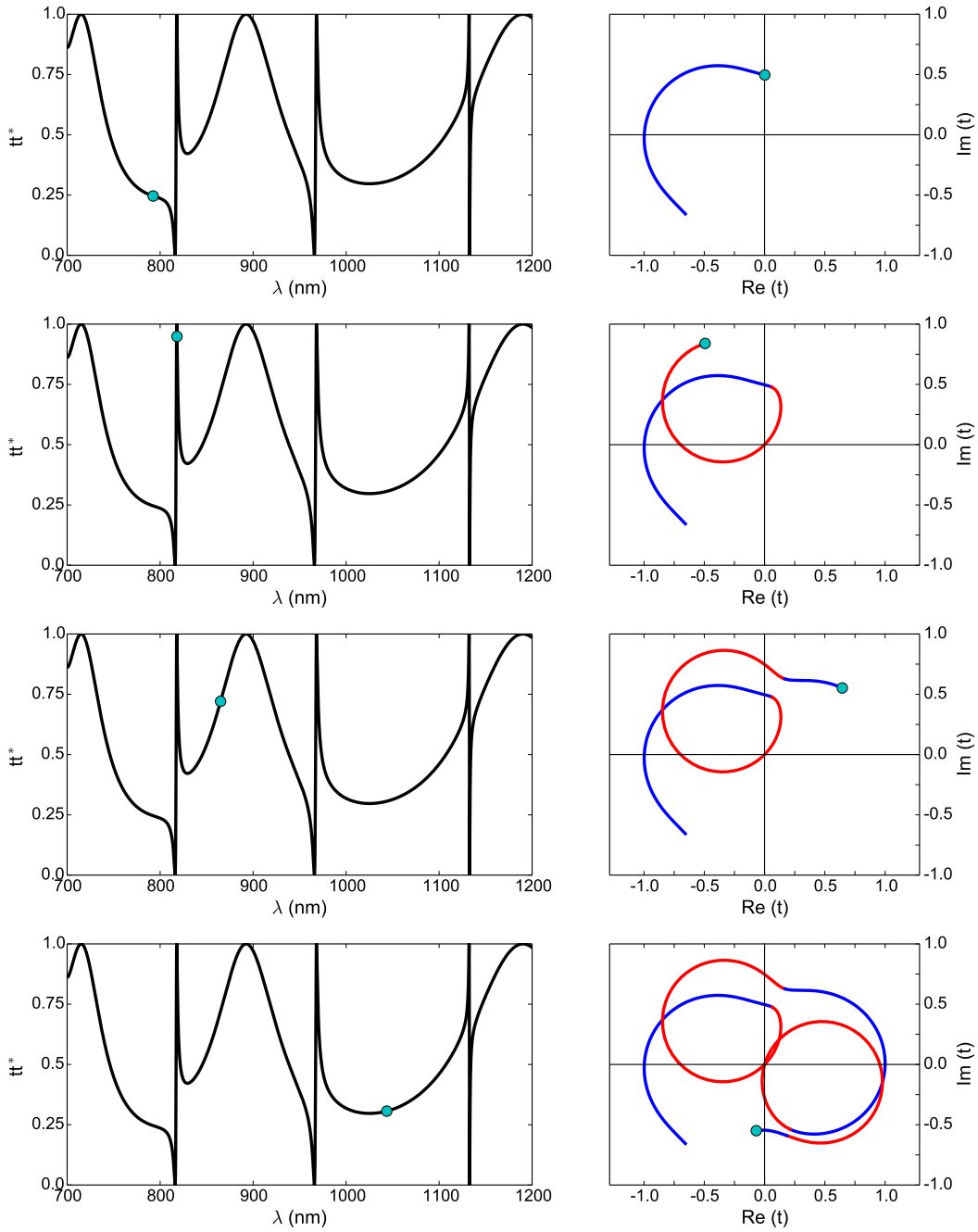


Figure 6.3: Selected frames from Visualization 1 in Paper 6.2 showing the evolution of t in the complex plane as a function of wavelength as well as the corresponding transmission spectrum (Fig. 4 from Paper 6.2). The trajectory of t is shown in red during guided mode resonances and in blue when dominated by the Fabry-Perot resonances.

Epilogue

In Paper 6.2 we examined how the symmetry properties of the guided mode resonances of dielectric gratings lead to broadband reflections. These features have many applications, including as cost-effective spectrum-splitting components in decoupled multi-junction SCs. In the next chapter we find that these same resonances can be engineered to absorb 100% of light of a certain wavelength, even when the gratings are of a deeply sub-wavelength thickness.

Chapter 7

Total Light Absorption in Ultra-thin Gratings

*The sunlights differ,
but there is only one darkness*

Ursula K. Le Guin

Up to now we have studied a variety of nanostructures that may improve the performance of SCs either by enhancing the broadband absorption of thin-film SCs or by splitting the solar spectrum and directing the correct wavelengths to each subcell of multi-junction SCs. In this chapter, our focus is somewhat less on solar applications (for which the absorption across a wide spectrum is crucial), instead choosing to maximise the absorption of ultra-thin structures at a single wavelength. In particular we investigate the *total absorption* of light in deeply-subwavelength layers, which has a range of applications and is a classic problem of great appeal in its own right.

7.1 Applications of Ultra-thin Absorbers

The applications of ultra-thin ($|n|h \ll \lambda$), highly absorbing structures include photodetection and SCs, as well as as all-optical modulators and filters. The former applications make use of the absorbed photons that are converted to electron-hole pairs, while in the latter applications the absorption is a byproduct.

Photodetectors and Extremely-thin Solar Cells

As discussed in Sect. 2.2.6 in the context of the power conversion efficiency of SCs, the non-radiative recombination of a device is proportional to the density of non-radiative recombination centres and its volume. In SCs non-radiative recombinations constitute lost energy, while in photodetectors they contribute to the noise of the device. In order to maximise the signal-to-noise ratio of photodetectors it is therefore advantageous to minimise their volume, while maximising the absorption (the signal).

For solar applications the motivation to use extremely-thin absorbers is the potential to use very inexpensive earth-abundant semiconductors, such as FeS_2 , CuO , and Zn_3P_2 [63, 64]. The electrical properties of these materials generally dictate that the SCs are less than 100 nm thick. This means that, although the intrinsic absorption of these materials is quite high, light management techniques are still required to boost their performance. The advantage offered by earth-abundant semiconductor SCs over organic and dye-sensitized SCs is not efficiency (having $\eta < 10\%$), but rather greater stability and longevity. However, prospects of earth-abundant SCs have declined with the rapid improvement in the efficiency of Perovskite SCs to $\eta > 20\%$.

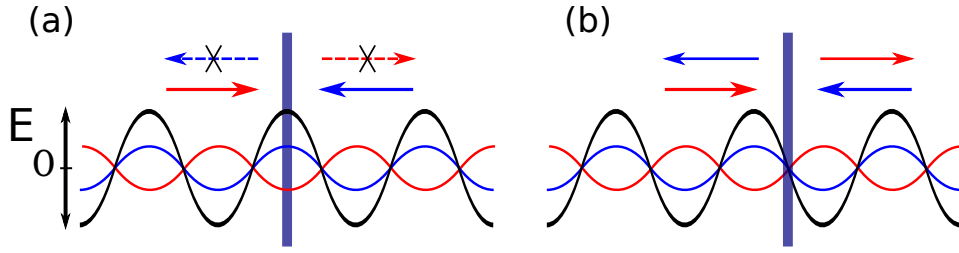


Figure 7.1: Schematic of how the standing wave (black) formed by two coherent, counter-propagating waves (red and blue) lead to (a) high absorption in a thin film when the absorber is placed at the anti-node of the interference pattern, or (b) very low absorption when placed at a node.

Controlling Light with light

Ever since Huygens formulated his principle of the linear superposition of light [220], it has been thought that the modulation of light using light requires high light powers (lasers) and nonlinear media. Being able to control light with light, for example in an all-optical modulator [221], is the premise of many applications, such as ultra-high speed all-optical data networking. These applications have spurred a great deal of the research into nonlinear optics [222].

It was recently shown that nanostructures, in particular ultra-thin absorbers, provide avenues for directly controlling light with light, in linear materials [223]. This is demonstrated in Figs. 7.1(a) and 7.1(b), which show how the interference of two counter-propagating beams creates a standing wave that is sensitive to the intensity and phase of the beams, as well as the position of the absorber relative to the standing wave. When the ultra-thin structure is located at the anti-node of the standing wave, as in Fig. 7.1(a), the absorption may be large (we will show that it can be 100%), meanwhile when the structure is at a node of the standing wave, as in Fig. 7.1(b), the absorption is very small. In this way the amplitude of one beam can be modulated by adjusting the phase of the second beam.

Prelude to Paper 7.2

We now present the paper in which we demonstrate the total absorption of visible light in ultra-thin lamellar gratings, along with its supplementary material:

B. C. P. Sturmberg, T. K. Chong, T. P. White, D.-Y. Choi, L. C. Botten, K. B. Dossou, C. G. Poulton, K. R. Catchpole, R. C. McPhedran and C. M. de Sterke. “Total absorption of visible light in ultra-thin weakly-absorbing semiconductor gratings”. *Optica (Submitted)*

Total absorption of visible light in ultra-thin weakly-absorbing semiconductor gratings

BJÖRN C. P. STURMBERG^{1,6,*}, TECK K. CHONG^{2,6}, DUK-YONG CHOI², THOMAS P. WHITE², LINDSAY C. BOTTEN^{3,4}, KOKOU B. DOSSOU⁴, CHRISTOPHER G. POULTON⁴, KYLIE R. CATCHPOLE², ROSS C. MCPHEDRAN¹, AND C. MARTIJN DE STERKE¹

¹CUDOS and IPOS, School of Physics, University of Sydney, Sydney, 2006, Australia

²Centre for Sustainable Energy Systems, Research School of Engineering, The Australian National University, Canberra, 2601, Australia

³National Computational Infrastructure, Australian National University, Canberra, Australia

⁴CUDOS, School of Mathematical and Physical Sciences, University of Technology Sydney, Sydney, 2007, Australia

⁵Laser Physics Centre, Research School of Physics and Engineering, Australian National University, Canberra, 2601, Australia

⁶Equal contribution first authors

*Corresponding author: bjorn.sturMBERG@sydney.edu.au

Compiled February 8, 2016

The perfect absorption of light in subwavelength thickness layers generally relies on exotic materials, metamaterials or thick metallic gratings. Here we demonstrate that total light absorption can be achieved in ultra-thin gratings composed of conventional materials, including relatively weakly-absorbing semiconductors, which are compatible with optoelectronic applications such as photodetectors and optical modulators. We fabricate a 41 nm thick antimony sulphide grating structure that has a measured absorptance of $A = 99.3\%$ at a visible wavelength of 591 nm, in excellent agreement with theory. We infer that the absorption within the grating is $A = 98.7\%$, with only $A = 0.6\%$ within the silver mirror. A planar reference sample absorbs $A = 7.7\%$ at this wavelength. © 2014 Optical Society of America

OCIS codes: (050.0050) Diffraction and gratings; (310.6628) Subwavelength structures, nanostructures; (350.4238) Nanophotonics and photonic crystals.

<http://dx.doi.org/10.1364/optica.XX.XXXXXX>

1. INTRODUCTION

Completely absorbing light within a layer of deeply subwavelength thickness, with zero reflection and zero transmission, is a challenge of both fundamental theoretical interest and of importance for practical applications such as photodetectors [1], optical switches, modulators and transducers [2, 3]. Total light absorption (TLA) can be achieved in two ways: by adiabatically introducing a complex refractive index change over the space of many wavelengths; or by creating a critically coupled resonance. While the first approach exhibits TLA across a broad bandwidth, it is inconsistent with the use of thin films [4]. The critical coupling condition required for resonant perfect absorption is typically satisfied over a modest bandwidth, but may be achieved in structures of subwavelength thickness.

Resonant perfect absorbers typically couple light into either a longitudinal standing wave in a homogeneous (or homogenised metamaterials) layer, as in Fig. 1(a) [1–3, 5–11], or a sideways propagating Surface Plasmon Polariton (SPP) on the surface of

a corrugated metal, as in Fig. 1(b) [12, 13]. TLA has also been demonstrated using plasmonic nanocomposites [14, 15] and plasmonic metasurfaces [16, 17], however plasmons are only excited by Transverse Magnetically (TM) polarized light. The very strong absorption of unpolarized light has been achieved using crossed or bi-periodic metallic gratings [12, 18], and arrays of single layer doped graphene nano-disks [19]. The fabrication of metamaterial and nanoplasmonic structures is challenging because their minimum feature sizes are on the order of tens of nanometers at infrared and visible wavelengths. The use of metals also makes them incompatible with optoelectronic applications where a photocurrent must be extracted.

Here we experimentally demonstrate the total absorption of light in lamellar gratings of deeply subwavelength thickness and provide a comprehensive theoretical treatment of the phenomenon using the EMUstack package [20–22] for numerical simulations. Figures 1(c) and 1(d) show our theoretical and experimental configurations respectively. In our experiments we show that Transverse Electrically (TE) polarized light, where the

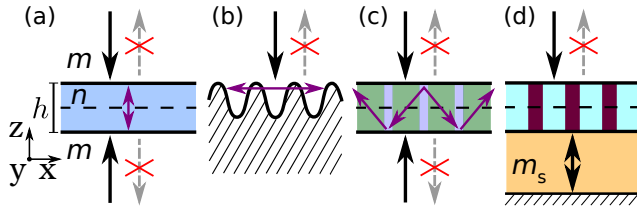


Fig. 1. (a) TLA achieved by coherent illumination of a homogeneous film. (b) TLA achieved with a surface grating on a metal, which couples light into sideways propagating SPPs. (c) TLA in volume gratings occurs at different values of n because higher order grating modes propagate with a significant sideways component. (d) TLA in a one-port system is achieved by placing a mirror behind the absorber at a spacing that ensures the light incident from below is in phase with the light from above.

E-field is along the grating rulings (y -axis in Fig. 1), is totally absorbed in gratings composed of *relatively weakly-absorbing semi-conductors* that have a complex refractive index, $n = n' + in''$, with $n'' \ll n'$. Such materials are abundant in nature and are compatible with optoelectronic applications. Furthermore, our structures have minimum feature sizes close to 100 nm even when targeting visible wavelengths, and can be patterned using standard techniques. We also show numerically that TM polarized light (H-field along y -axis) can be totally absorbed in ultra-thin gratings, and that this requires metallic materials with $n'' > n'$ ($\text{Re}(\epsilon) < 0$), because it relies on the excitation of Surface Plasmon Polaritons (SPPs).

The paper is organized as follows: we begin by reviewing the fundamental limits to absorption in ultra-thin structure; in Sect. A we derive the conditions for TLA in uniform layers; in Sect. 3 we investigate absorption in gratings showing that TLA occurs at very different refractive indices than in uniform layers; in Sect. 4 we demonstrate TLA experimentally in weakly absorbing semiconductor gratings illuminated from one side; in Sect. 5 we show theoretically that TLA in ultra-thin gratings can be achieved using a very wide range of materials; and we conclude in Sect. 6.

2. TOTAL LIGHT ABSORPTION IN ULTRA-THIN LAYERS

Before investigating TLA in ultra-thin gratings we briefly examine TLA in homogeneous ultra-thin films. An ultra-thin structure (*i.e.*, $|n|h \ll \lambda$, where h is the layers thickness) can absorb at most 50% of the incident power when surrounded symmetrically by uniform media (refractive index m) and illuminated from one side [23–25]. This limit arises because the incident energy is equipartitioned between the two longitudinal modes of these structures: one has an even electric field symmetry (anti-node in the centre of the layer as in Fig. 2(a)(i)); the other has an odd symmetry (node in the centre of Fig. 2(a)(ii)) and therefore does not contribute to the absorption because it has negligible field inside the layer. The maximum absorption of $A = 50\%$ occurs when the even mode is totally absorbed.

In order to increase the absorption beyond 50%, the excitation of the odd mode must be suppressed; TLA requires the structure either to not support an odd mode, or for the excitation of the odd mode to be forbidden by the symmetry of the incident field. With the odd mode not excited, TLA occurs when the even mode is fully absorbed. In Fig. 1(a) the absorbing layer is illuminated

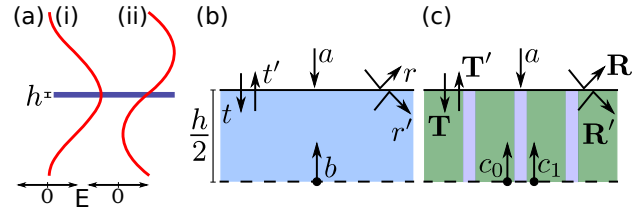


Fig. 2. (a) An ultra-thin layer in a symmetric background supports an even (i), and an odd mode (ii). The symmetry of coherent perfect absorption allows the analysis to focus on one half of the Fabry-Perot etalon: (b) a homogeneous layer; (c) a lamellar grating. Marked are the definitions of the modal amplitudes (a , b) and their reflection and transmission coefficients (r' , and t'), which in (b) are expressed in scattering matrices (R' , and T').

from both sides by coherent light of equal intensity, which totally suppresses the excitation of the odd mode and excites a longitudinal standing wave across the layer. This *coherent perfect absorption* (CPA) configuration [2] produces $A = 100\%$ with the same combination of n , m and h that produces $A = 50\%$ when illuminated from one side.

A. Homogeneous (and homogenized) layers

Previous studies [2, 10] have noted that TLA occurs in homogeneous layers when,

$$r = -\gamma^2, \quad (1)$$

where $r = (m - n)/(m + n)$ is the Fresnel reflection coefficient with normal incidence from the outside, and $\gamma = e^{ink_0h/2}$ is the change in phase *and* amplitude acquired by a mode with complex propagation constant $nk_0 = 2\pi n/\lambda$ upon propagating a distance $h/2$ (see Fig. 2(b)). While Eq. 1 has been reported previously [2, 10], its origin has not been completely clarified. Here we derive Eq. 1 in an intuitive, rigorous manner that generalizes to multimoded structures.

We note that Eq. 1 is consistent with critical coupling, where the loss rate of the resonance is set equal to the rate of incident energy (see Supplementary Materials for derivation). Critical coupling has been used to analyze SPP mediated TLA on corrugated metal surfaces [1]. Piper *et al.* showed theoretically that a monolayer of graphene can achieve TLA when placed on top of a photonic crystal whose energy leakage rate matches the absorption rate of the graphene layer [26].

B. Derivation of Equation 1

In the symmetric configuration shown in Fig. 1(a) we can simplify our analysis by considering the properties of one half of the Fabry-Perot etalon with one incident beam. We begin with the resonance condition for a driven system in the presence of loss; with reference to Fig. 2(b) this is

$$\gamma r' \gamma b + \gamma t a = b, \quad (2)$$

where the first term represents a loop through the structure starting in the centre of the layer (where the amplitude b is marked), and the second term describes the contribution of the driving field to the resonance (also evaluated at the centre). In the absence of a driving field ($a = 0$), Eq. 2 reduces to the Fabry-Perot resonance condition, or equivalently the condition for a bound waveguide mode.

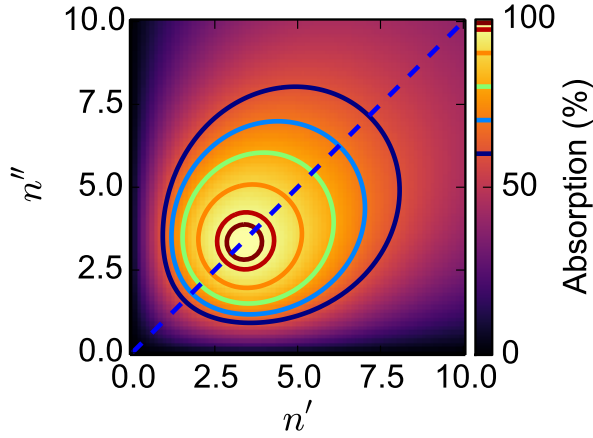


Fig. 3. Absorption of $h = \lambda/70$ thick film as a function of n' and n'' , when illuminated at normal incidence from both sides by in-phase light.

For total absorption we require a further condition: the amplitude of the outgoing wave must vanish,

$$t'\gamma b + ra \equiv 0. \quad (3)$$

This expression also consists of two terms: the leakage from the resonant mode into the superstrate; and Fresnel reflection off the top interface. Finally, Eq. 1 is obtained by solving the simultaneous equations (Eqs. 2 and 3), using the relationship $-rr' + tt' = 1$ [27].

C. Requirements on n' and n''

Rearranging Eq. 1 yields a transcendental expression for the complex refractive index required for TLA, which holds for structures of any thickness,

$$n = \frac{im}{\tan(nk_0h/2)}. \quad (4)$$

Focussing on ultra-thin structures, we take the Taylor expansion of the tangent function in Eq. 4 for small arguments up to third order (derivation in Supplementary Materials). This yields

$$n \simeq \sqrt{\frac{im\lambda}{\pi h} + \frac{1}{3}m^2}, \quad (5)$$

which produces results consistent with the expression derived by Hägglund *et al.* (Eq. 3 in [10]). While Eq. 5 does not extend to the case where the substrate and superstrate have different refractive indices, its far simpler form allows us to obtain further insights.

Equation 5 reveals that TLA in ultra-thin layers, where $\lambda/h \gg m$, is always possible in principle, and requires $n' \sim n''$ with n'' the slightly smaller. Furthermore $|n| \propto \sqrt{\lambda/h}$ in these cases, which allows TLA to be achieved with only moderately large $|n|$ even with very small h . Figure 3 shows the absorption as a function of the real and imaginary parts of n , for a uniform film of thickness $h = \lambda/70$ arranged as in Fig. 1(a) and confirms that TLA occurs where $n' \sim n''$. Throughout our simulations we take $m = 1$.

Very few natural materials satisfy the condition $n' \sim n''$, making TLA a truly unusual effect; examples include dyes [6]

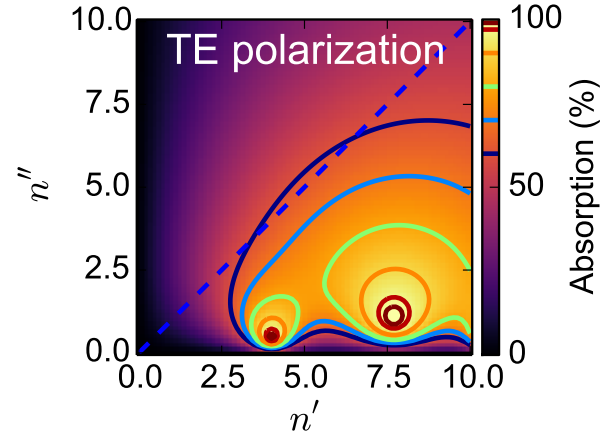


Fig. 4. Absorption of $h = \lambda/70$ thick gratings as a function of n' and n'' , when illuminated at normal incidence from both sides by in-phase TE polarized light. The grating parameters are fixed at $d = 66\lambda/70$ and $f = 0.5$.

and the phase change material VO₂ (when heated to precisely 342 K) [11]. TLA has also been demonstrated using metamaterials, whose subwavelength sized meta-atoms (typically a combination of inductive and capacitive metallic elements) are engineered to give an homogenized effective permittivity and permeability of $\text{Re}(\epsilon_{\text{eff}}) \approx 0$, $\text{Re}(\mu_{\text{eff}}) \approx 0$ on resonance [1, 8, 9], which is consistent with $n'_{\text{eff}} \sim n''_{\text{eff}}$. The Taylor expansion used to derive Eq. 5 is accurate only when $nk_0h/2 \ll 1$, which explains how CPA has also been demonstrated in thick ($nh/\lambda > 385$) wafers of silicon at wavelengths where n'' is three orders of magnitude smaller than n' [2, 7].

3. TOTAL ABSORPTION IN LAMELLAR GRATINGS

Having seen that TLA is difficult to achieve in uniform ultra-thin layers, we now investigate how ultra-thin gratings made of common materials can achieve TLA. We consider the volume gratings illustrated in Figs. 1(c) and 2(c), a fraction f of which has refractive index n and the remainder of which is air, illuminated at normal incidence. The period of the gratings d is chosen so that multiple Bloch modes (each corresponding to superpositions of diffraction orders) propagate within the grating, but that only the specular diffraction order propagates away from the grating in the surrounding medium. These conditions require $n_{\text{eff}}d > \lambda$ and $md < \lambda$ respectively, where n_{eff} of the grating is calculated using the linear mixing formula of the permittivity for TE polarization (the inverse linear mixing formula must be used for TM polarization).

The absorption of TE and TM polarized light in $h = \lambda/70$ thick lamellar gratings is shown in Figs. 4 and 5 respectively, where the gratings have $d = 66\lambda/70$ and $f = 0.5$. Comparing these to the results for a uniform layer of the same thickness (Fig. 3) we see that higher order diffractive grating modes drive TLA at dramatically different values of n than for homogeneous layers, and that the required n differs greatly between the polarizations.

A. TE polarized light: slab waveguide modes

For TE polarized light, Fig. 4 shows that TLA occurs with refractive indices with $n'' \ll n'$ (far below the diagonal in Fig. 4

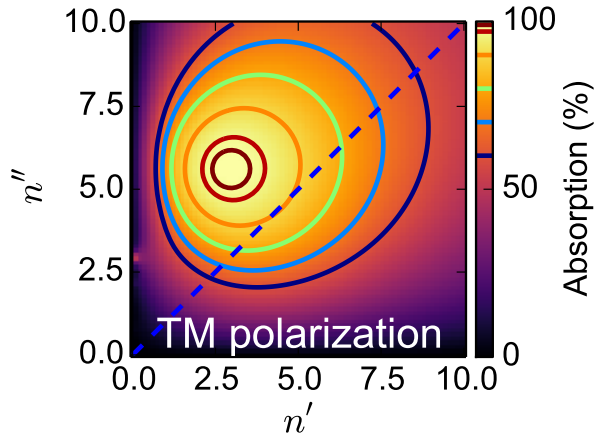


Fig. 5. Absorption of $h = \lambda/70$ thick gratings as a function of n' and n'' , when illuminated at normal incidence from both sides by in-phase TM polarized light. The grating parameters are fixed at $d = 66\lambda/70$ and $f = 0.5$.

indicating that the gratings can be made of conventional, weakly-absorbing semiconductors. We have established that TLA occurs due to the excitation of the fundamental TE leaky slab waveguide mode, which has no cut-off. Such guided mode resonances have previously been studied in detail for their broadband reflection properties [28–30], however TLA has not been reported using this effect. Examining the dispersion relation of the equivalent waveguide mode of the homogenized grating [31] indicates that the absorption peak at $n' \sim 4$ corresponds to the waveguide mode being excited by the grating's first reciprocal lattice vectors, $\pm G = \pm 2\pi/d$, whereas the peak at $n' \sim 7$ is excited by $\pm 2G$. While the value of n' ensures that the guided mode is phase matched to the incident light, the corresponding n'' determines the absorption loss rate of the mode that must be equal to the mode's radiative loss rate in order to fulfil the critical coupling condition and achieve TLA.

B. TM polarized light: surface plasmon polaritons

The results for TM polarized light (using the same gratings as in Fig. 4) are shown in Fig. 5. The refractive index that produces TLA has $n'' > n'$, i.e., $\text{Re}(\epsilon) < 0$, which implies a different underlying mechanism. TM polarized light, unlike TE polarized light, can excite SPPs that propagate in the x -direction, along the interface between the surrounding medium and a metallic grating, with $\text{Re}(\epsilon) > 0$ and $\text{Re}(\epsilon) < 0$ respectively. In ultra-thin gratings, the SPPs of the top and bottom interfaces couple, producing two modes: the Long Range SPP (LRSP) and the Short Range SPP (SRSP), which is more lossy because it is more tightly confined within the absorber. TLA occurs due to the SRSP because its dominant electric field component has an even symmetry in the xy -plane, whereas the LRSP has an odd symmetry. The SRSP creates a single absorption peak in Fig. 5 because its propagation constant is $\beta > 0$, while $\text{Re}(\epsilon) < 0$.

4. EXPERIMENTAL DEMONSTRATION

We now present our experimental demonstrations of TLA of TE polarized light using antimony sulphide (Sb_2S_3) semiconductor gratings, placed above a metallic reflector as illustrated in Fig. 1(d). TLA in this asymmetric configuration is driven by the

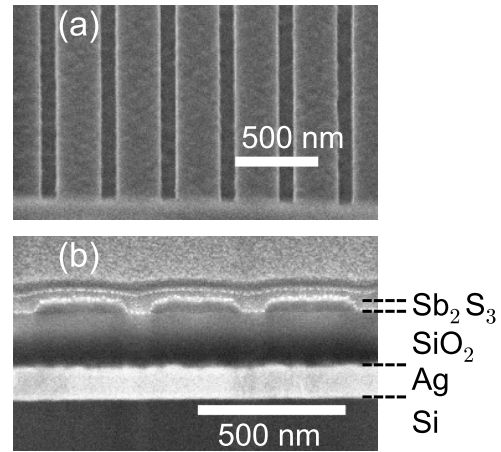


Fig. 6. (a) Scanning electron micrograph at an angle of at 45° of the Sb_2S_3 grating structure with $d = 388$ nm etched groove width 97 nm (designed for TLA at $\lambda = 605$ nm). (b) Focused ion beam cut cross-sectional view where individual layers and the grating are clearly distinguished and labelled.

same underlying physics as in Figs. 1(c), but allows for TLA with only a single incident beam and is experimentally far simpler. Sb_2S_3 was chosen as the absorbing layer because it is a stable semiconductor that can be deposited in thin films using thermal evaporation and it has a suitable refractive index and absorption coefficient (in its as-deposited amorphous form) to meet the TLA requirements close to $\lambda = 600$ nm. We emphasize that the results of Sect. 3 demonstrate that TLA in ultra-thin gratings is a general effect that can be achieved using a very wide range of common materials.

A. Fabrication

Figures 6(a) and 6(b) show SEM images of a fabricated grating structure on a polished Si wafer with light incident from air. From bottom to top, the structure consists of: a 130 nm Ag reflector deposited by thermal evaporation; a $h_s = 245$ nm thick SiO_2 spacer layer (refractive index m_s) deposited by plasma-enhanced chemical-vapour-deposition (PECVD); and a 41 nm thick amorphous Sb_2S_3 layer deposited by thermal evaporation. The grating was fabricated using electron-beam-lithography to define a mask in a PMMA resist, followed by an inductively-coupled plasma (ICP) etch using CHF_3 gas. Further details of the deposition and processing conditions are provided in the Supplementary Material.

The SiO_2 spacer layer is crucial for TLA in the asymmetric configuration because the light striking the absorber from below must be exactly in phase with the light incident from above to prevent the excitation of the odd mode. In the idealised case of an infinitesimally thick absorber and a perfect mirror [5] the required spacer thickness is $h_s = \lambda/4m_s$. However at the wavelengths of interest in our demonstration, $\lambda \sim 600$ nm, Ag is an imperfect metal, which requires $h_s < \lambda/4m_s$ (details in Supplementary Materials).

We here focus on two 41 nm thick gratings, designed to achieve TLA at $\lambda = 591$ nm and $\lambda = 605$ nm, which have $d = 375$ nm, $f = 72\%$, and $d = 385$ nm, $f = 75\%$ respectively. The measured refractive indices of Sb_2S_3 at these wavelengths are $n_{\text{Sb}_2\text{S}_3} = 3.342 + 0.096i$ and $n_{\text{Sb}_2\text{S}_3} = 3.298 + 0.074i$

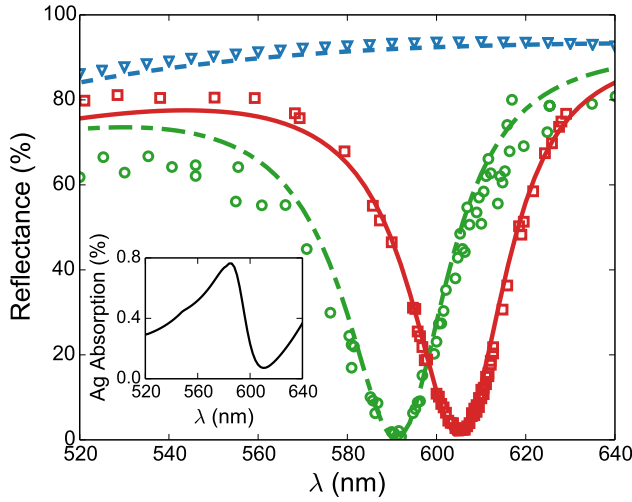


Fig. 7. Reflectance of the fabricated gratings designed for TLA of TE polarized light at $\lambda = 591$ nm (green) and $\lambda = 605$ nm (red) and the planar reference structure (blue). The measured values (triangles, circles and squares respectively) and simulated predictions (dashed, dot-dashed and solid curves) show excellent agreement, in particular in the vicinity of reflectance minima. The inset shows the simulated absorption in the Ag reflector below the grating optimized for $\lambda = 591$ nm.

respectively, corresponding to absorption coefficients of $\alpha = 2.04 \times 10^4 \text{ cm}^{-1}$ and $\alpha = 1.54 \times 10^4 \text{ cm}^{-1}$, and single pass absorptances of $A = 8.0\%$ and 6.1% .

B. Results

Optical reflection measurements were performed in a confocal microscope using a $20\times$, $\text{NA} = 0.4$ objective lens, and a broadband supercontinuum light source. Reflected light was collected by a $100 \mu\text{m}$ core multimode fiber and coupled into a spectrometer for detection. The reflection spectrum from a planar, unpatterned region was compared to the spectrophotometer-measured reflectance of the same sample, and this was used to calibrate the reflectance from the patterned region. The measured (symbols) and simulated (curves) reflection spectra are plotted in Fig. 7, and show excellent quantitative agreement, especially in the wavelengths in the vicinity of the reflectance minima, for which they are calibrated.

The minimum measured reflectance is $0.7 \pm 0.5\%$ at 591 nm, which corresponds to an absorption of $A = 99.3 \pm 0.5\%$ since the Ag mirror is sufficiently thick to prevent any transmission to the substrate. Although it is not possible to measure the absorption in the Sb_2S_3 and in the Ag separately, we can infer these values with some confidence from simulations given the excellent agreement between the modelled and measured results. The simulations indicate that, at $\lambda = 591$ nm, the planar Sb_2S_3 film absorbs $A = 7.7\%$, and the Ag mirror absorbs $A = 0.3\%$ ($A = 8.0\%$ total). After patterning the semiconductor layer, the calculated absorption increases to $A = 98.9\%$ within the Sb_2S_3 grating and $A = 0.6\%$ in the Ag (the simulated absorption spectrum of the Ag layer is shown in the inset in Fig. 7(c)). We therefore infer $A = 98.7\%$ in the experimentally realised Sb_2S_3 grating. For the second grating the maximum absorption at $\lambda = 605$ nm is $A = 97.4 \pm 0.5\%$, which we infer is $A = 96.6\%$ in the Sb_2S_3 grating. This is an even larger increase relative to the

planar sample ($A = 6.1\%$ at $\lambda = 605$ nm) because the absorption coefficient of Sb_2S_3 decreases noticeably with increasing wavelength, from $\lambda = 591$ nm to $\lambda = 605$ nm.

5. GENERALITY OF TLA EFFECT

Having shown that TLA can be achieved experimentally and numerically using a specific material, we now investigate what range of material parameters are compatible with TLA in ultra-thin gratings. To do this we consider gratings with a range of $\epsilon h/\lambda$ values, and numerically optimize the d and f of the grating such that the absorption is maximized. Our optimizations were carried out in terms of $\epsilon h/\lambda$ because we established that the properties of ultra-thin lamellar gratings depend only on this parameter. The relation $|n| \propto \sqrt{\lambda/h}$ therefore applies to both homogeneous layers and gratings. Our proof of this property, presented in the Supplementary Material, involves reducing the finitely conducting lamellar grating formulation [32] to the grating layer formulation of Petit and Bouchitté [33] in the limit of infinitesimal thickness, and is consistent with the formulation of perfectly conducting zero thickness gratings [34].

The results of the optimization for TE and TM polarized light are shown in Figs. 8(a) and 8(b) respectively. Here the coloured contours show the maximum absorption obtained at each value of $\epsilon h/\lambda$, and the black dashed curves indicate the $\epsilon h/\lambda$ of ultra-thin layers of common materials across the visible spectrum, $350 \text{ nm} < \lambda < 800 \text{ nm}$. In Fig. 8(a) the dashed curves correspond to $h = \lambda/30$ layers of CdTe, InP, GaAs (left to right), and $h = 41\lambda/605$ layers of Sb_2S_3 (furthest right). The values of our experimental demonstrations in Sb_2S_3 at $\lambda = 591$ nm, 605 nm are marked by a magenta triangle and circle respectively. In Fig. 8(b) meanwhile, the dashed curves show the values for $h/\lambda = 1/20$ thick layers of Cu, Au, and Ag [35] (top to bottom), across the same visible wavelength range. Comparing these trajectories with the optimized absorption indicates that TLA can be achieved across almost the whole visible spectrum. The position of the dashed curves expand/contract radially from the origin when the h/λ ratio is decreased/increased.

A. Theoretical analysis of absorption in gratings

In order to analyse TLA in gratings we examine the coupling coefficients between the grating modes and the plane waves of the surrounding medium (Fig. 2(c)); for example, t_{00} is the coupling coefficient of the incident specular plane wave with the “fundamental” grating mode (labelled BM0), while r'_{01} describes the reflection of the fundamental grating mode into the “higher order” grating mode (labelled BM1). We consider the case of normal incidence upon a grating in which only two modes propagate, whose amplitudes are c_0, c_1 ; when more modes propagate (such as at non-normal incidence) the expressions generalize with scattering matrices representing the coupling between all propagating modes.

In the case of two propagating modes, the resonance condition of BM1 is given by

$$\gamma_1 t_{01} a + \gamma_1 r'_{01} \gamma_0 c_0 + \gamma_1 r'_{11} \gamma_1 c_1 = c_1. \quad (6)$$

From left to right, these terms represent: the light incident from the surrounding medium; the coupling between BM0, and BM1; and the Fabry-Perot resonance of BM1. Combining this with the resonance condition of BM0 (including cross coupling), and the requirement of no outgoing wave, we find that TLA occurs

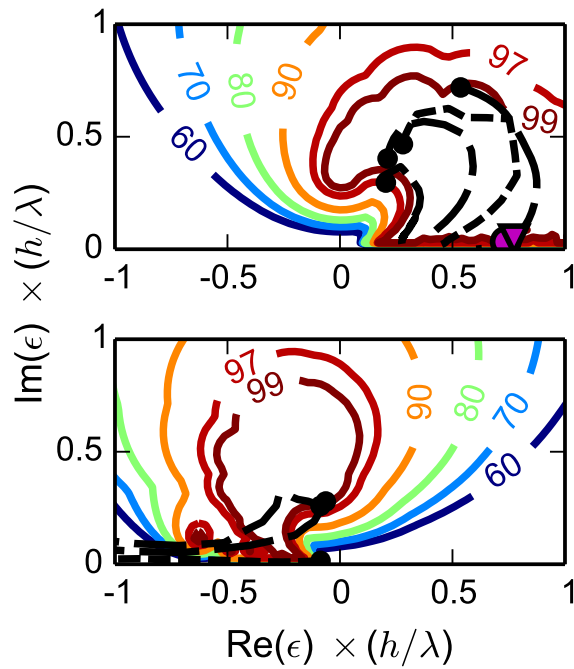


Fig. 8. Absorption as a function of $\text{Re}(\epsilon)h/\lambda$ and $\text{Im}(\epsilon)h/\lambda$, where d and f have been optimized at each $\epsilon h/\lambda$ (coloured contours). The dashed black curves indicate $\epsilon h/\lambda$ values of common materials at visible wavelengths between 350 nm (marked by circle) and 800 nm. In (a) the dashed curves correspond to $h = \lambda/30$ layers of CdTe, InP, GaAs (left to right), and $h = 41\lambda/605$ layers of Sb_2S_3 (furthest right), while in (b) the curves show the values of $h = \lambda/20$ layers of Cu, Au, and Ag (top to bottom). The values of our experimental demonstrations in Sb_2S_3 at $\lambda = 591$ nm, 605 nm are marked as a magenta triangle and circle respectively.

when

$$\det \begin{bmatrix} r_{00} & t'_{00}\gamma_0 & t'_{10}\gamma_1 \\ \gamma_0 t_{00} & \gamma_0 r'_{00}\gamma_0 - 1 & \gamma_1 r'_{10}\gamma_0 \\ \gamma_1 t_{01} & \gamma_1 r'_{01}\gamma_0 & \gamma_1 r'_{11}\gamma_1 - 1 \end{bmatrix} = 0. \quad (7)$$

The top left quadrant of Eq. 7 reproduces the condition for TLA in uniform films (*i.e.* Eq. 2, and 3), where only one mode propagates within the absorber. Equation 7 accurately predicts the complex refractive indices that maximise the absorption of ultra-thin gratings (Figs. 4 and 5) and we now draw on it to understand the differences between the total absorption of TE and TM polarized light.

B. Comparison between polarizations

A striking difference between Figs. 4 and 5 is that there is no absorption peak due to the excitation of the fundamental TM waveguide mode in Figs. 5, even though this mode also has no cut-off. This is because the field of this mode is concentrated almost totally within the air surrounds in ultra-thin structures, with only very little field inside the absorber, which is expressed in a modal effective index of the mode being $n_{\text{eff}} \simeq 1$ [36]. This field distribution prevents the mode from contributing noticeably to the absorption and also means the mode is very weakly

excited, because there is a negligible overlap between the guided mode and the incident field. The analysis using Eq. 7 leads to the same conclusion; the phase of r'_{11} is approximately 0 and π , for TE and TM respectively, corresponding to a node and an anti-node of the electric field close to the grating's interface [37]. In order to observe an absorption peak for TM polarized light in gratings with $n'' < n'$, the refractive index range must be increased to $|n| \approx 40$, which is unrealistic, or the thickness of a structure with $n'_{\text{eff}} \sim 5$ must be increased to $h > 100$ nm, at which point the structure is no longer ultra-thin.

6. CONCLUSION AND DISCUSSION

We have shown theoretically and experimentally that ultra-thin gratings made of a wide range of weakly-absorbing semiconductors can absorb nearly 100% of TE polarized light. We also showed theoretically that TM polarized light can be totally absorbed in ultra-thin gratings made of metals. We measure a peak absorptance of $A = 99.3 \pm 0.5\%$ at $\lambda = 591$ nm, in a structure with a 41 nm thick Sb_2S_3 grating, where $A = 98.7\%$ within the grating. Our findings show that the total absorption of shorter visible wavelengths can be straightforwardly achieved by using thinner gratings or materials with smaller ϵ . Our gratings are far simpler to design and fabricate than existing ultra-thin perfect absorbers which rely on exotic materials and metamaterials, and may be generalized to achieve TLA of both polarizations simultaneously by using bi-periodic structures. Ultra-thin perfect absorbers made of weakly-absorbing semiconductors may be used in optoelectronic applications such as photodetectors, where the use of semiconductors provides the possibility of extracting a photocurrent or measuring the photoresistivity.

7. SUPPLEMENTARY MATERIAL

Additional information regarding sample fabrication, optical characterization, and the effects of non-ideal metal back reflectors. Critical coupling derivation of Eq. 1, derivation of Eq. 5 and proof of the invariance of the properties of ultra-thin gratings for constant $\epsilon h/\lambda$.

FUNDING INFORMATION

This work was supported by the Australian Renewable Energy Agency, and the Australian Research Council Discovery Grant and Centre of Excellence (CE110001018) Schemes.

ACKNOWLEDGMENTS

We acknowledge the assistance of Y. Osario Mayon with FIB and ellipsometry measurements and X. Fu with the reflectance measurements. Computational resources were provided by the National Computational Infrastructure, Australia and the NeCTAR Research Cloud, Australia. Experimental facilities were provided by the Australian National Fabrication Facility and Centre for Advanced Microscopy at the Australian National University.

REFERENCES

1. C. M. Watts, X. Liu, and W. J. Padilla, "Metamaterial electromagnetic wave absorbers." *Adv. Mater.* **24**, OP98–120 (2012).
2. Y. D. Chong, L. Ge, H. Cao, and A. D. Stone, "Coherent perfect absorbers: Time-reversed lasers," *Phys. Rev. Lett.* **105**, 1–4 (2010).

3. J. Zhang, K. F. MacDonald, and N. I. Zheludev, "Controlling light-with-light without nonlinearity," *Light Sci. Appl.* **1**, 1–5 (2012).
4. K. X. Wang, Z. Yu, V. Liu, M. L. Brongersma, T. F. Jaramillo, and S. Fan, "Nearly Total Solar Absorption in Ultrathin Nanostructured Iron Oxide for Efficient Photoelectrochemical Water Splitting," *ACS Photonics* **1**, 235–240 (2014).
5. W. W. Salisbury, "Absorbent Body for Electromagnetic Waves," (1952).
6. J. R. Tischler, M. S. Bradley, and V. Bulović, "Critically coupled resonators in vertical geometry using a planar mirror and a 5 nm thick absorbing film." *Opt. Lett.* **31**, 2045–2047 (2006).
7. W. Wan, Y. Chong, L. Ge, H. Noh, A. D. Stone, and H. Cao, "Time-reversed lasing and interferometric control of absorption." *Science* **331**, 889–892 (2011).
8. N. I. Landy, S. Sajuyigbe, J. J. Mock, D. R. Smith, and W. J. Padilla, "Perfect Metamaterial Absorber," *Phys. Rev. Lett.* **100**, 207402 (2008).
9. X. Liu, T. Starr, A. F. Starr, and W. J. Padilla, "Infrared Spatial and Frequency Selective Metamaterial with Near-Unity Absorbance," *Phys. Rev. Lett.* **104**, 207403 (2010).
10. C. Hägglund, S. P. Apell, and B. Kasemo, "Maximized optical absorption in ultrathin films and its application to plasmon-based two-dimensional photovoltaics." *Nano Lett.* **10**, 3135–41 (2010).
11. M. A. Kats, D. Sharma, J. Lin, P. Genevet, R. Blanchard, Z. Yang, M. M. Qazilbash, D. N. Basov, S. Ramanathan, and F. Capasso, "Ultra-thin perfect absorber employing a tunable phase change material," *Appl. Phys. Lett.* **101**, 221101 (2012).
12. E. Popov, D. Maestre, R. C. McPhedran, M. Nevière, M. C. Hutley, and G. H. Derrick, "Total absorption of unpolarized light by crossed gratings." *Opt. Express* **16**, 6146–55 (2008).
13. D. Maestre, "Diffraction gratings: An amazing phenomenon," *Comptes Rendus Phys.* **14**, 381–392 (2013).
14. M. K. Hedayati, F. Faupel, and M. Elbahri, "Tunable broadband plasmonic perfect absorber at visible frequency," *Appl. Phys. A Mater. Sci. Process.* **109**, 769–773 (2012).
15. M. K. Hedayati and M. Elbahri, "Perfect plasmonic absorber for visible frequency," **1**, 259–261 (2013).
16. Y. Zhang, T. Wei, W. Dong, K. Zhang, Y. Sun, X. Chen, and N. Dai, "Vapor-deposited amorphous metamaterials as visible near-perfect absorbers with random non-prefabricated metal nanoparticles." *Sci. Rep.* **4**, 4850 (2014).
17. G. M. Akselrod, J. Huang, T. B. Hoang, P. T. Bowen, L. Su, D. R. Smith, and M. H. Mikkelsen, "Large-Area Metasurface Perfect Absorbers from Visible to Near-Infrared," *Adv. Mater.* pp. 1–7 (2015).
18. K. Aydin, V. E. Ferry, R. M. Briggs, and H. A. Atwater, "Broadband polarization-independent resonant light absorption using ultrathin plasmonic super absorbers," *Nat. Commun.* **2**, 517 (2011).
19. S. Thongrattanasiri, F. H. L. Koppens, and F. J. García de Abajo, "Complete Optical Absorption in Periodically Patterned Graphene," *Phys. Rev. Lett.* **108**, 047401 (2012).
20. "EMUstack: An open-source package for Bloch mode based calculations of scattering matrices," .
21. K. B. Dossou, L. C. Botten, A. A. Asatryan, B. C. P. Sturmberg, M. A. Byrne, C. G. Poulton, R. C. McPhedran, and C. M. de Sterke, "Modal formulation for diffraction by absorbing photonic crystal slabs," *J. Opt. Soc. Am. A* **29**, 817–831 (2012).
22. B. C. P. Sturmberg, K. B. Dossou, F. J. Lawrence, C. G. Poulton, R. C. McPhedran, C. M. de Sterke, and L. C. Botten, "EMUstack: an open source route to insightful electromagnetic computation via the Bloch mode scattering matrix method," *Computer Physics Communications* (In Press) .
23. L. N. Hadley and D. M. Dennison, "Reflection and Transmission Interference Filters," *J. Opt. Soc. Am.* **38**, 483 (1948).
24. R. Petit and G. Bouchitté, "On The Properties Of Very Thin Metallic Films In Microwaves : The Concept Of An Infinitely Conducting And Infinitely Thin Ohmic Material Revisited," in "Proc. SPIE 1029, Scatt. Diffraction," (1989).
25. L. C. Botten, R. C. McPhedran, N. A. Nicorovici, and G. H. Derrick, "Periodic models for thin optimal absorbers of electromagnetic radiation," *Phys. Rev. B* **55**, R16072–R16082 (1997).
26. J. R. Piper and S. Fan, "Total Absorption in a Graphene Monolayer in the Optical Regime by Critical Coupling with a Photonic Crystal Guided Resonance," *ACS Photonics* **1**, 347–353 (2014).
27. M. Born and E. Wolf, "Principles of Optics," (2005).
28. R. Magnusson and S. S. Wang, "New principle for optical filters," *Appl. Phys. Lett.* **61**, 1022–1024 (1992).
29. S. S. Wang and R. Magnusson, "Theory and applications of guided-mode resonance filters." *Appl. Opt.* **32**, 2606–2613 (1993).
30. S. Collin, "Nanostructure arrays in free-space: optical properties and applications," *Reports Prog. Phys.* **77**, 126402 (2014).
31. A. W. Snyder and J. D. Love, *Optical Waveguide Theory* (Chapman and Hall, 1983).
32. L. C. Botten, M. Craig, R. C. McPhedran, J. Adams, and J. Andrewartha, "The Dielectric Lamellar Diffraction Grating," *Opt. Acta Int. J. Opt.* **28**, 413–428 (1981).
33. G. Bouchitté and R. Petit, "On the concepts of a perfectly conducting material and of a perfectly conducting and infinitely thin screen," *Radio Sci.* **24**, 13 (1989).
34. L. Botten, R. McPhedran, and G. Milton, "Perfectly Conducting Lamellar Gratings: Babinet's Principle and Circuit Models," *J. Mod. Opt.* **42**, 2453–2473 (1995).
35. P. B. Johnson and R. W. Christy, "Optical Constants of the Noble Metals," *Phys. Rev. B* **6**, 4370–4379 (1972).
36. When $|n|h/\lambda \ll 1$, the dispersion relation of TM mode remains close to the light line for all but very large transverse wavevectors, which are not excited by gratings with $d \sim \lambda$.
37. Consistent with the phases of the TE and TM Fresnel coefficients of a homogeneous interface at angles of incidence just beyond total internal reflection (equivalent transverse wavevector as BM1).

Total absorption of visible light in ultra-thin weakly-absorbing semiconductor gratings: Supporting Information

BJÖRN C. P. STURMBERG^{1,6,*}, TECK K. CHONG^{2,6}, DUK-YONG CHOI², THOMAS P. WHITE², LINDSAY C. BOTTEN^{3,4}, KOKOU B. DOSSOU⁴, CHRISTOPHER G. POULTON⁴, KYLIE R. CATCHPOLE², ROSS C. MCPHEDRAN¹, AND C. MARTIJN DE STERKE¹

¹CUDOS and IPOS, School of Physics, University of Sydney, Sydney, 2006, Australia

²Centre for Sustainable Energy Systems, Research School of Engineering, The Australian National University, Canberra, 2601, Australia

³National Computational Infrastructure, Australian National University, Canberra, Australia

⁴CUDOS, School of Mathematical and Physical Sciences, University of Technology Sydney, Sydney, 2007, Australia

⁵Laser Physics Centre, Research School of Physics and Engineering, Australian National University, Canberra, 2601, Australia

⁶Equal contribution first authors

*Corresponding author: bjorn.sturMBERG@sydney.edu.au

Compiled February 8, 2016

Additional information regarding sample fabrication, optical characterization, and the effects of non-ideal metal back reflectors. Critical coupling derivation of Eq. 1, derivation of Eq. 5 and proof of the invariance of the properties of ultra-thin gratings for constant eh/λ . © 2016 Optical Society of America

<http://dx.doi.org/> [supplementary document doi]

1. EFFECT OF AN IMPERFECT METAL REFLECTOR

Figures S1(a) and S2(a) show the absorption of a $h = \lambda/70$ thick uniform layer illuminated from one side, with a spacer layer and reflector on the other side. This absorber layer is therefore the same as shown in Fig. 3(a) of the main text, except that it is arranged in the asymmetric configuration of Fig. 1(e) rather Fig. 1(c). In Fig. S1(a) the reflector is made of a perfect conductor and in S2(a) it is made of silver. TLA occurs at a smaller $|n|$ than in the case of coherent illumination from both sides (Fig. 3(a)) because the light entering the layer from below has a lower amplitude than the light incident from above (it has passed through the absorber at least once). The condition $n' \sim n''$ is preserved because it is a fundamental requirement of critically coupling the standing wave inside the absorber with the incident propagating wave.

For each value of n we numerically optimize the thickness of the spacer layer, h_s , which are presented in Figs. S1(b) and S2(b) for the perfect conductor and silver back reflectors respectively. In the case of the perfect conductor the optimal spacer layer thickness is $h_s = \lambda/4m_s$ (indicated by the red curve). Silver

however is not an ideal metal at $\lambda \sim 600$ nm, and while its reflection coefficient has a magnitude close to unity, its phase is not precisely π , as it is for a perfect conductor. The spacer thickness required for TLA (which occurs at a value of n just below the diagonal) is $h_s < \lambda/4m_s$.

2. SAMPLE FABRICATION

The Sb₂S₃ grating stack was fabricated in the following way. Ag of $h = 130$ nm was thermally deposited on top of a polished silicon substrate at a deposition rate of $3 \text{ \AA}\cdot\text{s}^{-1}$ using an Angstrom thermal evaporator. Subsequently, a 245 nm thick SiO₂ film was deposited using an Oxford Plasmalab 100 dual frequency plasma-enhanced-chemical-vapour-deposition (PECVD) tool at a temperature of 300°C and deposition rate of $0.92 \text{ nm}\cdot\text{s}^{-1}$. The resulting SiO₂ film has a refractive index n of 1.47 at $\lambda = 600$ nm, measured by ellipsometry. A thin layer of Sb₂S₃ was then thermally evaporated on top of the SiO₂ film using an Angstrom system with a deposition rate of $0.3 \text{ \AA}\cdot\text{s}^{-1}$. The resulting Sb₂S₃ film thickness was 41 nm.

To form the grating, a layer of positive photo resist (950

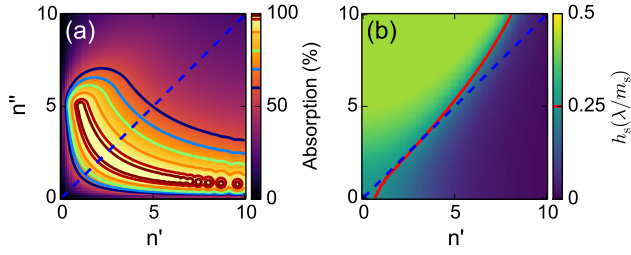


Fig. S1. (a) Absorption as a function of complex refractive index for a uniform film with $h = \lambda/70$, placed above a perfect conductor with a spacer layer of refractive index m_s and a thickness h_s shown in (b). The thickness of the spacer layer has been optimized to maximize the absorption. The TLA point lies slightly below the diagonal dashed line, where $h_s = \lambda/4m_s$.

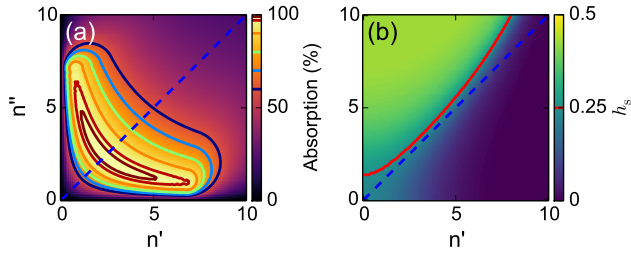


Fig. S2. (a) Absorption as a function of complex refractive index for a uniform film with $h = \lambda/70$, placed above a silver reflector with a spacer layer of refractive index m_s and a thickness h_s shown in (b). The thickness of the spacer layer has been optimized to maximize the absorption. The TLA point lies slightly below the diagonal dashed line, where $h_s < \lambda/4m_s$.

PMMA A4) was spin-coated onto the stack (Si/Ag/SiO₂/Sb₂S₃) and baked on a hotplate for 3 minutes at 180°C. Gratings of size 100 $\mu\text{m} \times 100 \mu\text{m}$ with varying period and line width were exposed in the PMMA using a Raith 150 electron-beam-lithography (EBL) system with a writing dose of 200 $\mu\text{C}\cdot\text{cm}^{-2}$. The exposed patterns were developed in MIBK/IPA developer solution for 1 minute followed by an IPA rinse to prevent over-development.

Sb₂S₃ can be etched using inductively-coupled-plasma (ICP) etch using CHF₃ gas. A range of etching parameters was initially trailed on test patterns to identify the conditions for etching a thin layer of Sb₂S₃. The optimal etching recipe was found to be: pressure = 15 mTorr, ICP power = 200 W, RF power = 75 W and CHF₃ flow rates of 50 sccm. With these conditions 60 s is sufficient to remove 41 nm of Sb₂S₃. Following the etching, the remaining PMMA was removed using oxygen plasma etch for 15 minutes.

3. OPTICAL CHARACTERIZATION

The grating reflectance spectra were measured in two steps. First, the reflectance of a large ($\sim 1 \text{ cm}^2$) unpatterned area of the sample was measured in a spectrophotometer with an integrating sphere attachment (Perkins Elmer). This provided an accurate ($\pm 1.3\%$) reflectance reference for calibrating the small-area reflectance measurements on the patterned areas of the sample.

The patterned sample was measured in a WITec 300s confocal

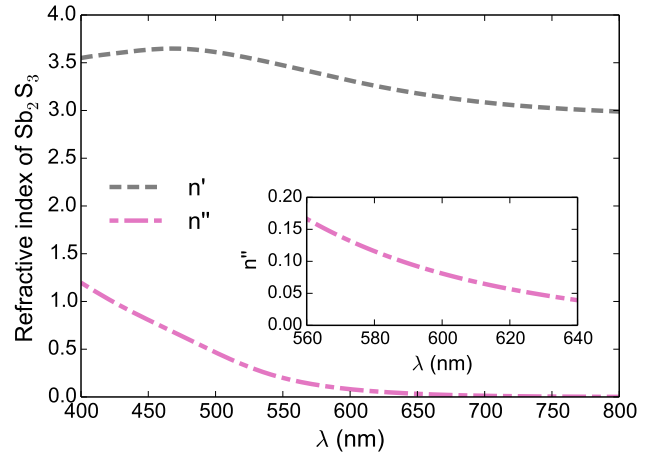


Fig. S3. The real (n') and imaginary (n'') parts of the refractive index of Sb₂S₃, as measured using ellipsometry. A thin layer ($h \sim 60 \text{ nm}$) of Sb₂S₃ was deposited directly on top of a polished silicon wafer. The band gap energy of the evaporated Sb₂S₃ is $\sim 1.82 \text{ eV}$, corresponding to $\lambda = 680 \text{ nm}$. For a 41 nm thick Sb₂S₃ film the single pass absorption at $\lambda = 605 \text{ nm}$ is 6.1% and 11.9% for double pass absorption at the vicinity of reflectance minimum.

microscope using a 20 \times , NA = 0.4 objective lens for illumination and collection of reflected light. Illumination was provided by a broadband supercontinuum source (Fianium SC450-2) that was filtered using an acousto-optical tunable filter (AOTF) fiber-coupled to the microscope. The AOTF was used to select eight closely-spaced wavelengths at a time for reflectance measurements, and measurements were repeated with different illumination wavelengths in order to span the spectral range of interest from $\lambda = 520 \text{ nm}$ to $\lambda = 640 \text{ nm}$. Reflected light was collected by a 100 μm multimode fiber and coupled into a NIR spectrometer (Princeton Instruments) for detection. Spectra of patterned and unpatterned regions were measured in this way and calibrated using the large-area reference reflectance data to obtain the grating reflectance. Reflectance measurements were repeated on several occasions using multiple samples and found to be highly reproducible. The main source of uncertainty in the reflectance measurements in the vicinity of the absorption peak is thought to be random fluctuations in the source intensity and/or spectrum. Based on analysis of the raw spectral data, we estimate the accuracy of the measured reflectance values to be $\pm 0.5\%$.

In Fig. S4 we present the reflection spectra of four Sb₂S₃ grating structures, all of thickness $h_s = 41 \text{ nm}$ (measured shown as symbols and simulated shown as curves). The gratings with reflection minima at $\lambda = 591 \text{ nm}$, $\lambda = 605 \text{ nm}$ are the same as in the main text, while those with reflection minima at $\lambda = 595 \text{ nm}$, $\lambda = 610 \text{ nm}$ have $d = 380 \text{ nm}$, $f \sim 73\%$, and $d = 390 \text{ nm}$, $f \sim 75\%$ respectively.

4. CRITICAL COUPLING

In this section we show that critical coupling is consistent with Eq. 1 in the main text. Consider a uniform film of refractive index $n = n' + in''$ and thickness $h/2$, enclosed on one side by a perfect mirror, and bounded on the other by a medium of refractive index m .

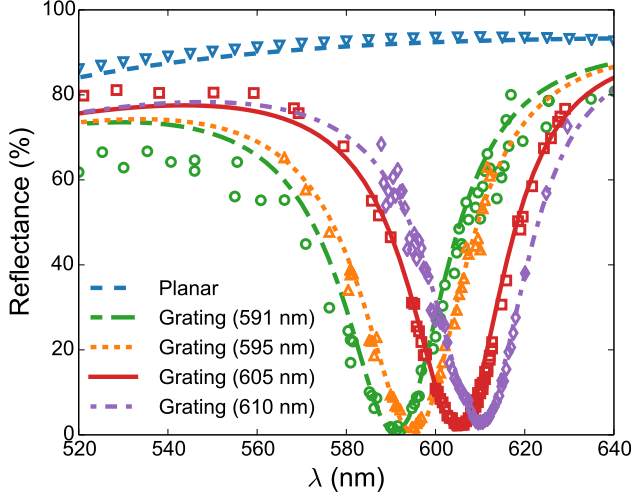


Fig. S4. Reflectance of various gratings and the reference planar structure. Measured results are shown as symbols and simulated results are shown as curves, which are referred to in the legend by the wavelength of their reflectance minimum. In the interest of clarity we only present measurements close to the reflectance minima at $\lambda = 595$ nm and $\lambda = 610$ nm.

Photons oscillating within the layer strike the interface between media n , m every hn'/c seconds, where c is the speed of light in vacuum. The probability of a photon remaining within the layer after striking the interface is $|r'|^2$, with r' defined in the main text. The probability of the same photon being within the layer after another round trip (at a time $t = (hn'/c)$ seconds later) is $|r'|^4$. The probability of the photon remaining within the layer therefore decays exponentially as $\rho_1(t) = \exp(-t/\tau_1)$, where the decay constant τ_1 is found from,

$$\rho_1(t) = (|r'|^2)^{ct/n'h} = e^{\ln(|r'|^2)ct/n'h} \quad (1)$$

$$= e^{\ln(1-(1-|r'|^2))ct/n'h} \quad (2)$$

$$= e^{-\ln(1-|r'|^2)ct/n'h}. \quad (3)$$

Therefore $\tau_1 = -n'h/\ln(|r'|^2)$.

Meanwhile the probability of a photon remaining within the film also decays exponentially due to absorption. Disregarding losses due to photons escaping the thin film cavity, the probability of a photon being remaining in the layer is

$$\rho_2(t) = e^{-4\pi n''h/\lambda} \quad (4)$$

$$= e^{-4\pi n''ct/\lambda n'}, \quad (5)$$

so that the associated decay constant is $\tau_2 = n'\lambda/4\pi n''c$.

At critical coupling $\tau_1 = \tau_2$, so setting $e^{\tau_1} = e^{\tau_2}$ we find,

$$e^{n'\lambda/4\pi n''c} = e^{-n'h/\ln(|r'|^2)} \quad (6)$$

$$e^{-4\pi n''h/\lambda} = e^{\ln(|r'|^2)} \quad (7)$$

$$|\gamma|^4 = |r|^2, \quad (8)$$

using the definition of γ and the relationship of the Fresnel coefficients that $|r'| = |r|$. Equation 8 is consistent with Eq. 1 from the main text, although it does not contain information about the relative signs of r and γ^2 .

5. DERIVATION OF EQ. 5

The Taylor expansion of the tangent function for small arguments up to third order is $\tan(x) = x + x^3/3$. The first order expansion of Eq. 4 in the main text is therefore

$$n = \frac{im}{nk_0h/2}, \quad (9)$$

while to third order we have

$$n = \frac{im}{nk_0h/2 + \frac{1}{3}(nk_0h/2)^3}. \quad (10)$$

Upon rearranging this is

$$im = n^2k_0h/2 + \frac{1}{3}(k_0h/2)^3n^4, \quad (11)$$

and substituting in Eq. 9 for n^4 ,

$$im = n^2k_0h/2 + \frac{1}{3}(k_0h/2)^3\left(\frac{-4m^2}{k_0^2h^2}\right), \quad (12)$$

$$= n^2k_0h/2 - \frac{1}{3}(k_0h/2)m^2, \quad (13)$$

$$n^2 = \frac{2im}{k_0h} + \frac{1}{3}m^2, \quad (14)$$

$$= \frac{im\lambda}{h\pi} + \frac{1}{3}m^2, \quad (15)$$

$$(16)$$

which is Eq. 5 in the main text.

6. DERIVATION OF GRATING SCALING LAW

We consider TE or E_{\parallel} polarization in which the electric field is aligned with the grooves of a lamellar grating of thickness h , located between $-h/2 \leq z \leq h/2$. Above and below the grating, the field is written in the respective plane wave expansions

$$E(x, y) = \sum_p \eta_p^{-1/2} (\delta_p \exp(-i\chi_p z) + r_p \exp(i\chi_p z)) e_p(x), \quad (17)$$

$$E(x, y) = \sum_p \eta_p^{-1/2} t_p \exp(-i\chi_p z) e_p(x) \quad (18)$$

where δ_p , r_p and t_p denote the incident, reflected and transmitted field amplitudes, $e_p = \exp(i\alpha_p x)/\sqrt{d}$ denotes the normalised plane wave Bloch field, $\alpha_p = \alpha_0 + 2\pi p/d$, $\chi_p = \sqrt{k^2 - \alpha_p^2}$, and $\eta_p = \chi_p/k$.

Within the grating, the field is represented in the Bloch mode expansion

$$E(x, y) = \sum_n (a_n \cos(\beta_n z) + b_n \sin(\beta_n z)) u_n(x) \quad (19)$$

where $u_n(x)$ is the Bloch mode field satisfying the quasiperiodic Sturm Liouville problem

$$u_n''(x) + k^2 \varepsilon(x) u_n(x) = \beta_n^2 u_n(x) \quad (20)$$

where $\varepsilon(x)$ defines the relative permittivity distribution across the lamellar grating profile, i.e., $\varepsilon(x) = \varepsilon_a = 1$ for $0 \leq x < c_a$, and $\varepsilon(x) = \varepsilon_b$ for $c_a \leq x < c_a + c_b = d$. While for lossless gratings, the $\{u_n(x)\}$ form a mutually orthogonal set, satisfying the orthogonality relation:

$$\int_0^d u_n(x) u_m(x) dx = \delta_{nm}, \quad (21)$$

the situation for lossy material necessitates the introduction of an adjoint set of modes $\{u_n^\dagger\}$ satisfying the same differential equation (20) but with adjoint quasiperiodicity, which are biorthogonal to the primal modes, i.e.,

$$\int_0^d u_n(x) u_m^\dagger(x) dx = \delta_{nm}, \quad (22)$$

Accordingly, at the top and bottom interfaces ($z = \pm h/2$), the E-field is expressed in the respective forms:

$$\sum \eta_p^{-1/2} (\delta_p + r_p) e_p(x) = \sum_n (\tilde{a}_n + \tilde{b}_n) u_n(x), \quad (23)$$

$$\sum \eta_p^{-1/2} t_p e_p(x) = \sum_n (\tilde{a}_n - \tilde{b}_n) u_n(x), \quad (24)$$

respectively. Then, adding and subtracting these to generate the field expression corresponding to symmetric and antisymmetric incidence:

$$\sum \eta_p^{-1/2} (s_p^+ + \delta_p) e_p = 2 \sum_n \tilde{a}_n u_n(x), \quad (25)$$

$$\sum \eta_p^{-1/2} (s_p^- + \delta_p) e_p = 2 \sum_n \tilde{b}_n u_n(x) \quad (26)$$

where $s_p^\pm = r_p \pm t_p$.

To solve the boundary value problem, we need to apply the continuity of the both the tangential components of the electric and magnetic fields at the interface. We therefore need the expression for the field component H_x which, for this polarisation, is proportional to dE/dy . The corresponding expressions to Eqs (23) and (24) for dE/dy at the top and bottom interfaces are:

$$\sum_p i \eta_p^{1/2} (s_p^+ - \delta_p) e_p = 2 \sum_n D_{1n} \tilde{a}_n^2 u_n(x), \quad (27)$$

$$\sum_p i \eta_p^{1/2} (s_p^- - \delta_p) e_p = 2 \sum_n D_{2n} \tilde{b}_n^2 u_n(x), \quad (28)$$

We then solve the boundary value problems for the symmetric and antisymmetric boundary value problem by a projection method in which we project one of the pair of field matching equations onto the Bloch mode basis of free space, i.e., the plane wave basis $\{e_p\}$, and the other member of the pair onto the Bloch modes of the lamellar structure, i.e., $\{u_n\}$.

For the antisymmetric problem, we project the electric field equation (26) onto the plane wave basis, and the magnetic field equation (28) onto the grating Bloch basis to derive:

$$s_- = -\delta + 2\eta^{1/2} J \tilde{b} \quad (29)$$

$$2D_2 \tilde{b} = i J^\dagger \eta^{1/2} (s_- - \delta), \quad (30)$$

where $J = [J_{pn}]$, $J^\dagger = [J_{np}^\dagger]$

$$J_{pn} = \int_0^d e_p^*(x) u_n(x) dx, \quad (31)$$

$$J_{np}^\dagger = \int_0^d e_p(x) u_n^\dagger(x) dx. \quad (32)$$

The completeness of the plane wave and Bloch mode bases, may be expressed in matrix form

$$J J^\dagger = I, \quad (33)$$

$$J^\dagger J = I, \quad (34)$$

the derivation of which is straightforward and exploits the orthogonality of the $\{e_p\}$, and the biorthogonality of the $\{u_n\}$ and $\{u_n^\dagger\}$.

Returning to the projection equations (29) and (30), we derive

$$s_- + \delta = -B(s_- - \delta), \quad (35)$$

where $B = -i\eta^{1/2} J^\dagger D_2^{-1} J \eta^{1/2}$ and $D_2 = \text{diag}(D_{2n})$. From this it follows:

$$s_- = (I + B)^{-1} (B - I) \delta. \quad (36)$$

For the symmetrised problem, it is most convenient to project the field matching equations differently to the manner that was adopted for the antisymmetric problem. This time, we project the magnetic field equation (27) onto the plane wave basis and the electric field equation (25) on the grating Bloch mode basis. This leads to

$$s^+ + \delta = 2i\eta^{1/2} J D_1 a \quad (37)$$

$$2a = J^+ (\delta + s^+). \quad (38)$$

from which it follows

$$s^+ - \delta = -A(\delta + s^+), \quad (39)$$

where $A = i\eta^{1/2} J D_1 J^+ \eta^{-1/2}$. Accordingly,

$$s^+ = (I + A)^{-1} (I - A) \delta, \quad (40)$$

$$= [-I + 2(I + A)^{-1}] \delta. \quad (41)$$

Having now solved the diffraction problem for the lamellar grating in the general case, we now consider the limit of this formulation for ultra-thin, dense gratings. To do so, we consider the limit as the conductivity or the permittivity of the rulings is increased to infinity, i.e., $\varepsilon_b = \tilde{\varepsilon}/h \rightarrow \infty$, as the thickness of the grating decreases, i.e., $h \rightarrow 0$. To proceed further, it is necessary to understand the the form of the dominant modes in this limit, i.e., those modes for which the transverse propagation constants γ_a and γ_b in each of the two lamellar regions a and b partition into two sets have bounded values, independent of h . We begin with the expressions for the transverse propagation constants:

$$\gamma_a^2 = k^2 - \beta^2, \quad (42)$$

$$\gamma_b^2 = k^2 \frac{\tilde{\varepsilon}}{h} - \beta^2, \quad (43)$$

which follow from the Helmholtz equation.

Within the air inclusions, i.e., $\varepsilon_a = 1$, the dominant modes have $\gamma_a = O(h^0)$, from which it follows that $\beta_a = O(h^0)$ and $\gamma_b = k^2 \tilde{\varepsilon}/h = O(h^{-1})$. We call these the a -type modes and, in fact, can show that $\gamma_n^{(a)} \approx n\pi/c_a$, and that the modal form is sinusoidal in air and vanishes in the dielectric in the limit as $h \rightarrow 0$ — matching the form of the in-air modes that arise in the formulation for a zero-thickness, perfectly conducting lamellar grating.

Correspondingly, within the dense (lossy) dielectric inclusions, i.e., $\varepsilon_b = \tilde{\varepsilon}/h$, the dominant modes have $\gamma_b = O(h^0)$, from which it follows that $\beta_b = k\sqrt{\tilde{\varepsilon}}/\sqrt{h} = O(h^{-1/2})$ and $\gamma_a = ik\tilde{\varepsilon}/h = O(h^{-1/2})$. We call these the b -type modes and, in fact, $\gamma_n^{(b)} \approx n\pi/c_b$, corresponding to a modal form that is sinusoidal in the dielectric and vanishes in air in the limit as $h \rightarrow 0$ — matching the form of the surface currents on the surface of the perfectly conducting strip of zero-thickness.

In this limit, only the a - and b -type modes are of interest, in the limit as the grating thickness vanishes and the grating becomes a “grating layer”, since all other modes have too high a spatial frequency to couple to the incident field. This partitioning of modes has implications for the completeness relations (33) and (34). Indeed it can be shown that

$$J_a J_a^\dagger + J_b J_b^\dagger = I, \quad (44)$$

$$J_a^\dagger J_a = I, \quad (45)$$

$$J_a^\dagger J_b = 0, \quad (46)$$

$$J_b^\dagger J_a = 0, \quad (47)$$

$$J_b^\dagger J_b = I. \quad (48)$$

Further, it can be shown that

$$J_b J_b^\dagger = F, \quad (49)$$

where

$$F_{pq} = \int_0^d f(x) e_p(x) e_q^*(x) dx. \quad (50)$$

Here, F is a Toeplitz matrix whose elements are derived from the coefficients of a complex Fourier series for

$$f(x) = 0 \quad \text{on interval } a \\ = 1 \quad \text{on interval } b,$$

which is useful result that we shall later exploit.

Having determined the form of the lamellar grating modes, and their partitioning in the grating layer limit, we return now to the understanding the asymptotics of the diffraction problem.

For the modes of type a , $\beta_a = O(h^0)$, and so

$$D_{2a} = \beta/k_0 \cot \beta h/2 \quad (51)$$

$$\approx 2/(k_0 h). \quad (52)$$

Correspondingly, for modes of type b , $\beta_b = k_0 \sqrt{\epsilon}/h$, and so

$$D_{2b} = (\beta/k_0)2/(k_0 h) \quad (53)$$

$$\approx 2/(k_0 h). \quad (54)$$

Accordingly, $D_2 \rightarrow \infty$ as $h \rightarrow 0$, and so $D_2^{-1} \rightarrow 0$, and $B \rightarrow 0$. It therefore follows that for the antisymmetric problem:

$$s^- = -\delta. \quad (55)$$

This result, together with Eq. (41), allows us to infer that

$$t = \frac{1}{2}(s^+ - s^-) = T\delta = (I + A)^{-1}\delta. \quad (56)$$

The asymptotics of the matrix A depends on the matrix $D_1 = -(\beta/k_0) \tan(\beta h/2)$. For the modes of type a , $\beta_a = O(h^0)$, and so

$$D_{1a} = -\beta/k_0 \tan \beta h/2 \quad (57)$$

$$\approx -\frac{\beta^2 h}{k} \quad (58)$$

$$\rightarrow 0 \quad (59)$$

Correspondingly, for modes of type b , $\beta_b = k_0 \sqrt{\epsilon}/h$, and so

$$D_{1b} = -\beta/k_0 \tan \beta h/2 \quad (60)$$

$$\approx -\frac{\beta^2 h}{k} \quad (61)$$

$$\rightarrow -\frac{k\epsilon}{2} \quad (62)$$

which is independent of h . It therefore follows that

$$A = i\eta^{-1/2} J D_1 J^\dagger \eta^{-1/2} \quad (63)$$

$$= i\eta^{-1/2} (J_a D_{1a} J_b^\dagger + J_b D_{1b} J_a^\dagger) \eta^{-1/2} \quad (64)$$

$$\approx -i \frac{k\epsilon}{2} \eta^{-1/2} J_b J_b^\dagger \eta^{-1/2} \quad (65)$$

$$= \frac{s}{2} \eta^{-1/2} F \eta^{-1/2}. \quad (66)$$

where

$$s = -ik\epsilon \quad (67)$$

$$\propto \frac{\lim_{h \rightarrow 0} \epsilon h}{\lambda} \quad (68)$$

In deriving Eq. (66), we have reduced the lamellar grating formulation to the result of grating layer result of Petit and Bouchitte [1], and have elucidated the dependence of the formulation on the factor $\lim_{h \rightarrow 0} \epsilon h/\lambda$ which determines the strength of the grating layer.

While this is the key result, we proceed one step further to derive another form of the transmission scattering matrix (56) with some straightforward manipulation as follows. Proceeding formally:

$$T = (I + A)^{-1} = I - A + A^2 + \dots \quad (69)$$

$$= I - \frac{s}{2} \eta^{-1/2} J_b J_b^\dagger \eta^{-1/2} \quad (70)$$

$$+ \frac{s^2}{4} \eta^{-1/2} J_b J_b^\dagger \eta^{-1/2} \eta^{-1/2} J_b J_b^\dagger \eta^{-1/2} + \dots \quad (71)$$

$$= I - \frac{s}{2} \eta^{-1/2} J_b [I - \frac{s}{2} J_b^\dagger \eta^{-1} J_b + \dots] J_b^\dagger \eta^{-1/2} \quad (72)$$

$$= I - \frac{s}{2} \eta^{-1/2} J_b [I + \frac{s}{2} J_b^\dagger \eta^{-1} J_b] J_b^\dagger \eta^{-1/2} \quad (73)$$

$$= I - \eta^{-1/2} J_b [\frac{2}{s} I + J_b^\dagger \eta^{-1} J_b]^{-1} J_b^\dagger \eta^{-1/2}. \quad (74)$$

In the limit as $s \rightarrow \infty$, we recover the result for the current mode formulation (74) for the strip lamellar grating derived in [2].

$$T \rightarrow I - \eta^{-1/2} J_b [J_b^\dagger \eta^{-1} J_b]^{-1} J_b^\dagger \eta^{-1/2} \quad (75)$$

Alternatively, if $s = 0$, as would occur in the “soft” limit whereby $\lim_{h \rightarrow 0} \epsilon h = 0$, the grating layer would be transparent, consistent with the result from (73) for which $T = I$.

The main result (66) represents the intermediate ground whereby provided that the critical parameter s is bounded, the ultra-thin grating reduces to the grating layer considered by Petit and Bouchitte [1].

REFERENCES

1. G. Bouchitté and R. Petit, “On the concepts of a perfectly conducting material and of a perfectly conducting and infinitely thin screen,” *Radio Sci.* **24**, 13 (1989).
2. L. Botten, R. McPhedran, and G. Milton, “Perfectly Conducting Lamellar Gratings: Babinet’s Principle and Circuit Models,” *J. Mod. Opt.* **42**, 2453–2473 (1995).

7.3.1 Total Absorption in Graphene Oxide

In addition to the experimental demonstration using antimony sulphide, presented in Paper 7.2, we have investigated gratings composed of graphene oxide (GO) and reduced graphene oxide (rGO) in collaboration with the group of Jia at Swinburne University. Graphene oxide is produced directly from graphite [224] using the economic and scalable method due to Hummer [225], and the grating rulings of rGO are defined into the GO layer through femtosecond laser ablation [226].

Figure 7.2(a) shows the numerically calculated absorption of TE polarised light, normally incident upon a 80 nm thick grating composed of GO and rGO, as a function of the gratings period (d) and the volume fraction of GO (f). As in Paper 7.2, the grating is placed above an Ag mirror, separated by a layer of SiO₂; the optimum thickness of the SiO₂ layer for each combination of d and f is shown in Fig. 7.2(b). The experimental implementation of this design is ongoing.

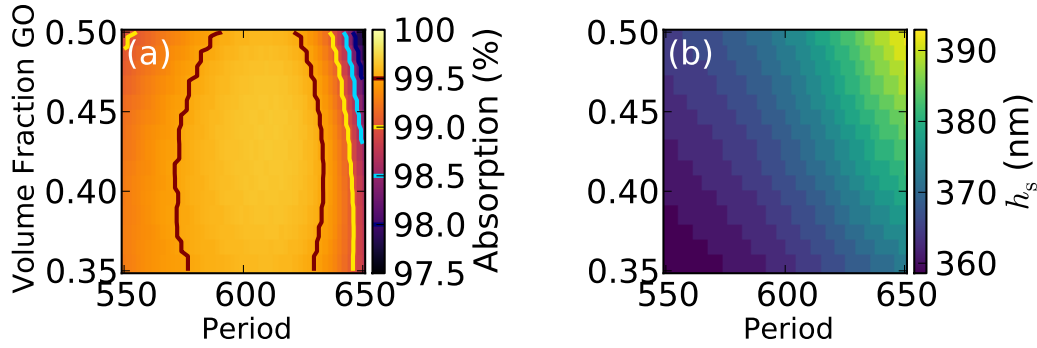


Figure 7.2: Numerical optimisation of the absorption in a 80 nm thick grating composed of GO and rGO, situated above a silver mirror, separated by a layer of silica. (a) Absorption as a function of grating period and GO volume fraction. (b) Optimum thickness of SiO₂ layer for each period and volume fraction.

Epilogue

This chapter presented the final results of this thesis, showing how ultra-thin gratings could absorb nearly 100% of light of a targeted wavelength. For TE polarisation we demonstrated experimentally that this could be realised in gratings composed of Sb₂S₃ and air. In the closing chapter we review the use of nanostructures in photovoltaic SCs, discuss how this thesis has contributed to the field, and outline where the field may be heading in the future.

Chapter 8

Conclusion and Outlook

The future will either be green, or not at all.

Bob Brown

The 2014 Nobel prize in physics was awarded for

“the invention of efficient blue light-emitting diodes which has enabled bright and energy-saving white light sources.” [227]

This dedication highlights the importance of sustainable energy technologies in addressing climate change as well as in improving living standards. There are currently 1.3 billion people without access to electricity [228]; as solar panels and white light LEDs continue to become more affordable these communities are able to leap-frog the prohibitively expensive infrastructure of the centralised electricity grid of the modern era, and go from burning kerosene and wood to owning their own self-sufficient renewable electricity and lighting systems (see for example [229, 230]).

In the past 5-10 years the prices of solar panel modules have been reduced by record amounts, which was largely due to the solar industry maturing: large-scale silicon production facilities purely dedicated to SCs were created, which reduced the cost of polysilicon from \$300 per kilogram in 2001 to roughly \$20 today; industrial processes improved rapidly, an effect known as “industrial learning” (see Fig. 2.1); and fierce competition forced companies to sell at (or even below) cost price [34]. These factors are not expected to continue, and price reductions are forecast to slow [34]. The continued reduction of the \$/W of solar energy therefore requires significant technical innovations; the inclusion of nanostructures into solar cells is one avenue by which such advances may be achieved.

In the following sections we review the research and development of nanostructures for photovoltaic solar cell applications, discuss the approaches pursued in this thesis, and provide an outlook on the likely future directions. The impact of the simulation package, EMUstack, that we created and released open-source was discussed in Ch. 3.

8.1 Optical Nanostructures for Photovoltaics

Over the previous decade the nanophotonics community has become increasingly engaged with the challenges of designing improved SCs, propelled by advances in nanofabrication and computational simulations that opened up a wide variety of new structures to explore. The community has primarily focused on nanostructures that enhance the absorption of thin film SCs, which are attractive because of their reduced consumption of expensive materials, as well as their ability to use materials of lower quality. These features were particularly appealing during the peak in the price of silicon. A subset of the structures investigated (discussed in Sect. 2.4.1) includes: of nanowires, nanocones, nanodomes, multi-diameter nanowires, nanoholes (photonic crystals), Mie scatterers, plasmonic scatterers.

Studies have generally found these nanostructures to be very effective in enhancing the absorption, and indeed it was shown that they can produce an absorption enhancement factor in excess of the Lambertian limit that applies to conventional light trapping structures, governed by ray optics. While most studies demonstrate an increase in the short circuit currents of SCs, it was recently shown that the strong concentration of fields within small absorber volumes also improves the ratio of radiative to non-radiative recombinations, thereby increasing the open circuit voltage of SCs. These findings indicate that there is much to be gained by incorporating nanostructures into PV SCs.

Whether this potential can be realised in practical devices with improved efficiencies remains, largely, to be seen. This question arises because almost all studies (including those of this thesis) have considered only the optical performance of SCs, assuming the electronic performance to either be ideal or unchanged from those of uniform reference structures. It is however well known that the high surface-area-to-volume ratios of nanostructures increases the impact of (non-radiative) surface recombinations, and that current fabrication methods tend to increase the surface defect density, exacerbating this problem. This is less of a problem for light trapping configurations with scatterers placed outside of the active region, in contrast to designs where the active absorber layer itself is structured. In all cases, these issues require further experimental investigation, and modelling using the optoelectronic techniques reviewed in Sect. 3.3.

We now review the developments of the structures examined in this thesis, before providing a general outlook in Sect. 8.2.

8.1.1 Nanostructured Absorbers

As the canonical types of nanostructured absorbers we studied nanowire and nanohole arrays as the active (absorbing) layer of thin film SCs in Chapters 4 and 5. The common approach of these studies was to examine the optical modes of the arrays as a means to obtaining physical insights that can be used to systematically design structures so as to maximise their absorption. Such insights had not been clearly articulated in the literature, partially as a consequence of the ubiquity of full field numerical tools that focus attention on quantities such as the absorption spectrum and the ultimate efficiency. An advantage of focusing on the modes is that it becomes straightforward to apply these insights to different materials, as was done in Paper 4.2.

The findings of Paper 5.1 are also general: the incorporation of NWs of differing radii into an array broadly enhances the absorption spectrum because the modes (determined by the radius) contribute resonant absorption peaks at different wavelengths. We showed how the radii of the NWs could be selected to maximise the absorption beyond what was achieved by any randomised samples, illustrating the advantage of physical insights over brute force numerical optimisation. In addition to designing NW array SCs made from arbitrary materials, this knowledge may also be applied to NW array LEDs [231] to shape their emission spectrum.

The analysis in Paper 5.2 led to the conclusion that improvements in absorption due to irregularly spacing the NWs was due to clusters of NWs approximating larger NWs. This suggests that the improvements observed by other studies, and by our own, due to disordered arrangements are conditional upon starting with suboptimal ordered arrays. The semi-analytic optimisation routine of Paper 4.2 allows future studies, for example of disorder or of the electrical properties of arrays, to avoid focussing on suboptimal optical structure. Paper 4.2 provided quantitative prescriptions and synthesises the different optical effects along with the relevant geometric parameters into a consistent framework, which will be of value as the field matures and more research is directed towards applications.

Although one of the oft-cited advantages of NW arrays is the incorporation of radial p-n junctions that allow the use of materials with low charge-carrier diffusion lengths, researchers are now generally focussing on developing III-V semiconductor NWs. This is because nanofabrication processes increase the cost of NW array SCs, even when made from cheap materials, beyond that which is competitive compared to unstructured thin film SCs. III-V materials are more promising because the monetary value of reducing the material

consumption is greater, and the thin films used in III-V SCs are also produced using growth techniques so the cost difference is less significant. Another important distinction of high quality III-V materials is that they have intrinsically high radiative efficiencies, which allows them to capitalise on the thermodynamic advantages of strong absorption in small volumes.

With the optical advantages of nanostructured absorbers now well established, their further development depends upon their fabrication, and how this effects their electrical performance. The critical issue for the SC performance of NW arrays is the passivation of the defect states on their large surface areas in order to reduce the non-radiative recombinations. Passivation techniques have steadily improved in the last five years, in particular for III-V semiconductors such as GaAs, for which InGaP and AlGaAs have been shown to be very effective [148, 157, 158]. Indeed the record efficiency of a NW SC of 15.3% was achieved by a GaAs NW SC [148] whose improved efficiency over previous NW SCs was mostly due to an increased V_{oc} of 0.923 V, which the authors attribute to improved passivation [148]. This type of GaAs NW SC is being commercialised by a company *Sol Voltaics* [232], who are using the patented substrate-less aerotaxy fabrication technique [233] that was also used to create the record efficiency SC. Motivated by the opportunities highlighted in Sect. 6.1.1, the company appears to be focussing on developing GaAs NW SCs for use in silicon-based tandem SCs, with a stated aim of increasing the efficiency of the silicon panels from 16% to 27% tandem SCs [234].

8.1.2 Dielectric Gratings

The latter half of this thesis focussed less strictly on PV applications, as we shifted our attention from structured absorbers to lossy dielectric gratings. In Ch. 6 we investigated how Fano resonances of dielectric gratings suspended in a low-index background produce broadband reflections, while in Ch. 7 we studied the total absorption of light in ultra-thin gratings.

Our investigations of dielectric gratings began with a search for grating designs that can blaze a large amount of energy into highly evanescent diffraction orders, which would produce a strong near-field absorption enhancement that could be harvested in an ultra-thin absorbing layer. Our exploration uncovered a distinct lack of any such physics, instead finding that all resonances are driven by propagating modes within the grating ($\text{Re}(k_{\perp}) > 0$), which limits the magnitude of the transverse wavevector (k_{\parallel}) and thereby the decay constant of the evanescent field outside of the grating.

Meanwhile the same types of gratings we were investigating were being assessed as wavelength selective filters in mechanically decoupled multi-junction SCs by the Atwater group, which we realised during a visit to this group. In addition to this solar application, the broadband reflections of high-contrast gratings are well established in a wide range of applications including: optical isolators [235]; cavities in hybrid lasers [236, 237]; and in enhancing the Purcell effect, creating polariton-based lasers and quantum circuits, and exotic quantum phases in polaritons [238]. It is not yet clear whether dielectric gratings are ultimately the best structures for these applications; for spectrum-splitting multi-junction SCs the questions of immediate interest concern the performance of gratings relative to Bragg stacks, comparing in particular the losses due to absorption and light directed to the wrong subcell.

In Paper 6.2, we considered the underlying mechanism that causes the broad reflections, which had not been addressed in previous numerical optimisations and experimental demonstrations. This required knowledge of the complex reflection coefficient as a function of complex frequencies. A limitation of our work was the consideration of linearly polarised light; lamellar gratings are strongly polarisation sensitive, whereas solar radiation is unpolarised and requires polarisation insensitive components to achieve reasonable efficiencies. While our fundamental insights regarding the symmetries of the Fano resonances extend in a straightforward manner to bi-periodic gratings (which are not polarisation sensitive) the realisation of effective structures for unpolarised light remains an open challenge. Additionally, future work may consider chirping the gratings to achieve broader spectral features (eg. absorption).

Our final results, presented in Ch.7, demonstrated that gratings of deeply subwavelength thickness can absorb nearly 100% of light at target wavelengths. This was shown numerically, explained with a comprehensive theoretical analysis, and verified experimentally using gratings composed of antimony sulphide in collaboration with researchers at the Australian National University. Our numerical results indicate that total absorption can be achieved in ultra-thin gratings composed of a very wide range of complex refractive indices; the critical parameter was found to be $\epsilon h/\lambda$. TLA in ultra-thin structures had previously been demonstrated in metallic structures, exotic materials with $n' \sim n''$, nanoplasmonics, and in metamaterials, whereas our study revealed that TLA could be achieved in very simple gratings made from common semiconductor-type materials. These findings significantly reduce the hurdles for ultra-thin absorbers to be incorporated into photodetectors and SCs, and may also enable further applications that have not been imagined for the complicated perfect absorbers.

8.2 Outlook

As mentioned in Ch. 2, the current conditions for emerging thin film SC technologies are challenging; silicon technologies are supremely well established in the marketplace and have achieved impressive economies of scale in production. Meanwhile the costs of installation now outweigh the costs of production, placing a greater emphasis on the absolute power conversion efficiency particularly in settings where the available space is limited. These conditions are refining the separations in the SC market as technologies must either have significantly lower costs, or substantially higher efficiencies, than silicon SCs in order to compete.

In the lower cost market segments there are many thin film technologies competing for applications where cost, flexibility, semi-transparency and weight are at a premium, such as in portable consumer goods [239], buildings, and (potentially) electric cars. For NW SCs the major difficulty lies in reducing fabrication costs, particularly as other technologies in the same efficiency range of $10\% < \eta < 15\%$, such as organic and dye-sensitised SCs, are typically inexpensive to produce [240, 241]. Conventional thin-film technologies have recently been overshadowed by a frenzied interest in perovskite SCs. The certified efficiencies of these SCs has risen at unprecedented rates in the last 5 years (see Fig. 2.10) to $\eta > 20\%$. This development is made even more remarkable by being built upon a highly sensitive and not yet fully understood class of materials. Some of the major unanswered questions relate to: isolating the role of different environmental factors in fabrication of high performance SCs; finding a high efficiency chemical composition that is free of toxins such as lead; improve the SCs stability and longevity. As these questions are addressed in the coming years, there may very well be a significant role for perovskite SCs to play in the solar market.

At the higher efficiency end of the market there has been interest in creating mechanically decoupled multi-junction SCs. Nanophotonics structures may have a crucial role in these devices, managing the separation of the solar spectrum between seven or more SCs. The efficiency target of these ultra-high efficiency device is $\eta > 50\%$, approximately 5% greater than the all-time SC efficiency record. The other type of high-efficiency SC attracting attention at the moment is silicon-based tandem SCs. We earlier noted that GaAs NW are being developed for this application [149, 232], as are perovskites [105, 191–195, 197]. The silicon-based tandem configuration holds the promise of improving efficiencies by over 5% in absolute terms, without a correspondingly substantial increase in costs [105, 232].

In addition to the recognised applications of the nanostructures to energy technologies, discussed in this thesis, there is significant scope for the optical physics to find uses in yet unforeseen ways. An example of alternative uses of NWs comes from Crozier *et al.*, who have developed NW array multicoloured photodetectors, where the pixels colour sensitivity is determined by tuning the radius of the NWs [242, 243], similar to our approach in Paper 5.1. Another promising research direction (facilitated by the equivalence of absorption and emission as stated in Kirchhoff's law) is use of nanophotonic structure in controlling the emission of light, for instance in enhancing the extraction-efficiency of LEDs or manipulating

their emission spectra. NW array LEDs are being commercialised by glō [244], where the emitted colour is tuned by varying the radius of the individual NWs. This approach can be used to create colour displays or alternatively they could be used to design the emitted colour spectrum of a light source [231]. As a final example of the potential for nanophotonics structures to address our energy needs we mention passive cooling device conceived and demonstrated by Fan *et al.* [245, 246]. The operating principle of this device is to weakly absorb/emit radiation of visible and near-infrared wavelengths ($0.3 < \lambda < 2.5 \mu\text{m}$), reflecting the incident photons from the sun, while simultaneously strongly emitting/absorbing mid-infrared wavelengths ($8 < \lambda < 13 \mu\text{m}$) where there is a transmission window in the atmosphere that allows the thermal emission from the device to efficiently radiate into (cold) outer-space. This approach has been demonstrated to have a cooling power of 40.1 Watts per square metre, cooling the device by 4.9 degrees Celsius below ambient air temperature when exposed to direct sunlight [246].

The developments of nanophotonics have provided us with a large amount of control over the interaction of light and matter, in particular allowing us to manipulate the propagation of light and its absorption/emission. One of the important applications of this knowledge is in improving the technologies that allow us to produce and consume electricity sustainably: photovoltaic solar cells and light emitting diodes. For these technologies to continue to progress, their optical performance must be improved, which in many cases may be achieved through the purposeful design of dielectric nanostructures.

While the advancement of solar energy technologies has too oft been hindered, there is a certain inevitability in its rise; the sheer abundance of the solar resource is simply too great to ignore in favour of non-renewable fuels. The crucial question is therefore: how many years and degrees will we let pass, before transitioning to a sustainable future?

Bibliography

1. B. C. P. Sturmberg, K. B. Dossou, L. C. Botten, A. A. Asatryan, C. G. Poulton, R. C. McPhedran and C. M. de Sterke. “Nanowire array photovoltaics: Radial disorder versus design for optimal efficiency”. *Appl. Phys. Lett.* **101**, 173902 (2012).
2. B. C. P. Sturmberg, K. B. Dossou, L. C. Botten, A. A. Asatryan, C. G. Poulton, R. C. McPhedran and C. M. de Sterke. “Absorption enhancing proximity effects in aperiodic nanowire arrays”. *Opt. Express* **21**, A964–A969 (2013).
3. B. C. P. Sturmberg, K. B. Dossou, L. C. Botten, A. A. Asatryan, C. G. Poulton, R. C. McPhedran and C. M. de Sterke. “Optimizing Photovoltaic Charge Generation of Nanowire Arrays: Simple Semi-Analytic Approach”. *ACS Photonics* **1**, 683–689 (2014).
4. B. C. P. Sturmberg, K. B. Dossou, L. C. Botten, R. C. McPhedran and C. M. de Sterke. “Fano resonances of dielectric gratings: symmetries and broadband filtering”. *Opt. Express* **23**, A1672 (2015).
5. B. C. P. Sturmberg, K. B. Dossou, F. J. Lawrence, C. G. Poulton, R. C. McPhedran, C. M. de Sterke and L. C. Botten. “EMUstack: an open source route to insightful electromagnetic computation via the Bloch mode scattering matrix method”. *Computer Physics Communications* (In Press).
6. B. C. P. Sturmberg, T. K. Chong, T. P. White, D.-Y. Choi, L. C. Botten, K. B. Dossou, C. G. Poulton, K. R. Catchpole, R. C. McPhedran and C. M. de Sterke. “Total absorption of visible light in ultra-thin weakly-absorbing semiconductor gratings”. *Optica* (Submitted).
7. J. L. Donnelly, B. C. P. Sturmberg, K. B. Dossou, L. C. Botten, A. A. Asatryan, C. G. Poulton, R. C. McPhedran and C. M. de Sterke. “Mode-based analysis of silicon nanohole arrays for photovoltaic applications”. *Opt. Express* **22**, A1343–A1354 (2014).
8. J. S. Brownless, B. C. P. Sturmberg, A. Argyros, B. T. Kuhlmeier and C. M. de Sterke. “Guided modes of a wire medium slab: Comparison of effective medium approaches with exact calculations”. *Phys. Rev. B* **91**, 155427 (2015).
9. The Intergovernmental Panel on Climate Change. *Climate Change 2014 Synthesis Report Summary Chapter for Policymakers*. 2014.
10. International Energy Agency. “2014 Key World Energy Statistics” (2014).
11. A.-E. Becquerel. “Recherches sur les effets de la radiation chimique de la lumière solaire au moyen des courants électriques”. *Comptes Rendus de l’Académie des Sciences* **9**, 145–149 (1839).
12. A.-E. Becquerel. “Mémoire sur les effets électriques produits sous l’influence des rayons solaires”. *Annalen der Physik und Chemie* **54**, 35–42 (1841).
13. D. M. Chapin, C. Fuller and G. Pearson. “A new silicon p-n junction photocell for converting solar radiation into electrical power”. *Journal of Applied Physics*, 676–677 (1954).
14. M. A. Green. “The path to 25% silicon solar cell efficiency: History of silicon cell evolution”. *Prog. Photovoltaics Res. Appl.* **17**, 183–189 (2009).
15. R. Perez and M. Perez. *The world’s energy reserves: a fundamental look*. 2009.
16. International Energy Agency. *Tracking Clean Energy Progress 2015*. 2015.

17. U. E. I. Administration. *Levelized Cost and Levelized Avoided Cost of New Generation Resources in the Annual Energy Outlook 2015*.
18. P. R. Epstein *et al.* “Full cost accounting for the life cycle of coal”. *Ann. N. Y. Acad. Sci.* **1219**, 73–98 (2011).
19. F. C. Moore and D. B. Diaz. “Temperature impacts on economic growth warrant stringent mitigation policy”. *Nat. Clim. Chang.* **5**, 127–131 (2015).
20. *International Technology Roadmap for Photovoltaic 2014 Results*. 2015.
21. C. D. Bailie *et al.* “Semi-transparent perovskite solar cells for tandems with silicon and CIGS”. *Energy Environ. Sci.* **8**, 956–963 (2015).
22. P. Fairley. “Edison’s Revenge: The Rise of DC Power”. *MIT Technol. Rev.* 11–13 (2012).
23. “Edison’s revenge”. *The Economist* (2013).
24. L. Bird, M. Milligan and D. Lew. *Integrating Variable Renewable Energy : Challenges and Solutions*. Tech. rep. September (2013).
25. “International Technology Roadmap for Photovoltaic 2010” (2010).
26. F. K. Lutgens and E. J. Tarbuck. *Essentials of Geology* (Prentice Hall, 2000).
27. R. Bernstein. *A Shortage Hits Solar Power*. 2006.
28. ENF Solar. *Polysilicon Manufacturers*.
29. J. Weiss. *Solar Energy Support in Germany A Closer Look*. 2014.
30. B. Burger. *Electricity production from solar and wind in Germany in 2014*. 2014.
31. A. Hobbs and B. Pierpont. “Improving Solar Policy: Lessons from the solar leasing boom in California Climate Policy Initiative” (2013).
32. T. Alafita and J. M. Pearce. “Securitization of Residential Solar Photovoltaic Assets: Costs, Risks and Uncertainty”. *Energy Policy* **67**, 488–498 (2014).
33. A. C. Goodrich, D. M. Powell, T. L. James, M. Woodhouse and T. Buonassisi. “Assessing the drivers of regional trends in solar photovoltaic manufacturing”. *Energy Environ. Sci.* **6**, 2811 (2013).
34. T. Edis. *Trina’s chief scientist: don’t expect a solar price plunge*. 2015.
35. P. Würfel. *Physics of Solar Cells* (Wiley, 2005).
36. L. C. Hirst and N. J. Ekins-Daukes. “Fundamental losses in solar cells”. *Prog. Photovoltaics Res. Appl.* (2010).
37. W. Shockley and H. J. Queisser. “Detailed balance Limit of Efficiency of p-n Junction Solar Cells”. *J. Appl. Phys.* **32**, 510–519 (1961).
38. T. O. M. Tiedje, E. Yablonovitch, G. D. Cody and B. G. Brooks. “Limiting Efficiency of Silicon”. *IEEE Trans. Electron Devices* **31**, 711–716 (1984).
39. G. Kirchhoff. “Ueber das Verhältniss zwischen dem Emissionsvermögen und dem Absorptionsvermögen der Körper für Wärme und Licht”. *Ann. der Phys. und Chemie* **185**, 275–301 (1860).
40. M. Planck. “Entropie und Temperatur strahlender Wärme”. *Ann. Phys.* **306**, 719–737 (1900).
41. M. Planck. “Ueber das Gesetz der Energieverteilung im Normalspectrum”. *Ann. Phys.* **309**, 553–563 (1901).
42. M. Peters, J. C. Goldschmidt, T. Kirchartz and B. Bläsi. “The photonic light trap-Improved light trapping in solar cells by angularly selective filters”. *Sol. Energy Mater. Sol. Cells* **93**, 1721–1727 (2009).
43. A. Polman and H. A. Atwater. “Photonic design principles for ultrahigh-efficiency photovoltaics”. *Nat. Mater.* **11**, 174–177 (2012).
44. U. Rau, U. W. Paetzold and T. Kirchartz. “Thermodynamics of light management in photovoltaic devices”. *Phys. Rev. B* **90**, 035211 (2014).

45. H. A. Atwater and A. Polman. “Reply to ‘On the thermodynamics of light trapping in solar cells’.” *Nat. Mater.* **13**, 104–5 (2014).
46. S. Sandhu, Z. Yu and S. Fan. “Detailed balance analysis of nanophotonic solar cells.” *Opt. Express* **21**, 1209–17 (2013).
47. A. Niv, M. Gharghi, C. Gladden, O. D. Miller and X. Zhang. “Near-Field Electromagnetic Theory for Thin Solar Cells”. *Phys. Rev. Lett.* **109**, 138701 (2012).
48. S. Sandhu, Z. Yu and S. Fan. “Detailed balance analysis and enhancement of open-circuit voltage in single-nanowire solar cells.” *Nano Lett.* **14**, 1011–5 (2014).
49. N. R. E. Laboratories. *Best Research-Cell Efficiencies*. 2015.
50. R. R. King *et al.* *Next-generation, high-efficiency III-V multijunction solar cells*. in *IEEE Conf. Photovolt. Spec.* (2000), 28–31.
51. C. H. Henry. “Limiting efficiencies of ideal single and multiple energy gap terrestrial solar cells”. *J. Appl. Phys.* **51**, 2294–4500 (1980).
52. T. Yamaguchi, Y. Ichihashi, T. Mishima, N. Matsubara and T. Yamanishi. “Achievement of More Than 25 % Conversion Heterojunction Solar Cell”. **4**, 1433–1435 (2014).
53. E. Yablonovitch, O. D. Miller, S. R. Kurtz, M. S. Division, L. Berkeley, C. Sciences and N. Renewable. “The Opto-Electronic Physics that Broke the Efficiency Limit in Solar Cells”. *IEEE Conf. Photovolt. Spec.* **3**, 1556–1559 (2011).
54. T. Gmitter and E. Yablonovitch. *Lift-off and subsequent bonding of epitaxial films*. 1989.
55. I. Gordon, F. Dross, V. Depauw, A. Masolin, Y. Qiu, J. Vaes, D. Van Gestel and J. Poortmans. “Three novel ways of making thin-film crystalline-silicon layers on glass for solar cell applications”. *Sol. Energy Mater. Sol. Cells* **95**, S2–S7 (2011).
56. R. Swanson. “Approaching the 29% limit efficiency of silicon solar cells”. *Proc. IEEE Photovolt. Spec. Conf.* (2005).
57. A. Descoeurdes *et al.* “Silicon Heterojunction Solar Cells: Towards Low-cost High-Efficiency Industrial Devices and Application to Low-concentration PV”. *Energy Procedia* **77**, 508–514 (2015).
58. H. Sai, T. Matsui, T. Koida, K. Matsubara, M. Kondo, S. Sugiyama, Y. Takeuchi and I. Yoshida. “Triple-junction thin-film silicon solar cell fabricated on periodically textured substrate with a stabilized efficiency of 13.6%”. *Appl. Phys. Lett.* **106**, 213902 (2015).
59. P. Jackson, D. Hariskos, R. Wuerz, O. Kiowski, A. Bauer, T. M. Friedlmeier and M. Powalla. “Properties of Cu(In,Ga)Se₂ solar cells with new record efficiencies up to 21.7%”. *Phys. Status Solidi - Rapid Res. Lett.* **9**, 28–31 (2015).
60. First Solar. *First Solar Builds the Highest Efficiency Thin Film PV Cell on Record*. 2014.
61. Greentechmedia. *Rest in Peace: The List of Deceased Solar Companies*. 2013.
62. R. Komiya, A. Fukui, N. Murofushi, N. Koide, R. Yamanaka and H. Katayama. “Improvement of the conversion efficiency of a monolithic type dyesensitized solar cell module”. *Technical Digest of the 21st International Photovoltaic Science and Engineering Conference* (2011).
63. D. M. K. Cyrus Wadia, A. Paul Alivisatos. “Materials Availability Expands the Opportunity for Large-Scale Photovoltaics Deployment”. *Environ. Sci. Technol* **43**, 2072–2077 (2009).
64. T. K. Todorov, K. B. Reuter and D. B. Mitzi. “High-efficiency Solar Cell with Earth-Abundant Liquid-Processed Absorber”. *Adv. Mater.* **22**, E156–9 (2010).
65. H. J. Snaith. “Perovskites: The Emergence of a New Era for Low-Cost, High-Efficiency Solar Cells”. *J. Phys. Chem. Lett* **4**, 3623–3630 (2013).
66. M. A. Green, A. Ho-Baillie and H. J. Snaith. “The emergence of perovskite solar cells”. *Nat. Photonics* **8**, 506–514 (2014).
67. V. Sivaram, S. D. Stranks and H. J. Snaith. “Out-shining Silicon”. *Sci. Am.* **313**, 54–59 (2015).

68. E. Cars, S. Power, W. Power and S. A. Post. *Perovskites Will Power New Low-Cost & Highly Efficient Solar Cells*. 2015.
69. U. Irfan. *Tandem Solar Cell May Boost Electricity from Sunlight*. 2015.
70. S. Saeed, E. M. L. D. de Jong, K. Dohnalova and T. Gregorkiewicz. “Efficient optical extraction of hot-carrier energy”. *Nat. Commun.* **5**, 1–5 (2014).
71. M. A. Green. “Third generation photovoltaics: Ultra-high conversion efficiency at low cost”. *Prog. Photovoltaics Res. Appl.* **9**, 123–135 (2001).
72. A. Luque and A. Martí. “Photovoltaics: Towards the intermediate band”. *Nat. Photonics* **5**, 137–138 (2011).
73. S. V. Boriskina and G. Chen. “Exceeding the solar cell Shockley–Queisser limit via thermal up-conversion of low-energy photons”. *Opt. Commun.* **314**, 71–78 (2014).
74. N. Aravantinos-Zafiris, M. M. Sigalas, M. Kafesaki and E. N. Economou. “Phononic crystals and elastodynamics: Some relevant points”. *AIP Adv.* **4**, 124203 (2014).
75. K. R. Catchpole and A. Polman. “Plasmonic solar cells.” *Opt. Express* **16**, 21793–800 (2008).
76. H. A. Atwater and A. Polman. “Plasmonics for improved photovoltaic devices.” *Nat. Mater.* **9**, 205–13 (2010).
77. P. Spinelli, V. E. Ferry, J. van de Groep, M. van Lare, M. A. Verschuuren, R. E. I. Schropp, H. A. Atwater and A. Polman. “Plasmonic light trapping in thin-film Si solar cells”. *J. Opt.* **14**, 024002 (2012).
78. V. E. Ferry, M. A. Verschuuren, H. B. T. Li, R. E. I. Schropp, H. A. Atwater and A. Polman. “Improved red-response in thin film a-Si:H solar cells with soft-imprinted plasmonic back reflectors”. *Appl. Phys. Lett.* **95**, 1–4 (2009).
79. I.-K. Ding *et al.* “Plasmonic Dye-Sensitized Solar Cells”. *Adv. Energy Mater.* **1**, 52–57 (2011).
80. J. F. Wise and J. F. Holt. *Wedged channel vertical junction silicon solar cell*. 1982.
81. P. Campbell and M. A. Green. “High performance light trapping textures for monocrystalline silicon solar cells”. *Sol. Energy Mater.* **65**, 369–375 (2001).
82. J. Zhao, A. Wang, P. Campbell and M. A. Green. “22.7% efficient PERL silicon solar cell module with a textured front surface”. *Proc. IEEE Photovolt. Spec. Conf.* 1133–1136 (1997).
83. www.pveducation.org/pvcdrom/design/surface-texturing.
84. E. Yablonovitch and G. D. Cody. “Intensity Enhancement in Textured Optical Sheets for Solar-Cells”. *IEEE Trans. Electron Devices* **29**, 300–305 (1982).
85. Z. Yu, A. Raman and S. Fan. “Nanophotonic light-trapping theory for solar cells”. *Appl. Phys. A* **105**, 329–339 (2011).
86. Z. Yu, A. Raman and S. Fan. “Fundamental limit of light trapping in grating structures.” *Opt. Express* **18 Suppl 3**, A366–A380 (2010).
87. D. M. Callahan, J. N. Munday and H. A. Atwater. “Solar cell light trapping beyond the ray optic limit”. *Nano Lett.* **12**, 214–218 (2012).
88. Z. Yu, N. P. Sergeant, T. Skauli, G. Zhang, H. Wang and S. Fan. “Enhancing far-field thermal emission with thermal extraction.” *Nat. Commun.* **4**, 1730 (2013).
89. N. Anttu. “Shockley–Queisser Detailed Balance Efficiency Limit for Nanowire Solar Cells”. *ACS Photonics* **2**, 446–453 (2015).
90. M. L. Brongersma, Y. Cui and S. Fan. “Light management for photovoltaics using high-index nanostructures.” *Nat. Mater.* **13**, 451–60 (2014).
91. K. X. Wang, Z. Yu, V. Liu, Y. Cui and S. Fan. “Absorption enhancement in ultrathin crystalline silicon solar cells with antireflection and light-trapping nanocone gratings”. *Nano Lett.* **12**, 1616–1619 (2012).
92. Y. Yao, J. Yao, V. K. Narasimhan, Z. Ruan, C. Xie, S. Fan and Y. Cui. “Broadband light management using low-Q whispering gallery modes in spherical nanoshells”. *Nat. Commun.* **3**, 664 (2012).

93. S. Zanotto, M. Liscidini and L. C. Andreani. “Light trapping regimes in thin-film silicon solar cells with a photonic pattern”. *Optics Express* **18**, 4260 (2010).
94. A. Bozzola, M. Liscidini and L. C. Andreani. “Photonic light-trapping versus Lambertian limits in thin film silicon solar cells with 1D and 2D periodic patterns”. *Optics Express* **20**, A224 (2012).
95. D. Liang, Y. Kang, Y. Huo, Y. Chen, Y. Cui and J. S. Harris. “High-Efficiency Nanostructured Window GaAs Solar Cells.” *Nano Lett.* **13**, 4850–6 (2013).
96. P. Spinelli, M. A. Verschuuren and A. Polman. “Broadband omnidirectional antireflection coating based on subwavelength surface Mie resonators.” *Nat. Commun.* **3**, 692 (2012).
97. P. Spinelli and A. Polman. “Light Trapping in Thin Crystalline Si Solar Cells Using Surface Mie Scatterers”. *IEEE J. Photovoltaics* **4**, 554–559 (2014).
98. J. Zhu, Z. Yu, G. F. Burkhard, C.-M. Hsu, S. T. Connor, Y. Xu, Q. Wang, M. McGehee, S. Fan and Y. Cui. “Optical Absorption Enhancement in Amorphous Silicon Nanowire and Nanocone Arrays”. *Nano Lett.* **9**, 279–282 (2009).
99. J. Zhu, C.-M. Hsu, Z. Yu, S. Fan and Y. Cui. “Nanodome Solar Cells with Efficient Light Management and Self-Cleaning”. *Nano Lett.* 1979–1984 (2010).
100. Y. Lu and A. Lal. “High-efficiency ordered silicon nano-conical-frustum array solar cells by self-powered parallel electron lithography.” *Nano Lett.* **10**, 4651–6 (2010).
101. Z. Fan *et al.* “Ordered Arrays of Dual-Diameter Nanopillars for Maximized Optical Absorption”. *Nano Lett.* **10**, 3823–3827 (2010).
102. B. Hua, B. Wang, M. Yu, P. W. Leu and Z. Fan. “Rational geometrical design of multi-diameter nanopillars for efficient light harvesting”. *Nano Energy*, 1–7 (2013).
103. L.-K. Yeh, K.-Y. Lai, G.-J. Lin, P.-H. Fu, H.-C. Chang, C.-A. Lin and J.-H. He. “Giant Efficiency Enhancement of GaAs Solar Cells with Graded Antireflection Layers Based on Syringelike ZnO Nanorod Arrays”. *Adv. Energy Mater.* **1**, 506–510 (2011).
104. B. Hua, Q. Lin, Q. Zhang and Z. Fan. “Efficient photon management with nanostructures for photovoltaics.” *Nanoscale* **5**, 6627–40 (2013).
105. T. P. White, N. N. Lal and K. R. Catchpole. “Tandem Solar Cells Based on High-Efficiency for > 30% Efficiency”. *IEEE J. Photovoltaics* **4**, 208–214 (2014).
106. www.rolith.com/technology/rolling-mask-lithography.
107. M. A. Verschuuren and H. A. van Sprang. “Large-area nanopatterns: improving LEDs, lasers, and photovoltaics”. *SPIE Newsroom*, 2–4 (2012).
108. Z. Geng, X. Guo, Q. Kan and H. Chen. “Optimization of substrate conformal imprint lithography (SCIL) and etching for nanostructure”. *AIP Adv.* **5**, 041308 (2015).
109. S. Jeong, L. Hu, H. R. Lee, E. C. Garnett, J. W. Choi and Y. Cui. “Fast and Scalable Printing of Large Area Monolayer Nanoparticles for Nanotexturing Applications”. *Nano Lett.* **10**, 2989–2994 (2010).
110. K. B. Dossou, L. C. Botten, A. A. Asatryan, B. C. P. Sturmberg, M. A. Byrne, C. G. Poulton, R. C. McPhedran and C. M. de Sterke. “Modal formulation for diffraction by absorbing photonic crystal slabs”. *J. Opt. Soc. Am. A* **29**, 817–831 (2012).
111. D. T. Grant, K. J. Weber, M. Stocks and T. P. White. *Optical Optimization of Perovskite-Silicon Reflective Tandem Solar Cells*. in Proceedings of the OSA Conference on Optical Nanostructures and Advanced Materials for Photovoltaics (2015).
112. M. G. Deceglie, V. E. Ferry, A. P. Alivisatos and H. A. Atwater. “Design of nanostructured solar cells using coupled optical and electrical modeling.” *Nano Lett.* **12**, 2894–900 (2012).
113. P. Bermel. “Photon management modeling and beyond for photovoltaics”. *Opt. Commun.* **314**, 66–70 (2014).
114. A. Shang, X. Zhai, C. Zhang, Y. Zhan, S. Wu and X. Li. “Nanowire and nanohole silicon solar cells: a thorough optoelectronic evaluation”. *Prog. Photovoltaics Res. Appl.* (2015).

115. N. M. Ali, N. K. Allam, A. M. Abdel Haleem and N. H. Rafat. “Analytical modeling of the radial pn junction nanowire solar cells”. *J. Appl. Phys.* **116** (2014).
116. B. M. Kayes, H. A. Atwater and N. S. Lewis. “Comparison of the device physics principles of planar and radial p-n junction nanorod solar cells”. *J. Appl. Phys.* **97**, 114302 (2005).
117. E. C. Garnett, M. L. Brongersma, Y. Cui and M. D. McGehee. “Nanowire Solar Cells”. *Annu. Rev. Mater. Res.* **41**, 269–295 (2011).
118. A. Kandala, T. Betti and A. Fontcuberta i Morral. “General theoretical considerations on nanowire solar cell designs”. *Phys. Status Solidi* **206**, 173–178 (2009).
119. M. Kevin, Y. H. Fou, A. S. W. Wong and G. W. Ho. “A novel maskless approach towards aligned, density modulated and multi-junction ZnO nanowires for enhanced surface area and light trapping solar cells.” *Nanotechnology* **21**, 315602 (2010).
120. L. Wen, X. Li, Z. Zhao, S. Bu, X. Zeng, J.-H. Huang and Y. Wang. “Theoretical consideration of III-V nanowire/Si triple-junction solar cells.” *Nanotechnology* **23**, 505202 (2012).
121. Z. Fan *et al.* “Three-dimensional Nanopillar-Array Photovoltaics on Low-Cost and Flexible Substrates”. *Nat. Mater.* **8**, 648–53 (2009).
122. L. Hu and G. Chen. “Analysis of Optical Absorption in Silicon Nanowire Arrays for Photovoltaic Applications”. *Nano Lett.* **7**, 3249–52 (2007).
123. C. Lin and M. L. Povinelli. “Optical absorption enhancement in silicon nanowire arrays with a large lattice constant for photovoltaic applications.” *Opt. Express* **17**, 19371–19381 (2009).
124. J. Kupec and B. Witzigmann. “Dispersion , Wave Propagation and Efficiency Analysis of Nanowire”. *Opt. Express* **17**, 5290–5298 (2009).
125. J. Kupec, R. L. Stoop and B. Witzigmann. “Light absorption and emission in nanowire array solar cells”. *Opt. Express* **18**, 4651–4656 (2010).
126. N. Anttu and H. Q. Xu. “Coupling of Light into Nanowire Arrays and Subsequent Absorption”. *J. Nanosci. Nanotechnol.* **10**, 7183–7187 (2010).
127. B. Wang and P. W. Leu. “Tunable and selective resonant absorption in vertical nanowires”. *Opt. Lett.* **37**, 3756–8 (2012).
128. A. W. Snyder and J. D. Love. *Optical Waveguide Theory* (Chapman and Hall, 1983).
129. B. C. P. Sturmberg, K. B. Dossou, L. C. Botten, A. A. Asatryan, C. G. Poulton, C. M. de Sterke and R. C. McPhedran. “Modal analysis of enhanced absorption in silicon nanowire arrays”. *Opt. Express* **19**, A1067–81 (2011).
130. K. T. Fountaine, C. G. Kendall and H. A. Atwater. “Near-unity broadband absorption designs for semiconducting nanowire arrays via localized radial mode excitation”. *Opt. Express* **22**, A930 (2014).
131. D. R. Abujetas, R. Paniagua-Domínguez and J. A. Sánchez-Gil. “Unraveling the Janus Role of Mie Resonances and Leaky/Guided Modes in Semiconductor Nanowire Absorption for Enhanced Light Harvesting”. *ACS Photonics* **2**, 921–929 (2015).
132. P. Kailuweit, M. Peters, J. Leene, K. Mergenthaler, F. Dimroth and A. W. Bett. “Numerical simulations of absorption properties of InP nanowires for solar cell applications”. *Prog. Photovoltaics Res. Appl.* **20**, 945–953 (2011).
133. J. Li, H. Yu and Y. Li. “Solar energy harnessing in hexagonally arranged Si nanowire arrays and effects of array symmetry on optical characteristics”. *Nanotechnology* **23**, 194010 (2012).
134. N. Huang, C. Lin and M. L. Povinelli. “Broadband absorption of semiconductor nanowire arrays for photovoltaic applications”. *J. Opt.* **14**, 24004 (2012).
135. P. M. Wu, N. Anttu, H. Q. Xu, L. Samuelson and M.-E. Pistol. “Colorful InAs nanowire arrays: from strong to weak absorption with geometrical tuning.” *Nano Lett.* **12**, 1990–5 (2012).
136. N. Anttu and H. Q. Xu. “Efficient light management in vertical nanowire arrays for photovoltaics”. *Opt. Express* **21**, 27589–27605 (2013).

137. H. Alaeian, A. C. Atre and J. A. Dionne. “Optimized light absorption in Si wire array solar cells”. *J. Opt.* **14**, 024006 (2012).
138. Y. Cui *et al.* “Efficiency enhancement of InP nanowire solar cells by surface cleaning”. *Nano Lett.* **13**, 4113–4117 (2013).
139. J. Wallentin *et al.* “InP Nanowire Array Solar Cells Achieving 13.8% Efficiency by Exceeding the Ray Optics Limit”. *Science* **339**, 1057–60 (2013).
140. M. Yao, N. Huang, S. Cong, C.-Y. Chi, M. A. Seyedi, Y.-T. Lin, Y. Cao, M. L. Povinelli, P. D. Dapkus and C. Zhou. “GaAs nanowire array solar cells with axial p-i-n junctions.” *Nano Lett.* **14**, 3293–303 (2014).
141. B. M. Kayes *et al.* “Radial p-n Junction, Wire Array Solar Cells”. *Proc. IEEE Photovolt. Spec. Conf.* 1–5 (2008).
142. E. C. Garnett and P. Yang. “Silicon Nanowire Radial p-n Junction Solar Cells”. *J. Am. Chem. Soc.* **130**, 9224–5 (2008).
143. O. Gunawan, K. Wang, B. Fallahazad, Y. Zhang, E. Tutuc and S. Guha. “High performance wire-array silicon solar cells”. *Prog. Photovoltaics Res. Appl.* **19**, 307–312 (2010).
144. E. C. Garnett and P. Yang. “Light trapping in silicon nanowire solar cells.” *Nano Lett.* **10**, 1082–7 (2010).
145. M. Law, L. E. Greene, J. C. Johnson, R. Saykally and P. Yang. “Nanowire dye-sensitized solar cells”. *Nat. Mater.* **4**, 455–459 (2005).
146. S. Ren, L.-Y. Chang, S.-K. Lim, J. Zhao, M. Smith, N. Zhao, V. Bulović, M. Bawendi and S. Gradecak. “Inorganic-organic hybrid solar cell: bridging quantum dots to conjugated polymer nanowires.” *Nano Lett.* **11**, 3998–4002 (2011).
147. N. Huang, S. Member and M. L. Povinelli. “Design of Passivation Layers on Axial Junction GaAs Nanowire Solar Cells”. *IEEE J. Photovoltaics* **4**, 1511–1517 (2014).
148. I. Åberg *et al.* “A GaAs Nanowire Array Solar Cell with 15 . 3 % Efficiency at 1 Sun”. *IEEE J. Photovoltaics*, 3–5 (2015).
149. M. Yao, S. Cong, S. Arab, N. Huang, M. L. Povinelli, S. B. Cronin, D. P. Dapkus and C. Zhou. “Tandem solar cells using GaAs nanowires on Si: Design, Fabrication, and Observation of voltage addition”. *Nano Lett.* *acs.nanolett.5b03890* (2015).
150. J. D. Christesen, X. Zhang, C. W. Pinion, T. A. Celano, C. J. Flynn and J. F. Cahoon. “Design principles for photovoltaic devices based on Si nanowires with axial or radial p-n junctions.” *Nano Lett.* **12**, 6024–9 (2012).
151. N. Huang, C. Lin and M. L. Povinelli. “Limiting efficiencies of tandem solar cells consisting of III-V nanowire arrays on silicon”. *J. Appl. Phys.* **112**, 064321 (2012).
152. C. T. Chen, D. B. Turner-Evans, H. Emmer, S. Aloni and H. A. Atwater. “Design and growth of III-V on Si microwire array tandem solar cells”. *Proc. IEEE Photovolt. Spec. Conf.* 3397–3401 (2013).
153. P. Zhang, P. Liu, S. Siontas, A. Zaslavsky, D. Pacifici, J.-Y. Ha, S. Krylyuk and A. V. Davydov. “Dense nanoimprinted silicon nanowire arrays with passivated axial p-i-n junctions for photovoltaic applications”. *J. Appl. Phys.* **117**, 125104 (2015).
154. D. Kohen, C. Morin, P. Faucherand, A. Brioude and S. Perraud. “Enhanced photovoltaic performance of vapor-liquid-solid grown silicon nanowire array with radial heterojunction”. *Phys. Status Solidi* **211**, 1143–1149 (2014).
155. R. Kapadia, Z. Fan, K. Takei and A. Javey. “Nanopillar photovoltaics: Materials, processes, and devices”. *Nano Energy* **1**, 132–144 (2012).
156. J. Y. Kwon, D. H. Lee, M. Chitambar, S. Maldonado, A. Tuteja and A. Boukai. “High efficiency thin upgraded metallurgical-grade silicon solar cells on flexible substrates.” *Nano Lett.* **12**, 5143–7 (2012).
157. R. R. LaPierre *et al.* “III-V nanowire photovoltaics: Review of design for high efficiency”. *Phys. status solidi - Rapid Res. Lett.* **16** (2013).

158. G. Mariani, A. C. Scofield, C.-H. Hung and D. L. Huffaker. “GaAs nanopillar-array solar cells employing in situ surface passivation”. *Nat. Commun.* **4**, 1497 (2013).
159. A. Chutinan, N. P. Kherani and S. Zukotynski. “High-efficiency photonic crystal solar cell architecture.” *Opt. Express* **17**, 8871–8 (2009).
160. S.-F. Leung, M. Yu, Q. Lin, K. Kwon, K.-L. Ching, L. Gu, K. Yu and Z. Fan. “Efficient photon capturing with ordered three-dimensional nanowell arrays.” *Nano Lett.* **12**, 3682–9 (2012).
161. G. Gomard, E. Drouard, X. Letartre, X. Meng, A. Kaminski, A. Fave, M. Lemiti, E. Garcia-Caurel and C. Seassal. “Two-dimensional photonic crystal for absorption enhancement in hydrogenated amorphous silicon thin film solar cells”. *J. Appl. Phys.* **108**, 123102 (2010).
162. G. Gomard, R. Peretti, S. Callard, X. Meng, R. Artinyan, T. Deschamps, P. Roca i Cabarrocas, E. Drouard and C. Seassal. “Blue light absorption enhancement based on vertically channelling modes in nano-holes arrays”. *Appl. Phys. Lett.* **104**, 051119 (2014).
163. L. Genzel and T. P. Martin. “Infrared Absorption by Surface Phonons and Surface Plasmons in Small Crystals”. *Surf. Sci.* **34**, 33–49 (1973).
164. D. A. G. Bruggeman. “Berechnung verschiedener physikalischer Konstanten von heterogenen Substanzen”. *Ann. Phys.* **416**, 636–664 (1935).
165. J. A. del Rio and S. Whitaker. “Maxwell’s Equations in Two-Phase Systems I: Local Electrodynamic Equilibrium”. *Transp. Porous Media* **39**, 159–186 (2000).
166. J. A. del Rio and S. Whitaker. “Maxwell’s Equations in Two-Phase Systems II: Two-Equation Model”. *Transp. Porous Media* **39**, 259–287 (2000).
167. N. J. Hutchinson, T. Coquil, A. Navid and L. Pilon. “Effective optical properties of highly ordered mesoporous thin films”. *Thin Solid Films* **518**, 2141–2146 (2010).
168. A. Navid and L. Pilon. “Effect of polarization and morphology on the optical properties of absorbing nanoporous thin films”. *Thin Solid Films* **516**, 4159–4167 (2008).
169. K. R. Waters, J. Mobley and J. G. Miller. “Causality-imposed (Kramers-Kronig) relationships between attenuation and dispersion”. *IEEE Trans. Ultrason. Ferroelectr. Freq. Control* **52**, 822–833 (2005).
170. E. Akkermans. *Mesoscopic Physics of Electrons and Photons*, 588 (Cambridge University Press, 2007).
171. B. I. Shklovskii and A. L. Efros. *Electronic properties of doped semiconductors* (Izdatel’stvo Nauka, 1979).
172. J. E. Lye, L. Fallani, M. Modugno, D. S. Wiersma, C. Fort and M. Inguscio. “Bose-Einstein condensate in a random potential”. *Phys. Rev. Lett.* **95**, 10–13 (2005).
173. A. Aspect and M. Inguscio. “Anderson localization of ultracold atoms”. *Phys. Today* **62**, 30–35 (2009).
174. S. John. “Strong localization of photons in certain disordered dielectric superlattices”. *Phys. Rev. Lett.* **58**, 2486–2489 (1987).
175. D. S. Wiersma, P. Bartolini, A. Lagendijk and R. Righini. “Localization of light in a disordered medium”. *Nature* **390**, 671–673 (1997).
176. P. Sebbah and C. Vanneste. “Random laser in the localized regime”. *Phys. Rev. B* **66**, 1–10 (2002).
177. H. Noh, J. K. Yang, S. F. Liew, M. J. Rooks, G. S. Solomon and H. Cao. “Control of lasing in biomimetic structures with short-range order”. *Phys. Rev. Lett.* **106**, 1–4 (2011).
178. M. Burresti, F. Pratesi, F. Riboli and D. S. Wiersma. “Complex Photonic Structures for Light Harvesting”. *Adv. Opt. Mater.* **3**, 722–743 (2015).
179. H. Bao and X. Ruan. “Optical absorption enhancement in disordered vertical silicon nanowire arrays for photovoltaic applications.” *Opt. Lett.* **35**, 3378–80 (2010).

180. Q. G. Du, C. H. Kam, H. V. Demir, H. Y. Yu and X. W. Sun. “Broadband absorption enhancement in randomly positioned silicon nanowire arrays for solar cell applications.” *Opt. Lett.* **36**, 1884–6 (2011).
181. C. Lin, N. Huang and M. L. Povinelli. “Effect of aperiodicity on the broadband reflection of silicon nanorod structures for photovoltaics”. *Opt. Express* **20**, A125 (2011).
182. Q. G. Du, C. H. Kam, H. V. Demir, H. Y. Yu and X. W. Sun. “Enhanced optical absorption in nanopatterned silicon thin films with a nano-cone-hole structure for photovoltaic applications.” *Opt. Lett.* **36**, 1713–1715 (2011).
183. K. Vynck, M. Burrese, F. Riboli and D. S. Wiersma. “Photon management in two-dimensional disordered media”. *Nat. Mater.* **11**, 1–6 (2012).
184. F. Pratesi, M. Burrese, F. Riboli, K. Vynck and D. S. Wiersma. “Disordered photonic structures for light harvesting in solar cells”. *Opt. Express* **21**, A460 (2013).
185. A. Oskooi, M. D. Zoysa, K. Ishizaki and S. Noda. “Experimental Demonstration of Quasi-resonant Absorption in Silicon Thin Films for Enhanced Solar Light Trapping”. *ACS Photonics* **4** (2013).
186. D. A. R. Barkhouse, O. Gunawan, T. Gokmen, T. K. Todorov and D. B. Mitzi. “Device characteristics of a 10.1% hydrazine-processed $\text{Cu}_2\text{ZnSn}(\text{Se,S})_4$ solar cell”. *Prog. Photovoltaics Res. Appl.* **20**, 6–11 (2012).
187. C. Lin, L. J. Martinez and M. L. Povinelli. “Experimental broadband absorption enhancement in silicon nanohole structures with optimized complex unit cells”. *Opt. Express* **21**, A872–A882 (2013).
188. A. Bozzola, M. Liscidini and L. C. Andreani. “Broad-band light-trapping with disordered photonic structures in thin film silicon solar cells”. *Prog. Photovoltaics Res. Appl.* **22**, 1237 (2014).
189. S. Wu, C. Zhang, X. Li and Y. Zhan. “Proximity effect assisted absorption enhancement in thin film with locally clustered nanoholes.” *Opt. Lett.* **40**, 792–5 (2015).
190. S. Enoch and N. Bonod. *Plasmonics: from basics to advanced topics*, 39–83 (Springer, 2012).
191. S. De Wolf, J. Holovsky, S.-J. Moon, P. Löper, B. Niesen, M. Ledinsky, F.-J. Haug, J.-H. Yum and C. Ballif. “Organometallic Halide Perovskites: Sharp Optical Absorption Edge and Its Relation to Photovoltaic Performance”. *J. Phys. Chem. Lett.* **5**, 1035–1039 (2014).
192. N. N. Lal, T. P. White and K. R. Catchpole. “Optics and Light Trapping for Tandem Solar Cells on Silicon”. *IEEE J. Photovoltaics* **4**, 1380–1386 (2014).
193. P. Löper *et al.* “Organic – Inorganic Halide Perovskites: Perspectives for Silicon-Based Tandem Solar Cells”. *IEEE J. Photovoltaics* **4**, 1545–1551 (2014).
194. C. D. Bailie and M. D. McGehee. “High-efficiency tandem perovskite solar cells”. **40**, 681–686 (2015).
195. H. Uzu, M. Ichikawa, M. Hino, K. Nakano, T. Meguro, J. L. Hernández, H.-S. Kim, N.-G. Park and K. Yamamoto. “High efficiency solar cells combining a perovskite and a silicon heterojunction solar cells via an optical splitting system”. *Appl. Phys. Lett.* **106**, 013506 (2015).
196. S. Essig, S. Ward, M. A. Steiner, D. J. Friedman, J. F. Geisz, P. Stradins and D. L. Young. “Progress Towards a 30% Efficient GaInP/Si Tandem Solar Cell”. *Energy Procedia* **77**, 464–469 (2015).
197. D. Zhang, W. Soppe and R. E. Schropp. “Design of 4-terminal Solar Modules Combining Thin-film Wide-Bandgap Top Cells and c-Si Bottom Cells”. *Energy Procedia* **77**, 500–507 (2015).
198. A. De Vos and H. Pauwels. “On the Thermodynamic Limit of Photovoltaic Energy Conversion”. *Appl. Phys.* **25**, 119–125 (1981).

199. J. Zhao, A. Wang, M. A. Green and F. Ferrazza. “19.8% Efficient “Honeycomb” Textured Multicrystalline and 24.4% Monocrystalline Silicon Solar Cells”. *Appl. Phys. Lett.* **73**, 1991 (1998).
200. W. S. Yang, J. H. Noh, N. J. Jeon, Y. C. Kim, S. Ryu, J. Seo and S. I. Seok. “High-performance photovoltaic perovskite layers fabricated through intramolecular exchange”. *Science* **348**, 1234–1237 (2015).
201. M. Grätzel. “The light and shade of perovskite solar cells”. *Nat. Mater.* **13**, 838–842 (2014).
202. A. Kojima, K. Teshima, Y. Shirai and T. Miyasaka. “Organometal Halide Perovskites as Visible-Light Sensitizers for Photovoltaic Cells”. *J. Am. Chem. Soc.* **131**, 6050–6051 (2009).
203. S. H. Im, C.-S. Lim, J. A. Chang, Y. H. Lee, N. Maiti, H.-J. Kim, M. K. Nazeeruddin, M. Grätzel and S. I. Seok. “Toward interaction of sensitizer and functional moieties in hole-transporting materials for efficient semiconductor-sensitized solar cells.” *Nano Lett.* **11**, 4789–93 (2011).
204. M. A. Green and T. Bein. “Photovoltaics: Perovskite cells charge forward”. *Nat. Mater.* **14**, 559–561 (2015).
205. M. H. Kumar *et al.* “Lead-Free Halide Perovskite Solar Cells with High Photocurrents Realized Through Vacancy Modulation”. *Adv. Mater.* **26**, 7122–7127 (2014).
206. N. J. Jeon, J. H. Noh, W. S. Yang, Y. C. Kim, S. Ryu, J. Seo and S. I. Seok. “Compositional engineering of perovskite materials for high-performance solar cells”. *Nature* **517**, 476–480 (2015).
207. Z. Xiao, Y. Yuan, Y. Shao, Q. Wang, Q. Dong, C. Bi, P. Sharma, A. Gruverman and J. Huang. “Giant switchable photovoltaic effect in organometal trihalide perovskite devices”. *Nat. Mater.* **14**, 193–198 (2014).
208. M. D. McGehee. “Perovskite solar cells: Continuing to soar”. *Nat. Mater.* **13**, 845–846 (2014).
209. J. H. Noh and S. I. Seok. “Steps toward efficient inorganic–organic hybrid perovskite solar cells”. *MRS Bull.* **40**, 648–653 (2015).
210. M. A. Green, K. Emery, Y. Hishikawa, W. Warta and E. D. Dunlop. “Solar cell efficiency tables (version 39)”. *Prog. Photovoltaics Res. Appl.* **20**, 12–20 (2012).
211. J. P. Mailoa, C. D. Bailie, E. C. Johlin, E. T. Hoke, A. J. Akey, W. H. Nguyen, M. D. McGehee and T. Buonassisi. “A 2-terminal perovskite/silicon multijunction solar cell enabled by a silicon tunnel junction”. *Appl. Phys. Lett.* **106**, 121105 (2015).
212. A. G. Imenes and D. R. Mills. “Spectral beam splitting technology for increased conversion efficiency in solar concentrating systems: a review”. *Sol. Energy Mater. Sol. Cells* **84**, 19–69 (2004).
213. S. Kim, S. Kasashima, P. Sichanugrist, T. Kobayashi, T. Nakada and M. Konagai. “Development of thin-film solar cells using solar spectrum splitting technique”. *Sol. Energy Mater. Sol. Cells* **119**, 214–218 (2013).
214. A. Goetzberger, J. Goldschmidt, M. Peters and P. Loper. “Light trapping, a new approach to spectrum splitting”. *Sol. Energy Mater. Sol. Cells* **92**, 1570–1578 (2008).
215. C. N. Eisler, Z. R. Abrams, M. T. Sheldon, X. Zhang and H. A. Atwater. “Multijunction solar cell efficiencies: effect of spectral window, optical environment and radiative coupling”. *Energy Environ. Sci.* **7**, 3600–3605 (2014).
216. C. N. Eisler, E. C. Warmann, C. A. Flowers, M. Dee, E. D. Kosten and H. A. Atwater. “Design improvements for the polyhedral specular reflector spectrum-splitting module for ultra-high efficiency (>50%)”. *2014 IEEE 40th Photovolt. Spec. Conf.* 2224–2229 (2014).
217. M. D. Escarra, S. Darbe, E. C. Warmann and H. A. Atwater. “Spectrum-splitting photovoltaics: Holographic spectrum splitting in eight-junction, ultra-high efficiency module”. *2013 IEEE 39th Photovolt. Spec. Conf.* 1852–1855 (2013).

218. C. N. Eisler, E. D. Kosten, E. C. Warmann and H. A. Atwater. “Polyhedral specular reflector design for ultra high spectrum splitting solar module efficiencies (>50%)”. **8821**, 88210B (2013).
219. M. S. Leite, R. L. Woo, J. N. Munday, W. D. Hong, S. Mesropian, D. C. Law and H. A. Atwater. “Towards an optimized all lattice-matched InAlAs/InGaAsP/InGaAs multijunction solar cell with efficiency >50%”. *Appl. Phys. Lett.* **102**, 033901 (2013).
220. C. Huygens and W. Ostwald. “Abhandlung über das Licht: worin die Ursachen der Vorgänge bei seiner Zurückwerfung und Brechung und besonders bei der eigenthümlichen Brechung des isländischen Spathes dargelegt sind”. *W. Engelmann* **20** (1903).
221. V. R. Almeida, C. A. Barrios, R. R. Panepucci and M. Lipson. “All-optical control of light on a silicon chip”. *Nature* **431**, 1081–1084 (2004).
222. R. W. Boyd. *Nonlinear optics* (Academic press, 2003).
223. J. Zhang, K. F. MacDonald and N. I. Zheludev. “Controlling light-with-light without non-linearity”. *Light Sci. Appl.* **1**, 1–5 (2012).
224. www.graphenea.com/pages/reduced-graphene-oxide.
225. W. S. Hummers Jr. and R. E. Offeman. “Preparation of Graphitic Oxide”. *J. Am. Chem. Soc.* **80**, 1339–1339 (1958).
226. X. Zheng, H. Lin, L. Qiu, D. Li, B. Jia and M. Gu. “Subwavelength Focusing”. *Nat. Commun.* **6**, 1–7 (2015).
227. Nobelprize.org. *The Nobel Prize in Physics 2014*.
228. International Energy Agency. *World Energy Outlook*.
229. pollinateenergy.org.
230. www.bboxx.co.uk.
231. D. Wang, X. Bao, B. Xiang, C. Soci and D. Aplin. *Nanowire array-based light emitting diodes and lasers*. US Patent 8,426,224. 2013.
232. www.solvoltaics.com.
233. M. Heurlin, M. H. Magnusson, D. Lindgren, M. Ek, L. R. Wallenberg, K. Deppert and L. Samuelson. “Continuous gas-phase synthesis of nanowires with tunable properties.” *Nature* **492**, 90–94 (2012).
234. E. U. E. A. for Small and M.-s. Enterprises. *Accelerating Commercialization of Nanowire Solar Cell Technologies*.
235. T. Glaser, S. Schröter, H. Bartelt, H.-J. Fuchs and E.-B. Kley. “Diffractive optical isolator made of high-efficiency dielectric gratings only.” *Appl. Opt.* **41**, 3558–3566 (2002).
236. C. Chang-Hasnain and W. Yang. “High-contrast gratings for integrated optoelectronics”. *Adv. Opt. Photon.* **4**, 379–440 (2012).
237. A. Taghizadeh, J. Mørk and I.-S. Chung. “Ultracompact resonator with high quality-factor based on a hybrid grating structure”. *Opt. Express* **23**, 17282–17287 (2015).
238. Z. Wang, B. Zhang and H. Deng. “Dispersion Engineering for Vertical Microcavities Using Subwavelength Gratings”. *Phys. Rev. Lett.* **114**, 73601 (2015).
239. MIT Technology Review. *Alta Devices Plans a Fast-Charging Solar iPad Cover*. 2012.
240. A. M. Bagher. “Introduction to Organic Solar Cells”. *Sustain. Energy* **2**, 85–90 (2014).
241. J. Kalowekamo and E. Baker. “Estimating the manufacturing cost of purely organic solar cells”. *Sol. Energy* **83**, 1224–1231 (2009).
242. K. Seo, M. Wober, P. Steinvurzel, E. Schonbrun, Y. Dan, T. Ellenbogen and K. B. Crozier. “Multicolored vertical silicon nanowires.” *Nano Lett.* **11**, 1851–6 (2011).
243. K. Seo, M. Wober, P. Steinvurzel, E. Schonbrun, Y. Dan and K. Crozier. *Light absorption and filtering properties of vertically oriented semiconductor nano wires*. US Patent 9,000,353. 2015.

244. glo. *Nanowire LED Technology*.
245. E. Rephaeli, A. Raman and S. Fan. “**Ultrabroadband photonic structures to achieve high-performance daytime radiative cooling.**” *Nano Lett.* **13**, 1457–1461 (2013).
246. A. Raman, M. A. Anoma, L. Zhu, E. Rephaeli and S. Fan. “**Passive radiative cooling below ambient air temperature under direct sunlight**”. *Nature* **515**, 540–544 (2014).